Molecular Imprinting of Glycoprotein Recognition Sites Using Surface Initiated Radical Polymerization

Philippa A. Mitchell

A thesis submitted to The University of Birmingham for the Degree of DOCTOR OF PHILOSOPHY School of Chemical Engineering College of Engineering and Physical Sciences

The University of Birmingham

October 2018

Abstract

Since the importance of glycoproteins and their role in the development of diseases are becoming increasingly recognised there is a growing need for highly sensitive and selective glycoprotein recognition platforms. Herein, a novel molecularly imprinted glycoprotein sensor that displays a high affinity for its target glycoprotein was developed using surface-initiated radical polymerisation. The sensor was developed by first fabricating a suitable self-assembled monolayer (SAM) that was then used as the foundation from which the polymerisation procedure to later be used for the imprinting procedure was developed. Particular focus was given to establishing control over the polymerisation reaction in order to optimise the thickness of the polymer layer to the desired depth. Alongside these investigations, complexation studies aimed at elucidating the binding of a functional boronic acid monomer to the model glycoprotein, RNase B, were undertaken using mass spectrometry. Here, we aimed to optimise the binding conditions to encourage the monomer ligand to bind the glycoprotein, whilst also ensuring that the protein remained stable in these conditions. Finally, we brought together these studies to then form imprints for RNase B. Several imprints were fabricated and then extensively characterised, following which surface plasmon resonance (SPR) was used to examine their binding affinities towards the RNase B target and control glycoproteins.

Chapter 1 – A Review of Glycoprotein Sensing Systems

This chapter presents an:

a) *Introduction to glycosylation and its role in the development of diseases such as cancer*

b) Introduction to SAMs and their application in fabricating biosensors such as molecular imprinted surfaces using radical polymerisation processes.

The improvements in imprinting biomolecules such as glycoproteins will be discussed.

Chapter 2 – Surface Characterisation Techniques.

Outlines the background theory behind each of the surface characterisation techniques and protein analysis techniques used in this work.

Chapter 3 – Formation and Characterisation of Surfaces Suitable for Polymerisation

This Chapter explores the fabrication of two different initiator SAMs which are first characterised and then tested for their suitability to produce polymers. Using the most suitable SAM, the polymerisation conditions are then optimised to polymer thicknesses suitable for imprinting.

Chapter 4 – Complexation of the Model Glycoprotein with a Functional Monomer

This Chapter examines the complexation of the model glycoprotein, RNase B, with a functional boronic acid monomer. The optimal conditions to produce complexes are explored using mass spectrometry and the conformational stability of the RNase B is then examined using circular dichroism.

Chapter 5 – Synthesis of Glycoprotein Molecular Imprints

This Chapter describes the synthesis of molecular imprints of the RNase B-boronic acid monomer complex using the polymerisation procedure developed in Chapter 3. The imprinted surfaces are then tested for target rebinding using SPR.

Chapter 6 – Conclusions and Future Work

Provides and overview of each chapter alongside the future studies that could be undertaken from the basis of this thesis.

Chapter 7 – Experimental Procedures, Protocols and Synthesis.

Describes the experimental procedures used during the investigations performed in this work.

An overview of the thesis layout comprising the above sections of this work is shown below in figure a.

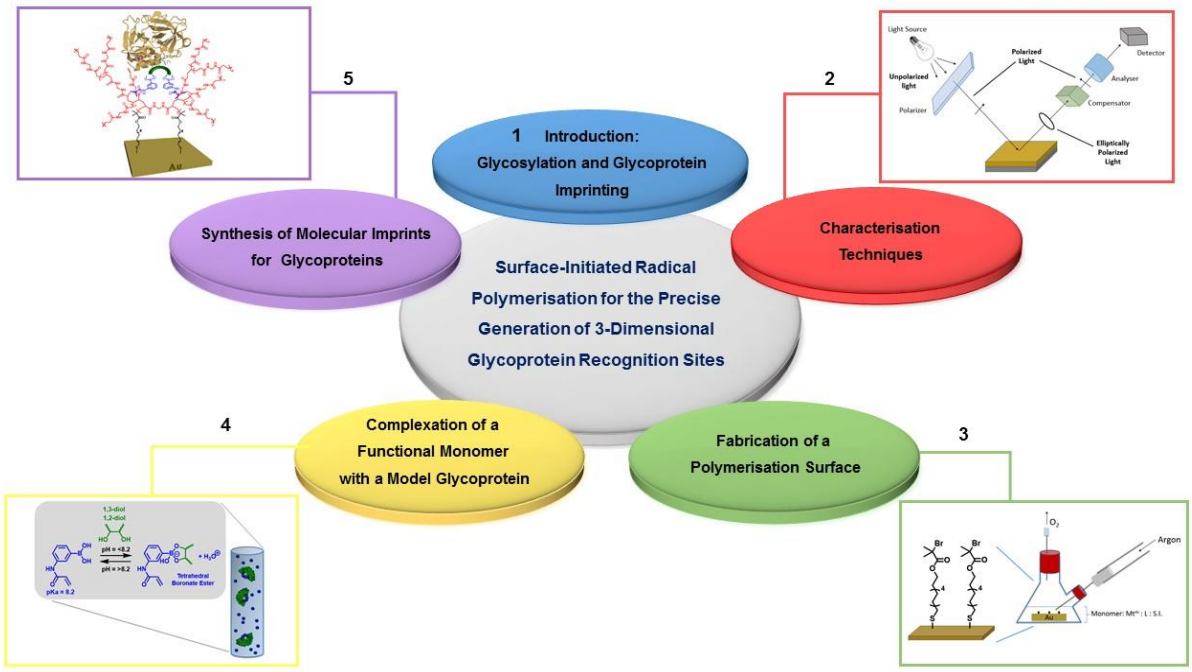

Figure a: Schematic representation of the thesis layout, with numbers shown referring to the each chapter.

Acknowledgements

This thesis is the outcome of three years research work at the School of Chemical Engineering, the School of Chemistry and the School of Bioscience of the University of Birmingham, kindly funded by the EPSRC.

Firstly, I would like to thank Prof. P. M. Mendes for her supervision and support throughout the three years of experimental work and writing. Your input has been essential in the outcome of this work and I will always appreciate your guidance. Secondly, I would like to thank Dr Lewis Hart, Dr Stefano Tommasone and Dr Eduardo Anya for their unrivalled support in guiding this study - both in their scientific expertise and their continued faith in me. Thank you all. Special thanks goes to Dr James Bowen for his help with the ellipsometry and AFM data, Dr James Mcgettrick and Dr Neal Fairley with the XPS and Dr Chi Tsang for the mass spectrometry. Thank you all for your expertise, recommendations and patience.

I would also like to thank the members of the Mendes Group, both old and new – Monika Köpf, Bárbara Santos-Gomes, Giuseppe Di Palma, Simone Basile, Fatima Zia, Francia Allabush, Zarrar Hussain, Kamlesh Patel, Joshua Norman, Dr Joshua Gibson, Alice Di Pasquale, Barbara Simoes, Yazmin Tagger and James Walker.

Lastly and most importantly, I would like to thank my incredible friends and family for all they have done to keep me sane throughout this time. Becca, thank you for always being there no matter what life throws at us. Babs and Monika – thank you for being the best lab mates and most kind, understanding friends. Will, thank you for your love and for always making me laugh. Mum, Dad, Ali and Katie, Tommy and Lauren, Nanny and Gran and Grandad – Thank you all, I would not have been able to complete this without your support, encouragement and love.

Table of Contents

List of Figures and Tables

Figures

Tables

List of Definitions and Abbreviations

11-DTMBD: 11,11'Dithiobis[1-(2-bromo-2-methylpropionyloxy)undecane]

2-bp: 2,2'-bipyridial

AFM: Atomic Force Microscopy

BA: Boronic Acid

CD: Circular Dichroism

E-2-BB: Ethyl-2-bromoisobutyrate

ESI-MS: Electrospray Ionisation Spectroscopy

MEBA: *N,N'*-Methylenebisacrylamide

MUD: 11-mercaptoundecanol

SPR: Surface Plasmon Resonance

UDT: 1-undecanethiol

XPS: X-ray Photoelectron Spectrometry

Chapter 1: A Review of Glycoprotein Sensing Systems

Chapter Outline

This chapter presents a review of the literature that covers a broad range of topics to provide the reader with an understanding of the history and recent advances in glycoprotein sensing systems. We begin with an introduction to carbohydrates, following which we then introduce the roles that these structures play when attached to proteins in the process known as glycosylation. We then discuss how aberrant glycosylation of proteins plays a major role in the development of diseases and discuss the standard methods, such as lectin and antibody assays, that have been used for carbohydrate and glycoprotein sensing. We then introduce boronic acids and their use as the sensing functionality in sugar and saccharides detection systems.

In the latter half of the chapter we introduce the fabrication of nanotechnology sensing platforms with focus on those that use self-assembled structures as the foundation of the sensor. We then cover how SAMs have been used to develop newer sensing techniques such as molecular imprinting technologies. We discuss the different forms of polymerisation that can be employed to fabricate these synthetic receptors, before covering a range of molecular imprinting systems that have been recently reported for glycoproteins. Within this section we pay particular attention to systems that have incorporated boron functionalities within their design in order to target the saccharide chains of biomolecules. Finally, we conclude the review by summarising the challenges faced to improve glycoprotein detection, before presenting an overview of the glycoprotein imprinting system outlined within the remainder of this thesis.

1.0 Introduction to Carbohydrates

Saccharides are one of the fundamental components used in nature for a multitude of physiological processes. Saccharides show a broad array of structural sizes and complexities, which range from the most basic monosaccharide units (such as glucose, fructose or galactose) to the large and complex carbohydrate structures found at cell interfaces. Their varied characteristics enable them to be used for a variety of functions, for example by working as effectors for cellular communication and recognition processes, providing structural support to the cell, or as source of energy to help maintain homeostasis [1]. As they are inherently fundamental to biological systems there is a demand for suitable saccharide detection methods that can sense both the concentration and type of saccharide present. The classic examples of such saccharide detection methods are systems that employ enzymes, antibodies or lectins to detect the analyte of interest [2-5]. However, several drawbacks to these setups include the fragility of these biomolecules when used in non-optimal conditions, interference from contaminants in the matrix, as well as consumption of the target analyte due to enzymatic catalysis [6]. To this end, the development of novel methods to identify both simple and complex saccharides that improve upon these limitations are much needed and have continued to be explored during the past two decades.

1.1 The Monosaccharide

The most basic unit of any saccharide structure is the monosaccharide. Each unit is comprised of a carbon backbone with hydroxyl moieties spaced at distinct intervals along the length of the chain. The typical empirical formula for each unit is $(C\text{-}H_2O)_n$,

with *n* ranging between three to seven repeats [7]. Due to the high number of chiral carbons along the length of each molecule, monosaccharides are inherently heterogenic in their chemical nature due to their forming structural isomers. This has led to developing methods that enable the distinction between the subtle differences in the position of the hydroxyl moieties of the molecules.

Before touching upon more complex carbohydrates that arise from covalently binding several monosaccharides together *via* hydrolysis reactions, we must first address the different ways in which saccharides can be presented. The most commonly used projections are the Fischer or Haworth projections. Here, the saccharide is presented in its open chain or cyclic form, respectively. The advantage of the Fischer projection is that the carbon stereo centres are more clearly observed, whereas the cyclic Haworth projection provides a better presentation of the spatial arrangements of the hydroxyl moieties. Examples of both aforementioned configurations are shown in figure 1.1, a and b using a D-glucose molecule. In aqueous solutions, saccharides are in constant equilibrium between their linear and cyclic forms, with the latter form being preferred [8]. Cyclisation occurs due to one of the hydroxyl moieties (for example, the hydroxyl found off carbon 4 or 5 of figure 1.1, a) attacking the ketone or aldehyde group of the anomeric carbon (i.e. carbon 1 of figure 1.1, a) to form an intramolecular hemi-acteyl. Typically, 6 membered ‘pyranose’ rings are formed during cyclisation, however 5 membered ‘furanose’ rings are also possible but less common due to constraints on the structure [9].

During the process of cyclisation, there are two possible configurations that the hydroxyl moiety attached to the carbon 1 of the figure 1.1 a and b can take relative to the ring structure. The hydroxyl group can either be pointing down in the α, axial position or alternatively up in the β, equatorial arrangement. These differences are

likewise observed in the open chain Fischer projections shown in figure 1.2 to produce the D- and L- anomers of glucose which correspond with the α and β configurations, respectively. It is important to note however, that in aqueous solution the anomers can switch between the D- and L- configurations in a process known as mutarotation. This event changes the ratio of the α and β ring configurations present in solution over time with the β configuration dominating with respect to the α configuration at ~2:1 [10, 11].

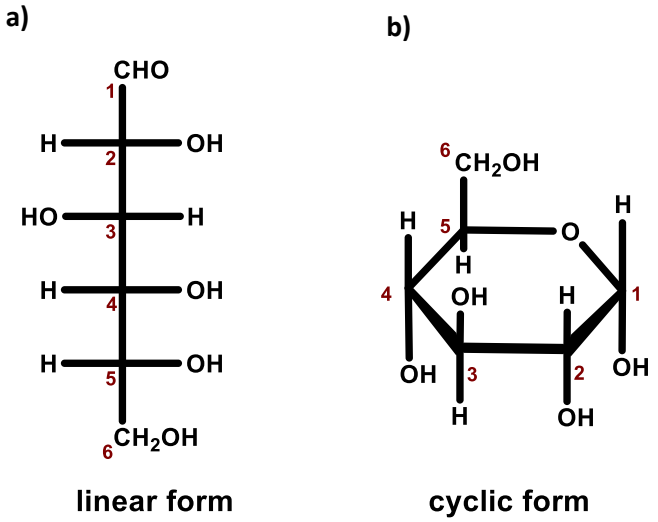

Figure 1.1: Schematic of **a)** the Fischer and **b)** the Haworth projections of α-D-glucose.

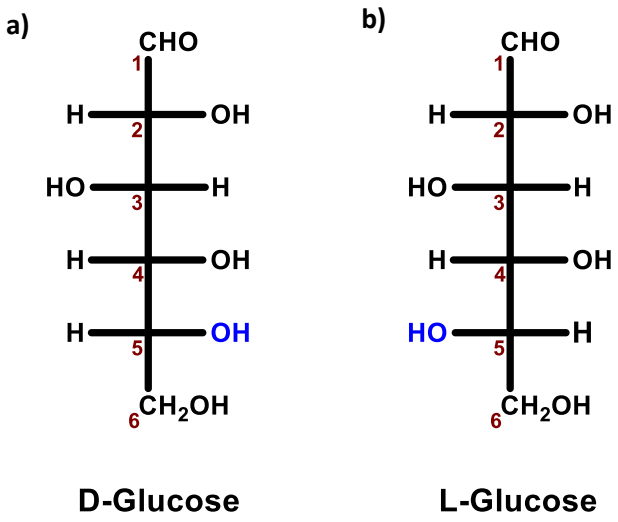

Figure 1.2: Depicts the glucose molecule in either **a)** the D- or **b)** the L- configuration. The arrangement of the hydroxyl moiety found on the chiral carbon at position five is highlighted in blue.

When considering the positioning of the saccharide functional groups it is important to note that the situation is further complicated when the length of the saccharide chain of the molecule is increased, as this also coincides with an increase in the number of carbon stereo centres. For example, 16 stereoisomers exist when considering all the possible arrangements of the functional groups of the hexoses, such as D-glucose, that arise from the four stereo centres [12]. In summary, the wide variety of conformational arrangements that are possible for the monosaccharides produce a broad array of sugars that are in continuous equilibrium within solution. This diversity give rise to even more diversity when these saccharides are incorporated into larger and possibly highly branched structures as observed in the process known as glycosylation.

2.0 Introduction to Glycosylation

As the roles of saccharides continue to be elucidated it is apparent that they are key to intracellular communication processes such as enabling recognition, signalling and facilitating the sorting of molecules during transport [13, 14]. Due to this increased understanding of the functions and roles of saccharides within complex physiological processes there has been a surge of interest in the vast research area of glycomics within the past two decades [13]. This includes for more established areas such glycolipidomics, alongside recent emerging fields such as glycoinformatics [15-17].

Arguably one of the fastest growing areas of interest is glycoproteomics which is the study of the structure and function of proteins that have had saccharides attached to

a particular amino acid residue(s) in the process known as glycosylation [18]. Glycosylation is one of the forms of post translational modification (PTM) that is a process used to modify biomolecules as shown in figure 1.3 [19, 20].

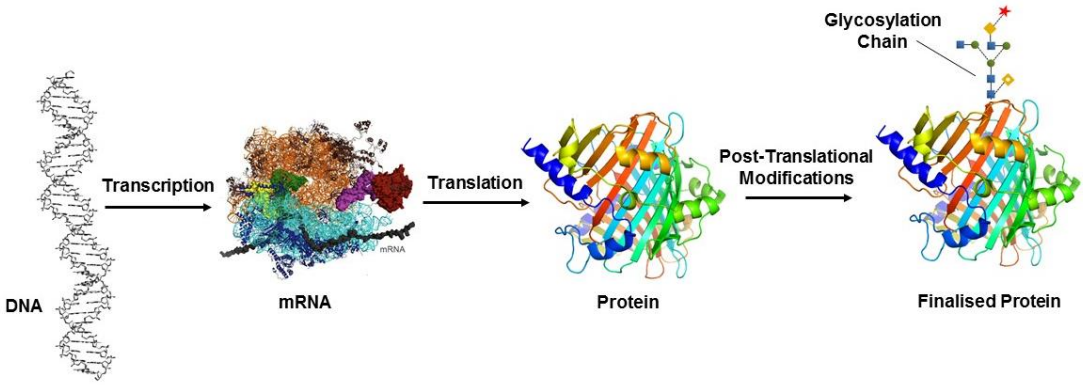

Figure 1.3: Simplified schematic of the processes required to synthesise proteins, including the final step of protein synthesis that occurs in the Golgi apparatus of eukaryotes, post-translational modification.

Proteins can undergo several types of PTMs that include phosphorylation, methylation and ubiquitination, as well as more specialized alterations such as the attachment of fatty acids, isoprenoids and phospholipids [21][22]. However, around one fifth of all cellular proteins are thought to be glycosylated making it one of the most important PTMs [23]. We now discuss the two types of protein glycosylation, the factors which can affect the glycan attachment process and cases where aberrant glycan changes have led to disease.

2.1 N- or O- Linked Glycosylation

Saccharides are attached to a biomolecules by either N- or O-linked glycosylation. These two forms of glycosylation differ from each other by the moieties to which the saccharide is attached, as well as the mechanisms employed to do so [24]. When examining glycosylation, one must consider several factors of the attached glycan

chain. These include: 1) the total number of glycosylation sites, 2) the choice of each monosaccharide incorporated within the glycosylation chain, 3) the relative positions of the linkages (α or β) between each monosaccharide unit of the chain, 4) the degree of branching of each chain and 5) any further modifications to units of the chain [25, 26]. Subtle changes to these factors, for example changing the linkage of one sugar to another, for example an α2-3 linkage of a sialic acid sugar to an α2-6 linkage, can drastically change the cellular signalling role of the molecule [27, 28].

N-linked glycosylation involves 14 preassembled sugars being transferred *via* an amide moiety of an asparagine residue indicated by the sequence *'asparagine-X-serine/threonine'* (*X* being any amino acid expect proline) [29]. This form of glycosylation can be sub-grouped into three types as shown in figure 1.4 which are oligomannose, complex and hybrid glycans [29, 30]. Each description relates to the linkages of the sugar chains relative to the aforementioned sequence with the standard protocol for such structures according to Harvey *et al.* (2009) [30].

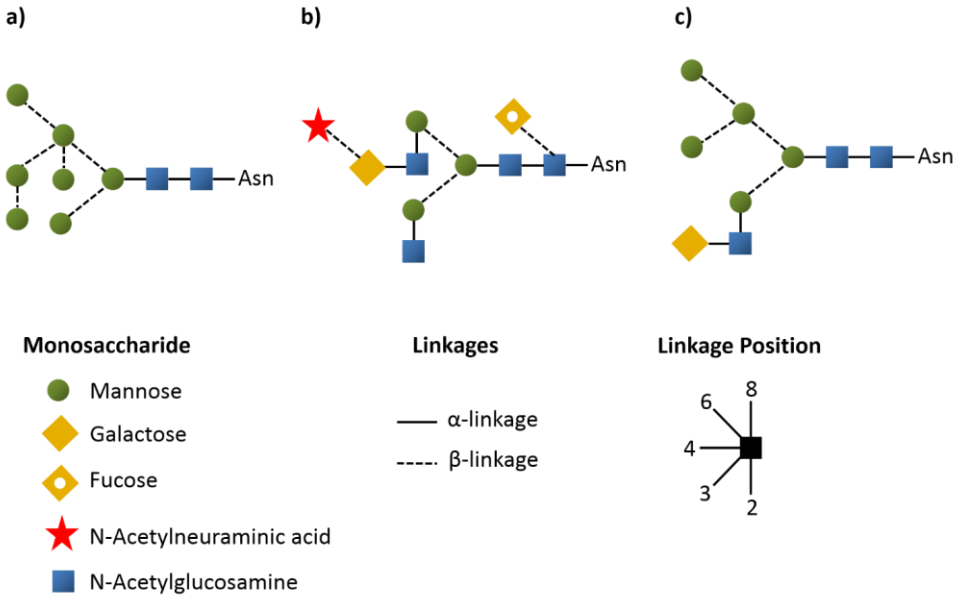

Figure 1.4: Schematic representation of the three main N-linked glycan structures as adapted from Gilgunn *et al.* (2003) [29] with the monosaccharide, linkages and linkage positions presented in the style as proposed by Harvey *et al.* (2009) [30]. The core sequence Manα1-6(Manα1-3) Manβ1-4GlcNAcβ1-4GlcNAcβ1-Asn-X-Ser/Thr is shared by all N-linked glycans. **a)** An oligomannose glycan – only mannose residues are attached to the core sequence **b)** A complex glycan – 'antennae' are attached to the core structure **c)** Hybrid glycan – attached to the Manα1-6 arm of the core are solely mannose residues, however one or two antennae can be attached to the Manα1-3 arm.

Extensive research has shown both N- and O-linkages are essential to maintain normal eukaryotic cellular function and abhorrent changes are responsible for a number of severe diseases [25, 29, 31-34]. Subsequently, there has been a shift in research strategies to enable the identification of these disease associated glycan biomarkers [35].

For example, glycan changes within cancer are being studied to better identify the stage and progression of tumours [25]. These include for example the truncation of chains [36-38], over [39] or under [40, 41] expression of certain glycan structures, and in some cases the production of novel N- or O-linked glycans [29]. Due to the

complexity of the glycome this can be a challenging prospect to fully elucidate as unique glycan structures can be observed from individual to individual. Moreover, correctly detecting and then characterising these changes can be expensive and laborious due to the limitations of the current diagnostic techniques. Nevertheless, an example where significant progress has been made in understanding glycosylation changes and their relevance to disease progression is for prostate cancer (PCa).

2.2 Changes in the Glycosylation of PSA with Prostate Cancer

PCa is the most common cancer in men in the western world [42-44]. The current biomarker used to detect PCa is the prostate specific antigen (PSA) glycoprotein. Serum PSA levels are used to determine whether a male may have PCa using the 'gold standard' PSA enzyme-linked immunosorbent assay (ELISA) [43-47]. However, much controversy has arisen from using this ELISA as a screening tool because of several issues with the test [46, 48-56].

One of these issues is that the ELISA fails to effectively discriminate between the various glycoforms of PSA [57]. The PSA glycoprotein has a single, N-linked glycan composed of a N-acetyl-lactosamine bound to an α2-3-linked sialic acid [29, 58-60]. Past studies assumed that this glycan structure did not vary between individuals, however it is now known that changes to the sialyation and core fucosylation of the PSA glycan are common in PCa. For example, it has been shown that the sialylation patterns of the glycan in PCa patients are more heterogeneous than the glycans of non-cancerous patients [61-65]. Furthermore, cancer specific changes to the fucosylation of the N-glycans' sialic acids have also been reported [66-68].

In summary, these recent studies of PSA collectively conclude that research should now focus on targeting the sialyation and fucosylation changes of the N-linked PSA glycan to produce a more specific test capable of discriminating between the range of PSA glycoforms [44, 48-51, 69]. Alternative techniques such as lectin assays that can selectively detect α2-6 sialic acid linkages of the PSA glycan have been explored as new tools to improve the PCa detection [70]. However, there are significant drawbacks to using lectin-based systems for saccharide sensing as thoroughly discussed below.

3.0 Saccharide Recognition Molecules

3.1 Lectins

Lectins are proteins that are able to bind and recognise specific saccharides including the glycans attached to biomolecules such as glycopeptides and glycoproteins. Lectins act as the molecular recognition element for a range of processes including cell-division, protein-transport and cell-cell interactions [71]. Moreover, they are widely found within nature having evolved as the recognition element in a number of plant and animal congenital immune responses [72-74].

The binding of a lectin to a specific saccharide structure arises from the precise sequence of amino acid residues within the peptide, as well as the folding of the polypeptide chain to produce a complementary binding site. This binding region is referred to as the carbohydrate binding domain (CBD) [73]. Owing to the fact that lectins are able to distinguish between subtle differences in the linkage arrangements of sugars, for example between an α1-2 or α1-3 sugar linkage, they offer specificity and selectivity for saccharide recognition. Moreover, in comparison

with glycan specific monoclonal antibodies they are far less laborious to obtain and purify with a greater yield and therefore are significantly cheaper to incorporate into saccharide sensing systems [75]. Subsequently, they have been widely employed as the recognition element in a range of biotechnology applications including glycoproteomics and diagnostics [76] [77, 78]. Moreover, their saccharide specificity has enabled agglutination and enzyme-linked lectin (ELLA) assays to be developed for many diseases, including PCa [63, 64, 79-81].

However, there are several drawbacks to using lectins as the molecular recognition element in such systems. The first is that due to a low affinity and therefore sensitivity for their target they provide poor limits of detection within the low mM range [82]. The second is the difficulty in finding unique lectins that bind less-common saccharide structures in order to target novel aberrant glycan structures [82]. Thirdly, as lectins are polypeptides they are susceptible to destructive environmental changes such as high temperatures or pH which can denature their function [83, 84]. For these reasons, alternative saccharide specific recognition systems that are not limited by such factors are required to overcome these issues.

3.2 Boronic Acids

First isolated in 1860 by Frankland, boronic acids are molecules that can selectively bind the sugars of a glycosylated molecule to form a boronic acid-sugar complex. This is possible as the boron can covalently bind monomers of a saccharide through the monomers 1-2 or 1-3 *cis* diols to form boronate esters, as shown in figure 1.5 [85].

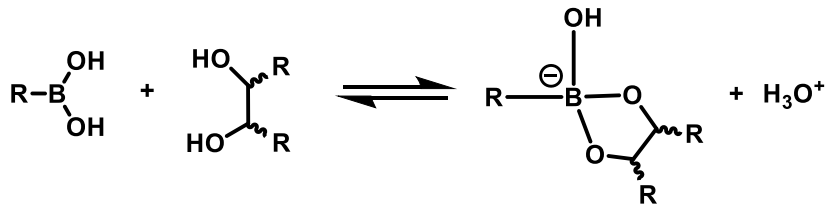

Figure 1.5: Schematic of the boronate esterification reaction of a Lewis base in coordinating solvent. The boronic acid binds the 1-2 or 1-3 *cis* diol to form the cyclic boronate ester. Adapted from [86].

The boron-saccharide binding phenomenon was first observed in 1959 by Lorand and Edwards who reported that this interaction was pH dependent [87]. They observed that complexation with phenylboronic acid was not favourable at acidic and neutral pHs, however covalent binding was induced upon using alkaline conditions. The pH dependency of this interaction arises from the electron arrangement of the boron, as shown in figure 1.6. At low pH, a tri-substituted boron resides in a sp^2 hybridised trigonal planar arrangement, however upon binding an available anion in alkaline conditions the hybridisation changes to the sp^3 form. This is due to the free *p* orbital of the boron being attacked by the OH^- nucleophile from solution which changes the geometric arrangement from the trigonal planar to the tetrahedral form [85]. This optimal geometric arrangement then encourages binding to the saccharide and the resultant sugar-boron complex is a tetrahedral boronate ester. In aqueous conditions this binding is dynamic and so the complex is continuously cycling between the unbound and cyclic boronate ester species.

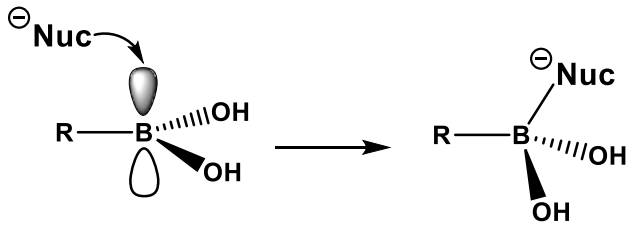

Figure 1.6: Schematic demonstrating the change in the sp^2 hybridisation of the boron to sp^3 upon attack from a nucleophile. Adapted from [85].

Due to the pH dependency of this reaction, earlier studies using phenylboronic acid were therefore limited to conditions that reside above the boronic acids pKa of 8.7. However, it was later discovered that by using additional functional groups located close to the boron atom, the pKa of the molecule could be lowered and hence these phenyl boronic acid derivatives could be utilised in a broader range of conditions. For example, the addition of carbonyl or sulfonyl groups attached to the phenyl ring act as electron withdrawing groups (figure 1.7, c and d) [88, 89]. These groups decrease the electron density around the boron atom, increasing its ionisation and Lewis acidity to consequently decrease the overall pKa of the molecule. Similarly, benzoboroxoles (figure 1.7, b) which are cyclic analogues of boronic acids also have a lower pKa than phenylboronic acid as upon binding to a diol the B-O ring strain is minimised [88, 90].

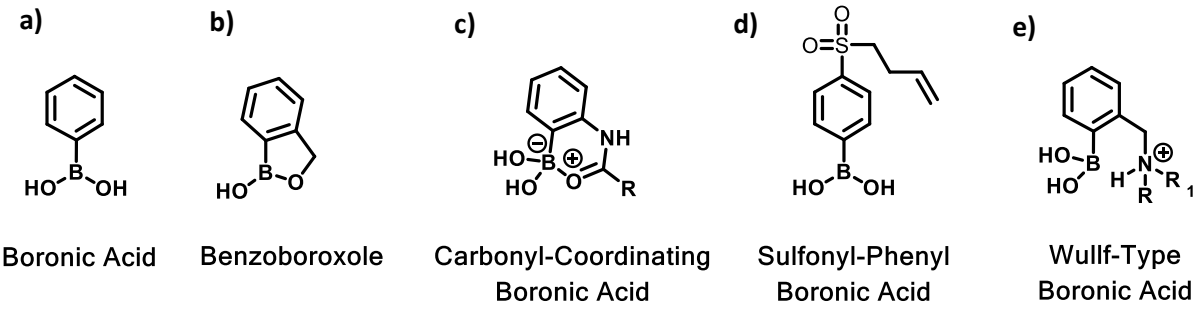

Figure 1.7: Examples of different types of boronic acids.

Alongside using additional groups, intramolecular N-B bonds have also been exploited to likewise increase the ionisation of the boron (figure 1.7, e) [91-94]. In this case, a secondary or tertiary amine proximal to the boron can form a co-ordinate complex with the boron by acting as a Lewis base**.** Collectively, due to the increasing range of conditions within which boronic acids can be employed advances in the incorporation of boronic acid into a range of saccharide sensing applications and smart materials are continually being realised [95].

3.3 Utilising Boronic Acids for Saccharide Binding Applications

The saccharide sensing capabilities of boronic acids have been first been exploited for the detection and treatment of a wide variety of diseases [96]. One of these examples is in the development of novel treatments for cancers [97]. For example, Matsumoto *et al.* recently explored the binding behaviour of several nitrogen containing phenyl boronic acid towards a range of saccharides and found that several heterocyclic boronic acids showed selective binding to sialic acids over other sugars at an acidic pH [98]. Subsequently, these boronic acids can now be used to bind sialic acids in acidic environments such as at tumour cell surfaces and so can be developed for cancer detection or drug delivery [98]. Moreover, recently Ji *et al.* showed that boronic acids can also be used to enhance the effect of short-interfering RNA (siRNA) for cancer treatment [99]. siRNA is well known for being highly effective against cancerous cells, however its delivery is hampered due to destruction by cellular RNases [99]. In this case, the siRNA was encapsulated in polymer capsule coated with phenylboronic acid that could then enter the tumour cells by binding sialic acid found at the tumour cells surfaces, as shown in figure 1.8. The result enabled higher concentrations of siRNA to be released into the cancer cells [99].

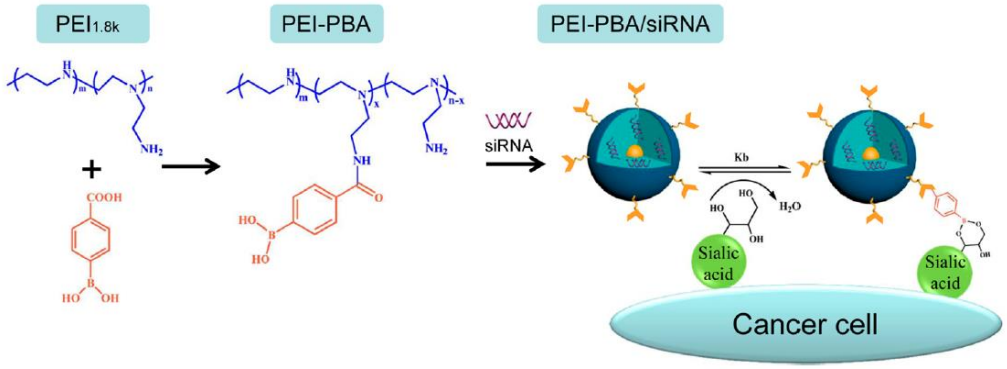

Figure 1.8: Schematic of the polyethylenimine-phenyl boronic acid (PEI-PBA) encapsulated siRNA that was then used to attack cancerous cells through sialic acid binding of glycoproteins at the tumour cell surface. Taken from [99]

Furthermore, pH responsive hydrogels capable of preventing the spread of HIV-1 have also been realised as reported by Kiser *et al.* [100]. Here, phenyl boronic acid (PBS) and salicylhydroxamic acid (SHA) polymers were shown to block the transmission of the HIV-1 virus at pH > 5.5 (figure 1.9) [100] and could now be taken forward to use as a vaginal barrier to prevent HIV-1 transmission.

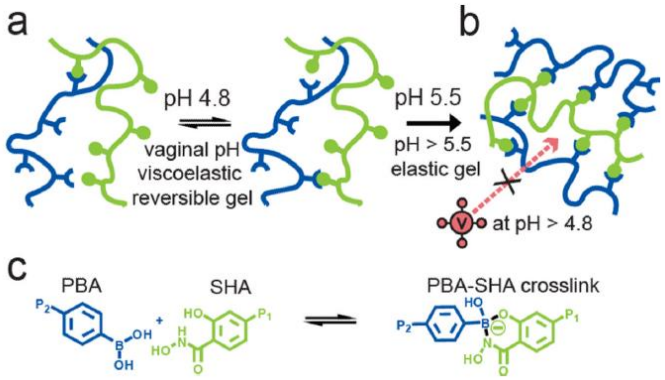

Figure 1.9: Schematic of the pH responsive gel developed by Kiser *et al.* to prevent the transmission of the HIV-1 virus. At vaginal pH (pH 4.5-5) the rate of hydrolysis of the crosslinked PBA (blue) and SHA (green) polymers is rapid (a), whereas at a higher pH (pH>5.5) the rate of hydrolysis is slower producing a gel that blocks the virus (b). Taken from [100].

Examples of other systems that likewise take advantage of the pH responsive capabilities of boronic acid to treat disease have also been reported. For instance, micelles co-polymerised from dextran-block-polylactide modified with 3-carboxy-5-nitrophenylboronic acid that encapsulate the antibiotic, doxorubin, have been described [101]. Similarly, phenyl boronic acid and lysine functionalised poly-ethlyene glycols (PEG) micelles that encapsulate small proteins have also been realised [102]. Both these pH responsive micelles release their cargo upon exposure to the acidic endoplasmic reticulum of the cell or fructose, respectively, and could easily be adopted to suit a number of other drug delivery systems including for sugar related diseases such as diabetes mellitus [103, 104].

In short, the saccharide binding abilities of boronic acids are continuing to be explored in novel applications as they show strong yet reversible affinities for sugars [105, 106]. Their reversible binding capabilities can be tuned to the desired pH by controlling the proximal or distal electron withdrawing groups close to the boron to lower its pKa [94]. These qualities offer molecular engineers a distinct advantage over traditional saccharide or glycan binding methods as boronic acids can be elegantly arranged in rational design approaches tailored to the saccharide of interest [88, 107, 108]. Moreover, they can be used in a wide range of conditions otherwise destructive to lectins or antibodies whilst also being relatively smaller, non-toxic and stable under normal atmospheric conditions [109, 110]. Collectively, these reasons make them an attractive choice to be incorporated with ease into nano-scale devices. The following section therefore discusses one of these nano-scale platforms widely used for the fabrication of sensing technologies known as self-assembled monolayers [81].

4.0 Self-Assembled Monolayers

Self-assembled monolayers [81] are formed from molecules that can self-assemble from the vapour or liquid phase when incubated with a suitable substrate, such as Au, Ag or Pt, into a ordered, well packed monolayers, both on planar surfaces and 3-dimensional (3D) objects [111, 112]. Organosulfur alkanethiols as shown in figure 1.10 are typically used for this purpose as they possess the three necessary characteristics to form high quality, well packed surfaces. The first is the thiol moiety at the tail end of the molecule that can form a covalent bond with material surfaces such as gold.

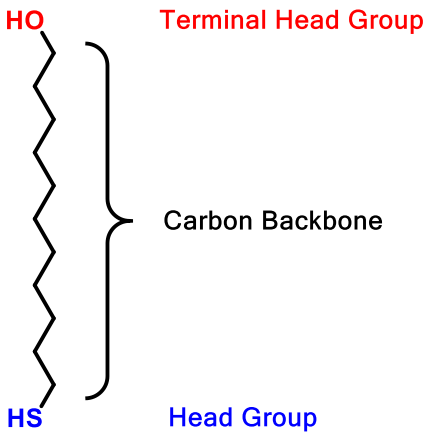

Figure 1.10: Schematic of an example alkanethiol molecule, that possess a thiol (SH) head group (blue), carbon backbone (black) and terminal head group (red).

The second is the carbon backbone that enables a tightly packed formation to be achieved as weak but numerous intermolecular forces (for example, Van der Waals and dipole-dipole interactions) can form between adjacent molecules. Moreover, the carbon chain can be tailored to the desired length to offer a range of desired monolayer thicknesses. Finally, the terminal head group of the alkanethiol can also be tailored to include particular chemical functionalities to produce surfaces with distinct qualities. For example $-CH_3$ and $-CF_3$ end groups produce hydrophobic SAMs, whereas -COOH or -OH groups produce hydrophilic SAMs [112]. Furthermore, in some cases the head group can be further reacted to enable different interfaces with varying qualities and functionalities to be formed [113, 114].

Overall, the attractiveness of using SAMs is due to their ease of formation (using 1-2 mM amounts of thiols) and analysis with surface characterisation techniques such as contact angle, ellipsometry and XPS, alongside their commercial availability. Furthermore, they offer material and bio-engineers the flexibility to tailor multiple factors of the surface characteristics, including packing density, functionality,

wettability and thickness, as well as enabling mixtures of various alkanethiols to be explored [115].

4.1 The Process of Self-Assembly

When an alkanethiol is first exposed to a substrate, the molecule must undergo several distinct stages to eventually form a well-packed monolayer. This can be divided into several stages as shown in figure 1.11 which are physisorption, chemisorption and re-organisation. The kinetics of this process can be categorized into roughly two stage as the physisorption occurs within the first few minutes within solution, whereas the chemisorption and re-organisation stages require ~15-24 hrs to enable high quality SAM formation [116], however it should be noted that this is highly simplified for the benefit of the reader.

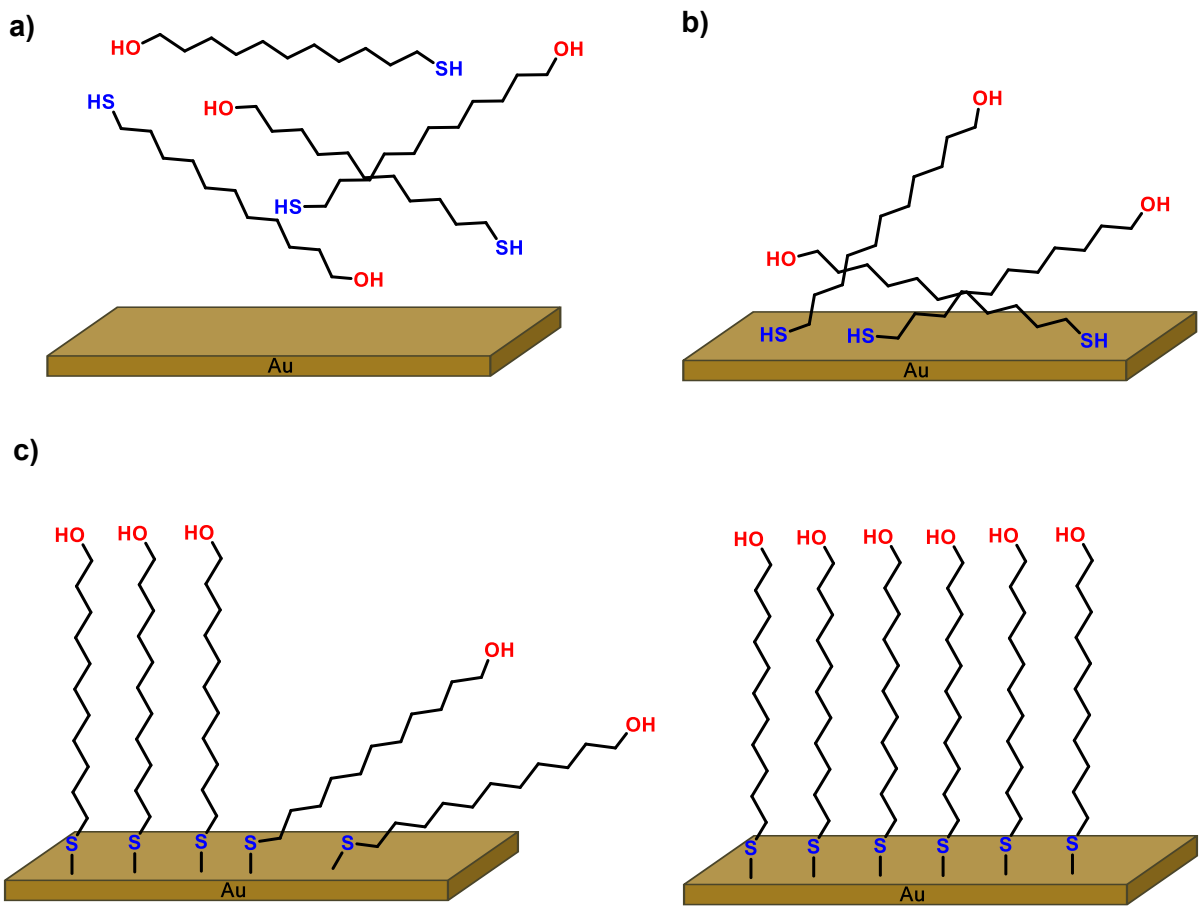

Figure 1.11: Schematic of the process of self-assembly. The alkanethiols in solution (a) physisorp onto an Au (III) substrate (b). The molecules then chemisorp onto the surface to form covalent bonds with the Aug *via* their sulfur head groups (c).Finally, through reorganisation of the surface a well-ordered monolayer is formed (d).

Physisorption (figure 1.11, b) is the immediate binding of the molecules to the substrate from solution (figure 1.11, a) when first exposed to the surface. As Bain *et al.* showed in their early studies this is occurs within minutes of exposure by the apparent rapid change in the contact angle of the surface to ~90 % of its final angle [117, 118]. However, this is not a covalent interaction and therefore given enough time and the correct solvation conditions the thiol will then undergo chemisorption (figure 1.11, c) to form a covalent bond to the substrate. This can lead to random arrangements of the thiols upon the surface which likewise do not show good

packing and homogeneity. Therefore the final stage is the reorganisation of the chemisorbed thiols where through continual desorption and reabsorption the molecules form more ordered and tightly packed island arrays upon the surface. The carbon backbone of the molecules within these islands facilitate the reorganisation process by forming stabilising intermolecular interactions, which encourage further thiols to bind. Eventually these islands coalesce to form an ordered array (figure 1.11, d) and the final well-ordered monolayer can then be examined or subjected to further functionalisation. Overall, the concentration, chemical composition and incubation time of the selected thiols will directly affect the physical monolayer formed.

4.2 SAM Defects

It is important to note that when discussing SAM formation that the ideal scenario is a well-packed and highly uniform monolayer free from defects or contamination from other molecules. However, the reality is that in the majority of cases defects to varying degrees within the monolayer can be expected. Examples of defects include a) domain defects, b) pin-hole defects and c) disorder defects, as shown in figure 1.12.

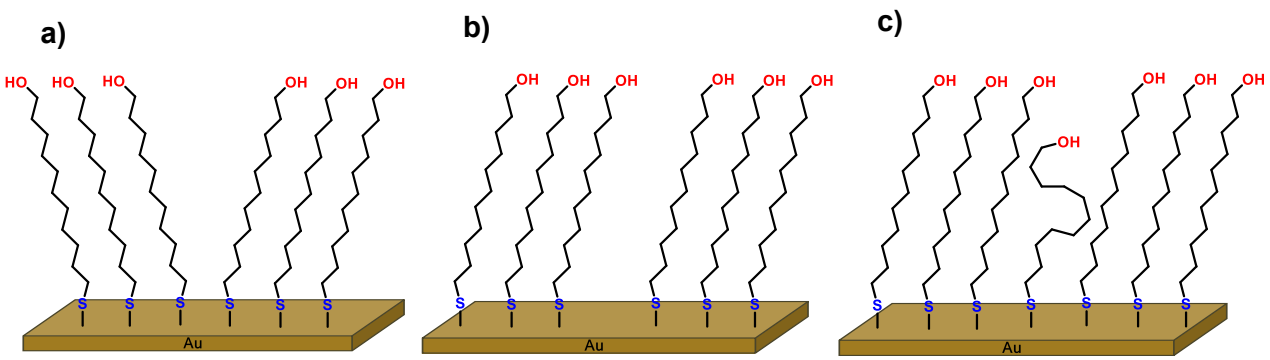

Figure 1.12: Schematic of domain (a), pin-hole (b) and disorder (c) SAM defects.

Domain defects occur due to imperfections in the frontier of the underlying lattice. Consequently, the SAMs arrange themselves in more than one orientation upon the substrate [119]. Pin-hole defects occur due to molecular vacancies from the failure of the alkanethiol to bind a vacant site on the substrate to subsequently cause isolated islands of monolayers to form [119]. Finally disordered defects, such as a gauche defect as pictured in figure 1.12, c, are caused by disordered conformations of the alkanethiol chains so that they are not fully stretched with respect to the other chains of the SAM [120]. The number of these defects is heavily influenced by both the chain length of the alkanethiol and the terminal head group functionality [121]. Ideally, protocols for SAMs should be optimised so as to produce monolayers with as limited defects as possible.

5.0 Molecular Imprinting

A molecularly imprinted polymer (MIP) is defined as the creation of a synthetic binding site within a polymer matrix that is complementary to the shape and functionalities of the template molecule with which it was synthesised. As these cavities are synthesised within a polymer material they are commonly known as ‘plastic antibodies’ or ‘artificial receptors’, as like their biologically counterparts they possess an artificial memory of the template molecule. Nature provides numerous examples of molecules such as antibodies and lectins that have evolved highly specific and selective bio-molecular recognition abilities. However, the attractiveness of replacing such bio-recognition elements with MIPs in sensing applications lies in their resistance to degradation by chemical and physical external factors such as pH, temperature and mechanical stress [122]. Moreover, the synthesis of imprints can be easily controlled using feedstocks of the monomer(s) and unlike for biological counterparts do not require laborious and expensive bioengineering processes to synthesise and isolate [123]. These advantages have led to imprinting being used to design cavities for a vast array of molecules ranging from the nano- to micro-meter scale [124].

5.1 The History of Imprinting

The first work to investigate the concept of molecular imprinting was undertaken by Polyakov in the 1930s, where silica matrices were used to create a number of small molecule imprints [125]. The resulting silica imprints displayed strong affinities towards the small molecules with which they were polymerised and so the concept of forming a synthetic material that was receptive to a target template molecule was

born. From the 1950s onwards, the uptake of this idea then led to the gradual development of molecular imprinting technologies (MIT), with progress notably accelerating in the 1970s following the pioneering work by Wulff and colleagues who used imprints within organic matrices for biocatalysis [126, 127]. Today MIT is a broad field of research attracting the attention of engineers, chemists and biologists to develop imprints for a wide range of applications [128]. A brief overview of these applications includes purification and separation technologies (chromatography or monoliths) [129-131], drug delivery systems [132], novel catalysis methods [133], and sensing and diagnostic technologies [134, 135].

The earlier examples of imprints were primarily for the production of monoliths for small organic molecules such as herbicides, pesticides and antibiotics [136-139]. However, monolithic materials commonly suffer from issues such as poor mass transport when trying to imprint larger and more complex molecules [140]. Therefore recent MIT methodologies have shifted towards creating imprints within thinner 3D hydrogels and sol-gels, as well as 2D surfaces. As advances in research fields such as analytical chemistry, bio- and nano- technology, and polymer science continue to develop this will continue to coincide with innovations within MIT [141].

5.2 General MIP Synthesis

As shown in figure 1.13, the typical protocol employed to form a MIP involves mixing the template molecule with both mono-functional and di-functional monomers to enable them associate either covalently or non-covalently with areas of the template (figure 1.13, a) and then triggering the polymerisation reaction to form a polymer matrix around the template (figure 1.13, b). The resultant cavity is then

complementary in its size, shape and chemical functionalities to the template. The template is then removed from the cavity (figure 1.13, c) and the rebinding capabilities with fresh target analyte tested (figure 1.13, d). Ideally, the MIP should exhibit high specificity and selectivity for the target, whilst showing low affinities for competing molecules.

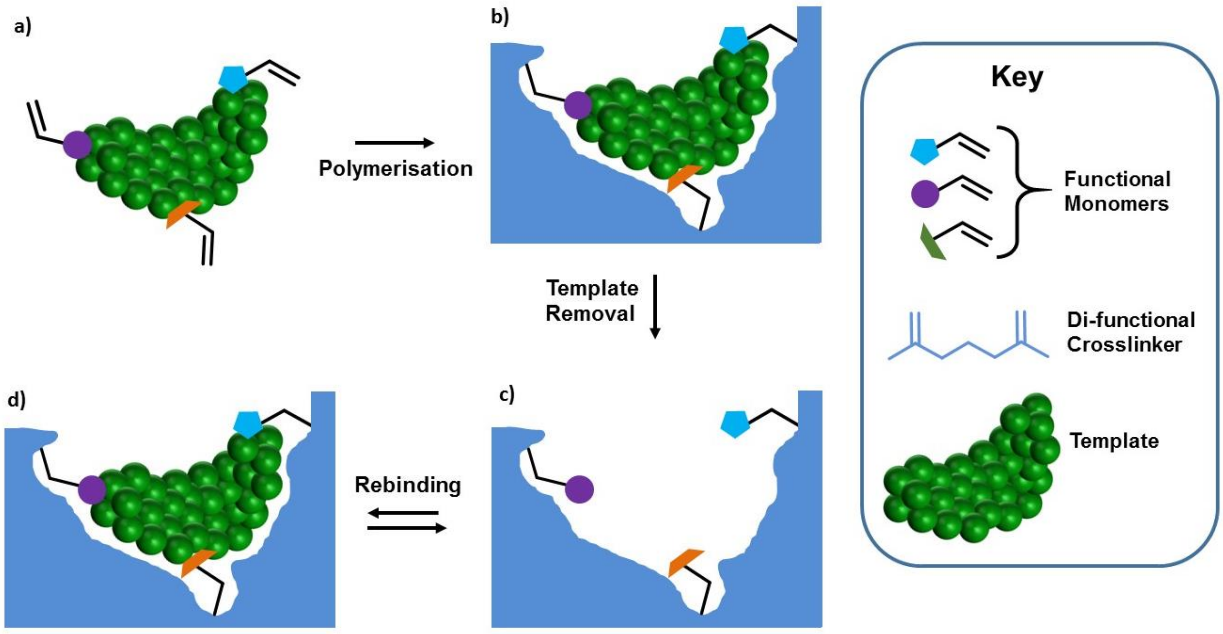

Figure 1.13: Schematic of the general procedure used for MIP synthesis. Functional monomers associate with the template molecule (a), polymerisation is triggered around the template (b), the template is then removed from the pocket (c) and finally the imprint is assessed for rebinding (d).

When designing an imprint the choice of several parameters that include the selection of monomer(s), their relative ratios, and their chemical functionalities (that can interact with functionalities of the target) are paramount to the imprinting outcome. Moreover, functional monomers that can form a particular covalent bond with the template molecule should also be considered. Finally, factors such as

polymerisation method, polymerisation time and solvent should also be investigated as these can drastically affect the MIP sensitivity and selectivity.

Typically, imprints have been created to take advantage of either interactions using either one of two methods: non-covalent imprinting or covalent imprinting. Non-covalent relies on using electrostatic interactions (e.g. Van der Waals forces or hydrogen bonds) or ionic bonding to form interactions between the monomer(s) and the template, whereas covalent relies on covalently binding a ligand - such as a saccharide binding a boronic acid. The latter then requires the covalent bond to be broken in order to free the template molecule using a washing step (e.g.an acidic or basic wash), whereas removal of the template in non-covalent protocols requires milder conditions.

5.3 Types of Polymerisation Processes for Molecular Imprinting

MIPs can be created by several different means of polymerisation where the reaction is triggered by ionic bonding (anionic or cationic), transition-metal-mediated interactions or by radical production (either chemically or UV derived) [142]. Controlled radical polymerisation (CRP) is a category within conventional radical polymerisation (RP) and is the preferred choice for synthesising 2D MIPs as the propagation of the reaction can be finely tuned to produce highly controlled polymers [143, 144].

There are several forms of CRP that are widely used for imprinting such as reversible addition-fragmentation chain-transfer polymerization (RAFT), atom-transfer radical polymerisation (ATRP) and nitroxide-mediated radical polymerisation (NMRP) [145-147]. All rely on the generation of a radical species which enable

monomers to be added during propagation to create polymer chains in a controlled manner [148]. In the molecular imprinting work present within this thesis we have used ATRP to form our imprints and therefore the following covers this form of CRP in detail.

5.3.1 Polymers Synthesised Using ATRP

ATRP was first developed by Matyjaszweski in 1995 and has become a widely employed technique for the well-controlled synthesis of polymers [149, 150]. ATRP offers exceptional regulation over the length, polydispersity index (PDI) and molecular weight of polymerisation to produce highly uniform polymers. ATRP can be undertaken in a range of conditions and has been applied to a variety of different applications for both small and industrial scale processes [151].The general scheme for ATRP, showing a summary of the process of radical formation, propagation and finally termination of the polymer is outlined in figure 1.14.

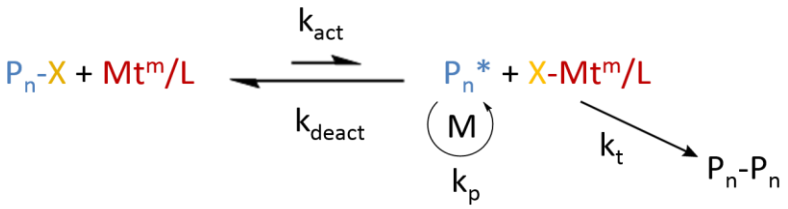

Figure 1.14: General reaction scheme for ATRP. During K_{act}, the transition metal-ligand (Mt^m/L) causes homolytic cleavage of the halogenated-substrate (P_n-X) to produce the substrate free radical species (P_n*) which can then propagate (k_p) with monomer (M) to create a polymer. This reversible reaction is then terminated (k_t) by chain end termination or radical disproportionation. Adapted from Matyjaszewski *et al.* [152]

An ATRP utilises the production of a radical to reversibly activate a dormant, halogenated species to enable the propagation of monomers into a polymer chain.

This is possible through employing a ligated (L) redox-transition metal catalyst (Mt^m/L) that reacts with a halide-terminated dormant substrate (Pn-X). The first step of an ATRP is activation (K_{act}) where the Mt^m/L catalyst is oxidised by halogen atom transfer whilst the halide-terminated substrate (P_n-X) is reduced to form a free radical species (Pn*). This occurs due to homolytic cleavage of the P_n-X bond *via* inner sphere electron transfer (ISET) [153, 154]. Typically, the Mt^m is copper based and L is a nitrogen containing ligand such as 2,2'-bipyridine (2-bpb) [155, 156].

The radical species can then react with monomer present during propagation (K_p) to form the polymer. However, the propagation is intermittent, due to the ligated transition metal catalyst (Mt^m/L) continually changing its oxidation state to activate or deactivate the P_n-X substrate. In this way, an equilibrium is formed between the rate of activation (K_{act}) and deactivation (K_{deact}) to give the overall K_{ATRP}.

Several key factors contribute towards the rate of polymer growth as the kinetics of an ATRP are governed by multiple factors. These include the concentrations of the alkyl halide, monomer, ligand, transition metal, as well as time, pressure, temperature and solvent [146]. The ideal ATRP equilibrium is pushed further to the left so that the dormant, halogenated species (P_n-X) dominates in comparison with the radical species (P_n*). One would first assume that this is detrimental to obtaining a successful reaction. However, this is in fact favourable as a larger K_{deact} produces more uniform chain growth which results in a low PDI of the polymer. PDI is defined as (M_w/M_n), where M_w is the weight average molecular weight and M_n the number average molecular weight of the polymer, with the optimal PDI for polymers =1. For solution based polymers the PDI can be analysed with ^{1}H NMR and gel permeation chromatography (GPC) [157], whereas tethered polymers require cleaving from their

substrates [158-162]. Due to the breadth of systems that can be discussed the following section will focus on ATRPs conducted within aqueous solvents as this area is still in its infancy [163].

5.3.2 ATRP in Aqueous Solvents – An Evolving Area

Historically, ATRPs and other aforementioned CRPs were typically undertaken in organic solvents such as DMF or acetonitrile [164]. However, due to increased demand for 'green chemistry' processes there has been a push towards using more sustainable and environmentally friendly solvents [165]. Water is therefore an ideal solvent for ATRP due its availability and environmental and bio-compatibility [166]. Furthermore, it allows sufficient heat dissipation and provides a low viscosity to prevent the aggregation of larger polymer structures [166] . ATRPs in aqueous suspensions and emulsions were the first to be widely undertaken, following which the use of surfactants enabled reactions within mini- and micro-emulsions to be explored [167, 168]. Following these advances, ATRPs within dispersed aqueous solutions have increasingly been reported, either using solely water or alongside various ratios of organic solvents (for example water:methanol mixtures) [169-173]. However, there are three main drawbacks to using aqueous media for ATRPs [174] as outlined below:

5.3.2.1 Disproportionation of the Dormant Initiator

The left hand side of an aqueous ATRP reaction can suffer from two disproportionation issues as shown in figure 1.15. The first is the disproportionation of the dormant halogenated ATRP initiator (Pn-X) by attack from the solvent (green). The result is either termination of

the initiator chain ends to prevent growth from their sites, or hydrolysis to replace their halide moieties with a hydroxyl group [174].

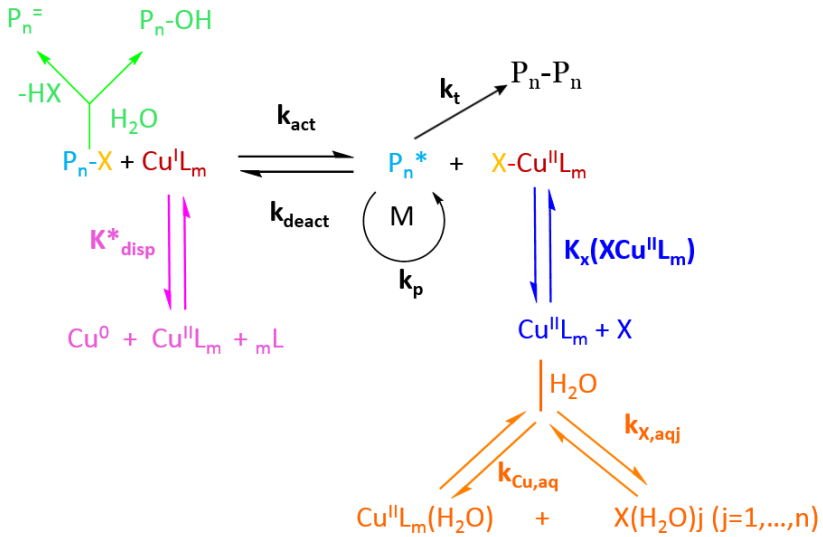

Figure 1.15: General scheme for ATRP within aqueous solvents and the possible issues that can arise.
Moving from the left to the right of the scheme, the first is the disproportionation ($P_n^=$) or hydrolysis (P_n-OH) of the initiator or dormant chain end shown in green. Second is disproportionation (K^*_{disp}) of the ATRP activator ($Cu^I L_m$) shown in pink. Third, is a loss of the ATRP deactivator (X-$Cu^{II}L_m$) by dissociation of the halide ligand (K_x) as shown in blue, which can then be proceeded by the fourth issue of the dissociated complex or ligand complexing with the solvent ($K_{Cu,aq}$) or ($K_{X,aqj}$) as shown in orange. Adapted from Matyjaszewski *et al.* [175].

The second is the disproportionation of the ATRP activator ($Cu^I L_m$) to form $Cu^{II}Lm$ and Cu^0 [156, 176, 177]. However, if K^*_{disp} is a significant issue a proportion of another ligand, for example an excess of pyridine with a 2,2'bypyridial system, can be used to supress the disproportionation of the $Cu^I L_m$ complex [178].

5.3.2.2 Disproportionation of the Halide and Complexation with the Solvent

The second issue that can arise from using an aqueous solvent is that the increase in the polarity of the medium (relative to an apolar organic solvent) can cause dissociation of the halide-ligand from the higher oxidation state transition metal-

ligand (X-$Cu^{II}L_m$), as shown in figure 1.15 (blue) [165, 175]. For example, dissociation of 2,2'-bipyridine-Br from a Cu^{II}-(2,2'-bipyridine)$_2$Br complex. This dissociation then results in the Cu^{II} complex or the ligand being susceptible to co-ordination instead with the solvent (orange). Due to the loss of this deactivator species from the system, this can then lead to polymerisation being extremely fast and uncontrolled due to a high K_{act} producing high PDI values [164, 170, 179]. However, this problem can be overcome by the addition of a halide salt (such as CuBr or CuCl) to enable the Cu^{II} to re-complex with the aforementioned halide-ligand to increase K_{deact} and re-establish control over the polymerisation [170].

In summary, the rate of K_{ATRP} reactions using copper catalysts are solvent dependent with polar, protic solvents producing high rates of reaction [175, 179]. However, provided that reasonable precautions are taken to prevent the dissociation of the halide-ligand complex, employing water as a solvent for ATRP is an attractive choice for polymerising in eco- and biologically compatible conditions. The following sections discuss imprinting systems that have been synthesised using ATRP, with focus on reactions undertaken within aqueous media.

6.0 Designing Molecular Imprints for Proteins – Challenges and Perspective

When designing imprints for any molecule there are multiple factors to consider in order to achieve the optimum system. The following outlines the key factors to consider with regards to synthesising protein imprints.

6.1 Scale

Firstly, it is important to acknowledge that the proteome is vast and proteins vary significantly in their size depending on their native role. Therefore, an imprinting strategy for one protein of a particular size may not be appropriate for another. Moreover, progress towards creating MIPs for lower molecular weight compounds has been substantial because their dimensions and functionalities are less complex [180-183]. As shown in figure 1.16, with an increase in molecular size comes a greater probability of increased chemical complexities, functional groups and interaction sites. Consequently, progress towards imprinting larger molecules such as proteins and nucleic acids has been slower as highlighted in several reviews [140, 184].

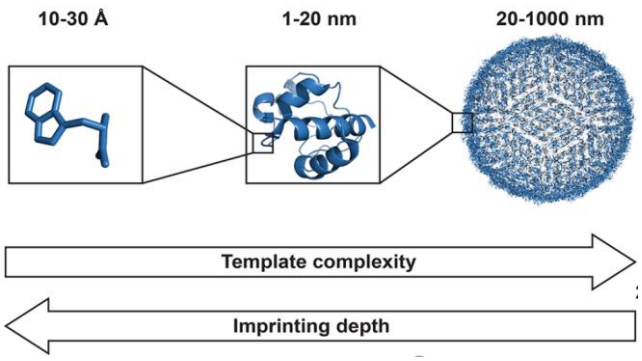

Figure 1.16: Schematic to show the adaption of the scale considerations when the size of the template molecule is increased from a few Ångstroms to several hundred nano-meters. Taken from [185]

The increase in mass can also create problems with mass transfer issues and entrapment of the molecule inside the deeper imprinted cavity. In this respect the imprint should be designed to show the best affinity, selectivity and specificity for the target molecule but using the minimal amount of polymer to do so [140].

6.2 Chemical Functionality and Arrangement

The chemical functionality and spatial arrangement of functionalities within the protein should be considered when imprinting. The typical example of globular proteins (such as enzymes) have a tertiary conformation that consists of a hydrophobic core where aliphatic, less polar residues are buried in order to be shielded from the surrounding polar aqueous solvent. Conversely, the more hydrophilic residues that can undertake ionic, covalent or induced interactions (including hydrogen-bonding and Van der Waals forces) with the solvent are usually found on the external facing surface. The overall tertiary conformation therefore influences the total number of recognition sites available for potential interactions. These features should therefore be taken advantage of when designing protein imprints by utilising functional monomers that can bind to these areas by either charge or shape interactions.

6.3 Solvation

Arguably, the greatest initial challenge to overcome when creating protein imprints is the selection of an appropriate solvent within which the polymerisation reaction can take place that also does not harm the conformational integrity of the protein template. When protein imprinting was first emerging this matter was highlighted as a key challenge to overcome as most CRPs were typically restricted to non-polar, organic solvents [140, 145, 185]. These conditions can potentially cause denaturation (i.e. unfolding of the tertiary structure) of a biomolecule. The ideal scenario is to therefore create imprints using a non-denaturing protein solvent which also enables solvation of the most suitable monomers to promote selectivity and

sensitivity of the imprints. In some cases, the optimal monomer does not dissolve in the optimal solvent for the protein and thus creates difficulties in creating an effective imprint with a high target affinity.

However, the recent advances in CRP have led to strategies to overcome this solvation barrier as previously discussed [156, 186]. Consequently, more imprinting systems within suitable solvents have been reported over the past decade. Over the duration of the research undertaken in this thesis there has been substantial progress in glycoprotein imprinting facilitated by the uptake in using boronate interactions within MIT technologies. As our work focusses on this area, the following section provides examples of glycoprotein imprinting systems to give the reader an up-to-date overview of the field. Included are the earlier examples of bulk glycoprotein imprinting following which surface and nano-particle based glycoprotein imprinting platforms are then presented.

6.4 Glycoprotein Imprints Incorporating Boronate Interactions:

6.4.1 Monolithic Protein and Glycoprotein

The earliest imprints reported for proteins were undertaken using the bulk polymerisation method to produce cavities within an extensive monolithic polymer matrix. Typically these monoliths are formed within a cylinder akin to those used for chromatography. To form a monolithic imprint the template is incubated with the monomers and the solution triggered to form the polymer, however the polymer is then ground to a fine powder. The ground polymers are then washed to remove the template protein, sieved to be sorted into their desired range of sizes and then re-assessed for their rebinding characteristics using for example high performance

liquid chromatography (HPLC) and UV/Vis of the protein filtrates. Overall, this method is popular as it allows for the simple identification and separation of proteins, however its main drawback is that its results in the destruction of a large proportion of the imprinting sites which can produce heterogeneous binding sites, low loadings and high consumption of both the monomers and template [1, 134, 187].

Monolithic imprints for a variety of different proteins have been reported. For example, Lin *et al.* were one of the first to report the synthesis of two different 'hybrid' MIP monoliths for bovine serum albumin (BSA) protein and lysozyme [188]. Following this work, another BSA imprint was synthesised using acrylic acid (AA) and *N,N'*-Methylenebisacrylamide (MEBA) by Deng *et al.* [189]. These two early examples highlight the initial progress in monolithic protein imprinting. However, only recently have examples of monolithic imprints for glycoproteins been reported.

For example, Lin *et al.* reported a monolithic system for the capture and separation of a selection of glycoproteins using their 'one-pot' approach, as shown in figure 1.17 [188]. In this case, no template protein was used to form any specific imprint and instead 4-vinylphenylboronic acid (VPBA) was included solely as a functional monomer to capture the target glycoproteins through their glycans.

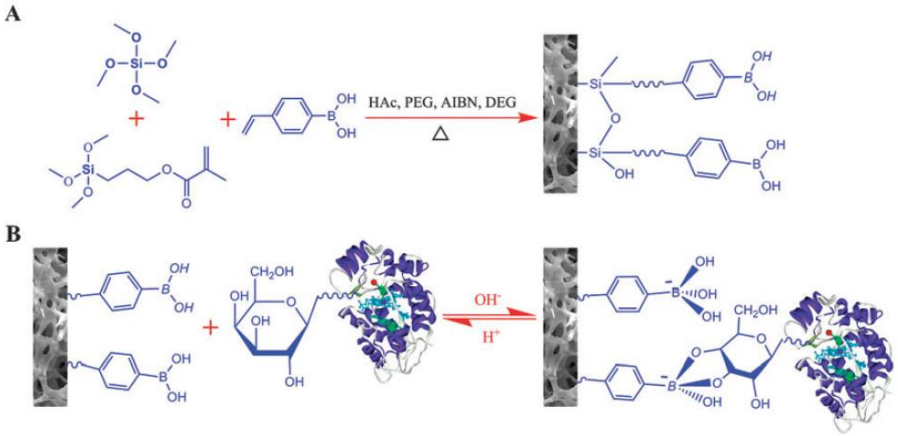

Figure 1.17: Schematic to the silica sol-gel monolithic protein imprint synthesised by Lin *et al.* using γ-MAPS and TMOS [188].

The resultant ‘hybrid’ monolith was shown to easily elute non-glycosylated proteins from the column, whereas glycosylated proteins could be eluted in a controlled manner. Lui *et al.* later reported a similar benzoboroxole based monolithic column also for the capture of glycoproteins from non-glycosylated proteins [190, 191].

Lin *et al.* then used the basis of these two ‘hybrid’ systems to create the first monolithic glycoprotein imprints using glycoprotein templates [192]. As shown in figure 1.18, 4-vinylphenylboronic acid (VPBA) was used as the functional moiety to which the horse-radish peroxidase (HRP) glycoprotein was immobilized, following which the HRP imprints were then formed using dopamine. The HRP monolith showed selectivity for HRP over a number of non-glycosylated proteins and could also isolate HRP found within human serum.

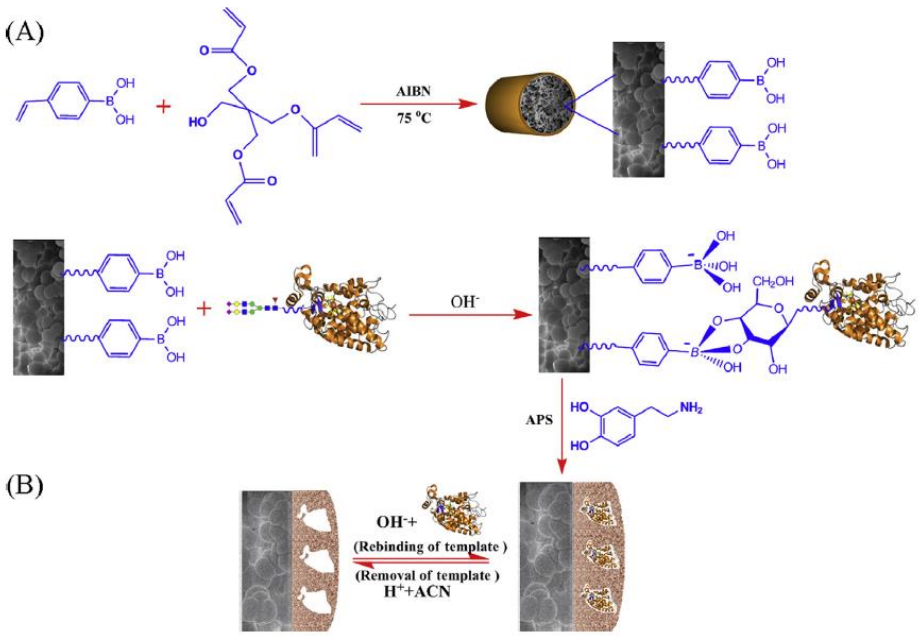

Figure 1.18: Schematic of the glycoprotein monolith synthesised using self-polymerisation of 4-vinyl phenylboronic acid with TMOS and γ-MAPS. Taken from Li *et al.* [192].

Finally, the most recent example of a monolithic glycoprotein imprinting system has been reported by Luo *et al.* where boronic acid functionalised graphene oxide (GO-

APBA) was used to create imprints for ovalbumin using silanes to create the GO-APBA MIPs [193].

In summary, these examples demonstrate that monolithic imprints provide a robust method for protein capture and purification from within complex mixtures of proteins. Good progress has now been made towards developing these set ups for glycoprotein detection and separation by employing boronate functionalities within their designs. However, the aforementioned issues with poor mass transfer and high synthesis costs still hinder the large industrial scale uptake of these techniques due to the extensive labour and quantities of protein required. For these reasons, thinner surface based protein detection and purification methods offer the advantage of overcoming poor mass transfer issues alongside preventing the formation of heterogeneous binding sites, as well as using less protein within the imprinting process. The following section therefore examines thinner 2D and 3D glycoprotein imprints formed within a range of platforms.

6.4.2 Surface Based Protein Imprints – Both 2D and 3D

One of the first unique glycoprotein sensing systems upon a 2D boronic acid functionalised silane surface was reported in 2004 by Wang *et al.* [194]. In this case the glycoprotein templates were first anchored to the surface *via* a boronic acid interaction following which an ultra-thin polymer layer was then grown around the molecules by co-polymerisation of a 1:1 ratio of dopamine and *m*-aminophenylboronic acid (APBA), as shown in figure 1.19. Imprints for the horse radish peroxidase (HRP), RNase B and transferrin glycoproteins were polymerised, and following synthesis, each template was removed from their imprinted cavity

using an acidic wash and then tested for rebinding using biolayer interferometry (BLI).

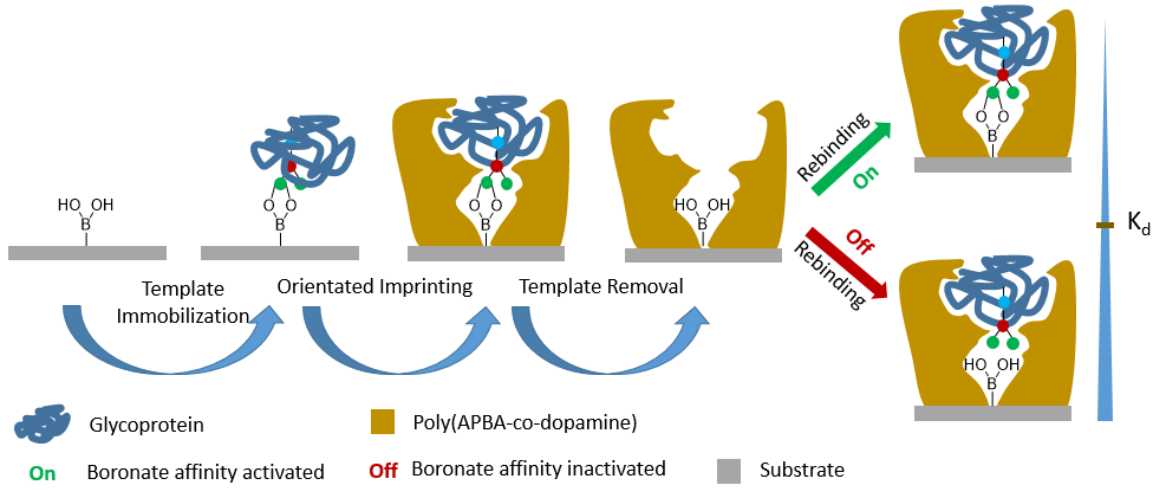

Figure 1.19: Schematic of the boronate affinity tunable orientated imprinting for glycoproteins. Adapted from Wang *et al.* [194].

Each MIP showed excellent binding affinities for their respective template glycoproteins and furthermore, these affinities were shown to be tunable by taking advantage of the pH dependency of the boronic acid's pKa [194]. At an alkaline pH the imprints showed higher binding due to the two fold effect of the boronic acid moiety forming the boronate ester with the target glycoprotein in concert with shape compatibility of the imprint. In contrast, at a lower pH binding was shown to arise primarily from the shape compatibility of the cavities which was reflected in the lower affinities observed. Overall, this system was one of the first to demonstrate the proof-of-concept for synthesising 2D glycoprotein imprints in aqueous conditions. Moreover, the anchoring of glycoproteins through a boronate moiety to the functionalised surface demonstrated that their orientation can be kept constant to create MIPs of high selectivity and nM affinities.

Drawing parallels with Wang *et al,* Saeki *et al.* very recently reported the synthesis of a chip-based glycoprotein imprinted SPR sensor for ovalbumin fabricated using ATRP [195]. The ovalbumin was first immobilized onto the surface by binding 4-carboxy-3-fluorophenyl boronic acid (CFPBA) pre-functionalised to a thiol within a mixed initiator SAM, as shown in figure 1.20.

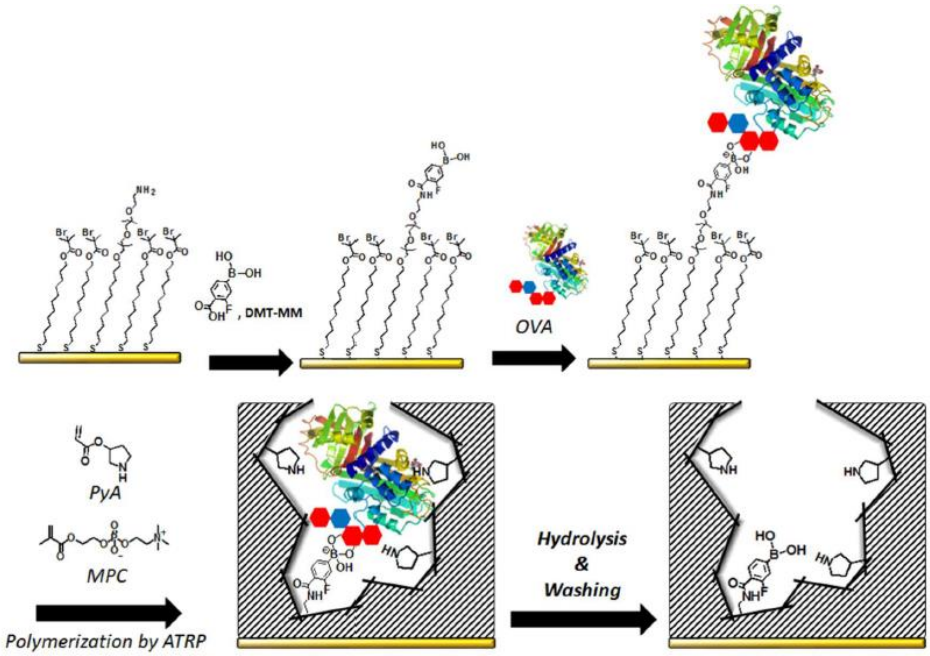

Figure 1.20: Schematic of the glycoprotein imprinting system developed for ovalbumin using 2-methacryloyloxyethl phosphocholine (MPC) and pyrrolidyl acrtlate (PyA) polymerised by ATRP. Taken from Saeki *et al.* [195].

The imprints were then polymerised within buffer for either 45 or 60 minutes to form the MIPs that measured thicknesses of approximately 9 nm and 12 nm, respectively. Overall, the binding results showed that both these MIPs showed selectivity for ovalbumin over a range of other glycoproteins (avidin, lysozyme, con-albumin, and human serum albumin (HSA)) in comparison with their NIP controls. Furthermore, the results also showed that control over the imprinting polymerisation time was crucial to achieve a good sensitivity of the surface as the thinner 45 minute MIPs

showed a 123 fold improvement in binding in comparison with the thicker 60 minute MIPs.

Overall, this system showed that MIPs with high affinities for glycoproteins can be obtained with ATRP. The concerted effect of the imprint cavity alongside the boronic acid moiety, as well as optimisation of the polymer thickness enabled excellent sensitivity of the target glycoprotein to be achieved. However, this bottom up' approach only allows the boronic acids to reside within one plane of the SAM therefore restricting the interaction of the glycans' diols to this 2D surface. Employing a protocol where the boronic acids not only anchor the protein but are also free to spatially arrange themselves in a complementary manner to the glycan could further enhance the sensitivity of this system.

Another recent example of a system that employed boronate binding capabilities within their glycoprotein imprinting strategy, but instead fabricated the imprints upon magnetic nanoparticles (MNPs) was reported by Lui *et al.* [196]. In this case they wished to imprint the glycan chain of RNase B in order to produce a replacement glycoprotein capture strategy to using lectins. As shown in figure 1.21, the imprints were synthesised using a three-step process. First, the N-glycans of the RNase B glycoprotein were cleaved from the protein and then ultra-centrifuged. The glycans were then immobilized onto pre-functionalized MNPs *via* a boronate affinity interaction using (3,5-difluoro-4-formylphenyl) boronic acid (DFFPBA), which were then polymerised in ethanol using a thin layer of TEOS polymer for either 30, 40 or 50 minutes to form imprinted MNPs. The imprinted MNPs were then washed to release the glycan and finally assessed for their RNase B rebinding capabilities using UV/Vis absorbance.

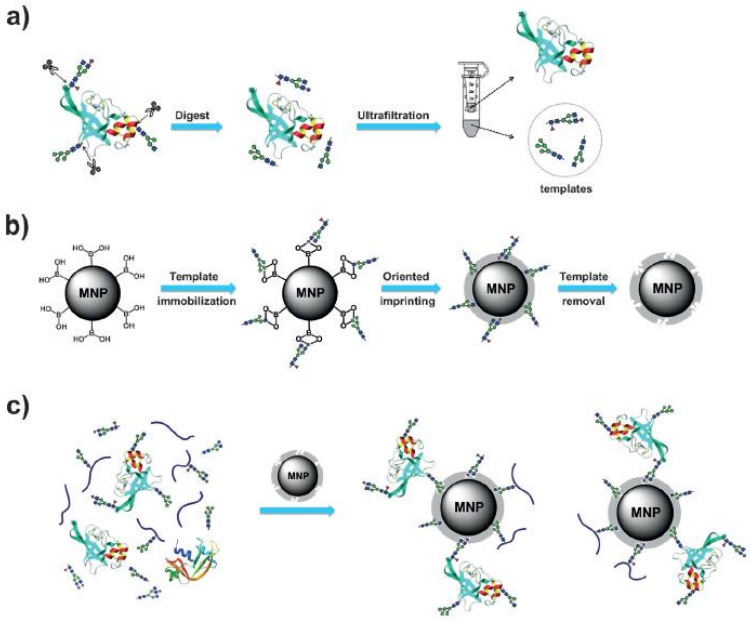

Figure 1.21: Schematic of the of the 3-step method for the MNP glycan imprints. The glycan is enzymatically cleaved from the protein and separated using ultra-centrifuged membrane filtration (a). Boronic acid functionalised MNPs are then incubated with the template and polymerised around to form the imprinted MNPs (b). The imprinted MNPs are then tested with either the glycan, a glycoprotein fragment or the intact glycoprotein for rebinding (c). Taken from Lui *et al.* [196].

The results showed that the 50 minute MNP MIPs exhibited the best imprinting factor of 8.4 when tested for RNase B rebinding and likewise showed a strong affinity for RNase B in comparison with the MNP NIP control. Furthermore, when the specificity of the MIPs were examined using RNase A (the non-glycosylated homologue of RNase B) as well as two other glycoproteins the MIPs exhibited a higher specificity and selectivity for RNase B.

Finally, the response of the MNP MIPs towards a directly representative glycol-peptide sample was also examined. Here, tryptic digests of both the RNase B and HRP glycoproteins were undertaken to cut their polypeptide backbones into smaller glycol-peptide fragments and from this mixture 3 glycol-peptide sources of equivalent molecular weight from each source were then mixed at a 1:1 ratio and incubated with

the MNP MIPs. Overall, only the RNase B peptide glycoforms were shown to bind to the MIPs as expected.

In summary, this platform is the first to show that a simple set-up can be used to produce MIPs towards specific glycans that offer an alternative to lectin glycan detection. However, the primary drawback of this protocol is that the glycoprotein polypeptide is destroyed before imprint synthesis which is not ideal if the sample is precious. Furthermore, the function of this platform is primarily for protein capture and not kinetic binding analysis, therefore additional development would be required to adapt this system to function as a sensor.

Following this paper, the same authors developed the aforementioned system to again create MIPs for the glycans of glycoproteins, but instead keeping a proportion of the peptide attached during the imprint synthesis, as shown in figure 1.22.

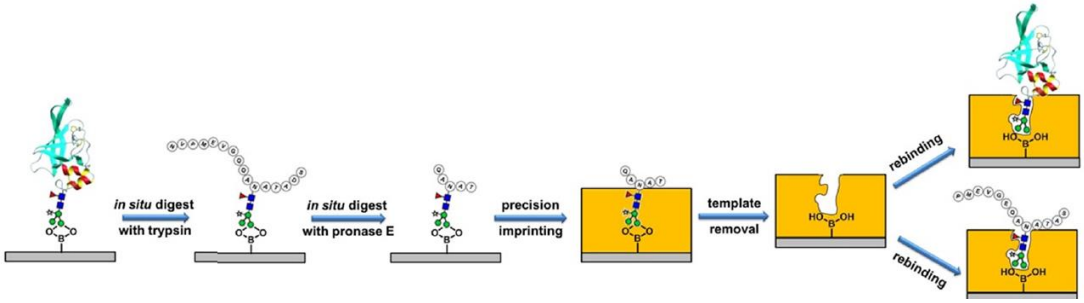

Figure 1.22: Schematic of the of the MNP glyco imprints. The glycan is enzymatically cleaved from the protein and separated using ultra-centrifuged membrane filtration (a). Boronic acid functionalised MNPs are then incubated with the template and polymerised around to form the imprinted MNPs (b). The imprinted MNPs are then tested with either the glycan, a glycoprotein fragment or the intact glycoprotein for rebinding (c). Adapted from Bie *et al.* [197].

In this case, the HRP glycoprotein was immobilised onto the pre-functionalised DFFPBA MNPs, following which two different enzyme digests (tryptic and Pronase A) were used to cut the protein backbone into smaller portions. As before, the HRP MNP MIPs were then synthesised using TEOS in ethanol and the binding measured by the UV/Vis absorbance. The resultant MNP MIPs again showed a high affinity to

the fully intact HRP glycoprotein in comparison to the NIP controls. As previously, the thickness of the TEOS layer was optimised to a thickness of 2.2 nm which produced the best imprinting factor of 10.7. Furthermore, the MNP MIPs showed excellent specificity to binding HRP as low binding was observed when tested with both glycosylated (RNase B and TRF) and non-glycosylated (RNase A and BSA) proteins. Moreover, as with the previous paper the specificity of the MIPs to the glycans on their own were also examined by using tryptic digests of RNase B and HRP. Once again 1:1 mixtures of the two glycans were incubated with the HRP imprinted MIPs and showed higher extraction of the HRP glycan structures as expected.

Overall, these two studies collectively demonstrate that glycan imprinting is possible and that developing these methods could offer a replacement for lectins. In this case the use of the fixed DFFPBA boronic acid alongside optimising the thickness of the TEOS polymer is crucial to achieving a successful imprint which should be taken into account in future imprinting studies. However, the drawbacks with these imprinting systems is firstly the destruction of the potentially precious template molecule and secondly the limitation of employing UV/Vis absorbance to measure target binding where no kinetic analysis is possible. In order to apply this format to a more informative sensing system such as SPR, both systems would require further development.

7.0 Concluding Remarks

As the role of glycosylation in the development of disease is increasingly understood, it is clear that there is a need for strategies that can detect N- and O- glycosylation changes. For diseases such as PCa where it is known that N-glycan changes occur to its glycoprotein biomarker with the progression of the disease, it is paramount that sensing methods evolve to enable the detection of these changes to be realised. The current methods adopted to detect biomolecule glycan changes, such as HPLC or capillary electrophoresis (CE) coupled with mass spectrometry, are satisfactorily sensitive however they require expensive, large set-ups [82, 198, 199]. In contrast, using lectins for example in ELLA and agglutination assays is significantly cheaper than these methods, however both of these techniques are hindered by the weak affinities of lectins that lead to poor sensitivities for target saccharide molecules [73, 200]. Moreover, cross-reactivity issues alongside the lack of commercially available lectins that bind unique saccharide structures also limits progress within glycan research [201, 202]. To this end, the development of novel glycan detection platforms that are sensitive to glycosylation changes including for biomolecules such as glycoproteins are required in order to meet this need for the healthcare industries.

From the above review, we have provided examples where molecular imprinting technologies (MITs) have been developed for the isolation and sensing of glycoproteins. Moreover, these systems have all used boronate interactions to target random saccharide moieties of the glycans of the target glycoproteins. However, in all cases the interface for the boronate interactions with respect to the glycan chains of the glycoproteins were strictly limited to a planar arrangement as the boron is primarily used as an anchoring moiety. Moreover, the binding of the boron moieties

to other *cis* diols of these glycan chains is therefore restricted by the design of these platforms. Developing glycoprotein imprinting systems where these interactions are not limited to a planar arrangement and hence target multiple diols of the glycans could offer improved glycan target specificity and selectivity. As outlined below, this thesis therefore explores the fabrication of a novel molecularly imprinted glycoprotein sensor that explores this avenue.

8.0 Aims and Objectives

The overall aim of this thesis is to develop a novel glycoprotein recognition platform capable of detecting the model glycoprotein, RNase B. This glycoprotein has a single N-linked glycosylation chain attached to its polypeptide backbone which is composed of several mannose sugar units. These sugar units are known to bind the boron moiety of the aforementioned boronic acid monomer *via* specific hydroxyl groups found within its glycan structure. To therefore target this glycan, the molecular imprinting system will incorporate a functional boronic acid monomer within its design. However, these monomers will be covalently complexed with the glycoprotein during the imprint synthesis and hence be arranged within a 3-dimensional display within the recognition sites. RNase B was chosen for these imprinting studies due to its thorough characterisation previously reported in the literature and its low cost with respect to most glycoproteins.

To synthesise the glycoprotein imprints, the project will employ ATRP, a well-known form of controlled radical polymerisation (CRP), to create the ultra-thin polymer matrices into which the impressions of RNase B will be formed. The MIPs will be

synthesised to be as complementary to the shape, size, spatial orientation and molecular functionality of RNase B as possible.

The strategy to achieve this goal is outlined in a three step process as shown in figure 1.23. The first step is to create a foundation layer on a gold surface from which the polymer matrix will be grown. To achieve this alkanethiols will be used to create SAMs on the gold surface which act as the initiator sites for the polymerisation reaction. Once fully analysed using various surface characterisation techniques to prove their formation the SAM surfaces can then be taken forward for polymerisation.

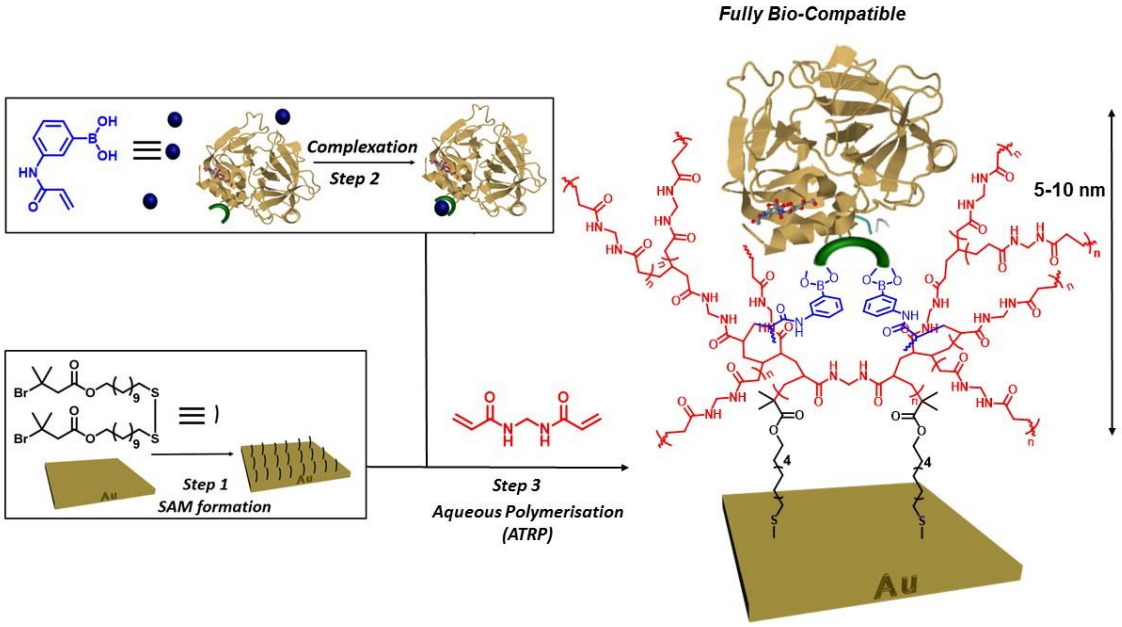

Figure 1.23: Schematic representation of the novel molecular imprinting protocol developed within this thesis. The project has been undertaken in three stages:

Step 1 is the synthesis and characterisation of a self-assembled monolayer on a gold substrate that provides initiator sites for the polymerisation reaction. **Step 2** is the incubation of the model glycoprotein with a vinyl boronic acid monomer to form a boronic acid-glycoprotein complex. **Step 3** is to integrate the first two steps to create molecular imprints for the glycoprotein-boronic acid complex using ATRP which are then assess for their target rebinding capabilities.

The second stage of the project that will be undertaken in parallel with the SAM development is the study of the complexation between the RNase B glycoprotein and the functional boronic acid monomer. The two species will be mixed together to create a complex that will then be used as the template to form the RNase B compatible imprint. The conditions to encourage the complexation will be investigated to ensure this binding is optimised.

The third step is to then bring together steps 1 and 2 to create the molecular imprints (MIPs). ATRP will be employed to grow the polymer from the initiator SAM surfaces at room temperature in aqueous, biocompatible conditions. These conditions have been selected in order to be as complimentary to the native protein environment as possible. Optimisation of the polymerisation system to gain suitable control over the polymer depth and characteristics will be explored in order to develop the optimal imprinting system for the glycoprotein. This work is the first to explore imprinting where the functionalities of the boron-glycan interactions are not limited to a 2D plane.

References

1. Prestegard, J.H., Lui. J., and Widmalm G., *Oligosaccharides and Polysaccharides.*, in *Essentials of Glycobiology*, C.R. Varki A, Esko JD, et al., Editor. 2017, Cold Spring Harbor (NY): Cold Spring Harbor Laboratory Press; 2015-2017.
2. J. L. Garcia., A.Lopez-Munguia., and E. Galindo., *Modeling the non-steady-state response of an enzyme electrode for lactose.* Enzyme and Microbial Technology, 1991. **13**(8): p. 672-675.
3. Yakovleva, M., et al., *A novel combined thermometric and amperometric biosensor for lactose determination based on immobilised cellobiose dehydrogenase.* Biosens Bioelectron, 2012. **31**(1): p. 251-6.
4. Goriushkina, T.B., A.P. Soldatkin, and S.V. Dzyadevych, *Application of amperometric biosensors for analysis of ethanol, glucose, and lactate in wine.* J Agric Food Chem, 2009. **57**(15): p. 6528-35.
5. Song, Y., et al., *Graphene oxide: intrinsic peroxidase catalytic activity and its application to glucose detection.* Adv Mater, 2010. **22**(19): p. 2206-10.
6. Rocchitta, G., et al., *Enzyme Biosensors for Biomedical Applications: Strategies for Safeguarding Analytical Performances in Biological Fluids.* Sensors (Basel), 2016. **16**(6).
7. Stick, R.V. and S.J. Williams, *Carbohydrates: The Essential Molecules of Life*. 2 ed. 2009: Elsevier Science. 496.
8. Lowry, T.M., J Chem Soc, 1899. **75**: p. 211-212.
9. Bentley, R., *The transformation of linear to cyclic monosaccharide structures.* Biochemical Education, 1998. **26**(3): p. 205-210.
10. Ouellette, R.J. and J.D. Rawn, *Carbohydrates*, in *Principles of Organic Chemistry*. 2015, Elsevier. p. 343-370.
11. Blanco, A., and Blanco, G., *Carbohydrates*, in *Medical Biochemistry*. 2017, London, United Kingdom ; San Diego, CA : Academic Press, an imprint of Elsevier, [2017]. p. 73-97.
12. Raymond, K.W., *Carbohydrates*, in *General Organic and Biological Chemistry: An Integrated Approach*. 2013, Wiley. p. 370-401.
13. Cummings, R.D., and J.M. Pierce., *The challenge and promise of glycomics.* Chem Biol, 2014. **21**(1): p. 1-15.
14. Zhao, Y.Y., et al., *Functional roles of N-glycans in cell signaling and cell adhesion in cancer.* Cancer Sci, 2008. **99**(7): p. 1304-10.
15. Baycin Hizal, D., et al., *Towards Integrative Glycoinformatics for Glycan Based Biomarker Cancer Research and Discovery.* Journal of Glycobiology, 2013. **s1**(01).

16. Egorova, K.S., and P.V. Toukach., *Glycoinformatics: bridging isolated islands in the sea of data.* Angew Chem Int Ed Engl, 2018.
17. Han, X., and X. Jiang., *A review of lipidomic technologies applicable to sphingolipidomics and their relevant applications.* Eur J Lipid Sci Technol, 2009. **111**(1): p. 39-52.
18. Lu, H., Y. Zhang., and P. Yang., *Advancements in mass spectrometry-based glycoproteomics and glycomics.* National Science Review, 2016. **3**(3): p. 345-364.
19. Ellgaard, L., and A. Helenius., *Quality control in the endoplasmic reticulum.* Nature Reviews Molecular Cell Biology, 2003. **4**: p. 181.
20. Thaysen-Andersen, M.P., and Schulz, B.L., *Maturing Glycoproteomics Technologies Procide Unique Structural Insights into the N-glycoproteoms and its Regulation in Health and Disease.* The American Society for Biochemistry and Molecular Biology, 2016. **15**(6): p. 1773-1790.
21. Prabakaran, S., et al., *Post-translational modification: nature's escape from genetic imprisonment and the basis for dynamic information encoding.* Wiley interdisciplinary reviews. Systems biology and medicine, 2012. **4**(6): p. 565-583.
22. Resh, M.D., et al., *Covalent lipid modifications of proteins.* Curr Biol, 2013. **23**(10): p. R431-5.
23. Khoury, G.A., R.C. Baliban., and C.A. Floudas., *Proteome-wide post-translational modification statistics: frequency analysis and curation of the swiss-prot database.* Sci Rep, 2011. **1**.
24. Schwarz, F., and M. Aebi., *Mechanisms and principles of N-linked protein glycosylation.* Current Opinion in Structural Biology, 2011. **21**(5): p. 576-582.
25. Cummings, R.D., et al., *Essentials of Glycobiology, 2nd edition*, ed., 2009, Cold Spring Harbor (NY): Cold Spring Harbor Laboratory Press.
26. Tharmalingam, T., K. Mariño., and P.M. Rudd., *Platform technology to identify potential disease markers and establish heritability and environmental determinants of the human serum N-glycome.* Carbohydrate Research, 2010. **345**(10): p. 1280-1282.
27. Leung, H.S., et al., *Entry of influenza A Virus with an Alpha2,6-linked Sialic Acid Binding Preference Requires Host Fibronectin.* J Virol, 2012. **86**(19): p. 10704-13.
28. Hayakawa, T.A., et al., *Human Specific Changes in Sialic Acid Biology*, in *Post-Genome Biology of Promates, Primatology Monographs*, 2012, Springer. p. 123-148.
29. Gilgunn, S., et al., *Aberrant PSA glycosylation- a sweet predictor of prostate cancer.* Nat Rev Urol, 2013. **10**(2): p. 99-107.
30. Harvey, D.J., et al., *Proposal for a standard system for drawing structural diagrams of N- and O-linked carbohydrates and related compounds.* Proteomics, 2009. **9**(15): p. 3796-801.

31. van Reeuwijk, J., et al., *POMT2 mutations cause alpha-dystroglycan hypoglycosylation and Walker-Warburg syndrome.* J Med Genet, 2005. **42**(12): p. 907-12.
32. Christiansen, M.N., et al., *Cell surface protein glycosylation in cancer.* Proteomics, 2014. **14**(4-5): p. 525-46.
33. Schedin-Weiss, S., et al., *The role of protein glycosylation in Alzheimer disease.* FEBS J, 2014. **281**(1): p. 46-62.
34. Venkatakrishnan. V,. et al., *Host mucin glycosylation plays a role in bacterial adhesion in lungs of individuals with cystic fibrosis.* Exper Rev Respir Med, 2013. **7**(5): p. 553-576.
35. Adamczyk, B., Tharmalingam, T., and Rudd, P.M., *Glycans as cancer biomarkers.* Biochim Biophys Acta, 2012. **1820**(9): p. 1347-53.
36. Radhakrishnan, P., et al., *Immature truncated O-glycophenotype of cancer directly induces oncogenic features.* Proc Natl Acad Sci U S A, 2014. **111**(39): p. E4066-75.
37. Dennis, J.W., et al., *Beta 1-6 branching of Asn-linked oligosaccharides is directly associated with metastasis.* Science, 1987. **236**(4801): p. 582-5.
38. Lau, K.S., and Dennis, J.W., *N-Glycans in cancer progression.* Glycobiology, 2008. **18**(10): p. 750-60.
39. Guo, H.B., Randolph, M., and Pierce, M., *Inhibition of a Specific N-Glycosylation Activity Results in Attenuation of Breast Carcinoma Cell Invasiveness-related Phenotypes: Inhibition Of Epidermal Growth Factor-Induced Dephosphorylation Of Focal Adhesion Kinase.* Journal of Biological Chemistry, 2007. **282**(30): p. 22150-22162.
40. Miyazaki, K., et al., *Loss of Disialyl Lewis a, the Ligand for Lymphocyte Inhibitory Receptor Sialic Acid-Binding Immunoglobulin-Like Lectin-7 (Siglec-7) Associated with Increased Sialyl Lewis a Expression on Human Colon Cancers.* Cancer Research, 2004. **64**(13): p. 4498-4505.
41. Tsuchida, A., et al., *Synthesis of disialyl Lewis a (Le(a)) structure in colon cancer cell lines by a sialyltransferase, ST6GalNAc VI, responsible for the synthesis of alpha-series gangliosides.* J Biol Chem, 2003. **278**(25): p. 22787-94.
42. Grönberg, H., *Prostate cancer epidemiology.* The Lancet, 2003. **361**(9360): p. 859-864.
43. Potosky, A.L., et al., *The role of increasing detection in the rising incidence of prostate cancer.* Jama, 1995. **273**(7): p. 548-52.
44. Velonas, V.M., et al., *Current status of biomarkers for prostate cancer.* Int J Mol Sci, 2013. **14**(6): p. 11034-60.
45. Malatesta, M., et al., *Prostate-Specific Antigen Synthesis and Secretion by Human Placenta: A Physiological Kallikrein Source during Pregnancy1.* The Journal of Clinical Endocrinology & Metabolism, 2000. **85**(1): p. 317-321.

46. Kuriyama, M., et al., *Quantitation of prostate-specific antigen in serum by a sensitive enzyme immunoassay.* Cancer Research, 1980. **40**(12): p. 4658-62.
47. Kuriyama, M., et al., *Use of Human Prostate-specific Antigen in Monitoring Prostate Cancer.* Cancer Research, 1981. **41**(10): p. 3874.
48. Zavaski, M.E., et al., *Differences in prostate-specific antigen testing among urologists and primary care physicians following the 2012 uspstf recommendations.* JAMA Internal Medicine, 2016. **176**(4): p. 546-547.
49. Wang, M.C., et al., *Purification of a human prostate specific antigen.* Invest Urol, 1979. **17**(2): p. 159-63.
50. Andriole, G.L., et al., *Prostate cancer screening in the randomized Prostate, Lung, Colorectal, and Ovarian Cancer Screening Trial: mortality results after 13 years of follow-up.* J Natl Cancer Inst, 2012. **104**(2): p. 125-32.
51. Martin, R.M., et al., *Effect of a Low-Intensity PSA-Based Screening Intervention on Prostate Cancer Mortality: The CAP Randomized Clinical Trial.* JAMA, 2018. **319**(9): p. 883-895.
52. Gronberg, H., et al., *Prostate cancer screening in men aged 50-69 years (STHLM3): a prospective population-based diagnostic study.* Lancet Oncol, 2015. **16**(16): p. 1667-76.
53. Steineck, G., et al., *Quality of Life after Radical Prostatectomy or Watchful Waiting.* New England Journal of Medicine, 2002. **347**(11): p. 790-796.
54. Siegel, T., et al., *The Development of Erectile Dysfunction in Men Treated for Prostate Cancer.* The Journal of Urology, 2001. **165**(2): p. 430-435.
55. Loeb, S., et al., *Systematic review of complications of prostate biopsy.* Eur Urol, 2013. **64**(6): p. 876-92.
56. Stamey, T.A., et al., *The prostate specific antigen era in the United States is over for prostate cancer: what happened in the last 20 years?* J Urol, 2004. **172**(4 Pt 1): p. 1297-301.
57. Constantinou, J., and M.R. Feneley., *PSA testing: an evolving relationship with prostate cancer screening.* Prostate Cancer Prostatic Dis, 2006. **9**(1): p. 6-13.
58. Tajiri, M., Ohyama, C., and Wada, Y., *Oligosaccharide profiles of the prostate specific antigen in free and complexed forms from the prostate cancer patient serum and in seminal plasma: a glycopeptide approach.* Glycobiology, 2008. **18**(1): p. 2-8.
59. Bélanger, A., et al., *Molecular mass and carbohydrate structure of prostate specific antigen: Studies for establishment of an international PSA standard.* The Prostate, 1995. **27**(4): p. 187-197.

60. Saldova, R., et al., *Core fucosylation and alpha2-3 sialylation in serum N-glycome is significantly increased in prostate cancer comparing to benign prostate hyperplasia.* Glycobiology, 2011. **21**(2): p. 195-205.
61. Wang, X., et al., *Overexpression of alpha (1,6) fucosyltransferase associated with aggressive prostate cancer.* Glycobiology, 2014. **24**(10): p. 935-44.
62. Barthel, S.R., et al., *Alpha 1,3 fucosyltransferases are master regulators of prostate cancer cell trafficking.* Proc Natl Acad Sci U S A, 2009. **106**(46): p. 19491-6.
63. Tabares, G., et al., *Different glycan structures in prostate-specific antigen from prostate cancer sera in relation to seminal plasma PSA.* Glycobiology, 2006. **16**(2): p. 132-45.
64. Ohyama, C.F., and Hosono, M., *Carbohydrate structure and differential binding of PSA to Maackia amurensis lectin between prostate cancer and benign prostate hypertrophy.* Glycobiology, 2004. **14**(8): p. 671-679.
65. Yoneyama, T., et al., *Measurement of aberrant glycosylation of prostate specific antigen can improve specificity in early detection of prostate cancer.* Biochem Biophys Res Commun, 2014. **448**(4): p. 390-6.
66. Kyselova, Z., et al., *Alterations in the serum glycome due to metastatic prostate cancer.* J Proteome Res, 2007. **6**(5): p. 1822-32.
67. Chandrasekaran, E.V., et al., *Biosynthesis of the carbohydrate antigenic determinants, Globo H, blood group H, and Lewis b: a role for prostate cancer cell α1,2-L-fucosyltransferase.* Glycobiology, 2002. **12**(3): p. 153-162.
68. Matsumoto, K., et al., *N-Glycan fucosylation of epidermal growth factor receptor modulates receptor activity and sensitivity to epidermal growth factor receptor tyrosine kinase inhibitor.* Cancer Sci, 2008. **99**(8): p. 1611-7.
69. Brewster, D.H., et al., *Rising incidence of prostate cancer in Scotland: increased risk or increased detection?* BJU Int, 2000. **85**(4): p. 463-72; discussion 472-3.
70. Meany, D.L., et al., *Glycoproteomics for prostate cancer detection: changes in serum PSA glycosylation patterns.* J Proteome Res, 2009. **8**(2): p. 613-9.
71. Feizi, T.E., and Haltiwanger, R.S., *Editorial overview: Carbohydrate-protein interactions and glycosylation: Glycan synthesis and recognition: finding the perfect partner in a sugar-coated life.* Curr Opin Struct Biol, 2015. **34**: p. vii-ix.
72. Coelho, L.C., et al., *Lectins, Interconnecting Proteins with Biotechnological/Pharmacological and Therapeutic Applications.* Evid Based Complement Alternat Med, 2017. **2017**: p. 1594074.

73. Hendrickson, O.D. and Zherdev, A.V., *Analytical Application of Lectins.* Crit Rev Anal Chem, 2018. **48**(4): p. 279-292.
74. De Schutter, K., and Van Damme, E.J., *Protein-carbohydrate interactions as part of plant defense and animal immunity.* Molecules, 2015. **20**(5): p. 9029-53.
75. Etzler, R.D., et al., *Antibodies and Lectins in Glycan Analysis*, in *Essentials of Glycobiology (2nd Edition)*, 2009, Cold Spring Laboratory Press: Cold Spring Harbor (NY).
76. Kaji, H., et al., *Lectin affinity capture, isotope-coded tagging and mass spectrometry to identify N-linked glycoproteins.* Nature Biotechnology, 2003. **21**: p. 667-672.
77. Hirabayashi, J., et al., *Lectin microarrays: concept, principle and applications.* Chem Soc Rev, 2013. **42**(10): p. 4443-58.
78. Couzens, L., et al., *An optimized enzyme-linked lectin assay to measure influenza A virus neuraminidase inhibition antibody titers in human sera.* J Virol Methods, 2014. **210**: p. 7-14.
79. Khan, K.R., et al., *Lectins as markers for blood grouping.* MedSciMonit, 2002. **8**(12): p. 293-300.
80. Meany, D.L., et al., *Glycoproteomics for Prostate Cancer Detection: Changes in Serum PSA Glycosylation Patterns.* Journal of Proteome Research, 2009. **8**(2): p. 613-619.
81. Samsonov, R., et al., *Lectin-induced agglutination method of urinary exosomes isolation followed by mi-RNA analysis: Application for prostate cancer diagnostic.* Prostate, 2016. **76**(1): p. 68-79.
82. Haab, B.B., et al., *Using lectins in biomarker research: addressing the limitations of sensitivity and availability.* Proteomics Clin Appl, 2012. **6**(7-8): p. 346-50.
83. Singh, A.P.S., et al., *Effect of Temperature, pH and Denaturing Agents on Biological Activity of MCJ Lectin.* Chemical Science Transactions, 2013. **2**(4): p. 1508-1512.
84. Marcos, M., et al., *pH-dependent thermal transitions of lentil lectin.* FEBS Letters, 1999. **443**(2): p. 192-196.
85. Nishiyabu, R., et al., *Boronic acid building blocks: tools for sensing and separation.* Chem Commun (Camb), 2011. **47**(4): p. 1106-23.
86. Frankmarken, K., et al., *Exploiting the reversible covalent bonding of boronic acids - recognition, sensing and assembly.* Accounts of Chemical Research, 2012. **46**(2): p. 312-326.
87. Lorand, J.P., and Edwards, J.O., *Polyol Complexes and Structure of the Benzeneboronate Ion.* The Journal of Organic Chemistry, 1959. **24**(6): p. 769-774.
88. Brooks, W.L., and Sumerlin, B.S., *Synthesis and Applications of Boronic Acid-Containing Polymers: From Materials to Medicine.* Chem Rev, 2016. **116**(3): p. 1375-97.

89. Li, X., et al., *Synthesis of Sulfonamide- and Sulfonyl- Phenylboronic Acid Modified Silica Phases for Boronate Affinity Chromatography at Physiological pH.* Analytical Biochemistry, 2008. **372**(2): p. 227-236.

90. Tomsho, J.W., et al., *Ring Structure and Aromatic Substituent Effects on the pK a of the Benzoxaborole Pharmacophore.* ACS Med Chem Lett, 2012. **3**(1): p. 48-52.

91. Wiskur, S.L., et al., *pKa values and Geometries of Secondary and Tertiary Amines Complexed to Boronic Acids - Implications for Sensor Design.* Organic Letters, 2001. **3**(9): p. 1311-1314.

92. Wulff, G., and Lauer, M., *Arylboronic acids with Intramolecular B-N interactions - convenient synthesis through orth-lithiation of substituted benzylamines.* Journal of Organometallic Chemistry, 1983. **256**(1): p. 1-9.

93. Collins, B.E., Sorey, S., and Hargrove, A. E., *Probing intramolecular B-N interactions in ortho-aminomethyl arylboronic acids.* J. Org. Chem, 2009. **74**(11): p. 4055-4060.

94. Collins, B.E., Metola, P., and Anslyn, E.V., *On the Rate of Boronate Ester Formation in ortho-Aminomethyl Functionalized Phenyl Boronic Acids.* Supramol Chem, 2013. **25**(2): p. 79-86.

95. Zhai, W., Sun, X., James, T.D., and Fossey, J.S., *Boronic Acid-Based Carbohydrate Sensing.* Chemistry - An Asian Journal, 2015. **10**(9): p. 1836-1848.

96. Cambre, J.N., and Sumerlin, B.S., *Biomedical applications of boronic acid polymers.* Polymer, 2011. **52**(21): p. 4631-4643.

97. Zhang, X., et al., *Boronic acid liposomes for cellular delivery and content release driven by carbohydrate binding.* Chem Commun (Camb), 2018. **54**(48): p. 6169-6172.

98. Matsumoto, A., et al., *Heterocyclic boronic acids display sialic acid selective binding in a hypoxic tumor relevant acidic environment.* Chem Sci, 2017. **8**(9): p. 6165-6170.

99. Ji, M., et al., *Sialic Acid-Targeted Nanovectors with Phenylboronic Acid-Grafted Polyethylenimine Robustly Enhance siRNA-Based Cancer Therapy.* ACS Appl Mater Interfaces, 2016. **8**(15): p. 9565-76.

100. Jay, J.I., et al., *Modulation of Viscoelasticity and HIV Transport as a Function of pH in a Reversibly Crosslinked Hydrogel.* Adv Funct Mater, 2009. **19**(18): p. 2969-2977.

101. Zhao, Z., et al., *Boronic Acid Shell-Crosslinked Dextran-b-PLA Micelles for Acid-Responsive Drug Delivery.* Macromolecular Bioscience, 2014. **14**(11): p. 1609-1618.

102. Ren, J., et al., *pH/sugar dual responsive core-cross-linked PIC micelles for enhanced intracellular protein delivery.* Biomacromolecules, 2013. **14**(10): p. 3434-43.

103. Lee, J., et al., *Glucose-Responsive Trehalose Hydrogel for Insulin Stabilization and Delivery.* Macromol Biosci, 2018. **18**(5): p. e1700372.

104. Dong, Y., et al., *Injectable and Glucose-Responsive Hydrogels Based on Boronic Acid-Glucose Complexation.* Langmuir, 2016. **32**(34): p. 8743-7.

105. Muthuchamy, N., Gopalan, A., and Lee, K.P., *Highly selective non-enzymatic electrochemical sensor based on a titanium dioxide nanowire–poly(3-aminophenyl boronic acid)–gold nanoparticle ternary nanocomposite.* RSC Advances, 2018. **8**(4): p. 2138-2147.

106. Elsherif, M., et al., *Glucose Sensing with Phenylboronic Acid Functionalized Hydrogel-Based Optical Diffusers.* ACS Nano, 2018. **12**(3): p. 2283-2291.

107. Das, B.C., et al., *Boron chemicals in diagnosis and therapeutics.* Future Med Chem, 2013. **5**(6): p. 653-76.

108. Zhang, X.C., et al., *Rational Design of d-PeT Phenylethynylated-Carbazole Monoboronic Acid Fluorescent Sensors for the Selective Detection of α-Hydroxyl Carboxylic Acids and Monosaccharides.* JACS, 2009. **131**(47): p. 17452-17463.

109. Hall, D.G., *Structure, Properties, and Preparation Of Boronic Acid Derivatives. Overview of Their Reactions and Applications.In Boronic Acids, D.G. Hall* (2006).

110. Soriano-Ursua, M.A., et al., *Boron-containing acids: preliminary evaluation of acute toxicity and access to the brain determined by Raman scattering spectroscopy.* Neurotoxicology, 2014. **40**: p. 8-15.

111. Laibinis, P.E., et al., *Comparisons of self-assembled monolayers on silver and gold: mixed monolayers derived from HS(CH2)21X and HS(CH2)10Y (X, Y = CH3, CH2OH) have similar properties.* Langmuir, 1991. **7**(12): p. 3167-3173.

112. Vericat, C., et al., *Self-assembled monolayers of thiols and dithiols on gold: new challenges for a well-known system.* Chem Soc Rev, 2010. **39**(5): p. 1805-34.

113. Flink, S., et al., *Functionalization of self-assembled monolayers on glass and oxidized silicon wafers by surface reactions.* Journal of Physical Organic Chemistry, 2001. **14**(7): p. 407-415.

114. Rakhmatullina, E., et al., *Functionalization of Gold and Silicon Surfaces by Copolymer Brushes Using Surface-Initiated ATRP.* Macromolecular Chemistry and Physics, 2007. **208**(12): p. 1283-1293.

115. Jones, J.A., et al., *Instability of self-assembled monolayers as a model material system for macrophage/FBGC cellular behavior.* J Biomed Mater Res A, 2008. **86**(1): p. 261-8.

116. Sarswat, P.K., Sathyapalan, A., and Free, M.L., *Current trends in molecular functional monolayers.* 2015: p. 331-348.

117. Schwartz, D.K., et al., *Mechanisms and Kinetics of Self-Assembled Monolayer Formation.* Annu. Rev. Phy. Chem, 2001. **52**: p. 107-137.

118. Bain, C.D., Evall, J., and Whitesides, G.M., *Formation of Monolayers by the Coadsorption of Thiols in Gold: Variation in the Head Group, Tail Group, and Solvent.* J Am Chem Soc, 1989. **111**(18): p7155-7164.

119. Vericat, C., Vela, M.E., and Salvarezza, R.C., *Self-assembled monolayers of alkanethiols on Au(111): surface structures, defects and dynamics.* Phys Chem Chem Phys, 2005. **7**(18): p. 3258-68.

120. Schreiber, F., et al., *Structure and Growth of Self-Assembling Monolayers.* Progress in Surface Science, 2000. **65**: p. 151-256.

121. Chen, J., et al., *Quantifying Gauche Defects and Phase Evolution in Self-Assembled Monolayers through Sessile Drops.* ACS Omega, 2017. **2**(5): p. 2072-2084.

122. Ansell, O.R., et al., *Molecular imprinting technology - challenges and prospects for the future.* Chirality, 1998. **10**: p. 195-209.

123. Sommerfeld, S., and Strube, J., *Challenges in biotechnology production—generic processes and process optimization for monoclonal antibodies.* Chemical Engineering and Processing: Process Intensification, 2005. **44**(10): p. 1123-1137.

124. Mujahid, A., Mustafa, G., and Dickert, F.L., *Label-Free Bioanalyte Detection from Nanometer to Micrometer Dimensions-Molecular Imprinting and QCMs (dagger).* Biosensors (Basel), 2018. **8**(2).

125. Polyakov, M.V., et al., *Adsorption properties and structure of silica gel.* Zhur. Fiz. Khim, 1931. **2**: p. 799–805

126. Wulff, G., et al., *Molecular Imprinting in Cross-Linked Materials with the Aid of Molecular Templates - A Way towards Artifical Antibodies.* Angew Chem Int Ed Engl, 1995. **34**(17): p. 1812-1832.

127. Wulff, G., et al., *Enzyme-analogue built polymers and their use for the resolution of racemates.* Tetrahedron Letters, 1973. **14**(44): p. 4329-4332.

128. Alexander, C., et al., *Molecular imprinting science and technology: a survey of the literature for the years up to and including 2003.* J Mol Recognit, 2006. **19**(2): p. 106-80.

129. Yang, S., et al., *Molecularly Imprinted Polymers for the Identification and Separation of Chiral Drugs and Biomolecules.* Polymers, 2016. **8**(6): p. 216.

130. Aşır, S., et al., *Ion-selective Imprinted Superporous Monolith for Cadmium Removal from Human Plasma.* Separation Science and Technology, 2005. **40**(15): p. 3167-3185.

131. Wang, X., Xia, N., and Liu, L., *Boronic Acid-based approach for separation and immobilization of glycoproteins and its application in sensing.* Int J Mol Sci, 2013. **14**(10): p. 20890-912.

132. Alvarez-Lorenzo, C., and Concheiro, A., *Molecularly imprinted polymers for drug delivery.* J Chromatogr B Analyt Technol Biomed Life Sci, 2004. **804**(1): p. 231-45.

133. Li, W.L., et al., *Molecular imprinting: A versatile tool for separation, sensors and catalysis.* Adv. Polym. Sci. , 2007. **206**: p. 191-210.

134. Vasapollo, G., et al., *Molecularly imprinted polymers: present and future prospective.* Int J Mol Sci, 2011. **12**(9): p. 5908-45.

135. Guan, G., et al., *Imprinting of Molecular Recognition Sites on Nanostructures and Its Applications in Chemosensors.* Sensors (Basel), 2008. **8**(12): p. 8291-8320.

136. Kröger, S., Turner, A. P. F., Mosbach, K., and Haupt, K., *Imprinted Polymer-Based Sensor System for herbicide using differential-pulse voltammetry on screen-printed electrodes.* Anal Chem, 1999. **71**(17): p. 3698-3702.

137. Meng, L., et al., *Study of an online molecularly imprinted solid phase extraction coupled to chemiluminescence sensor for the determination of trichlorfon in vegetables.* J Agric Food Chem, 2011. **59**(24): p. 12745-51.

138. Muldoon, M.T., et al., *Molecularly Imprinted Solid Phase Extraction of Atrazine from Beef Liver Extracts.* Anal Chem, 1997. **69**(5): p. 803-808.

139. Schirmer, C., and Meisel, H., *Synthesis of a molecularly imprinted polymer for the selective solid-phase extraction of chloramphenicol from honey.* J Chromatogr A, 2006. **1132**(1-2): p. 325-8.

140. Turner, N.W., et al., *From 3D to 2D: a review of the molecular imprinting of proteins.* Biotechnol Prog, 2006. **22**(6): p. 1474-89.

141. Chen, L., et al., *Molecular imprinting: perspectives and applications.* Chem Soc Rev, 2016. **45**(8): p. 2137-211.

142. Mikos, M.C., et al., *Synthetic Polymers*, in *Principles of Regenerative Medicine* 2011, Academic Press. p. 587-622.

143. Matyjaszewski, K., et al., *Polymer Chemistry: Current Status and Perspective*, in *Chemistry International*. 2017. p. 7.

144. Li, Y., et al., *Selective recognition and removal of chlorophenols from aqueous solution using molecularly imprinted polymer prepared by reversible addition-fragmentation chain transfer polymerization.* Biosens Bioelectron, 2009. **25**(2): p. 306-12.

145. Tian, X., et al., *Recent Advances in RAFT Polymerization: Novel Initiation Mechanisms and Optoelectronic Applications.* Polymers, 2018. **10**(3): p. 318.

146. Matyjaszewski, K., et al., *Atom Transfer Radical Polymerization (ATRP): Current Status and Future Perspectives.* Macromolecules, 2012. **45**(10): p. 4015-4039.

147. Detrembleur, C., et al., *Controlled Nitroxide-Mediated Radical Polymerization of Styrene, Styrene/Acrylonitrile Mixtures, and Dienes Using a Nitrone.* Macromolecules, 2002. **35**(19): p. 7214-7223.

148. Grubbs, R.B., et al., *Nitroxide-Mediated Radical Polymerization: Limitations and Versatility.* Polymer Reviews, 2011. **51**(2): p. 104-137.

149. Matyjaszewski, K., Sumerlin, B.S., Tsarevsky, N.V., and Chiefari, J., *Controlled Radical Polymerization: Mechanisms*, Vol. 1187. 2015: American Chemical Society. 1-326.

150. Matyjaszewski, K., et al., *Advanced Materials by Atom Transfer Radical Polymerization.* Advanced Materials, 2018. **30**(23): p. 1706441.

151. Jakubowski, W., et al., *Adapting Atom Transfer Radical Polymerization to Industrial Scale Production: The Ultimate ATRP Technology*, In *Progress in Controlled Radical Polymerization: Mechanisms and Techniques*. 2012, American Chemical Society. p. 203-216.

152. Matyjaszewski, K., and Spanswick, J., *Controlled/living radical polymerization.* Materials Today, 2005. **8**(3): p. 26-33.

153. Fischer, H., et al., *The persistent radical effect in controlled radical polymerizations.* Journal of Polymer Science Part A: Polymer Chemistry, 2000. **37**(13): p. 1885-1901.

154. Lin, C.Y., Coote, M.L., Gennaro, A., and Matyjaszewski, K., *Ab Initio evaluation of the thermodynamic and electrochemical properties of alkyl halides and radicals and their mechanistic implications for ATRP.* JACS, 2008. **130**: p. 12762−12774.

155. Tsarevsky, N.V., Wade, A,. Braunecker, A.V., Gans, P., and Matyjaszewski, K., *Competitive Equilibria in Atom Transfer Radical Polymerization* in *Radical Polymerization: Kinteics and Mechanism*. 2007, Macromolecular symposia: Ciocco (Italy). p. 60-70.

156. Fantin, M., et al., *Understanding the Fundamentals of Aqueous ATRP and Defining Conditions for Better Control.* Macromolecules, 2015. **48**(19): p. 6862-6875.

157. Bontempo, D., and Maynard, H.D., *Streptavidin as a Macroinitiator for Polymerization: In Situ Protein−Polymer Conjugate Formation.* Journal of the American Chemical Society, 2005. **127**(18): p. 6508-6509.

158. Jones, D.M., Brown, A.A., and Huck, W.T.S., *Surface-Initiated Polymerizations in Aqueous Media: Effect of Initiator Density.* Langmuir, 2002. **18**(4): p. 1265-1269.

159. Pasetto, P., et al., *Mechanistic Insight into Surface-Initiated Polymerization of Methyl Methacrylate and Styrene via ATRP from Ordered Mesoporous Silica Particles.* Macromolecules, 2009. **42**(16): p. 5983-5995.

160. Kruk, M., et al., *Grafting Monodisperse Polymer Chains from Concave Surfaces of Ordered Mesoporous Silicas.* Macromolecules, 2008. **41**(22): p. 8584-8591.

161. Xiang, P., et al., *Tuning structural parameters of polyethylene brushes on silica nanoparticles in surface-initiated ethylene "living" polymerization and effects on silica dispersion in a polyolefin matrix.* Polymer Chemistry, 2013. **4**(5): p. 1381-1395.

162. Kang, C., Crockett, R.M., and Spencer, N.D., *Molecular-Weight Determination of Polymer Brushes Generated by SI-ATRP on Flat Surfaces.* Macromolecules, 2014. **47**(1): p. 269-275.

163. Matyjaszewski, K. and Tsarevsky, N.V., *Nanostructured functional materials prepared by atom transfer radical polymerization.* Nat Chem, 2009. **1**(4): p. 276-88.

164. Fantin, M., et al., *ATRP in Water: Kinetic Analysis of Active and Super-Active Catalysts for Enhanced Polymerization Control.* Macromolecules, 2017. **50**(7): p. 2696-2705.

165. Wang, X.S., et al., *Facile synthesis of well-defined water-soluble polymers via atom transfer radical polymerization in aqueous media at ambient temperature.* Chemical Communications, 1999(18): p. 1817-1818.

166. Min, K. and Matyjaszewski, K., *Atom transfer radical polymerization in aqueous dispersed media.* Open Chemistry, 2009. **7**(4).

167. Vivaldo-Lima, E.W., et al., *An updated review on suspension polymerization.* Ind. Eng. Chem. Res, 1997. **36**: p. 939-965.

168. Chern, C.S., et al., *Emulsion polymerization mechanisms and kinetics.* Progress in Polymer Science, 2006. **31**(5): p. 443-486.

169. Cunningham, M.F., et al., *Controlled/living radical polymerization in aqueous dispersed systems.* Progress in Polymer Science, 2008. **33**(4): p. 365-398.

170. Ye Jianding, N.R., et al., *Water Assissted ATRP of N-isopropylacrylamide, Nature of Solvent and Temperature.* J Phys Chem, 2009. **113**: p. 676-681.

171. Kawaguchi, S., et al., *Dispersion Polymerization.*, in *Polymer Particles*, O. M., Editor., Springer, Berlin, Heidelberg.

172. Robinson, K.L., et al., *Controlled Polymerization of 2-Hydroxyethyl Methacrylate by ATRP at Ambient Temperature.* Macromolecules, 2001. **34**(10): p. 3155-3158.

173. Ye, J., and Narain, R., *Water-Assisted Atom Transfer Radical Polymerization of N-Isopropylacrylamide: Nature of Solvent and Temperature.* The Journal of Physical Chemistry B, 2009. **113**(3): p. 676-681.

174. Matyjaszewski, K., et al., *ATRP: The Chemistry: ATRP in Protic Media*. [Webpage] [cited 2018 16.08.2018]; ATRP: The Chemistry: ATRP in Protic Media]. Available from: https://www.cmu.edu/maty/chem/fundamentals-atrp/protic-media.html.

175. Nicolay, V., Tsarevsky, T.P., and Matyjaszewski, K., *Deactivation efficiency and degree of control over polymerization ATRP in protic solvents.* Macromolecules, 2004. **37**(26): p. 9768-9778.

176. Matyjaszewski, K., et al., *Role of Cu0 in controlled living radical polymerisation.* Macromolecules, 2007. **40**(22): p. 7795-7806.

177. Zhang, Y., et al., *Copper-Mediated CRP of Methyl Acrylate in the Presence of Metallic Copper: Effect of Ligand Structure on Reaction Kinetics.* Macromolecules, 2011. **45**(1): p. 78-86.

178. Percec, V., et al., *Ultrafast synthesis of ultrahigh molar mass polymers by metal-catalyzed living radical polymerisation of acrylates, methacrylates and vinyl chloride mediated by SET at 25 degrees.* 128, 2006. **43**: p. 14156–14165.

179. Horn, M., and Matyjaszewski, K., *Solvent Effects on the Activation Rate Constant in Atom Transfer Radical Polymerization.* Macromolecules, 2013. **46**(9): p. 3350-3357.

180. Masque, N., et al., *Synthesis and evaluation of a molecularly imprinted polymer for selective on-line solid-phase extraction of 4-nitrophenol from environmental water.* Anal Chem, 2000. **72**(17): p. 4122-6.

181. Mena, M.L., et al., *Molecularly imprinted polymers for on-line preconcentration by solid phase extraction of pirimicarb in water samples.* Analytica Chimica Acta, 2002. **451**(2): p. 297-304.

182. Li, S., et al., *Size matters: Challenges in imprinting macromolecules.* Progress in Polymer Science, 2014. **39**(1): p. 145-163.

183. Poma, A., Turner, A.P., and Piletsky, S.A., *Advances in the manufacture of MIP nanoparticles.* Trends Biotechnol, 2010. **28**(12): p. 629-37.

184. Hansen, D.E., *Recent developments in the molecular imprinting of proteins.* Biomaterials, 2007. **28**(29): p. 4178-91.

185. Culver, H.R. and Peppas, N.A., *Protein-Imprinted Polymers: The Shape of Things to Come?* Chemistry of Materials, 2017. **29**(14): p. 5753-5761.

186. Gai, Q., et al., *The preparation of bovine serum albumin surface-imprinted superparamagnetic polymer with the assistance of basic functional monomer and its application for protein separation.* J Chromatogr A, 2011. **1218**(22): p. 3489-95.

187. Haupt, K., *Imprinted Polymers - the next generation.* Anal Chem, 2003. **75**(17): p. 376-383.

188. Lin, Z., et al., *Preparation and evaluation of a macroporous molecularly imprinted hybrid silica monolithic column for recognition of proteins by high performance liquid chromatography.* J Chromatogr A, 2009. **1216**(49): p. 8612-22.

189. Deng, Q.L., et al., *Molecularly imprinted macroporous monolithic materials for protein recognition.* Chinese Chemical Letters, 2011. **22**(11): p. 1351-1354.

190. Aldrich, S. *Technical Bulletin: Ribonuclease B Glycoprotein Standard, Proteomics Grade*. [cited 2018 06/09/2018]; Product Information Sheet]. Available from: https://www.sigmaaldrich.com/content/dam/sigma-aldrich/docs/Sigma/Bulletin/r1153bul.pdf.

191. Li, H., et al., *A benzoboroxole-functionalized monolithic column for the selective enrichment and separation of cis-diol containing biomolecules.* Chemical Communications, 2012. **48**(34): p. 4115-4117.

192. Lin, Z., et al., *Preparation of boronate-functionalized molecularly imprinted monolithic column with polydopamine coating for glycoprotein recognition and enrichment.* J Chromatogr A, 2013. **1319**: p. 141-7.

193. Luo, J., et al., *Double Recognition and Selective Extraction of Glycoprotein Based on the Molecular Imprinted Graphene Oxide and Boronate Affinity.* ACS Appl Mater Interfaces, 2017. **9**(8): p. 7735-7744.

194. Wang, S., et al., *Affinity-tunable specific recognition of glycoproteins via boronate affinity-based controllable oriented surface imprinting.* Chemical Science, 2014. **5**(3): p. 1135.

195. Saeki, T., et al., *Orientationally Fabricated Zwitterionic Molecularly Imprinted Nanocavities for Highly Sensitive Glycoprotein Recognition.* Langmuir, 2018.

196. Liu, Z., et al., *Boronate-Affinity Glycan-Oriented Surface Imprinting: A New Strategy to Mimic Lectins for the Recognition of an Intact Glycoprotein and Its Characteristic Fragments.* Angew Chem Int Ed Engl, 2015. **54**(35): p. 10211-5.

197. Bie, Z., et al., *Precision Imprinting of Glycopeptides for Facile Preparation of Glycan-Specific Artificial Antibodies.* Anal Chem, 2018. **90**(16): p. 9845-9852.

198. Haab, B.B., et al., *Antibody-lectin sandwich arrays for biomarker and glycobiology studies.* Expert review of proteomics, 2010. **7**(1): p. 9-11.

199. Hirabayashi, J., et al., *Concept, strategy and realization of lectin-based glycan profiling.* J Biochem, 2008. **144**(2): p. 139-47.

200. Ghazarian, H., Idoni, B., and Oppenheimer, S.B., *A glycobiology review: carbohydrates, lectins, and implications in cancer therapeutics.* Acta histochemica, 2011. **113**(3): p. 236-247.

201. Li, Y., et al., *High-Throughput Lectin Microarray-Based Analysis of Live Cell Surface Glycosylation.* Current Protocols in Protein Science., Editorial Board, John E. Coligan et al., 2011. **Chapter 12**: Unit12.9.

202. Jin, S., et al., *Carbohydrate recognition by boronolectins, small molecules, and lectins.* Med Res Rev, 2010. **30**(2): p. 171-257.

Chapter 2: Surface Characterisation Techniques

Abstract: *In this chapter, a description of the surface characterisation techniques used in this work for the analysis of the substrate surfaces is provided. Since the surfaces presented are formed using sequential functionalisation it was necessary to determine the changes in their physio-chemical composition. The techniques covered include dynamic water contact angle, ellipsometry, atomic force microscopy, X-ray photoelectron spectroscopy and surface plasmon resonance. Each technique can provide insight into the success of each stage of functionalisation processes and therefore in concert provide a detailed analysis of the surface structure and chemical composition. Also covered are other techniques used for the analysis of biomolecules such as circular dichroism and electrospray ionisation mass spectrometry.*

1.0 Ellipsometry

First discovered by Drude in 1887 to probe the dielectric function of metals, ellipsometry is now widely employed in materials and interface science to determine the thickness and morphology of thin films and surfaces [1, 2]. As this optical technique is non-destructive, requires a simple set-up and can be undertaken in real-time, it is a popular choice for the characterisation of a broad range of surfaces [3]. Moreover, it can be applied to analyse films ranging from 1-1000 nm in thickness with high resolution to within 1 nm [4].

An ellipsometric measurement involves directing a beam of monochromatic, linearly polarised light onto a surface and measuring the elliptical change in the polarisation upon its reflection [5]. The thickness of a film or surface can then be derived from this change in the state of polarization. This is achieved through an indirect modelling process of the components of the elliptically polarized reflected light. Before proceeding further an understanding of the components of light will be covered for clarity:

As explained by Maxwell's theory, light is an electromagnetic wave consisting of two vectors: an electric field, E, and a magnetic field, B. These field vectors are mutually perpendicular as well as being perpendicular to the propagation direction of light, as given by the wave vector, k [3]. Both the E and B vectors themselves are formed from two components – a parallel component, 's', and a perpendicular component, 'p'.

For non-polarized light, E and B oscillate in random directions (i.e. in a number of planes). However, for linearly polarized light, E oscillates in the same direction as B (i.e. oscillation occurs in a single plane). For this linearly polarized scenario, both the 's' and 'p' components of E are equal in phase as shown in figure 2.1, a. However, if the 's' and 'p' components are out of phase, this causes E to rotate as the wave propagates. To produce a circular rotation as the wave propagates, the amplitude of the components must be of equal value as shown in figure 2.1, b, whereas if their amplitudes are unequal this produces an elliptical shape as the wave propagates as shown in figure 2.1, c. Ellipsometry therefore takes advantage of these principles by measuring the changes that occur to the 's' and 'p' components of the E vector of linearly polarised light upon reflection from a surface due to refraction by the surface molecules.

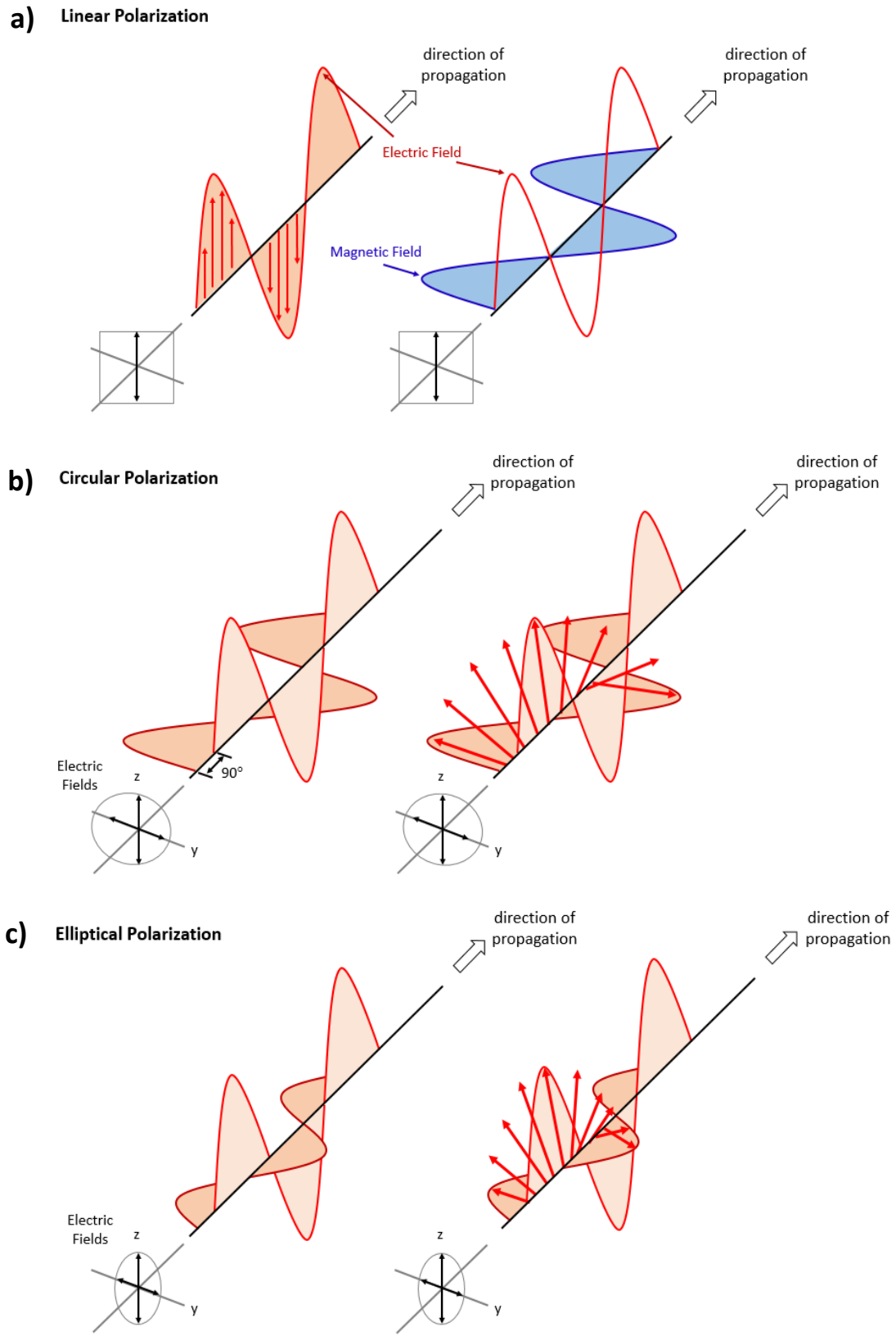

Figure 2.1: a) Depicts the electric and magnetic fields of a plane of linearly polarized light. **b)** Depicts right-handed circularly polarized light, which consists of two perpendicular electromagnetic plane waves of equal amplitude and with 90° difference in phases. **c)** Depicts right-handed elliptically polarized light, which consists of two perpendicular electromagnetic waves that are not of equal amplitude but still differ in phase by 90°.[6]

If we then apply these principles to a system whereby linearly polarised light is shone at a defined angle onto a surface which has been functionalised, for example with a self-assembled monolayer (SAM), the light will resolve into the aforementioned ‘s’ and ‘p’ components due to its refraction by the SAM molecules (figure 2.2).

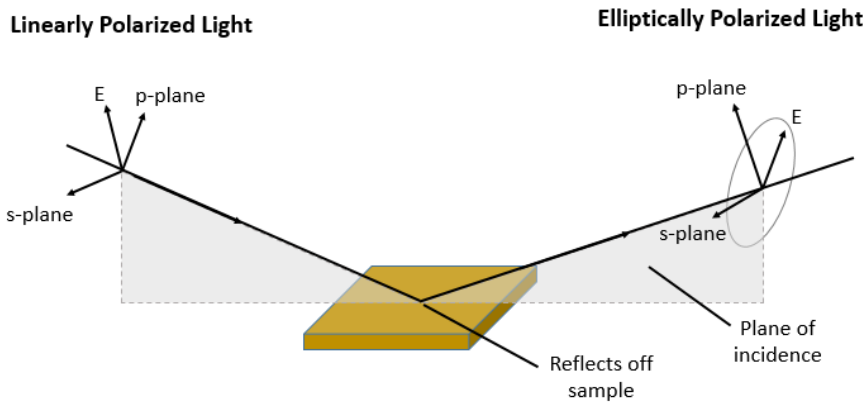

Figure 2.2: schematic diagram of the geometry of an ellipsometry experiment, whereby the ‘s’ and ‘p’ components are resolved due to diffraction from the sample surface.

The change in both the phase and amplitude of the ‘s’ and ’p’ components produces elliptically polarized light and these changes can be measured and quantified using an ellipsometer to derive information about a surface, such as the adsorbed SAM thickness. A typical ellipsometer setup is shown in figure 2.3.

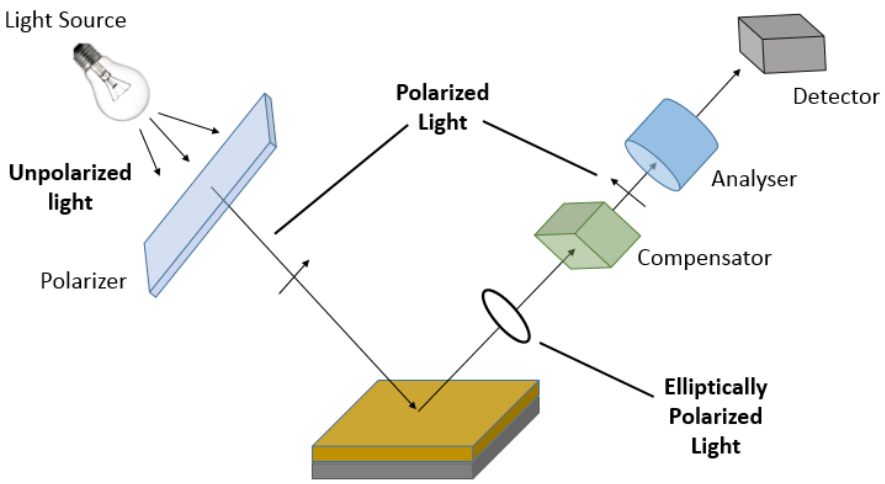

Figure 2.3: schematic diagram of a typical ellipsometer set up.

Here, the sample surface is mounted onto a stage to which the linearly polarised monochromatic beam of light is then directed. The subsequent reflected elliptically polarised beam is then sent through a compensator, analyser and finally a detector. The change in the phase and amplitude ratio between the 's' and 'p' components are then quantified which enables the reflection coefficient, ρ, to be calculated (equation 2.1). ρ is equal to the ratio between the 's' and 'p' reflection coefficients, and as equation 2.1 shows can also been expressed in terms of ψ, the amplitude ratio, and Δ, the phase difference.

$$\rho = \frac{r_\rho}{r_s} = \tan(\psi)e^{i\Delta} \qquad \text{Equation 2.1}$$

Since ellipsometry is an indirect method of determining the optical constants of a material, the ψ and Δ parameter must be processed using a layered model (for example, Substrate/SAM/Air) which takes into account the refractive index (n) and thickness of each individual layer within the whole system. The ψ and Δ parameters are calculated by applying a least-squared minimization iterative

process incorporating the Fresnel equations whereby the unknown optical constants are varied. For example, for SAMs a Cauchy model is used where the SAM layer is assumed to be transparent (k=0) with a refractive index of 1.49 [7]. The resultant thickness value is then selected from the value with the lowest Chi squared value (χ^2) to indicate the best agreement between the measured and calculated ψ and Δ parameters.

2.0 X-ray Photoelectron Spectroscopy

X-ray photoelectron spectroscopy (XPS) is a surface analysis technique used to identify and measure the concentrations of elements present at a surface. The basis of the technique is to use monochromatic X-rays as a probe that when fired at a material in an ultra-high vacuum (UHV) cause atoms of the elements present near the surface to release electrons that are then detected and analysed for their kinetic energy and intensity. XPS is a powerful tool that enables the top layer (1-10 nm) of a material to be analysed in order to identify the presence and chemical states of the elements present.

The basic set up of an XPS spectrophotometer is shown in figure 2.4.

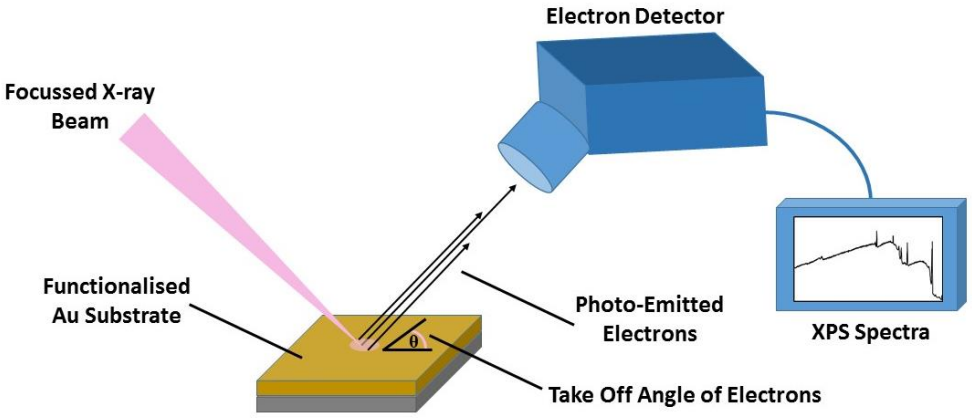

Figure 2.4: Schematic of an XPS system. The sample is mounted onto a platform within the UHV chamber that is then bombarded with Kα X-rays produced from a Mg or Al probe. The photoelectrons released from the sample are then collected by the detector to generate the XPS spectra.

The sample, here shown as a functionalised Au substrate, is mounted upon a stainless steel platform within the UHV chamber. The X-rays are then fired at a defined area of the material to release the photoelectrons. When an X-ray photon hits an electron of the core of an atom, for example a $1s^2$ electron (figure 2.5,a), it causes this electron to be emitted in the photoelectron process (figure 2.5, b) [8].

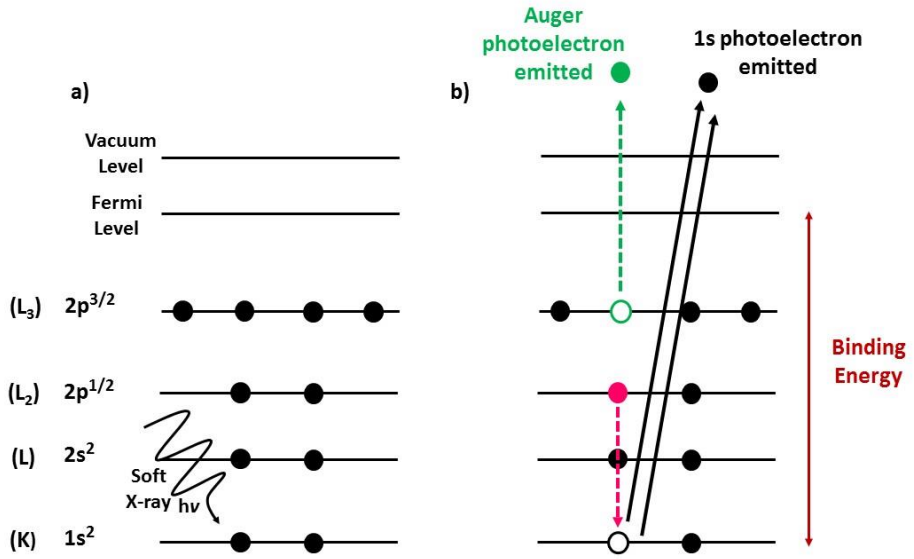

Figure 2.5: Schematic of photoelectron emission from the core shell of an atom. The soft X-ray causes the release of a $1s^2$ electron [9] that is then emitted from the material **(a).** Subsequently, another electron of a higher energy (pink) will drop down to fill this vacant position and the energy released either takes the X-ray fluorescence photoemission process or enables the release of an auger electron (green) **(b).**

When this electron is emitted, another electron from a higher energy level will drop down to fill the vacancy and releases energy in this process. This energy can take two options, either by releasing an X-ray or providing enough energy to release another electron, known as an auger electron. The kinetic energy released from this phenomena can then be used to calculate the binding energy of the electron using equation 2.2:

$$E_B = hv - E_K - W \qquad \text{Equation 2.2}$$

Where E_B is the binding energy, hv the X-ray photon energy, E_K the kinetic energy of the electron released and W the work function of the spectrometer. As the binding energy of an atom will be different when they are in a molecule this will reflected in the binding energies of an XPS spectra. An XPS spectra therefore consists of peaks with characteristic binding energies for each atom

and its chemical environments within the sample, which can collectively be used to analyse the surface material. Moreover, provided that the sample is homogenous analysis of the each peak area can provide quantitative data of the ratios of each element (A) to be, using equation 2.3:

$$C_A = \frac{\frac{I_A}{S_A}}{\sum_n \left(\frac{I_n}{S_n}\right)} \qquad \text{Equation 2.3}$$

Where, C_A typically expressed as atomic percentage and S_n denotes the sensitivity factor of each element.

3.0 Dynamic Water Contact Angle

Contact angle goniometry is a technique that provides insight into the wettability i.e the hydrophobicity or hydrophilicity of a surface by measuring the angle produced when a solvent comes into contact with a solid surface. From this angle surface tensions and energies of a solid material's surface can be calculated. The general set up of a contact angle measurement is shown in figure 2.6, where the solvent is deposited onto the surface from a syringe.

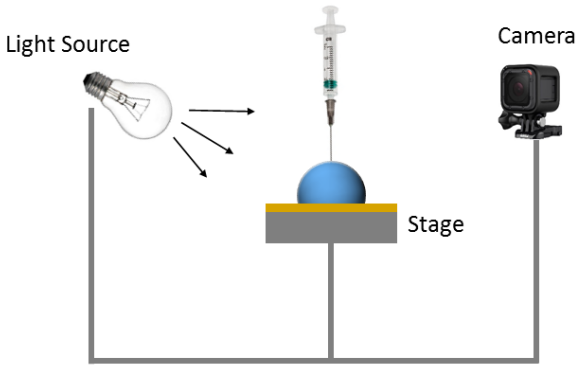

Figure 2.6: Schematic of the basic contact angle setup.

The contact angle θ is defined by *Youngs equation* (equation 2.4), where γ is the surface tensions and *LV, SV* and *SL* the liquid-vapour, solid-vapour and solid-liquid interfaces [10-12]:

$$\gamma LVCos\theta = \gamma SV - \gamma SL \qquad \text{Equation 2.4}$$

This equation describes the equilibrium between these three tensions when a droplet is deposited onto the surface [12]. The spreading of the droplet and thus the resultant contact angle is dependent upon the surfaces' hydrophilicity or hydrophobicity and surface tension, as shown in figure 2.7. Hydrophilic surfaces have a high surface energy that enables the deposited droplet to spread across the surface to produce low contact angles (<30 °). In contrast, hydrophobic surfaces have a low surface energy which prevents the droplet from spreading across the surface to produce high contact angles (>90 °).

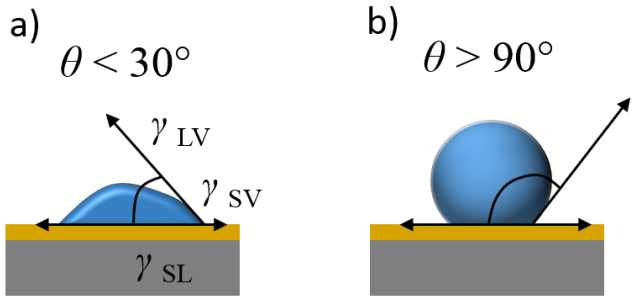

Figure 2.7: Schematic of hydrophilic a) and hydrophobic b) homogenous smooth surfaces that produces low and high contact angles, respectively.

Depending upon the set-up used the angles measured can be either the static contact angle (θ_c) or the dynamic (advancing θ_{Adv} and receding θ_{rec}) angles. In static contact angle measurements, the volume of the deposited droplet is kept

constant, whereas in dynamic measurements the volume is first increased to give θ_{Adv} and then decreased to give θ_{rec} (figure 2.8). The difference between these angles (θ_{Adv} - θ_{rec}) gives the hysteresis value θ_H of the surface. The θ_H can provide information as to the homogeneity and roughness of the surface in question. For non-contaminated, smooth or homogenous surfaces, we expect a small hysteresis of <10 °. However, for particularly contaminated, or rough or heterogeneous surfaces, we expect a large hysteresis >10 °.

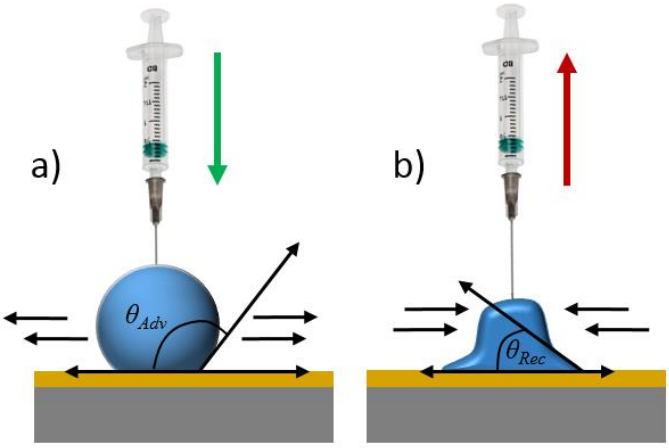

Figure 2.8: Schematic of the dynamic contact angle setup. The advancing angle a) is measured from the increase in the droplet volume whereas the receding angle b) is measured from the decrease.

Recent advancements in materials engineering and imagining technologies have enabled new adaptations of the basic contact angle technique to be developed, which include pairing contact angle measurements with confocal microscopy [13], atomic force microscopy (AFM) [14] and environmental scanning electron microscopy (ESEM) [15].

4.0 Atomic Force Microscopy (AFM)

Atomic force microscopy (AFM) is a 3-dimensional (3D) imaging technique used to visualise the structural topographies of objects or surfaces on the nanometre scale [16-19]. Unlike classic microscopy that uses line-of-sight to generate each pixel of an image, AFM uses the force of touch to 'blindly' measure local 3D-height differences, i.e. *z*-height differences, of the surface plotted against the *x*- and *y*- planes of the surface to generate each image. These height differences are then displayed by shading the resultant image with gradients of colour to show the depth differences within the sample.

A general schematic of the components used for AFM imaging are shown in figure 2.9.

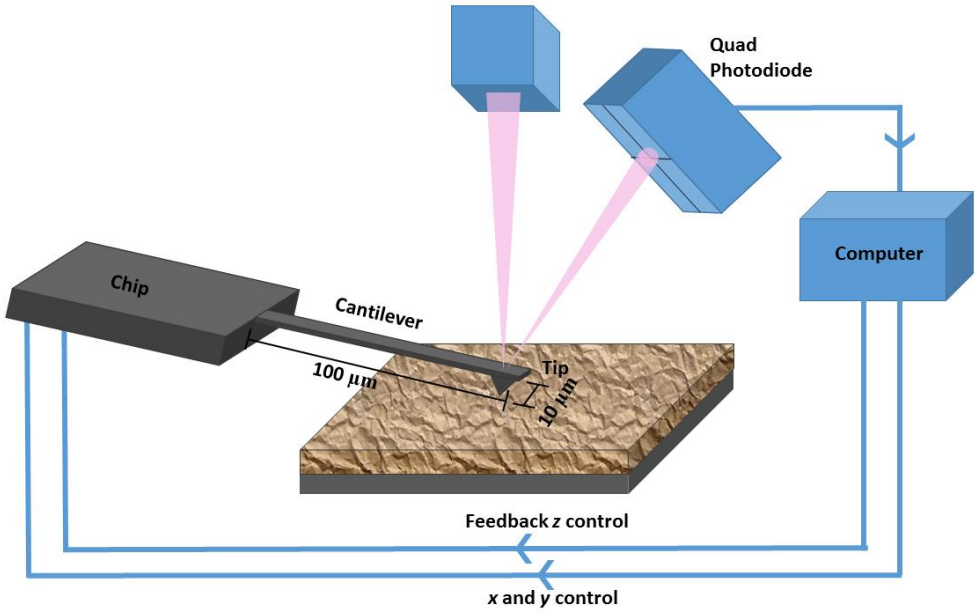

Figure 2.9: Schematic of the basic AFM set-up. A flexible silicon cantilever with a sharp tip (also known as a probe or needle) at its end is placed close to the surface of the sample, where the changes in its *z*-height due to its deflection from the surface are indirectly measured using the change in the position of the reflected laser onto the photodiode. The system modulates the piezo height in response to the *z* height measurements appropriately, as well as the *x* and *y* coordinates to move across the surface. Adapted from [20].

First, is the micro-fabricated cantilever that has a tip that lies close to the sample's surface. As the tip approaches or moves away from the surface due to attractive of repulsive forces, the flexibility of the cantilever enables it to bend under the influence of these forces. It is this deflection of the cantilever related to the upwards and downwards movements of the tip that is indirectly measured using a laser to determine the *z*-heights of the surface [20]. However, due to spring forces causing rotational movements of the cantilever as any tilt of the surface, all systems require a feedback system to continually offset for these variations during the measurement [20].

There are multiple types of AFM generally divided into three distinct types, however the following reports on the tapping mode (TM) method as this was used for the imaging studies of this thesis [21-23].

4.1 Tapping Mode Atomic Force Microscopy (TM-AFM)

TM-AFM relies on the cantilever tip vibrating up and down, i.e. oscillating close to its resonance frequency at a particular amplitude where it occasionally makes contact with the sample [24, 25]. Hence it is also known as intermittent contact or dynamic AFM. A schematic of these oscillating movements of the tip/cantilever are shown in figure 2.10,a. Here the resonance frequency and hence the oscillation of the tip/cantilever is constant as it is not close to the surface.

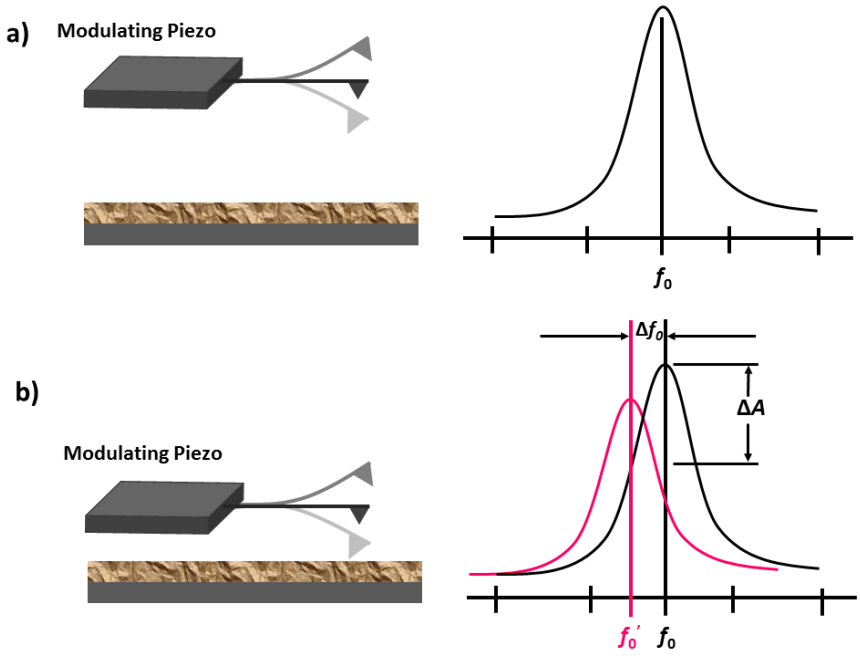

Figure 2.10: Schematic of the changes that occur in the resonance curve during a tapping mode AFM measurement cycle. The cantilever/tip modulates at a resonance frequency (f_0) when above the sample **(a).** When the cantilever/tip approaches the surface attractive forces cause a reduction in the frequency (f_0') of the resonance and the amplitude of the curve **(b)**.

If the piezo height is adjusted to be lower to the surface, the cantilever/tip begins to approach the surface from the pull of attractive Van der Waals forces [26]. This causes a decrease in the resonant frequency and the amplitude of the oscillation due to the change the vibrational frequency [27]. As the tip makes contact with the surface repulsive forces consequently repel the tip away to produce an increase in the resonant frequency. The overall change (Δf) in this frequency and oscillation of the resonance is constantly assessed by the feedback loop and the change in the deflection of the laser from the cantilever is then used to measure the *z*-height profiles of the surface [28, 29].

5.0 Surface Plasmon Resonance

Surface plasmon resonance is an optical sensing technique that utilises changes in the refractive index (RI) of a dielectric surface interface to measure the binding of an analyte in real time. SPR has rapidly become widely used for the study of surface-based biomolecular binding interactions of ligands to their respective target analytes [30]. The advantages of this sensing method are its ease of set up, relatively low running costs and real-time measurement of binding affinities and kinetics.

Before discussing a typical SPR set up one must first examine the generation of a surface plasmon wave (SPW) from a dielectric surface interface. When monochromatic '*p*' polarised light of a fixed wavelength is shone at a particular angle (θ_i) through a glass prism with a high refractive index (RI), which is in contact with a thin (~50 nm) conducting metal surface (typically Au or Ag), a SPW is generated. This is due to the total internal reflection (TIR) of the incident light enabling the excitation of the free electrons of the metal material to generate photon-plasmon surface electromagnetic waves, as shown in figure 2.11.

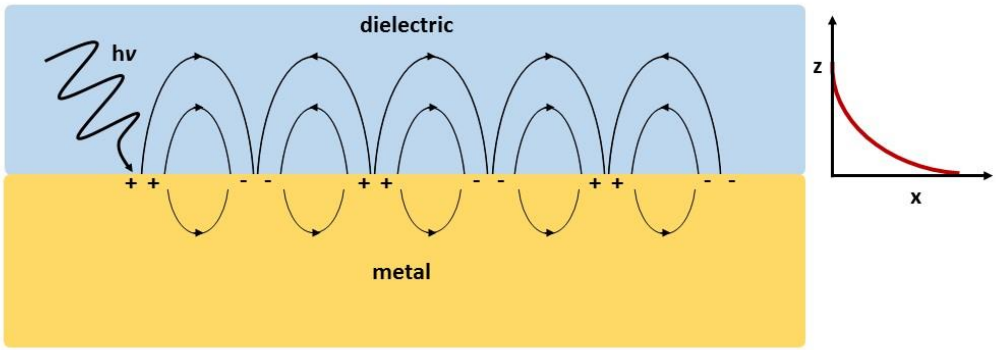

Figure 2.11: Schematic diagram of a surface plasmon wave propagating parallel to the dielectric surface, alongside the evanescent, exponential decay of each wave.

These waves are produced at the dielectric interface, i.e. the surrounding media (gas or liquid) that is in direct contact with the surface of the metal, provided that the dielectric media has a low RI. Each wave is able to propagate along the dielectric interface, however its optical field extends outwards from the interface and decays evanescently to ~200 nm away from the surface into the surrounding media [31].

The SPW is generated at a particular reflection angle (θ_i) and is extremely sensitive to changes in RI. Therefore, changes in the RI within the immediate vicinity of the dielectric interface can be detected when the system goes out of resonance. This is possible by measuring the change in the angle of the intensity minimum (θ_{rA} to θ_{rB}) of the reflected light when a resonance change occurs. These reflected angle changes ($\Delta\theta$) can be detected by a photodiode and monitored in real time using an SPR set up, as shown in figure 2.12.

Here, the system is first prepped by equilibrating a sensor chip (fabricated from Au sputtered onto a glass slide) placed on top of the prism with buffer (figure 2.12, a). Following equilibration, the analyte of interest is then injected into the flow channel and pumped through to meet the surface (figure 2.12, b). The analyte can then bind to the surface to cause a change in the RI, which in turn causes a change in the reflected angle intensity minimum (θ_{rA} to θ_{rB}) (figure 2.12, c). From recording these changes, the binding kinetics of the injected analyte onto a surface can be measured and the response plotted against time relating to the mass of analyte bound (figure 2.12, d).

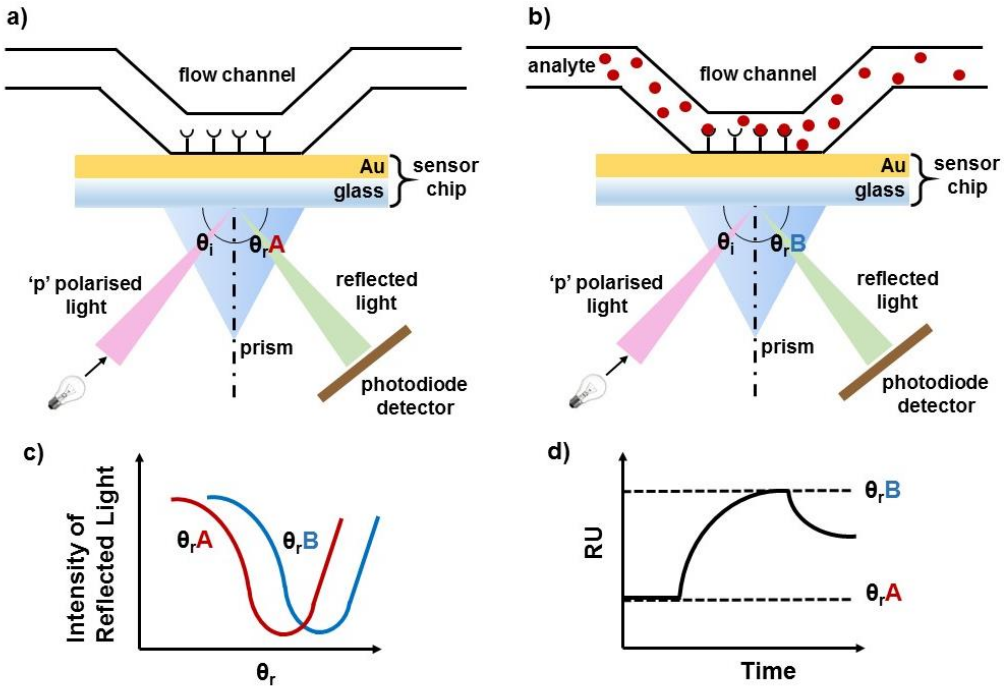

Figure 2.12: Schematic diagram of an SPR measurement using the Kretschmann set up. The functionalised Au/glass sensor chip is placed on-top of the prism and exposed to the flow channel. (a). When analyte is introduced and binds to the chip surface this causes a change in the RI (b). This change causes the intensity of the refracted light to dip (c) associated with the change in the angle (θ_rA) relates to the mass bound. The angle shifts to (θ_rB) when all the available mass has bound. These changes are monitored using a sensorgram (d) that is a plot of the resonance angle versus time.

6.0 Circular Dichroism (CD)

Circular dichroism (CD) is an optical technique used by biochemists and structural biologist to probe the conformation and secondary structural features of 'optically active' biomolecules. Similarly to ellipsometry, CD uses polarised light as the probe with which to elucidate these structural features.

To undertake a CD measurement, both left-handed and right-handed circularly polarised light (figure 2.13, a,i) is shone at the molecule of interest. If the molecule is optically active, i.e. it contains chiral chromophores within its

structure, it will absorb (A) the left-handed (A_L) and right handed (A_R) light to different extents due to its inherent asymmetry (figure 2.13, b). The outcome of this difference in absorbance is that the resulting transmitted radiation will be elliptically polarised due to the changes in its amplitude (figure 2.13, a,ii).

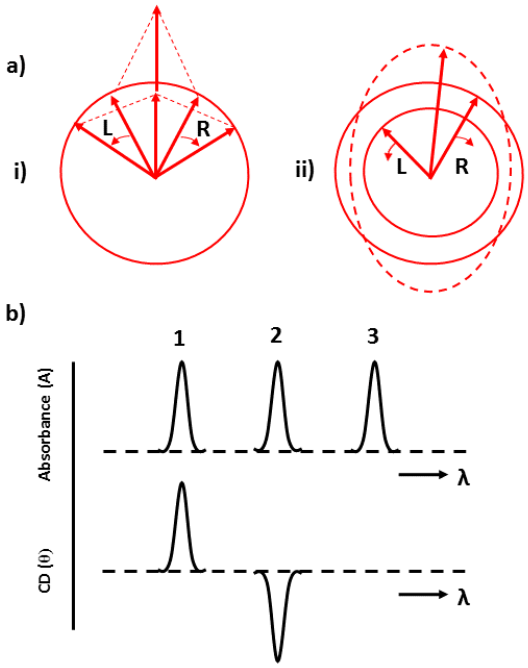

Figure 2.13: Schematic of the origin of the CD effect. If the left (L) and right (R) components of circularly polarised light have the same amplitude, when combined they will generate plane polarised radiation (a,i), however, if the components are of different magnitudes the radiation is elliptically (dashed line) polarised (a,ii). The relationship between CD and absorption is then depicted. Where L is absorbed more than R, a positive CD band is observed (b,1). Where R is absorbed more than L, a negative CD band is observed (b,2). Where L and R are absorbed but the chromophore is achiral, no CD band is observed (b,3). Adapted from [32].

CD is therefore a measure of the difference in this adsorption ($\Delta A = A_L - A_R$) of the circularly polarised light by a molecule that contains chiral chromophores measured over different wavelengths. As each CD spectrum is the sum of these changes it can therefore be used to gain quantifiable insight into structural

features of the molecule of interest [33]. As the CD studies undertaken within this thesis focussed solely on proteins, the following discussion will only address protein CD.

A typical CD spectra depicting the various types of secondary structural features, such as α-helices and β-sheets or β-turns, possible for proteins is shown in figure 2.14.

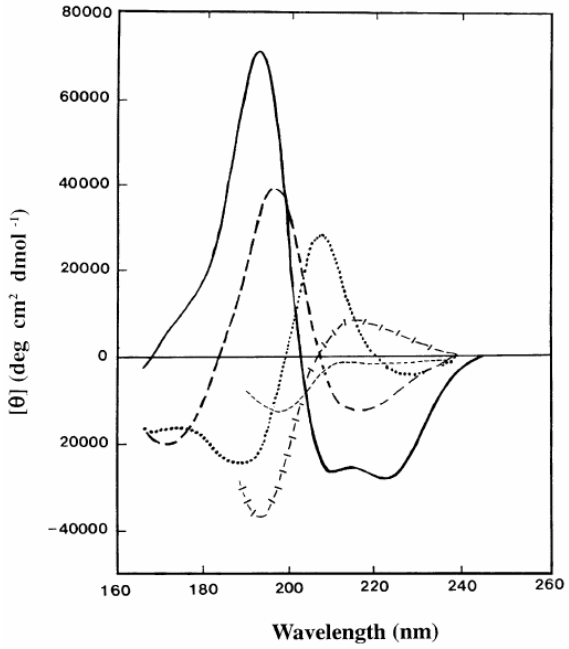

Figure 2.14: Examples of the typical CD spectra of secondary structure features: solid line, α-helix; long dashed line, anti-parallel β-sheet; dotted line, type I β-turn; cross dashed line, extended 3_1-helix or poly [34] II helix; short dashed line, irregular structure. Taken from Price *et al.* (2005) [32].

Overall, the main absorption regions are from 240 nm and below in the far ultraviolet (UV) region which arise from transitions that occur within the peptide backbone of the molecule [35]. For example, a typical protein will show a broad but weak $n \rightarrow \pi^*$ transition at 220 nm, whilst at 190 nm there is a more intense $\pi \rightarrow \pi^*$ transition. [32, 36] In certain cases we can also observe transitions further along in the UV spectrum that arise from additional chromophores that

may be present, such as the side chains of aromatic amino acids (typically between 260 to 320 nm), disulfide bridges (more broad bands around 260 nm), non-protein co-factors (~300 to 650 nm) and even ligands that are bound to the protein and thus obtain induced chirality. [32]

CD can measure changes to native proteins structures that are induced by changes in the surrounding environment for example with temperature, solvation or constituent concentration [37]. An advantage of CD in comparison with higher resolution structural probing techniques such as ^{1}H-NMR or x-ray crystallography is arguably its simple set up, rapid generation of results and small sample amounts requirement (≤ μM concentrations at maximum) that can be easily be recovered and reused after a study [37, 38]. It is therefore commonly used as a complementary technique to the aforementioned methods.

7.0 Mass Spectrometry

Mass spectrometry (MS) is a technique that vaporises an ionised molecule of interest (i.e. an analyte) to determine its mass-to-charge (*m*-*z*) ratio [39]. MS is a powerful technique widely employed for the characterisation of biomolecules. The basic set-up of all MS systems is shown in figure 2.15.

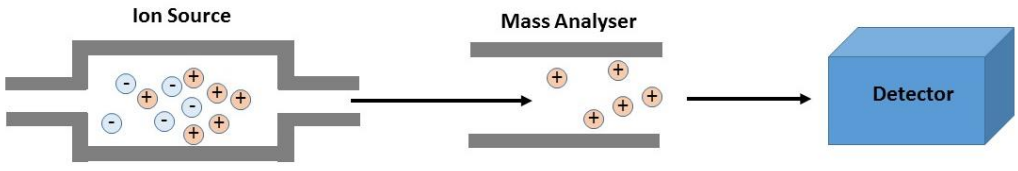

Figure 2.15: Schematic of the basic MS set-up, comprising the ion source, mass analyser and detector. Adapted from [40]

Here, the sample is first ionised to a vapour, following which it passes through the analyser system and finally the detector. Various techniques such as electron impact (EI), chemical ionisation (CI) or electrospray ionisation (ESI) can be employed to ionise the sample, as well as different analysers (such as quadrapoles or time-of-flight (TOF) analysers) depending upon the analysis required.

7.1 Electrospray Ionisation Mass Spectrometry (ESI-MS)

Electrospray ionisation mass spectrometry (ESI-MS) is a widely employed MS technique used to determine the mass of biomolecules. ESI-MS was developed following the discovery that as a 'soft' ionisation method it can determine mass-to-charge (*m-z*) ratios without destroying biomolecules unlike other vacuum-based MS techniques [41]. This is because any excess energy produced in the ionisation process is not retained by the analyte due to presence of small amounts of solvent surrounding its structure [42]. It is now a widely employed for the study of biomolecules, including carbohydrates, oligopeptides, and proteins [43-45]. Furthermore for larger molecule analysis it can be coupled to separation processes such as high performance liquid chromatography (HPLC) and capillary electrophoresis (CE), enabling the purified sample to be analysed directly from a liquid media [46, 47].

The basic ESI-MS set-up used to measure *m-z* ratios is shown in figure 2.16. Firstly, the sample containing the analyte is prepared in a suitable solution that is low in salts. This is essential as highly saline conditions can cause interference in the analyte detection by causing ion suppression or severe

adduction [48]. The addition of a small proportion of organic solvents is typically used to protonate the sample so that a wider range of ions can be generated [49].

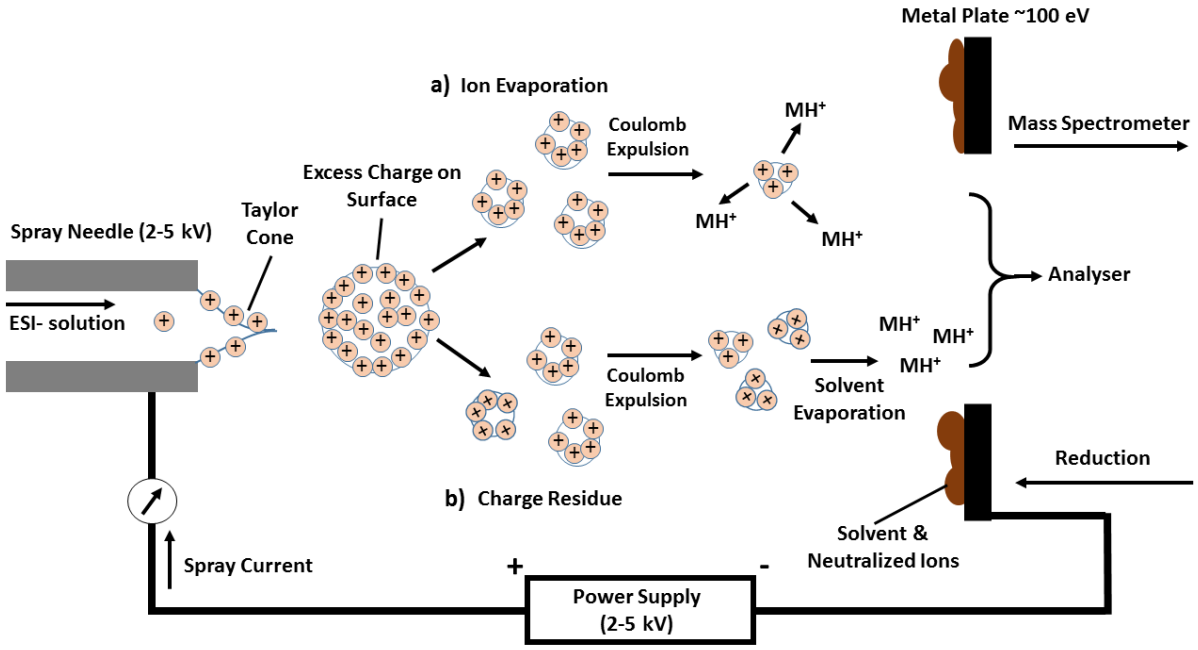

Figure 2.16: Schematic of the ESI-MS process in positive mode. The solution containing the molecule for which the mass to charge ratio is to be determined is pumped through a high voltage capillary. The formation of the Taylor cone with excess positive charge leads to oxidation and the formation of droplets which then evaporate and travel to the entrance of the mass spectrometer. The evaporation of more charge then leaves the charged analyte (MH^+) which hits the mass spectrometer and the mass-to-charge ratio can then be determined. Adapted from both [46] and [40].

Next, the sample is run through a narrow stainless steel or quartz capillary to which a small voltage (between 2-5 kV) is applied. The voltage produces a potential difference between the end of the capillary and the surrounding orifice [50]. At the end of the capillary a Taylor cone is formed and the ionised analyte in solution then goes through a redox reaction, here shown as oxidation, to form droplets within the gas phase of the orifice [51]. The ionised droplets then reduce in size as they travel downfield to the opposing electrode, however the

exact mechanism of how this occurs is still debated. The first proposed mechanism is *via* Ion Evaporation where the solvent ions leave the electric field at the droplet surface to eventually leave only the analyte ion (figure 2.16, a) [52, 53]. Evidence suggests that this is more common for smaller molecules. However, the Charge Residue model (figure 2.16, b) suggests that the analyte ions desolvate by the solvate ions forming their own smaller droplets to leave the analyte ion. This mechanism is suggested for larger species of multiple charge [54, 55].

Once desolvated, the analyte travels through a gap in the metal plate towards the analyser. For ESI-MS, typically either a quadrupole or time-of-flight (TOF) analyser are employed [40]. For quadrupole systems, the voltage of the four rods can be linearly ramped over time so that only ions of a particular stable *m/z* ratio can pass through at a set time [56]. In contrast, for TOF systems ions hit the analyser at different points in time based on differences in their mass. For example, for two ions that are of the same charge the one greater mass will travel slower through the system than the one of less mass, therefor hitting the analyser later [46].

For quadaropoles systems, the mass of the samples are then calculated according to the formula shown in equation 2.5, where (*m*-*z*) is the mass-to-charge ratio, *M* the molar mass of the molecule and *n* the number of associated protons[49].

$$m/z = (M + nH^+)/n \qquad \text{Equation 2.5}$$

For TOF systems, the mass of the samples are calculated according to formula shown in equation 2.6, where *E* is the voltage applied, *s* is the length of the ion acceleration region and *x* the length of the free flight region.

$$m/z = (tf^2\ 2\ E\ s)/(2s + x) \qquad \text{Equation 2.6}$$

The results of each *m*-*z* ratio detected are then plotted on the x-axis of the spectrum with the ion counts on the y-axis.

References

1. Drude, P., *Annalen der Physik.* 1887(268): p. 584.
2. Vedam, L., *Spectroscopic ellipsometry: a historical overview.* Thin Solid Films, 1998. **313-314**: p. 1-9.
3. Débora Gonçalves, E.A.I., *Fundamentals and Application of Spectroscopic Ellipsometry.* Química Nova, 2002. **25**(5): p. 794-800.
4. Aspnes, J.B.T.a.D.E., *Ellipsometry in Thin Films Analysis.* Annual Reviews in Materials Science, 1981(11).
5. Tompkins, H.G., *A User's Guide to Ellipsometry*. Mineola, New York: Dover Publications Inc.
6. *Index of Hyperphyics*. [cited 2016; Available from: http://hyperphysics.phy-astr.gsu.edu/hbase/phyopt/.
7. Ulman, A., *An Introduction to Ultrathin Organic Films from Langmuir-Blodgett to Self-Assembly*. 1991: Elselvier Academic Press.
8. Virgil Percec*, T.G., Janine S. Ladislaw, Anna Wistrand, Anna Stjerndahl, Monika J. Sienkowska, Michael J. Monteiro, and Sangrama Sahoo, *Ultrafast synthesis of ultrahigh molar mass polymers by metal-catalyzed living radical polymerisation of acrylates, methacrylates and vinyl chloride mediated by SET at 25degreed.* JACS, 2006. **128**(43): p. 14156–14165.
9. Brewster, D.H., et al., *Rising incidence of prostate cancer in Scotland: increased risk or increased detection?* BJU Int, 2000. **85**(4): p. 463-72; discussion 472-3.
10. Young, T., *An essay on the cohesion of fluids. .* Philos. Trans. R. Soc. Lond., 1805. **95**: p. 65–87.
11. Yuan, Y. and T.R. Lee, *Contact Angle and Wetting Properties*, in *Surface Science Techniques*, B.H. Gianangelo Bracco, Editor. 2013, Springer Berlin Heidelberg p. 3-34.
12. D.Y.Kwok, A.W.N., *Contact angle measurement and contact angle interpretation.* Advances in Colloid and Interface Science, 1999. **81**(3): p. 167-249.
13. Dussaud, A.V.-A., Michèle ; Dussaud, Anne, *Wetting Transition of n-Alkanes on Concentrated Aqueous.* Langmuir, 1997. **13**(3): p. 581-589.
14. Grimoldi, E., et al., *AFM and contact angle investigation of growth and structure of pp-HMDSO thin films.* The European Physical Journal D, 2009. **54**(2): p. 165-172.

15. Seemann, R., et al., *Wetting morphologies at microstructured surfaces.* Proc Natl Acad Sci U S A, 2005. **102**(6): p. 1848-52.
16. Binnig, G., Quate, C. F. and Gerber, Ch. , *Atomic Force Microscopy.* Phys. Rev. Lett, 1986. **56**(9): p. 930-934.
17. Magonov, S.N. and D.H. Reneker, *Characterization of Polymer Surfaces with Atomic Force Microscopy.* Annual Review of Materials Science, 1997. **27**(1): p. 175-222.
18. Charras, G.T. and M.A. Horton, *Single Cell Mechanotransduction and Its Modulation Analyzed by Atomic Force Microscope Indentation.* Biophysical Journal, 2002. **82**(6): p. 2970-2981.
19. Whited, A.M. and P.S.H. Park, *Atomic Force Microscopy: A Multifaceted Tool to Study Membrane Proteins and Their Interactions with Ligands.* Biochimica et biophysica acta, 2014. **1838**(1): p. 10.1016/j.bbamem.2013.04.011.
20. Haugstad, G., *Atomic Force Microscopy : Understanding Basic Modes and Advanced Applications*. 1 ed. 2012, Hoboken, New Jersey, US: Wiley.
21. Schmitz, I., et al., *Tapping-Mode AFM in Comparison to Contact-Mode AFM as a Tool for in Situ Investigations of Surface Reactions with Reference to Glass Corrosion.* Analytical Chemistry, 1997. **69**(6): p. 1012-1018.
22. Chih-Wen, Y., et al., *Imaging of soft matter with tapping-mode atomic force microscopy and non-contact-mode atomic force microscopy.* Nanotechnology, 2007. **18**(8): p. 084009.
23. Jalili, N. and K. Laxminarayana, *A review of atomic force microscopy imaging systems: application to molecular metrology and biological sciences.* Mechatronics, 2004. **14**(8): p. 907-945.
24. Rabe, U., K. Janser, and W. Arnold, *Vibrations of free and surface-coupled atomic force microscope cantilevers: Theory and experiment.* Review of Scientific Instruments, 1996. **67**(9): p. 3281-3293.
25. A, C.D., *High resolution chemical mapping using tapping mode AFM with phase contrast*. Proceeding sin Microscopy and Microanalysis. 1995.
26. Payton, O., et al., *Feedback-induced instability in tapping mode atomic force microscopy: theory and experiment.* Proceedings of the Royal Society A: Mathematical, Physical and Engineering Science, 2011. **467**(2130): p. 1801.
27. Gheorghe, S. and S.G. Richard, *Intermittent contact resonance atomic force microscopy.* Nanotechnology, 2014. **25**(24): p. 245702.

28. Bar, G., et al., *Factors Affecting the Height and Phase Images in Tapping Mode Atomic Force Microscopy. Study of Phase-Separated Polymer Blends of Poly(ethene-co-styrene) and Poly(2,6-dimethyl-1,4-phenylene oxide).* Langmuir, 1997. **13**(14): p. 3807-3812.
29. Burnham, N.A., et al., *How does a tip tap?* Nanotechnology, 1997. **8**(2): p. 67.
30. Yang, W., et al., *A novel type of fluorescent boronic acid that shows large fluorescence intensity changes upon binding with a carbohydrate in aqueous solution at physiological pH.* Bioorganic & Medicinal Chemistry Letters, 2003. **13**(6): p. 1019-1022.
31. Tang, Y., X. Zeng, and J. Liang, *Surface Plasmon Resonance: An Introduction to a Surface Spectroscopy Technique.* Journal of chemical education, 2010. **87**(7): p. 742-746.
32. Kelly, S.M., T.J. Jess, and N.C. Price, *How to study proteins by circular dichroism.* Biochim Biophys Acta, 2005. **1751**(2): p. 119-39.
33. Martin S.R., B.P.M., *Absorption and Circular Dichroism Spectroscopy*. Calcium-Binding Protein Protocols: Volume 2: Methods and Techniques. Vol. 173. 2002: Springer, Totowa, NJ.
34. Bentley, K.W., D. Proano, and C. Wolf, *Chirality imprinting and direct asymmetric reaction screening using a stereodynamic Bronsted/Lewis acid receptor.* Nat Commun, 2016. **7**: p. 12539.
35. Rocchitta, G., et al., *Enzyme Biosensors for Biomedical Applications: Strategies for Safeguarding Analytical Performances in Biological Fluids.* Sensors (Basel), 2016. **16**(6).
36. Jiang, J., et al., *Ultraviolet spectroscopy of protein backbone transitions in aqueous solution: combined QM and MM simulations.* J Phys Chem B, 2010. **114**(24): p. 8270-7.
37. Greenfield, N.J., *Using circular dichroism spectra to estimate protein secondary structure.* Nat Protoc, 2006. **1**(6): p. 2876-90.
38. Miles, A.J. and B.A. Wallace, *Circular dichroism spectroscopy of membrane proteins.* Chem Soc Rev, 2016. **45**(18): p. 4859-72.
39. Murray, K.K., et al., *Definitions of terms relating to mass spectrometry (IUPAC Recommendations 2013).* Pure and Applied Chemistry, 2013. **85**(7): p. 1515-1609.
40. El-Aneed, A., A. Cohen, and J. Banoub, *Mass Spectrometry, Review of the Basics: Electrospray, MALDI, and Commonly Used Mass Analyzers.* Applied Spectroscopy Reviews, 2009. **44**(3): p. 210-230.
41. Fenn J.B, M.M., Meng C.K, Wong S.F, Whitehouse C.M., *Electrospray Ionisation for Mass Spectrometry of Large Biomolecules.* Science, 1989. **246**(4926): p. 64-71.

42. Banerjee, S. and S. Mazumdar, *Electrospray ionization mass spectrometry: a technique to access the information beyond the molecular weight of the analyte.* Int J Anal Chem, 2012. **2012**: p. 282574.
43. Shen, X. and H. Perreault, *Characterization of carbohydrates using a combination of derivatization, high-performance liquid chromatography and mass spectrometry.* Journal of Chromatography A, 1998. **811**(1): p. 47-59.
44. Sforza, S., et al., *Study of the oligopeptide fraction in Grana Padano and Parmigiano-Reggiano cheeses by liquid chromatography electrospray ionization mass spectrometry.* Eur J Mass Spectrom (Chichester), 2004. **10**(3): p. 421-7.
45. Leney AC, H.A., *Native Mass Spectrometry: What is in the Name?* Journal of the American Society for Mass Spectrometry, 2017. **28**(1): p. 5-13.
46. Cech, N.B. and C.G. Enke, *Practical implications of some recent studies in electrospray ionization fundamentals.* Mass Spectrom Rev, 2001. **20**(6): p. 362-87.
47. Gelpi, E., *Biomedical and biochemical applications of liquid chromatography - mass spectrometry.* Journal of Chromatography, 1995. **703**(1-2): p. 59-80.
48. Sterling, H.J., et al., *Effects of Buffer Loading for Electrospray Ionization Mass Spectrometry of a Noncovalent Protein Complex that Requires High Concentrations of Essential Salts.* Journal of the American Society for Mass Spectrometry, 2010. **21**(6): p. 1045-1049.
49. Ashcroft, A.E., *Recent developments in electrospray ionisation mass spectrometry: noncovalently bound protein complexes.* Nat Prod Rep, 2005. **22**(4): p. 452-64.
50. Kebarle, P. and U.H. Verkerk, *Electrospray: from ions in solution to ions in the gas phase, what we know now.* Mass Spectrom Rev, 2009. **28**(6): p. 898-917.
51. Taylor, G., & McEwan, A., *The stability of a horizontal fluid interface in a vertical electric field.* Journal of Fluid Mechanics, 1965. **22**(1): p. 1-15.
52. Iribarne JV, T.B., *On the evaporation of small ions from charged droplets. .* J Chem Phys, 1976. **64**: p. 2287-2294.
53. Thomson BA, I.J., *Field induced ion evaporation from liquid surfaces at atmospheric pressure.* J Phys Chem, 1979. **71**: p. 4451-4463.
54. Winger, B.E., et al., *Observation and implications of high mass-to-charge ratio ions from electrospray ionization mass spectrometry.* Journal of the American Society for Mass Spectrometry, 1993. **4**(7): p. 536-545.

55. Fernandez de la Mora, J., *Electrospray ionization of large multiply charged species proceeds via Dole's charged residue mechanism.* Analytica Chimica Acta, 2000. **406**(1): p. 93-104.

56. Che, F.-Y., et al., *Analysis of 8-aminonaphthalene-1,3,6-trisulfonate-derivatized oligosaccharides by capillary electrophoresis–electrospray ionization quadrupole ion trap mass spectrometry.* Journal of Chromatography A, 1999. **858**(2): p. 229-238.

Chapter 3: Formation and Characterisation of Surfaces Suitable for Polymerisation

Abstract: *This chapter details the development of an ultra-thin polymer layer grown from a suitable self-assembled monolayer (SAM) using atom transfer radical polymerisation (ATRP) that exhibits elegant control to within nm thicknesses.*

Herein, we examine the fabrication and characterisation of several SAM alkanethiols onto a gold substrate and assess their ability to polymerize by ATRP. In the SAM studies, we first show the formation of a range of both pure and mixed SAMs. One of these SAMs is then functionalised to an initiator in preparation for the ATRP reaction.

We then discuss the outcomes of polymerising from this surface and justify using an alternative initiator SAM in order to overcome issues with variation in the length of the polymer synthesised from these surface. Finally, the chapter concludes with optimizing the thickness of this polymer synthesised from the more reliable SAM to within the desired nm length. We show that the polymer can be precisely controlled to within the nm scale and so is suitable for taking forward for the later glycoprotein imprinting studies.

Molecular imprinting for larger molecules such as glycoproteins is an emerging area that has seen significant growth within the past decade [1-3]. Steady progress has been made towards producing glycoprotein imprints, in particular with nanoparticle systems, however there is still a need for simple and robust polymerisation systems that can perform in aqueous conditions compatible with biological molecules [4-6].

From past studies of protein imprinting it has been shown that the thickness of the polymer imprint is crucial in the success of the imprints affinity and selectivity for its target. Monolithic protein imprints have demonstrated this as they can suffer from issues such as entrapment of the protein template within the polymer matrix and poor mass transfer of the target from solution when binding [1, 4, 7, 8]. Furthermore, from surface imprinting strategies reported

within the literature the thickness of polymer layer must be suitably tailored to the dimensions of the protein in question [6, 9, 10]. Moreover the polymerisation conditions used for imprinting must also be tailored to fulfil the requirements of the protein to reside in aqueous conditions in order to prevent abhorrent unfolding of the overall tertiary protein structure. Some recent systems have reported polymerising in such conditions, however protein imprinting using ATRP within aqueous solvents instead of denaturing organic solvents has been slower to develop.

To this end, in this chapter we aim to develop a novel aqueous ATRP system to produce ultra-thin polymers surfaces that can then be used for glycoprotein imprinting. We will focus on first producing a reliable foundation for the ATRP surface using self-assembled monolayers, following which we then aim to optimise the ATRP conditions and scale down the system to be more applicable to protein imprinting. The following outlines each objective that is required to achieve the formation of this polymer platform.

1.0 Objectives

1 Form pure and mixed SAMs of 11'-mercapto-1-undecanol (MUD) and 1-undecanethiol (UDT) that are then characterised by contact angle, ellipsometry and XPS.

2 Examine the extent to which the pure MUD monolayers can then be functionalised to 11-mercaptoundecyl-2-bromopropionate (MUBP) to determine the viability of using this SAM for the synthesis of the polymer surfaces.

3 Synthesise an alternative alkanethiol, 11,11'Dithiobis[1-(2-bromo-2-methylpropionyloxy)undecane] (11-DTMBD).

4 Characterise the formation of the 11-DTMBD SAMs by contact angle, ellipsometry and XPS to determine the successful formation of an ordered monolayer.

5 Compare the polymerisation from the MUBP and 11-DTMBD monolayers to form poly(MEBA) surfaces

6 Optimize the control over the poly(MEBA) polymer thickness to between 5-10 nm by exploring novel ATRP conditions.

2.0 Results and Discussion

2.1 Creation of Alkanethiols SAMs on a Gold Substrate

The SAMs were created by first cleaning the ~1 cm^2 gold substrates using piranha solution for 10 minutes following which they were then immersed in a solution of HPLC ethanol containing either: a) MUD (1 mM) b) UDT (1 mM) or c) varying concentrations of MUD and UDT as required. The chips were incubated for 24 h at room temperature (RT), then washed with an excess of ethanol and finally dried under a stream of argon. An example of one of these SAMs is shown in figure 3.1.

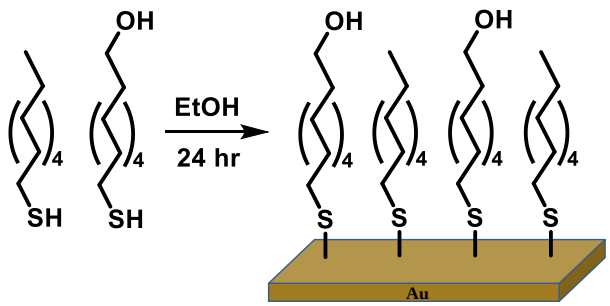

Figure 3.1: Schematic of the self-assembly of MUD and UDT in ethanol onto gold. In this case a 1:1 mixture of UDT:MUD is depicted.

In this example, the monolayer consists of a 1:1 incubation of UDT:MUD. To assess the successful formation of each monolayer the SAMs were characterized using contact angle, ellipsometry and XPS.

2.1.1 Dynamic Water Contact Angles of the SAMs

The pure and mixed MUD and UDT SAMs were first characterised with dynamic water contact angle to assess their wettability. As shown in figure 3.2 and in table 3.1, the advancing and receding water contact angles for pure UDT and MUD SAMs, as well as various ratios of the two alkane-thiols were measured. For the pure UDT and MUD SAMs, advancing angles of 106.2 ± 0.8 ° and 27.3 ± 0.9 ° were obtained, respectively, which are in agreement with 104 ° and 28 ° as reported in the literature [11-14]. As the advancing angle of the UDT SAM is >90 ° it is classed hydrophobic and has a low wettability, whereas for MUD the angle is <90 ° and therefore classed as hydrophilic with a high wettability [15].

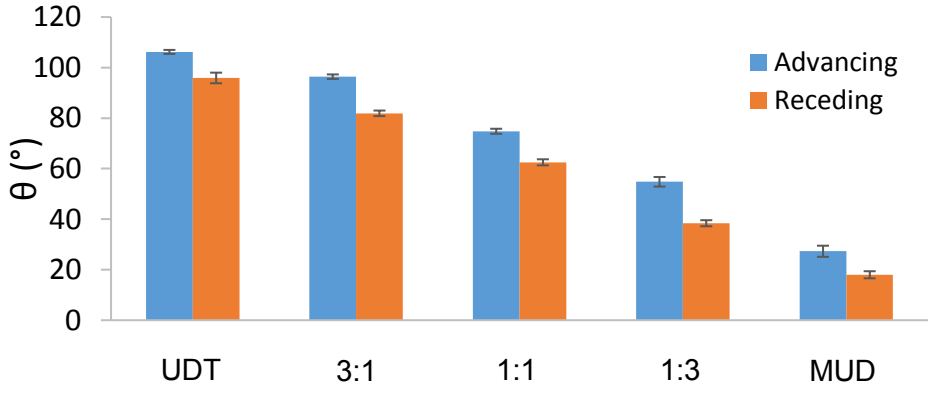

Figure 3.2: Contact angle of pure (UDT and MUD) and mixed SAMs (represented at a ratio of UDT:MUD). As the concentration of MUD within the SAM increases a decrease in both the advancing and receding angle is observed (n = 9).

Table 3.1: Reports the contact angle values of pure and mixed SAMs as shown in figure 3.2 (n = 9).

	Pure SAMs		Ratio of UDT:MUD		
	UDT	MUD	3:1	1:1	1:3
θ Advancing (°)	106.2 ± 0.8	27.3 ± 2.2	96.4 ± 0.9	74.8 ± 1.0	54.8 ± 1.9
θ Receding (°)	95.9 ± 2.1	18 ± 1.4	81.9 ± 1.1	62.5 ± 1.2	38.4 ± 1.2

For the mixed SAMs a sequential decrease in the both the advancing and receding angles are observed with increasing concentrations of MUD within the monolayers. The advancing angles decrease from 96.4 ± 0.9 ° to 74.8 ± 1.0 ° to 54.8 ± 1.9 ° with the 3:1 to 1:1 and 1:3 UDT:MUD ratio, respectively. This is due to the sequential increase in the minimisation of the free surface energy with the increase in the proportion of MUD that is incorporated within the mixed monolayers [15]. The MUD terminal hydroxyl group minimises the free surface energy by forming hydrogen bonds with the water to produce lower contact angles, whereas in comparison the UDT molecules are terminated with a hydrophobic methyl group and show no hydrogen bonding to produce higher angles.

Following these measurements the relative percentages of MUD and UDT within these monolayers were then determined using Cassie's Law [16]. This is necessary as the proportions of each alkanethiol used in the incubation solutions may not be representative of the proportions of each thiol bound to the gold substrate.

2.1.2 Derived Percentage of UDT and MUD present in the SAMs

Using the advancing contact angle values obtained from the 3:1, 1:1 and 1:3, UDT:MUD monolayer as shown in table 3.1 together with Cassie's Law (equation 3.1), the relative percentages of each thiol bound to the gold substrate can be calculated:

$$Cos\ \theta_c = f_1\ Cos\theta_1 + f_2\ Cos\theta_2 \qquad \text{Equation 3.1}$$

$$1 = f_1 + f_2 \qquad \text{Equation 3.2}$$

Where θ_c is the advancing angle of the mixed monolayer, θ_1 is the advancing angle for component 1, in this case a pure UDT monolayer, with area fraction f_1, and θ_2 is the advancing angle for component 2, in this case a pure MUD monolayer, with area fraction f_2.

Example calculation for the incubation of a gold chip in a 3:1 solution of UDT:MUD :

$$Cos(96.4) = f_1\ Cos(106.2) + f_2\ Cos(27.3) \qquad \text{Equation 3.3}$$

$$f_1 = 1 - f_2 \qquad \text{Equation 3.4}$$

$$Cos(96.4) = (1 - f_2\ )Cos(106.2) + f_2\ Cos(27.3) \qquad \text{Equation 3.5}$$

$$0.1675 = f_2(-Cos(106.2) + Cos(27.3) \qquad \text{Equation 3.6}$$

$$f_2 = 0.1435 \qquad \text{Equation 3.7}$$

$$f_2 = \mathbf{14.4\ \%\ MUD}$$

$$\therefore f_1 = \mathbf{85.6\ \%\ UDT}$$

The calculated values of each alkanethiol bound to the surface were then plotted as shown in figure 3.3. The values are presented as ratios expressed as percentages, i.e. 1:1 UDT:MUD = 50 % UDT and 50 % MUD. As figure 3.3 show, the proportion of the each alkanethiol bound to the gold relative to the incubation concentrations are not precisely linear as one might first assume. For the 50 % UDT with 50 % MUD, and the 25 % UDT with 75 % MUD incubations, the relative proportions bound were close to their incubation concentrations at 46 ± 1.5 % and 54 ± 1.5 %, and 27 ± 2.3 % and 73 ± 2.3 %, respectively. However, there was a notable difference observed between the bound proportions in comparison with the respective incubated concentrations for the 75 % UDT with 25 % MUD monolayers. Here, the percentage of bound MUD was much lower than expected at 14 ± 1.4 %.

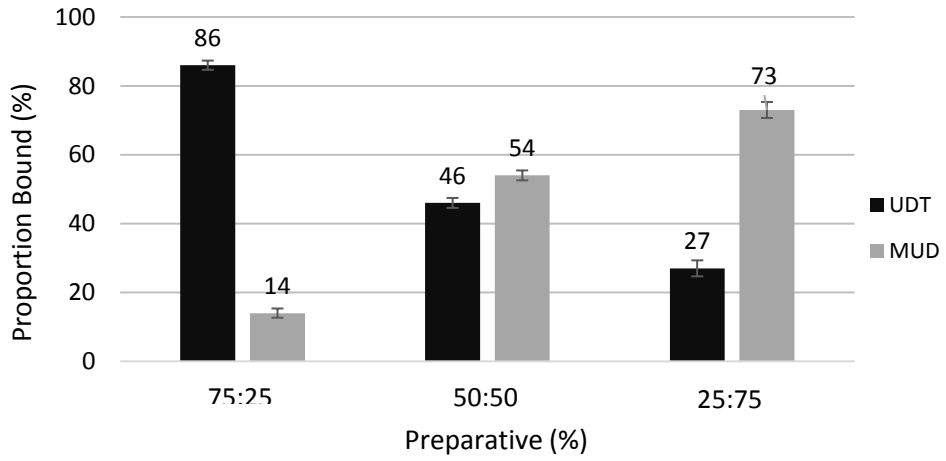

Figure 3.3: Reports the observed percentages of UDT and MUD bound to a gold substrate relative to the preparative percentages. The preparative values are derived from the proportions of each molecule in the substrate incubation solutions. Data is displayed as percentages of UDT:MUD (n =9).

This phenomena of the more polar OH terminated species binding less than its incubation concentration when co-adsorbed with a non-polar (i.e. CH_3

terminated) species has previously been reported by Whiteside's *et al.* [17]. In these studies as with our study, the various proportions of the UDT:MUD mixed thiols in the incubation solutions were adjusted accordingly for each mixed monolayer, however the total overall concentration of thiols in solution was kept constant at 1 mM. The results likewise reported that the absorption of the MUD thiol was similarly disfavoured over UDT at low MUD incubation concentrations (for example with 4:1, 3:2 and 2:3 solutions of UDT: MUD) in comparison with the higher (for example with 1:4 solutions of UDT: MUD) MUD incubation concentrations [17]. At the higher concentrations this effect is stabilised as the bound proportions of UDT:MUD begin to mirror their incubation proportions [13, 17].

The authors hypothesised that an explanation for this effect is that for the low MUD incubation concentrations the bound MUD molecules reside in a different environment in the monolayer from those bound from a more highly concentrated solution. That is to say, these polar MUD molecules are isolated from hydrogen bonding with the head groups of the other MUD thiols residing in solution. This therefore hinders the unbound MUD thiols in solution from going through the process of adsorption (i.e. aggregation, reorganisation and then further binding) with the Au surface [17]. In mixed thiol solutions where the MUD thiol is more concentrated this does not occur as sufficient hydrogen bonding is possible.

In summary, in a co-incubated monolayer comprised of a polar and non-polar alkane thiol, the proportion of the polar species (in this case MUD) bound at lower incubation concentrations is below the expected amount due to the absence of inter-species hydrogen bonding, however this effect is then

stabilised at the higher solution concentrations to form monolayers with bound proportions closer to the incubation values. These effects are likewise observed in our study of mixed UDT: MUD monolayers.

2.1.3 Ellipsometry of the UDT and MUD SAMs

Following the dynamic contact angle measurements, the thickness of the pure and mixed SAMs was then examined using ellipsometry. As shown in figure 3.4, the thickness of the SAMs ranged from 1.3 ± 0.1 nm and 1.4 ± 0.1 nm for the pure UDT and MUD SAMs, respectively. These are comparable with previous values reported in the literature of 1.2 nm [18] and 1.2 ± 0.6 nm [11, 19, 20], respectively. Furthermore, they are likewise comparable with the theoretical values calculated from ChemDraw3D of 1.4 and 1.5 nm, respectively.

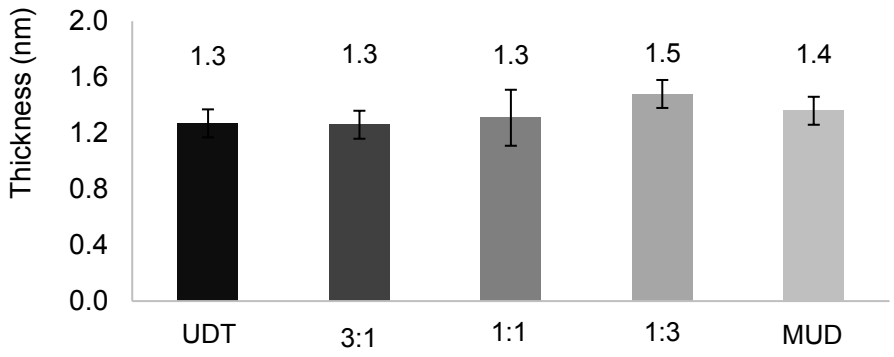

Figure 3.4: Ellipsometric thickness of pure and mixed SAMs are represented at a ratio of UDT:MUD. The thickness of each SAM is as expected and are agreeable with the literature (n=9).

The thicknesses of the mixed SAMs also fall within reasonable limits of this range, from 1.3 ± 0.1 nm with the 3:1 UDT:MUD monolayers, to 1.3 ± 0.2 nm with the 1:1 UDT:MUD monolayers, up to 1.5 ± 0.1 nm for the 1:3 UDT:MUD monolayers. This slight increase is the mixed SAMs thicknesses is expected as

the MUD thiol is longer than the UDT thiol as shown from the aforementioned ChemDraw3D values, and so the thicknesses sequentially become more comparable with the pure MUD monolayer.

Overall, thicknesses for these mixed proportions of UDT:MUD SAMs to our knowledge have not been reported in the literature, however all the values for these SAMs are within an acceptable range relative to the reported and theoretical values of the pure UDT and MUD monolayers. Furthermore, as previously shown in figures 3.2 and 3.3, the contact angle values as well as the derived percentages of each substrate bound to the gold in the mixed SAMs are as expected and therefore compliment the successful characterisation of these monolayers.

2.1.4 XPS of the Pure UDT and MUD SAMs

In order to further verify the successful creation of the pure UDT and MUD SAMs, XPS was undertaken to examine the elements present on each surface and their chemical environments. Quantification of the elemental ratios derived from appropriate fitting of the high resolution scans then provided further insight as to the proportions of each element present and their respective chemical environments which can aid in clarifying the cause of any issues related to for example defective adsorption, the efficiency of surface functionalisation reactions or contamination.

2.1.5 XPS Spectra of the UDT SAMs

The successful formation of the UDT SAMs were investigated using XPS. The expected structure of UDT is shown in figure 3.5.

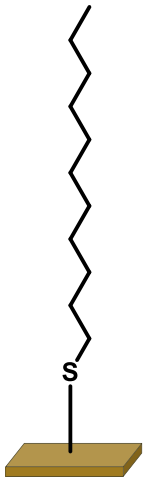

Figure 3.5: Expected chemical structure for the UDT SAMs.

As expected, the survey scan revealed the presence of Au, C, and S elemental species on the UDT incubated surfaces. Examination of the high resolution scans, as shown in figure 3.6, further confirmed the presence of all expected elements with signals from the Au (4f), C (1s) and S (2p) orbitals.

Firstly, the S (2p) spectra (figure 3.6, b) shows only one environment consisting of a doublet that corresponds to the S $2p_{3/2}$ and S $2p_{1/2}$ orbitals at 162.0 and 163.2 eV, respectively. The presence of the S peak therefore shows successful binding of the UDT alkanethiol to the Au substrate as expected. Next, the C (1s) spectra (figure 3.6, c) showed only one environment consisting of a sharp singlet at 284.9 eV corresponding to the C-C of the alkanethiol main chain. The absence of a C-O peak at a higher binding energy in the C (1s) spectrum demonstrates that no oxidised species are present. This is likewise reiterated by the lack of any oxygen peak in the O (1s) spectra (figure 3.6, d).

Finally, the C:S ratio quantified from these high resolution spectra was calculated 14.4:1 which is close but slightly higher than the expected 11:1 ratio. This can be attributed to a small amount of adventitious carbon adsorbing to the surface post removal from the incubation solution. In summary, the elements detected from the XPS characterisation of the UDT monolayers were as expected, with appropriate signals from Au, S and C. Likewise no peaks for O, N or Br were observed as expected. In concert with the ellipsometry and dynamic water contact angle measurements from the aforementioned studies, these characterisation techniques show that the UDT alkanethiols are bound to the gold substrate as expected and therefore can be relied upon as a spacer molecule within the UDT:MUD mixed monolayers.

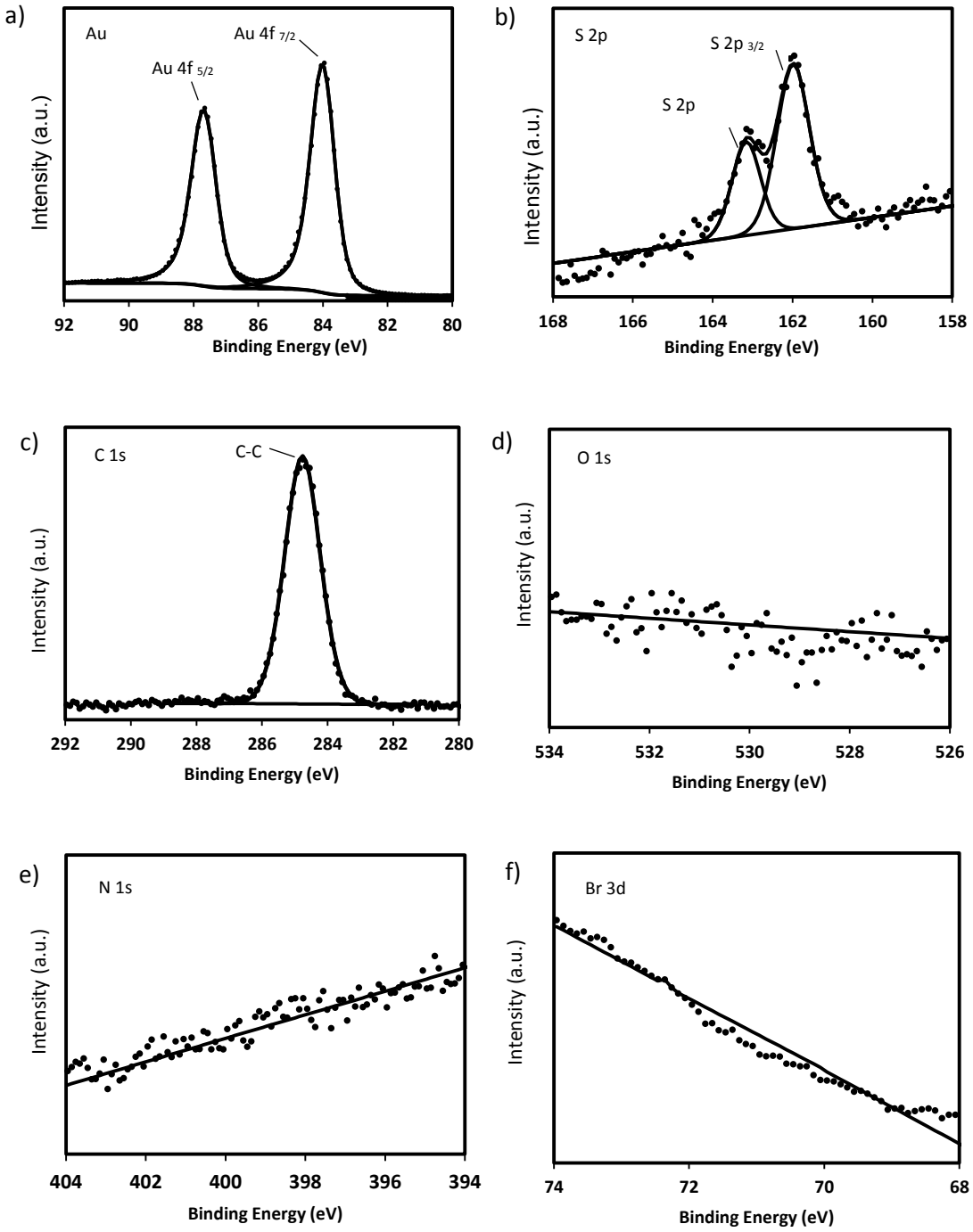

Figure 3.6. High resolution XPS spectra of a) Au 4f, b) S 2p, c) C 1s, d) O 1s, e) N 1s and f) Br 3d peaks of UDT.

2.1.6 XPS Spectra of the MUD SAMs

Following the characterisation of the UDT SAMs, the MUD SAMs were likewise investigated with XPS to elucidate the elemental composition and chemical environments of the monolayers. The expected structure of the MUD molecule is shown in figure 3.7.

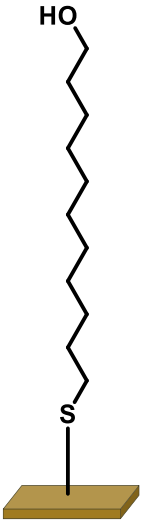

Figure 3.7: Expected structure for the MUD SAMs.

The high resolution scans then confirmed the successful self-assembly of the MUD molecules onto the gold substrate. As shown in figure 3.8, the high resolution scans show the presence of all the expected elements with signals from the C (1s), S (2p) and O (1s) orbitals.

The S (2p) spectra (figure 3.8, b) shows only one environment consisting of a doublet that corresponds to the S $2p_{3/2}$ and S $2p_{1/2}$ orbitals at 162.1 and 163.3 eV, respectively. As for UDT, the presence of S likewise shows that the MUD alkanethiols have covalently bound to the Au substrate as expected. Next, deconvolution of the C (1s) spectra (figure 3.8, c) showed two carbon

environments as expected. The first is a sharp, singlet at 284.7 eV corresponding to the C-C of the alkanethiol main chain and the second is found at a higher binding energy of 286.5 eV consistent with the C-O of the terminal hydroxyl group. Unlike for the UDT SAMs, the MUD surfaces show the presence of oxygen derived from the hydroxyl (OH) group found at the terminal end of the thiols. Furthermore, the O (1s) spectra likewise shows only one oxygen environment by the singlet at 532.9 eV, consistent with the C-O environment observed in the C (1s) scan.

The ratios generated from the quantification of the high resolution spectra are shown in table 3.2. The S:O ratio was calculated as 1.4:1 which is close to but slightly higher than the expected 1:1 ratio. The C:O ratio was calculated as 9.9:1 which is slightly lower than the expected 11:1 ratio. Finally, the C:S ratio was calculated as 13.9:1 which is slightly higher than the expected 11:1 value. In summary, the MUD monolayers are as expected from the XPS characterisation, however the quantified elemental ratios indicate that there is slight contamination of the surface by adventitious absorbed carbon. However, this contamination is not significant enough to be of concern for taking the MUD surface forward for functionalisation with an acid bromide to fabricate the initiator SAMs for the later polymerisation reactions.

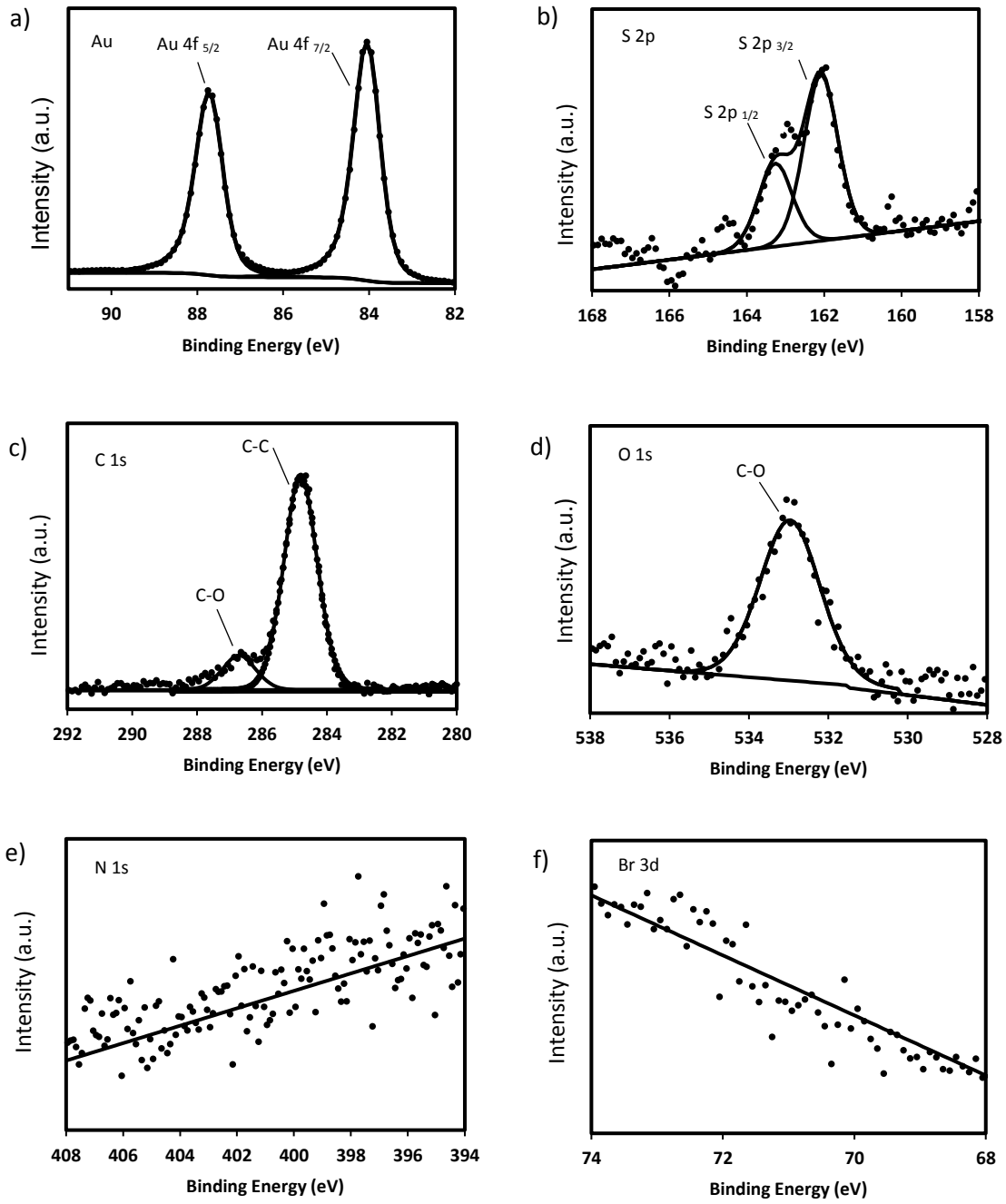

Figure 3.8: High resolution XPS spectra of a) Au 4f, b) S 2p, c) C 1s, d) O 1s, e) N 1s and f) Br 3d peaks of MUD.

Table 3.2: Expected and Measured ratios of the MUD SAM as determined by XPS.

Element	Expected Ratio	Measured Ratio
C/S	11	13.9
C/O	11	9.9
S/O	1	1.4

2.2 Functionalisation of the MUD SAMs to the ATRP Initiator, MUBP.

As aforementioned in Chapter 1.0, in order to form the initiator from which the polymer can then be grown using ATRP, the MUD SAMs must be functionalised to include a halogenated terminal end group [21, 22]. As the MUD molecules are terminated with a hydroxyl moiety they can react with an acid bromide, in this case 2-bromopropionylbromide (2-bpb), in the presence of a triethylamine (TEA) catalyst to form 11-mercaptoundecyl-2-bromopropionate (MUBP) as shown in figure 3.9 [23]. Conversely, as the UDT molecules are terminated with a methyl moiety they cannot react with the acid bromide and thus function as spacer molecules within the SAM. The presence of the bromide moiety of MUBP then enables the radical production required to trigger the ATRP reaction.

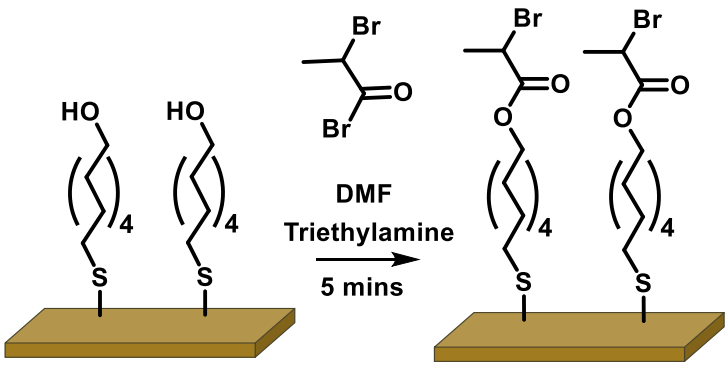

Figure 3.9: Schematic of the functionalisation of MUD thiols to MUBP *via* reaction with an acid bromide in anhydrous conditions.

Due to the length of MUBP being longer than that of MUD, a notable increase in the ellipsometric thickness should be observed upon functionalisation. Likewise, the advancing and receding contact angle values should both increase after functionalisation due to the change in the terminal end group from a hydroxyl

moiety to a halogenated ester. Moreover, the presence of this new end group comprising the aldehyde and bromide moieties of MUBP should also be clearly visible in the XPS C (1s), O (1s) and Br (3d) high resolution spectra. The functionalised MUBP SAMs were therefore characterised using the aforementioned techniques in order to deduce whether the reaction was successful and hence whether they are suitable to be taken forward for the polymerisation step.

2.2.1 Contact Angle and Ellipsometry of the Functionalised MUBP SAMs

As shown in table 3.3, upon the functionalisation of the pure MUD SAMs with the 2-bpb acid bromide a significant increase in the ellipsometric thickness and advancing contact angle of the surface is observed. The thickness of the SAMs show an increase of 0.6 nm, from 1.3 ± 0.1 to 1.9 ± 0.1 nm, which is in agreement with reported values from the literature as well as the calculated thickness of 1.9 nm of the MUBP molecule from ChemDraw [18].

Table 3.3. Collective ellipsometric thicknesses and advancing contact angles for the pure MUD SAMs and the functionalised ATRP initiator, MUBP. (n= 9).

	MUD	**MUBP**
Measured Thickness	1.4 ± 0.1	1.9 ± 0.1
ChemDraw3D Thickness	1.5	1.9
Measured θadv (°)	27.3 ± 2.2	64 ± 0.6
Reported θadv (°)	<14 ± 2	-

The advancing contact angle of MUD shows a large increase from 27.3 ± 2.2 ° to 64 ± 0.6 ° upon functionalisation with the acid bromide that further coincides with achieving functionalisation of the hydroxyl moieties. To further confirm the success of this reaction XPS of the MUBP functionalised surface was undertaken to examine whether the expected elemental environments as a result of the reaction were present. If functionalisation has successfully occurred peaks for the C=O and Br binding energies will be visible due to the esterification of the hydroxyl moieties.

2.2.2 XPS of the Functionalised MUBP SAMs

The XPS survey scan of the MUBP SAMs first revealed the presence of the expected Au, C, S, O and Br elemental species on the surface. The high resolution scans as shown in figure 3.10 then further confirmed the expected chemical environments for each of these elements, including the appearance of C=O and C-Br peaks to indicate successful functionalisation of the surface.

As figure 3.10 shows, signals for the Au (4f), C (1s), S (2p), O (1s) and Br (3d) orbitals of MUBP were present. As was likewise observed for the MUD SAMs, the MUBP surfaces showed S (2p) spectra with only one environment consisting of a doublet corresponding to the S $2p_{3/2}$ and S $2p_{1/2}$ orbitals at 161.8 and 163.2 eV, respectively (figure 3.10, b). The consistency of the S scans between the MUD precursor and the resultant MUBP surfaces shows that the binding of the thiols to the Au substrate is unaffected by the acid bromide reaction.

Next, examination of the C (1s) spectra as shown in figure 3.10, c, reports two carbon environments consistent with C-C and C-O moieties that were likewise observed for the MUD SAMs. However, the presence of two further environments consistent with the C-Br and C=O moieties at 285.9 and 289.1 eV, respectively, showed that the functionalisation of the MUD hydroxyl moieties with the acid bromide had indeed occurred. Furthermore, as shown in figure 3.10, d, a peak for the C=O bond was also observed in the O 1s spectra at a binding energy of 533.3 eV, which further provides evidence for the successful functionalisation of the MUD surface. Finally, the high resolution spectra observed for Br, as shown in figure 3.10, e, reported the presence of the $3d_{5/2}$ and $3d_{3/2}$ peaks at 67.7 and 68.9 eV, respectively consistent with C-Br bond observed in the C (1S) spectra.

The ratios generated from the high resolution spectra are as shown in table 3.4. The S:Br ratio was calculated as 0.9:1 which is in agreement with the expected 1:1 ratio. The C=O:Br ratio was quantified as 1.3:1 which likewise is in line with the expected 1:1 ratio as both environments are only found upon functionalisation of the hydroxyl moieties. However, the C-O:C=O ratio was 1.5:1 which was higher than the expected 1:1 ratio. This would indicate that either the reaction was not homogenous and that not all hydroxyl groups of the MUD SAM were functionalised with the acid bromide or that adventitious carbon is present upon the surface. The latter appears to be the case as both the C:S and C:Br ratio were calculated as 18.6:1 and 17.4:1, respectively, which are greater than the expected 14:1 ratios.

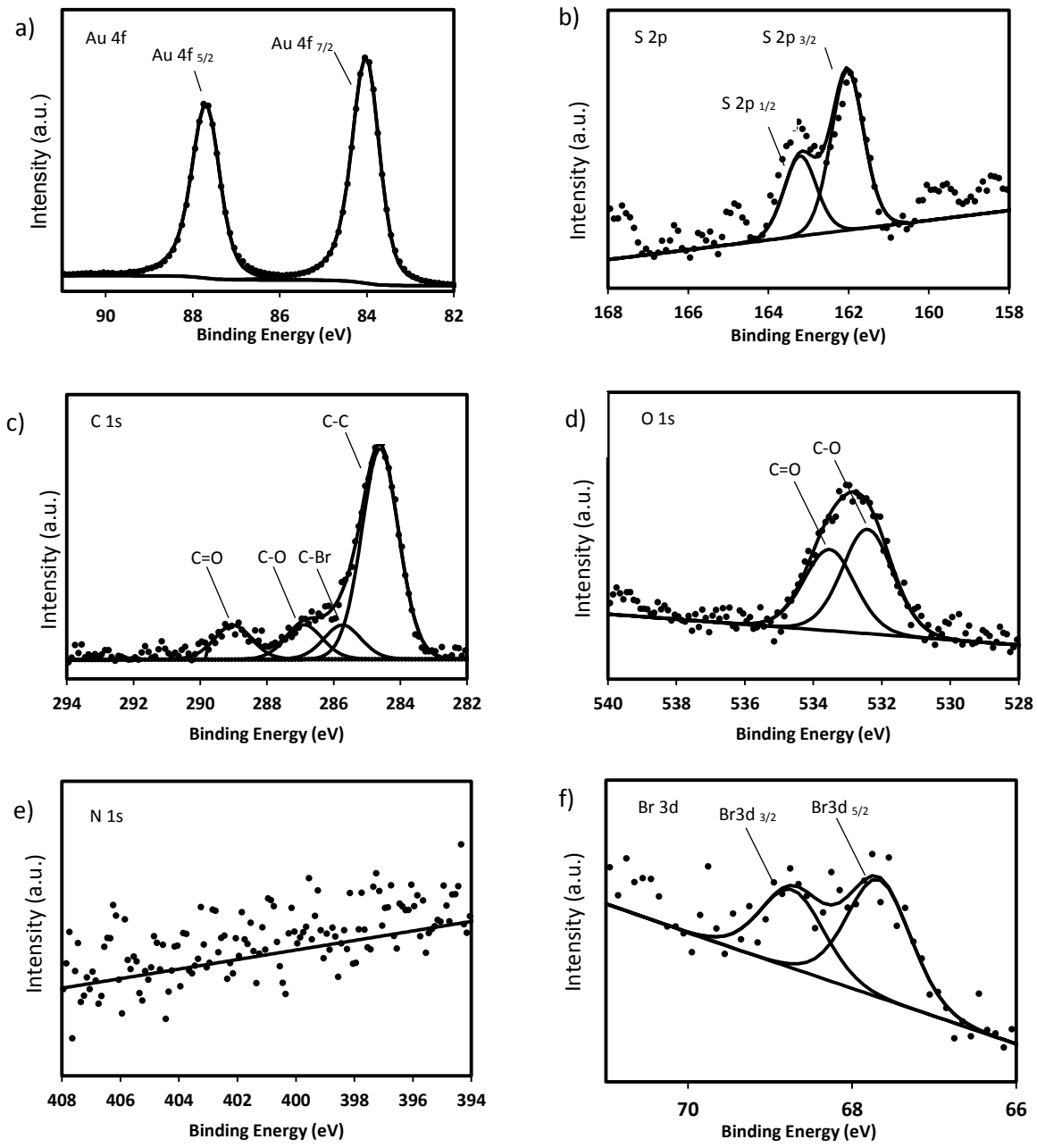

Figure 3.10: High resolution XPS spectra of a) Au 4f, b) S 2p, c) C 1s, d) O 1s, e) N 1s and f) Br 3d peaks of MUBP successfully functionalised from MUD.

Table 3.4: Expected and Measured ratios of the successfully functionalised MUBP SAM as determined by XPS.

Element	Expected Ratio	Measured Ratio
C/S	14	18.6
C/Br	14	17.3
C=O/Br	1	1.3
C-O/C=O	1	1.5

In summary, the presence of the C=O and Br environments in the high resolution scans provided evidence for the successful functionalisation of the MUD monolayers with the acid bromide to form MUBP surfaces. Alongside the XPS result, the successful fabrication of these SAMS is supported by the ellipsometry and contact angle results which show increases in the thickness and advancing angles, respectively.

However, several MUBP samples tested with XPS did not show the above expected spectra to indicate successful functionalisation of the MUD surface. Moreover, in these cases the samples failed to show the relevant occurrence of the C=O and C-Br chemical environments to indicate a failure to react with the acid bromide. An example spectra of one of these non-functionalised MUD surfaces is shown in figure 3.11.

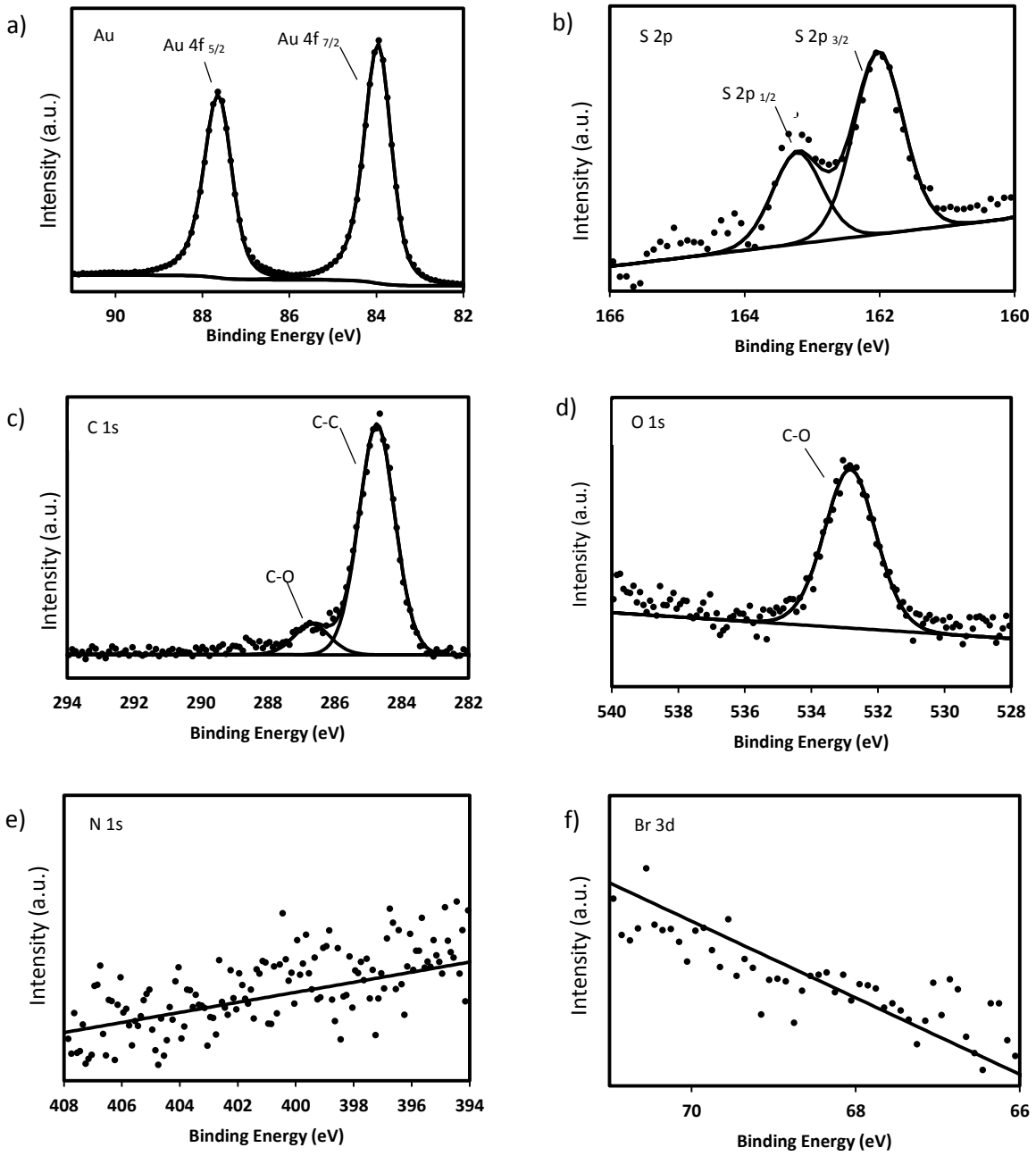

Figure 3.11: High resolution XPS spectra of a) Au 4f, b) S 2p, c) C 1s, d) O 1s, e) N 1s and f) Br 3d peaks of unsuccessfully functionalised MUBP.

As figure 3.11 shows, the high resolution spectra observed for these surfaces are in agreement with the MUD spectra previously shown in figure 3.8 (i.e. the MUD spectra above). Specifically, the C (1s) spectra shows only two carbon environments corresponding with the C-C and C-O moieties of the surface and

no peaks for the C-Br and C=O moieties. The C-O peak only corresponds to the non-functionalised hydroxyl moieties on the surface and not the esterified moiety of MUBP as previously observed in figure 3.10. This therefore indicates a failure of the hydroxyl moieties of the MUD SAM to successfully react with the acid bromide. Moreover, this is supported by the O 1(s) spectra as only one sharp peak corresponding to the C-O moiety of the surface is observed. The lack of a C=O peak likewise reiterates the failure of the MUD functionalisation to form MUBP SAMs. Finally, no peaks are observed in the Br high resolution scans to indicate any presence of bromide from the esterification reaction in line with the O (1s) and C (1s) spectra.

In summary, the XPS spectra shown in figure 3.10 and figure 3.11 demonstrated that the functionalisation of the MUD SAM to MUBP is unreliable due to its failure to react to consistently produce the desired initiator SAM. The XPS data shows that the same reaction can functionalise the identical MUD precursor surfaces to different extents despite employing the same procedure and reaction conditions. An explanation for the failure of this reaction to go to full completion is that the acid bromide has not been kept in fully anhydrous conditions and reacted with moisture in the atmosphere. Acyl halides are known for being extremely sensitive to moisture especially in the presence of an organic base such as TEA [24, 25]. In this case the 2-bpb dibromide has undergone hydrolysis to form a carboxylic acid and consequently cannot react with the hydroxyl residues of the MUD SAM.

The unreliability of the MUD surfaces to react in this way was problematic to the first overall objective of this study which was to produce uniform polymers with a controlled thickness from SAM initiator sites by ATRP. In order to produce a

controlled ATRP reaction the SAM initiator must be as reliable and homogenous as possible. Therefore in order to ensure that the surfaces would not suffer from the variation due to the number of initiator sites, a different initiator, 11-DTMBD, was investigated. Unlike the MUBP molecules, 11-DTMBD is a disulfide where the hydroxyl groups of the molecule are functionalised using acid bromide during its synthesis. Hence it already possesses the terminal bromide moiety before being exposed to the Au substrate and so no functionalisation of the surface is required post self-assembly. As such, it can provide a more stable and homogenous surface from which the polymerisation reaction can be initiated. The following section briefly outlines the synthesis and characterisation of the 11-DTMBD, following which ATRP polymerisations from both the MUBP and 11-DTMBD surfaces are then compared.

3.0 Synthesis of the Alternative ATRP Initiator, 11-DTMBD.

Following the protocols by Shah *et al.* (2000) and Belegrinou *et al.* (2010), 11,11'-Dithiobis[1-(2-bromo-2-methylpropionyloxy)undecane] (11-DTMBD) was synthesised using a two-step process as shown in figure 3.12 to obtain a highly pure stock of initiator [26, 27]. This synthesis was then characterised by ^{1}H NMR and mass spectrometry to confirm the reaction was successful.

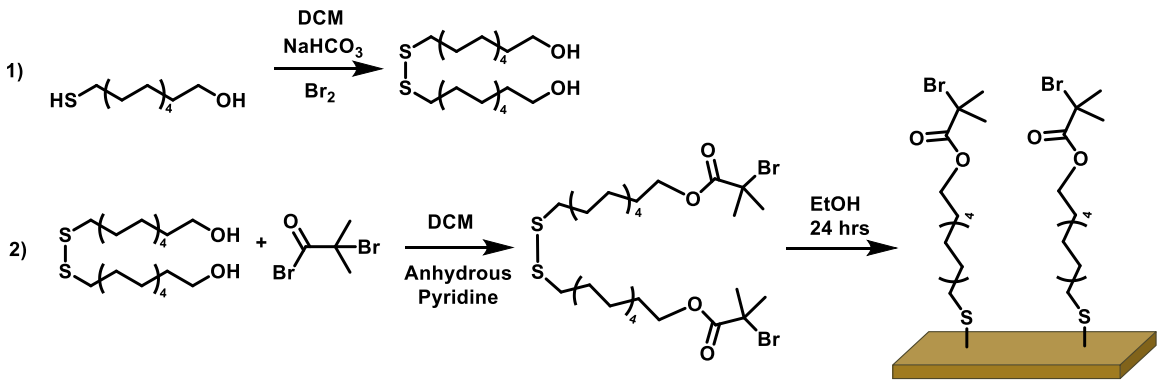

Figure 3.12: Schematic showing the reaction of **1)** MUD with bromine to synthesise the di-thiol, 11-DTBD, which was then further reacted with **2)** acid bromide to form 11-DTMBD. The 11-DTMBD was then incubated with the Au substrate to form SAMs of the 11-DTMBD initiator.

The molecule was then adsorbed onto the Au substrate to create monolayers of the 11-DTMBD initiator. The 11-DTMBD SAMs were characterised using ellipsometry, contact angle and XPS to assess whether they formed appropriate monolayers as expected. The primary advantage of using the di-thiol derived initiator as opposed to the MUBP initiator is that as shown above ^{1}H NMR and mass spectrometry can be employed, alongside the aforementioned surface characterisation techniques, to verify the correct synthesis and SAM formation of the molecule.

3.1 Contact Angle and Ellipsometry of the 11-DTMBD SAM

The average thickness observed for the 11-DTMBD derived SAMs was 1.7 ± 0.1 nm. This is slightly lower than the theoretical value of 1.9 nm determined from ChemDraw3D but can be attributed to a slight tilt of the SAMs on the surface of the gold [13, 28]. Furthermore, the average advancing angle of the

SAMs was measured as 73 ± 1.8 ° which is likewise in agreement with the value of 73 ° previously reported within the literature [18].

3.2 XPS of the 11-DTMBD SAM

Following the contact angle and ellipsometry measurements, the elemental composition and chemical environments of the 11-DTMBD derived SAMs were examined using XPS.

As expected, the high resolution scans confirmed the presence of all the expected elements and their chemical environments. As shown in figure 3.13, the high resolution scans observe signals for the Au (4f), C (1s), S (2p), O (1s) and Br (3d) orbitals. As observed for the MUBP SAMs, the 11-DTMBD SAMs showed S (2p) spectra with one environment, however in this case the S (2p) region was deconvoluted to show two doublets. Each doublet corresponds to the S $2p_{3/2}$ and S $2p_{1/2}$ orbitals of either bound S (at the lower binding energies) or unbound S (at the higher binding energies). This phenomena has previously been reported in 1996 by Castner *et al.* where the $S2p_{3/2}$ signals from unbound thiols or disulfide species were found from 163.5 to 164 eV [29]. These unbound thiol species can either be lying on top of or be buried within the monolayer. The authors report that extensive rinsing of the SAMs is necessary to displace unbound thiols from the monolayers. In this case for 11-DTMBD, the SAMs were extensively rinsed with HPLC grade ethanol before submitted for XPS analysis, however a small amount of unbound thiol remains as shown from the high resolution S spectra. Nonetheless, as shown in the later polymerisation studies, the presence of the unbound thiols does not adversely affect the

polymerisation reaction as there were no issues with variation in the polymer thicknesses generated from these SAMs.

Examination of the C (1s) spectra showed four carbon environments consistent with C-C, C-Br, C-O and C=O moieties that were likewise observed for the successfully functionalised MUBP SAMs. Furthermore, the C=O bond was observed in the O (1s) spectra at a binding energy of 533.3 eV alongside the C-O bond at 532.1 eV, which further indicates that the terminal end groups of the 11-DTMBD derived alkanethiols are present. Finally, the high resolution spectra of the Br (3d) shows the presence of the $3d_{5/2}$ and $3d_{3/2}$ peaks consistent with the C-Br bond observed in the C (1s) spectra. Collectively, the S (2p), C (1s), O (1s) and Br (3d) high resolution scans provide confirmation that the synthesised 11-DTMBD disulfhide can adsorb as expected onto the clean Au substrate to form a SAM with the correct elements and chemical environments.

To further confirm successful adsorption of the 11-DTMBD, the ratios of each of these elements were also calculated, as shown in table 3.5. The C=O:Br ratio was first quantified as 1.1:1 which was in line with the 1:1 expected value. The C-O:C=O ratio was also calculated as 1.2:1 which likewise is in line with the expected 1:1 ratio. The C:S ratio for the 11-DTMBD SAMs was calculated as 16.3:1 which is close to the expected 15:1 ratio. Finally, the C:Br ratio was calculated as 14.4:1 which is close to the expected value of 15:1.

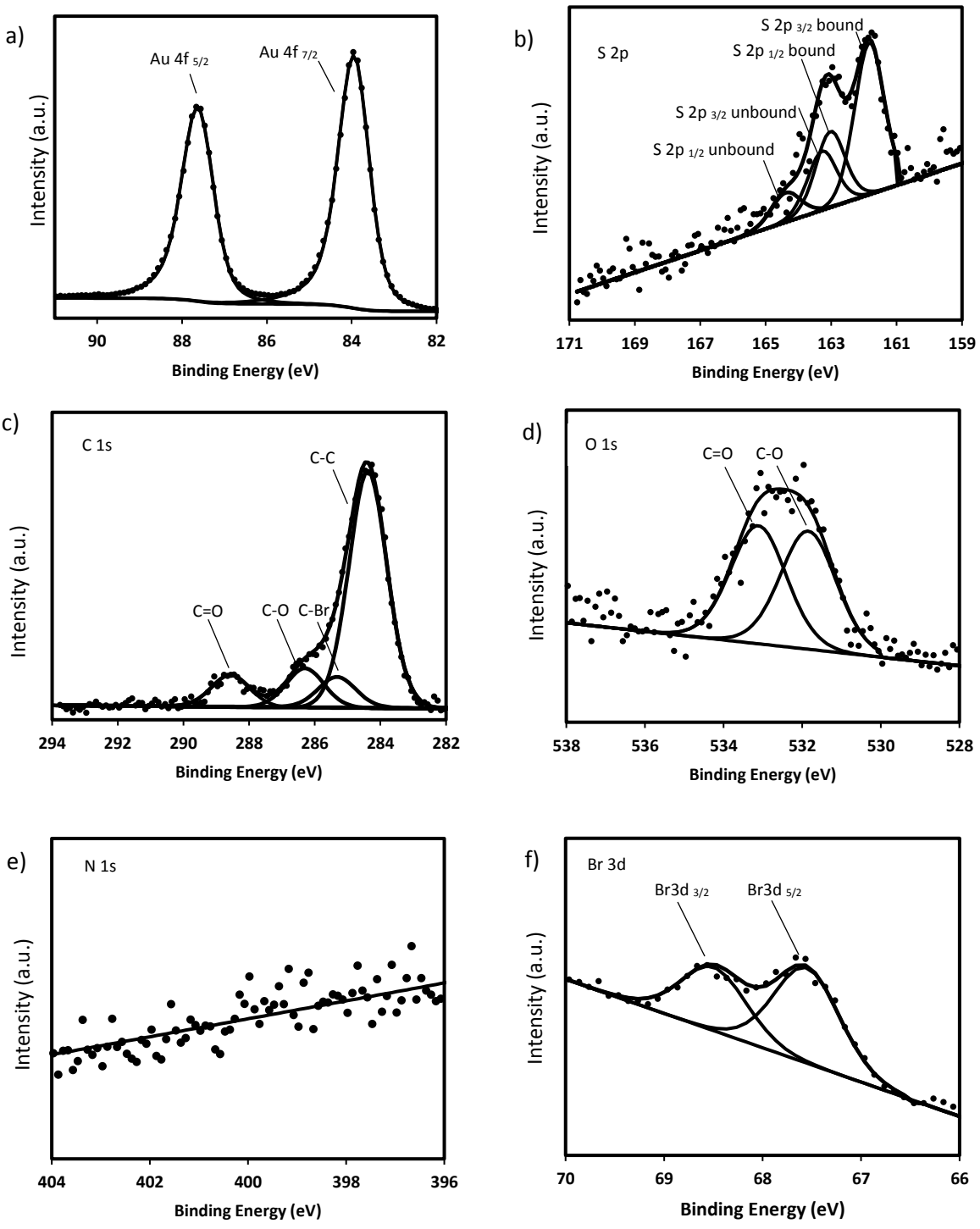

Figure 3.13: High resolution XPS spectra of a) Au 4f, b) S 2p, c) C 1s, d) O 1s, e) N 1s and f) Br 3d peaks of the 11-DTMBD SAMs.

Table 3.5. Depicts the ratios of the 11-DTMBD SAM quantified using XPS.

Element	Expected Ratio	Measured Ratio
C/S	15	16.3
C/O	7.5	6.7
O/S	2	2.4
C/Br	15	14.4
C=O/Br	1	1.1
C-O/C=O	1	1.2

In summary, the XPS spectra of the 11-DTMBD SAMs show all the expected elements alongside the correct chemical environments to indicate correct SAM formation. Unlike for the MUBP SAMs, the XPS spectra for these monolayers showed no significant variation between each sample tested in the chemical environments present across all surfaces. Moreover, the presence of the C=O and C-Br environments which were absent in some of the MUBP scans as shown in figure 3.11 were consistent throughout the three 11-DTMBD samples. As aforementioned, this is due to the esterification of the terminal hydroxyl moiety occurring during the synthesis stage and not after subsequent binding of the thiol to the Au substrate. Following the thorough characterisation of the 11-DTMBD monolayers we then undertook polymerisations from this surfaces using ATRP. The following provides the reader with a brief description of this reaction.

4.0 Synthesis and Optimisation of Polymer Brushes Grafted from the Initiator SAMs

4.1 Polymerisation of MEBA from the MUBP and 11-DTMBD SAMs

ATRP reactions from the 11-DTMBD SAMs were undertaken using N,N'-methylenebis(acrylamide) (MEBA) as shown in the scheme of figure 3.14 and figure 3.15,**a**.

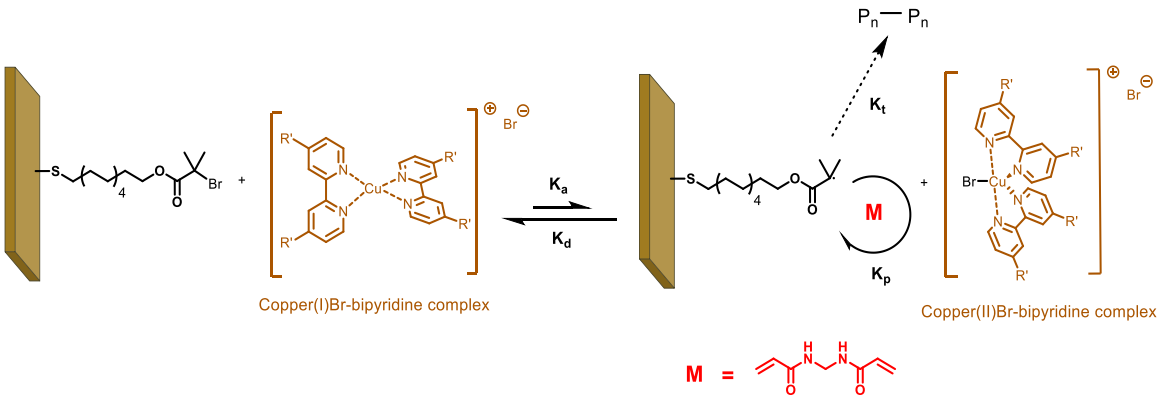

Figure 3.14: Scheme of the ATRP reaction undertaken using MEBA from the 11-DTMBD initiator surface. The copper-bipyridine complex enables the generation of the radical on the monolayer substrate that can then propagate with the MEBA to form poly(MEBA). Adapted from [30].

Alongside these studies, polymerisations from the MUBP surface were also examined (figure 3.15,**b)** to provide a comparison of the resultant polymer thickness. MEBA is a commonly used cross-linker for ATRP reactions and forms a hydrophilic polymer network across a surface when used as the primary monomer. For the ATRP reaction, a simple set up was employed whereby to a 50 mL dual-necked flask was added the solvent (H_2O, ultra-pure milliQ) that was degassed using argon for 2 hrs to remove all oxygen, as shown in figure

3.15,**c**. Following deoxygenation, the monomer, nitrogen containing ligand (L) and the transition metal catalyst (Mt^m) were then added. The L and Mt^m then complex to form the active catalyst (Mt^m/L). The pre-prepared MUBP and 11-DTMBD initiator SAMs were then added, allowed to equilibrate with the surface for 2 mins, following which the sacrificial initiator (S.I.) was injected to start the ATRP. The mixture was stirred for 1 minute at the start of the reaction in order to fully disperse the S.I., after which it was left to proceed for the stated time under argon. The reaction was finally terminated by the addition of excess water and exposure of the surface to air. These initial polymerisations were undertaken as per the ratios of each component of the system depicted later in system A of figure 3.17.

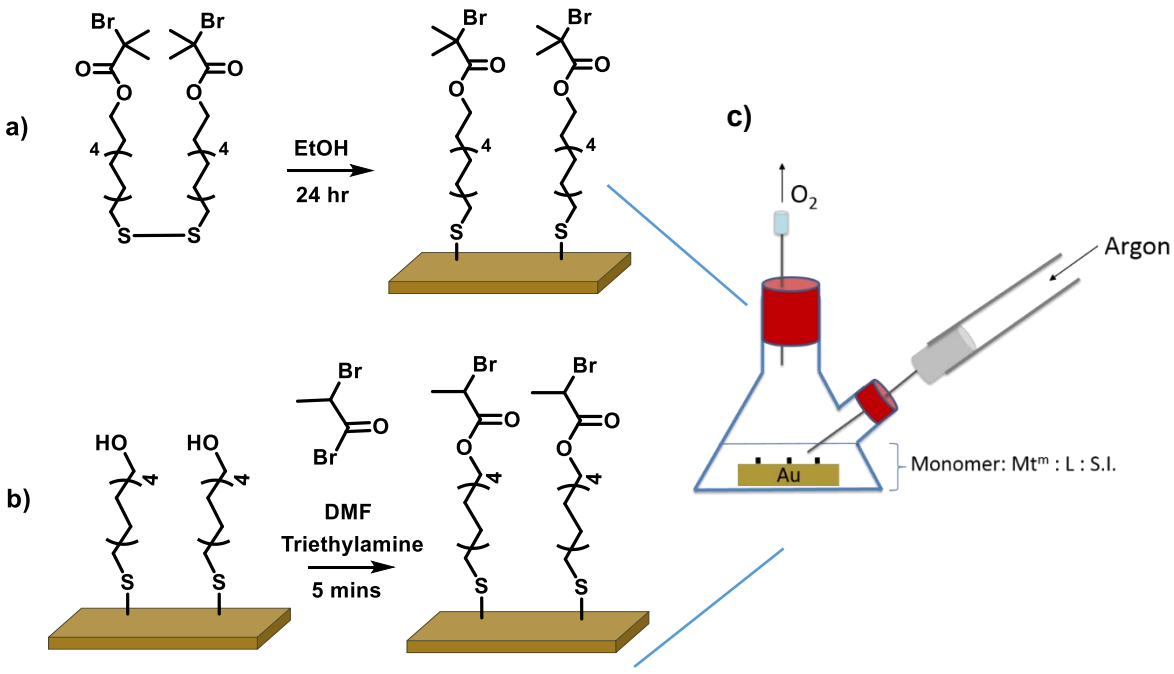

Figure 3.15: Schematic showing the formation of **a)** the 11-DTMBDand **b)** the MUBP SAM used as initiators for the ATRP reaction to produce the poly(MEBA) surfaces. **c)** Schematic of the general set up used for the polymerisations.

Following polymerisation each chip was removed from the reaction solution, extensively rinsed for 5 mins with excess milliq water, then a small volume of HPLC ethanol and finally dried under a stream of argon. The thickness of the polymer on each sample was measured using ellipsometry and the results fitted accordingly to a Cauchy model (assigned a refractive index of 1.5) [31]. The results from the polymerisation using either the 11-DTMBD or MUBP SAMs are shown in figure 3.16,**a** and **b**, respectively.

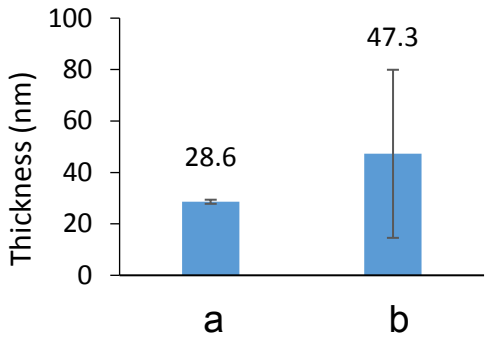

Figure 3.16: Reports the ellipsometric thickness of the MEBA polymers formed from either **a)** the 11-DTMBD or **b)** the MUBP SAMs (n=3).

As figure 3.16,**a** shows the average thickness of the poly(MEBA) surfaces grown from the 11-DTMBD SAMs were 28.6 ± 0.8 nm. This demonstrates that using this initiator SAM a low polymer thickness with limited variation in length is attainable. In contrast, the poly(MEBA) surfaces grown from the MUBP SAMs (figure 3.16,**b**) produced a much greater average thickness with high variation of 47.25 ± 29.8 nm. These results further reiterate the conclusions drawn from the XPS characterisation of these surfaces in that variation in the number of Br initiator sites of the SAMs produces high variation in the polymer thicknesses. Overall, polymerising from the 11-DTMBD SAMs provides far better control and

homogeneity of the ATRP reaction to produce more controlled polymer thicknesses.

The polymerisation conditions using the 11-DTMBD initiator SAMs were then further investigated to observe how each component within the polymerisation system affects the thickness of the poly(MEBA) layer. As stated previously, the overall objective of this chapter is to create a reliable system that enables a polymer thickness of between 5-10 nm to be synthesised from a SAM surface in order to match the dimensions of the template protein that will later be imprinted.

4.2 Optimisation of the Polymerisation from the 11-DTMBD SAMs.

The results of the polymerisation optimisation studies are shown in figure 3.17. In these studies, individual components of the polymerisation system (solvent volume, monomer, L, S.I. or the copper catalysts) were selectively varied to examine the effect on the poly(MEBA) thickness. Investigating the effects of varying these parameters using this particular system have not been investigated previously, so it was crucial to understand the limitations of this setup.

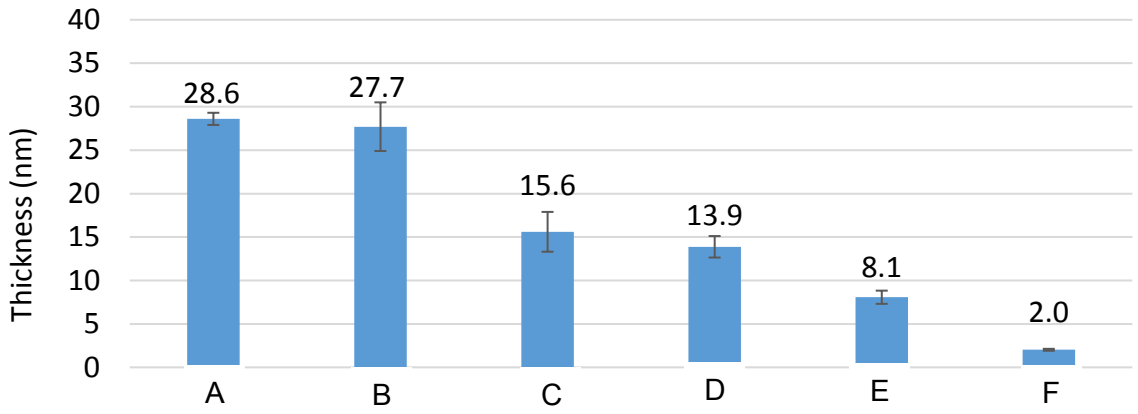

			A	B	C	D	E	F
Stoichiometry of Polymerisation System Components	Solvent	Water (mL)	35	70	70	70	70	70
	Monomer	MEBA	460	460	230	230	230	230
	Ligand	2,2'-bipyridine	2	2	2	2	2	2
	Sacrificial Initiator	Ethyl-2-bromoisobutyrate	1	1	1	1	1	1
	Metal(I)Br	Cu(I)Br	1	1	1	1	1	1
	Metal(II)Br	Cu(II)Br	0	0	0	1	1.5	2

Figure 3.17. Reports the ellipsometric thicknesses from a range of polymerisation conditions (top), the stoichiometry of which are as depicted in the table (bottom).

If we first examine the resultant thickness produced from the 11-DTMBD SAMs using conditions **b**, where the system was diluted by a half, the resulting thickness was 27.7 ± 2.8 nm. In comparison with the previous thickness of 28.6 ± 0.8 nm observed using conditions **a**, the dilution does not affect the rate of reaction to produce thinner polymer layers as the two values overlap in their deviation. However, when the proportion of monomer was reduced by a half as shown in conditions **c,** this produced a significant decrease in the thickness of the polymer layer to 15.6 ± 2.3 nm which was a step forward to decreasing the thickness to the desired 5-10 nm. Finally, system **c** was then further developed by examining the effect of exposing the system to a small proportion of Cu(II)Br.

The justification for including Cu(II)Br alongside Cu(I)Br is to prevent disproportionation of the complexed copper-bidendate catalyst that consequently slows the rate of reaction and to promote control over the polymer thickness [32]. The resultant polymerisations where either a 1:1, 1:1.5 or 1:2 ratio of Cu(I)Br:Cu(II)Br were employed are shown in figure 3.17, **d, e** and **f**, respectively. In comparison with the 15.6 ± 2.3 nm thickness obtained from conditions **c,** employing a 1:1 ratio of the two copper halides produced a slight decrease in the average polymer thickness to 13.9 ± 1.2 nm, however when accounting for the overlap in deviation there is no significant difference in the polymer thicknesses of **c** and **d**. However, as shown in the result from system **f**, when the ratio of Cu(II)Br is doubled relative to Cu(I)Br, the rate of reaction is slowed to the extent that polymerisation is barely occurring from the initiator SAM surface to produce a thickness of 2.0 ± 0.2 nm. Therefore by employing a Cu(I):Cu(II) ratio of 1:1.5 we elucidated the optimal conditions to produce a poly(MEBA) thickness of 8.1 ± 0.8 nm. This thickness falls within the desired 5-10 nm range and so conditions **e** were taken forward to be employed with the imprinting studies.

4.3 Examination of the Increase in Poly(MEBA) Thickness Over Time

Following the results of this initial optimisation study, conditions **e** were then further assessed for their ability to produce a controlled increase in the thicknesses over time. The 11-DTMBD surfaces were therefore incubated in conditions **e** for various times and the resulting polymer thicknesses measured. As shown in figure 3.18, **a**, the results show that the thickness of the poly(MEBA) surface is dependent upon the incubation time in the

polymerisation solution as the surfaces showed an increase in thickness over time as expected. For the first 30 minutes of the reaction, increases of 2.2 ± 0.1, 3.3 ± 0.2, 4.6 ± 0.7 nm were observed for the 5, 10 and 20 minute incubations, respectively. The reaction then reaches a plateau from 30 mins onwards with thicknesses of 8.1 ± 0.8, 8.4 ± 0.9 and 8.7 ± 1.1 nm for 30, 60 and 120 mins, respectively. Overall these results demonstrate that this system provides elegant control over the thicknesses of the polymer layer and that the thickness can easily be controlled by choosing the time spent incubated in the reaction solution. As such, this set-up offers the ideal platform for creating imprints with thicknesses tailored to the desired depth that is compatible with the template molecule. Moreover, tailoring the thickness of the polymer will avoid issues with template burial or on the contrary with too thin a polymer to create pockets within the matrix.

The final step towards developing the ideal system ready for the imprinting studies was to then to develop a set up that used a more appropriate volume of polymerisation solution. This was necessary in order to provide flexibility over the template molecule concentrations employed during the imprinting process. Moreover, the 70 mL volume used to polymerise from the surface with conditions **e** is too large a volume when incorporating the complexed boronic acid-glycoprotein template as over diluting the protein will consequently result in less imprinting sites within the polymer matrix. To this end, we then examined whether polymerising on the same 11-DTMBD SAM for 30 mins with 2 mL from the 70 mL polymerisation stock solution could produce the same thickness as was observed with the larger volume as this volume is ideal for the platform development.

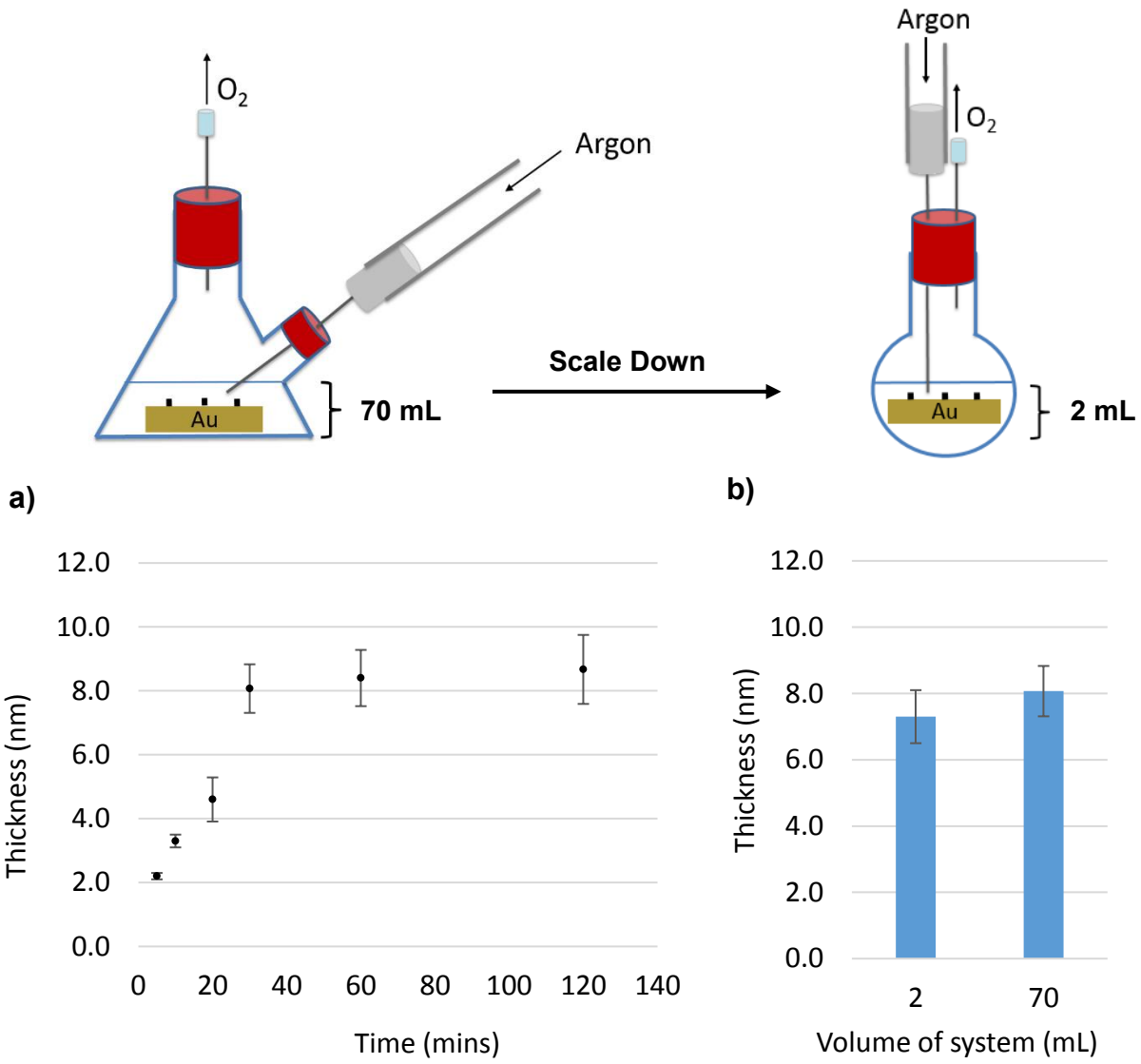

Figure 3.18: a) Reports the increase in the average thickness of the poly(MEBA) surfaces polymerised over time using system **e.** (n=3) **b)** Compares the average thickness of the poly(MEBA) surfaces polymerised for 30 mins using either 2 or 70 mL of system **e.** (n=3).

The results of the 2mL polymerisation are as shown in figure 3.18,**b.** In comparison with the 70 mL system which produced an average thickness of 8.1 ± 0.8 nm the 2 mL system produced a comparable average thickness of 7.3 ± 0.8 nm. When accounting for the overlap in the standard deviation of these averaged values no significant difference in the polymer thickness from using the smaller volume is therefore observed. This result demonstrated that the

thickness of the polymer surface is not dependent upon the volume of system **e** and therefore the rate of the polymerisation reaction is unaffected by this decrease in volume. In summary, this result further optimised the polymerisation set-up to be more suitable for creating imprints with the complexed template protein in the later imprinting studies.

5.0 Conclusions

The overall aim of the work undertaken in this first research chapter was to create and characterise a novel polymerisation procedure to produce a poly(MEBA) platform that can then be taken forward for the glycoprotein imprinting studies. In the opening section of this work we showed the successful binding of both MUD and UDT alkanethiols to an Au substrate by characterisation with ellipsometry, contact angle and XPS. By using a mixed MUD:UDT SAM with UDT acting as a spacer within the monolayers we hypothesised that we could use this spacer thiol to gain further control over the polymer surface characteristics by tuning for example the polymer network porosity. MUD was chosen as the functional alkanethiol as it is well known to form high quality SAMs that can then be modified in preparation for further fabrication processes. In this case we functionalised the MUD to an initiator, MUBP, that can then be used to develop the poly(MEBA) ATRP polymerisation procedure. However, the XPS results showed that the MUBP SAMs were not homogenous in their functionalisation with acid bromide and so this consequently produced variation in the resultant poly(MEBA) surface thicknesses.

In order to ensure that the polymer surfaces would not continue to suffer from this variation issue a different initiator species, 11-DTMBD, was synthesised, characterised and likewise polymerised to form poly(MEBA) surfaces. Using this initiator SAM polymers without significant variation in their thickness were produced and so were then taken forward for all further studies. The polymerisation system was then optimized with the goal of decreasing the polymer thickness to the desired length of between 5-10 nm to coincide with the dimensions of the glycoprotein which will be used as a template in the later imprinting studies.

The results of these optimisation studies showed that the aqueous ATRP reaction can be controlled by altering the ratios of each component of the system. Of note, we showed that we can decrease the poly(MEBA) thickness by halving the monomer concentrations and then incorporating a proportion of Cu(II)Br alongside Cu(I)Br to further slow the rate of reaction to achieve an acceptable thickness. Finally, we then showed that the thickness of the polymer layer was not compromised from scaling down this system from 70 mL to 2 mL, which is therefore a more suitable scale for imprinting glycoproteins. In summary, this optimised scaled down poly(MEBA) platform can now be taken forward with confidence for the glycoprotein imprinting studies.

References

1. Turner, N.W., et al., *From 3D to 2D: a review of the molecular imprinting of proteins.* Biotechnol Prog, 2006. **22**(6): p. 1474-89.
2. Verheyen, E., et al., *Challenges for the effective molecular imprinting of proteins.* Biomaterials, 2011. **32**(11): p. 3008-3020.
3. Chen, L., et al., *Molecular imprinting: perspectives and applications.* Chem Soc Rev, 2016. **45**(8): p. 2137-211.
4. Luo, J., et al., *Double Recognition and Selective Extraction of Glycoprotein Based on the Molecular Imprinted Graphene Oxide and Boronate Affinity.* ACS Appl Mater Interfaces, 2017. **9**(8): p. 7735-7744.
5. Saeki, T., et al., *Orientationally Fabricated Zwitterionic Molecularly Imprinted Nanocavities for Highly Sensitive Glycoprotein Recognition.* Langmuir, 2018. **35**(5): p. 1320-1326.
6. Liu, Z., et al., *Boronate-Affinity Glycan-Oriented Surface Imprinting: A New Strategy to Mimic Lectins for the Recognition of an Intact Glycoprotein and Its Characteristic Fragments.* Angew Chem Int Ed Engl, 2015. **54**(35): p. 10211-5.
7. Lin, Z., et al., *Preparation and evaluation of a macroporous molecularly imprinted hybrid silica monolithic column for recognition of proteins by high performance liquid chromatography.* J Chromatogr A, 2009. **1216**(49): p. 8612-22.
8. Lin, Z., et al., *Preparation of boronate-functionalized molecularly imprinted monolithic column with polydopamine coating for glycoprotein recognition and enrichment.* J Chromatogr A, 2013. **1319**: p. 141-7.
9. Wu, G., et al., *Template size matched film thickness for effectively in situ surface imprinting: a model study of glycoprotein imprints.* RSC Advances, 2015. **5**(58): p. 47010-47021.
10. Wang, S., et al., *Affinity-tunable specific recognition of glycoproteins via boronate affinity-based controllable oriented surface imprinting.* Chemical Science, 2014. **5**(3): p. 1135.
11. Pranzetti, A., et al., *Model Organic Surfaces to Probe Marine Bacterial Adhesion Kinetics by Surface Plasmon Resonance.* Advanced Functional Materials, 2012. **22**(17): p. 3672-3681.
12. Nicolau, D.V., et al., *Effect of various artificial surfaces on the colonization and viability of E. coli and S. aureus.* 2007. **6799**: p. 67990J.

13. Whitesides, C.D.B.a.G.M., *Modeling Organic Surfaces with Self-Assembled Monolayers.* Angew Chem Int Ed Engl, 1989. **1**(4): p. 506-512.
14. Persson, H.H.J., *Versatile Method for Chemical Reactions with Self-Assembled Monolayers of Alkanethiols on Gold.* Langmuir, 2001. **17**: p. 3643-3650.
15. Yuan, Y. and T.R. Lee, *Contact Angle and Wetting Properties*, in *Surface Science Techniques*, B.H. Gianangelo Bracco, Editor. 2013, Springer Berlin Heidelberg p. 3-34.
16. Cassie, A.B.D., *Contact Angles.* Discussions of the Faraday Society, 1948. **3**.
17. *Formation of Monolayers by the Coadsorption of Thiols in Gold: Variation in the Head Group, Tail Group, and Solvent.* J Am Chem Soc, 1989.
18. Darren M. Jones, A.A.B., and Wilhelm T. S. Huck, *Surface-Initiated Polymerizations in Aqueous Media: Effect of Initiator Density.* Langmuir, 2002. **18**: p. 1265-1269.
19. Zengin, A. and T. Caykara, *RAFT-mediated synthesis of poly[(oligoethylene glycol) methyl ether acrylate] brushes for biological functions.* Journal of Polymer Science Part A: Polymer Chemistry, 2012. **50**(21): p. 4443-4450.
20. Zhiyi Bao, M.L.B.a.G.L.B., *Rapid Growth of Polymer Brushes from Immobilized Initiators.* J Am Chem Soc, 2005.
21. Kim, J.-B., M.L. Bruening, and G.L. Baker, *Surface-Initiated Atom Transfer Radical Polymerization on Gold at Ambient Temperature.* Journal of the American Chemical Society, 2000. **122**(31): p. 7616-7617.
22. Flink, S., F.C.J.M. van Veggel, and D.N. Reinhoudt, *Functionalization of self-assembled monolayers on glass and oxidized silicon wafers by surface reactions.* Journal of Physical Organic Chemistry, 2001. **14**(7): p. 407-415.
23. Bao, Z., M.L. Bruening, and G.L. Baker, *Rapid Growth of Polymer Brushes from Immobilized Initiators.* Journal of the American Chemical Society, 2006. **128**(28): p. 9056-9060.
24. Bentley, T.W., G. Llewellyn, and J.A. McAlister, *SN2 Mechanism for Alcoholysis, Aminolysis, and Hydrolysis of Acetyl Chloride.* The Journal of Organic Chemistry, 1996. **61**(22): p. 7927-7932.
25. Compton, R.G., *Ester Formation and Hydrolysis and Related Reactions*. 1 ed, ed. R.G. Compton, Bamford, C.H., Tipper, C.F.H. . Vol. 10. 1972: Elsevier Science. 308.
26. Belegrinou, S., et al., *Efficient Two-Step Synthesis of 11,11'-Dithiobis[1-(2-bromo-2-methylpropionyloxy)undecane], a Conventional Initiator for Grafting Polymer Brushes from Gold Surfaces via ATRP.* Synthetic Communications, 2010. **40**(20): p. 3000-3007.

27. Shah, R.R., Merreceyes, D., Hendrick, J.L., *Using Atom Transfer Radical Polymerisation To Amplify Monolayers of Initiators Patterned by Microcontact Printing into Polymer Brushes for Pattern Transfer.* Macromolecules, 2000. **33**: p. 597-605.
28. Smith, R.K., P.A. Lewis, and P.S. Weiss, *Patterning self-assembled monolayers.* Progress in Surface Science, 2004. **75**(1-2): p. 1-68.
29. Castner, D.G., *x-ray photoelectron spectroscopy sulfur 2p study of organic thiol and disulfide binding interactions with gold surfaces.* Langmuir, 1996. **12**(21): p. 5083-5086.
30. Pintauer, T. and K. Matyjaszewski, *Atom transfer radical addition and polymerization reactions catalyzed by ppm amounts of copper complexes.* Chem Soc Rev, 2008. **37**(6): p. 1087-97.
31. Huang, W., G.L. Baker, and M.L. Bruening, *Controlled Synthesis of Cross-Linked Ultrathin Polymer Films by Using Surface-Initiated Atom Transfer Radical Polymerization.* Angewandte Chemie International Edition, 2001. **40**(8): p. 1510-1512.
32. Fantin, M., et al., *Understanding the Fundamentals of Aqueous ATRP and Defining Conditions for Better Control.* Macromolecules, 2015. **48**(19): p. 6862-6875.

Chapter 4: Complexation of the Model Glycoprotein with a Functional Monomer

Abstract: *This chapter details the study of the covalent binding of a boronic acid monomer to the sugar moieties of the glycan of the model glycoprotein, RNase B. Herein, we show that upon combining the protein with this vinyl boronic acid we observe the appearance of higher molecular weight ionised masses in the electrospray ionisation mass spectrometry (ESI-MS) spectra to indicate that covalent binding has occurred. However, we also show that this binding is dependent upon the successful co-solvation of the monomer with a proportion of an organic solvent.*

Following the ESI-MS study with RNase B, we then show that the protein's de-glycosylated homologue, RNase A, does not form any observable complexes with the monomer due to the absence of glycan sugar residues on the protein. Finally, we show that the native conformational structure of RNase B is not affected by the use of methanol as a co-solvent by analysis with circular dichroism (CD). To this end, we demonstrate for the first time ESI-MS evidence for the formation of a complex between boronic acid and the sugar moieties of the RNase B glycoprotein and show that this protein is structurally stable in an aqueous-organic mixed solvent system.

In summary, the outcomes of these studies provide the justification for taking this protein complex forward to work in conjunction with the polymerisation system developed in Chapter 3 to create molecular imprints for RNase B.

1.0 Introduction

The aim of this work was to demonstrate the covalent binding of a selected boronic acid monomer to the glycan of the glycoprotein, RNase B. This protein was selected as it is inexpensive and well characterised within the literature, and has been used for decades as a model protein to study glycosylation. RNase B is a relatively small protein of 14.9- 15.5 kDa and possesses a single glycan attached to Asparagine 34 (Asn^{34}) of its polypeptide backbone. This N-glycan is simple in its chemical composition as it contains mannose (Man) sugars that are attached to two N-acetylglucosamine (also commonly referred to GlcNAc or NAG) moieties, as shown in figure 4.1 [1, 2]. The extent of mannose addition within the glycan is not consistent

for each RNase B molecule due to the difficulty in controlling post translation modification during large-scale protein expression [3]. Commercial RNase B therefore consists of a mixture of 5 glycoforms. Each glycoform possesses the core pentasaccharide (Man_3-$GlcNAc_2$) with an additional two to six mannose residues, denoted as Man_5 to Man_9. The degrees of branching of these sugar residues varies between the glycoforms, with the larger glycan structures showing more branching than the smaller structures.

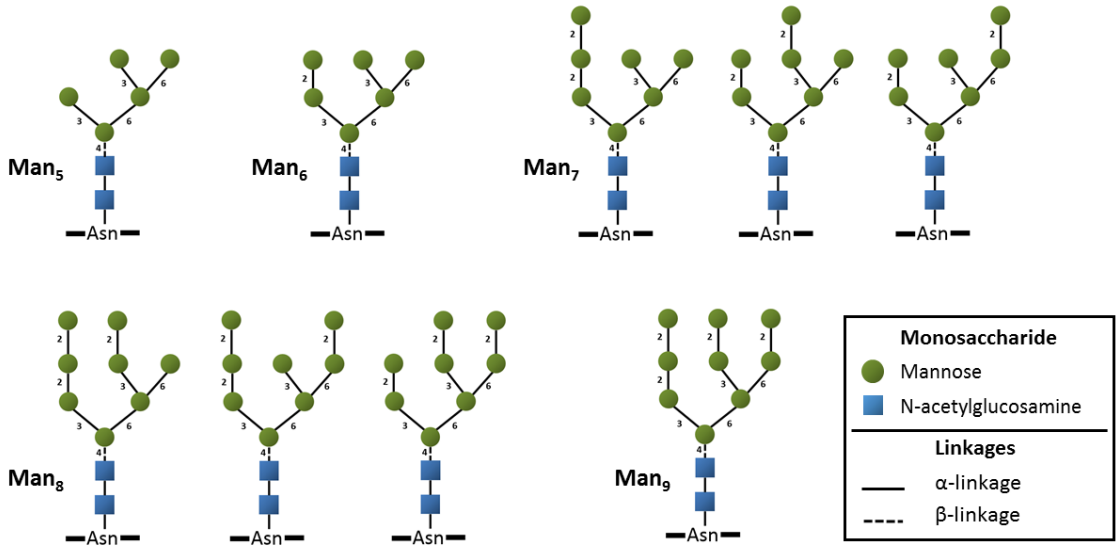

Figure 4.1: Schematic of the 5 high mannose N-glycans of RNase B. All mannose residues in this case are linked by α-linkages. Adapted from [4].

As discussed in the Chapter 1, sugars such as mannose can bind to ligands such as boronic acids with a high affinity *via* the 1-2 and 1-3 *cis* diols. Moreover, at a basic pH, the tetrahedral boronate ion of the boronic acid is able to form a covalent but reversible bond with these diols [5]. We therefore hypothesised that, by incorporating a boronic acid monomer into our glycoprotein imprinting strategy for RNase B, imprints which exhibit a high affinity for both the protein backbone and the N-glycan could be realised.

Various mass spectrometry studies using both intact RNase B or solely its N-glycan have previously been reported in the literature [4]. For example, Lin *et al.* used the N-glycan of RNase B to develop an ESI-MS protocol that improves the identification of glycoform glycosylation site occupancy, glycoform profiles and variation in glycoprotein sample concentrations [6]. Xia *et al.* used capillary electrophoresis-electrospray mass spectrometry (CE-MS) to report the masses of the five intact RNase B glycoforms from a commercial sample, as well as combining this technique with protease and glycosidase digestion to improve the characterization of each N-glycan [7]. Similarly, Thaysen-Anderson *et al.* used matrix-assisted laser desorption/ionisation time-of-flight mass spectrometry (MALDI-TOF-MS) on both intact RNase B and its cleaved N-glycan to also accurately identify the proportions of each glycoform within commercial samples [8].

Furthermore, the sugar binding properties of boronic acids have been exploited in several glycoprotein mass spectrometry studies to enable the enrichment and detection of complex samples [9, 10]. In these cases the boronic acids were primarily used to immobilise glycoproteins to a fixed scaffold such as nanoparticles that can then be washed to isolate the glycoprotein of interest. For example Sparbier *et al.* used boronic acid functionalised magnetic nanoparticles to isolate a number of different glycoproteins, including RNase B, from a complex mixture of glycoproteins that were then identified using MALDI-TOF-MS [11]. Similarly, Li *et al.* also used boronic acid functionalised beads to immobilise RNase B that were likewise analysed with MALDI-TOF-MS [12].

However, few studies have directly characterized the binding relationship between boronic acids and RNase B using mass spectrometry. Moreover, to our knowledge there are no studies to date that report evidence for the binding of the 3-

acrylamidophenyl boronic acid monomer to intact samples of the protein. To therefore investigate this binding we undertook ESI-MS studies on samples of intact RNase B complexed with this boronic acid in order to elucidate the extent to which the RNase B N-glycans can covalently bind this monomer. Furthermore, we wished to identify factors that can influence this complexation, including the monomer concentration and the solvation conditions in order to optimise this binding. This work therefore provides novel insight into the extent of the RNase B-boronic acid monomer binding and the factors which influence its success.

As a result of the findings from the optimisation studies we then undertook circular dichroism (CD) studies of the RNase B protein to examine its stability in an aqueous-organic mixed solvent system. This was necessary as within the literature there are numerous examples of proteins that have shown to be structurally unstable in both polar and apolar organic solvents [13]. However, the structural tolerance thresholds these solvents ranges significantly between each protein. For example, lysozyme has shown to have a relatively low tolerance to exposure to dimethyl sulfoxide (DMSO) of 10 % (v/v) [14]. Similarly, the PZase enzyme has been reported to show essentially no resilience to organic solvents as for example only 5 % (v/v) methanol (MeOH) destabilises its tertiary structure [15]. However, some proteins report a high resilience to large percentages of organic solvents. For example, the halophilic enzyme family generally shows higher tolerances to large percentages of organic solvents due to their evolution in highly saline conditions [16, 17]. Moreover, CD studies of the lipase 6B and HaBla halophilic enzymes showed these proteins have a high resilience to MeOH exposure of up to 60 % (v/v) and 40 % (v/v), respectively [18, 19].

These tolerances cannot be directly compared, however these studies reinforce the importance of considering each protein-solvent interaction on an individual, case-by-case basis. CD studies of RNase A (the non-glycosylated homologue of RNase B) have also been reported [20-22]. However, due to the lack of structural data within the literature that examines the stability of RNase B to different organic solvents it was necessary to elucidate any effect of employing in this case a percentage of MeOH to its stability. The following therefore outlines each objective of this chapter following which the ESI-MS and CD results are presented.

2.0 Objectives

1 Examine the covalent binding of the RNase B glycoprotein to the vinyl-boronic acid monomer by ESI-MS.

2 Examine whether the binding of this boronic acid monomer occurs through the sugar residues of the glycan attached to the body of the RNase B protein.

3 Explore the complexation conditions by varying the solvation of the glycoprotein and boronic acid

4 Examine the conformational stability of the RNase B glycoprotein within the optimal complexation conditions with CD.

3.0 Results and Discussion

3.1 ESI-MS Analysis of RNase B-Boronic Acid Complexes

3.1.1 Complexation of RNase B with an Excess of Boronic Acid in Aqueous Solution

For the complexation studies, 0.1mM of RNase B protein was dissolved in a 0.1 % ammonium acetate buffered solution where the pH was adjusted using KOH to 8.6 to reside above the monomer's pKa of 8.2. The 3-acylamidophenyl boronic acid monomer was then added at either a x20 or x100 excess relative to the protein (figure 4.2). At this alkaline pH the boron is 'trapped' in its bound tetrahedral form due to the excess hydroxyl ions in solution [5]. The boron in this tetrahedral form is therefore less likely to unbind the 1-2 or 1-3 *cis* diols than in its trigonal form. Once complexed the samples were then subjected to ESI-MS and the resultant masses detected and analysed. We hypothesised that upon complexation we should observe a clear increase in the masses for the protein, whilst no complexation would result in masses identical to the un-complexed control. The following sections reports each complexation study alongside its respective control and discusses the effect of varying solvent and monomer concentration on these observed ESI masses.

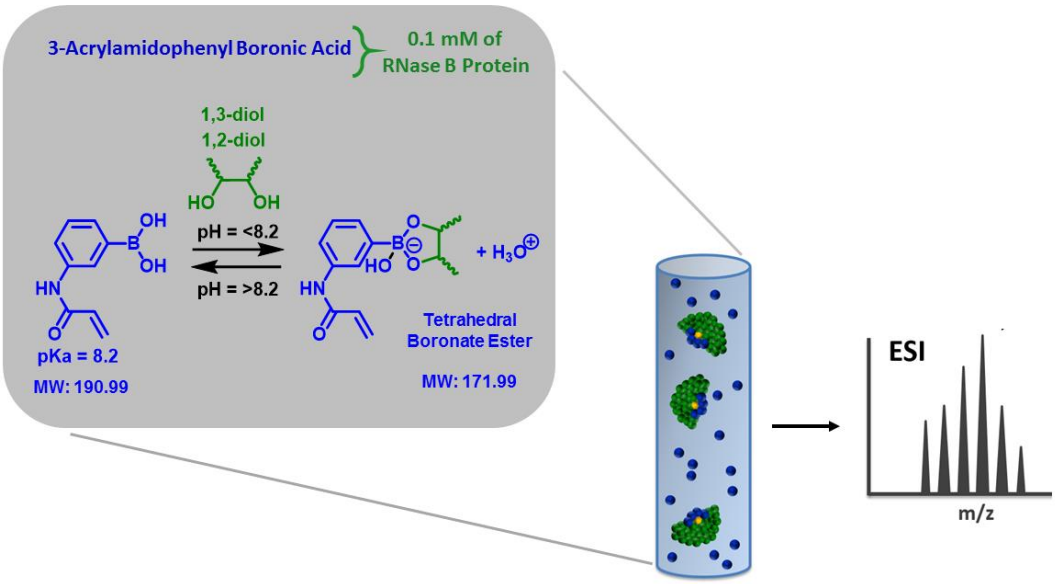

Figure 4.2: Schematic of the pH sensitive complexation of the 3-acrylamidophenyl boronic acid monomer with the RNase B glycoprotein. At an alkaline pH above the boronic acid's pKa, the monomer binds the diol to forms a cyclic tetrahedral boronate ester. However, if the pH is below the acids pKa, the complex can disassociate due to the boronate no longer being "trapped" in its more stable tetrahedral form by available hydroxyl ions.

3.1.2 ESI-MS of RNase B Control

In the first MS study the RNase B protein was dissolved in the 0.1 % ammonium acetate buffer without 3-acrylamidophenyl boronic acid and then subjected to ESI-MS (positive mode). As shown in figure 4.3, the ESI-MS spectra shows a number of mass peaks (figure 4.3, a, b, c, d and e) that correspond to the five mannose glycoforms (Man_5, Man_6, Man_7, Man_8 and Man_9) of RNase B. The glycoforms are sequentially separated by a mass of 162 Da which corresponds to each additional mannose (minus a water molecule from each subsequent hydrolysis reaction from mannose addition) bound to the main core penta-saccharide (Man_3-$GlcNAc_2$) chain.

The most prominent masses with the highest intensities are 14,900 Da (**a**) and 15,061 Da (**b**), which correspond to the Man_5 and Man_6 glycoforms, respectively. These two glycoforms have previously been reported as the most prominent glycoforms present in commercial RNase B samples [7]. The three remaining glycoforms (**c, d** and **e**) are also present but are found at much lower intensities than the Man_5 and Man_6 glycoforms. These 5 peaks are in agreement with previous spectra observed in the literature for RNase B acquired using MALDI-TOF-MS and CE-EMS [7, 12]. A small number of hybrid glycans have also been reported within the literature which can account for some of the masses found alongside the main 5 glycoforms observed [23]. Furthermore, the protein suppliers acknowledge that slight variation in the glycosylation profile of the RNase B can be present due to the aforementioned difficulty in controlling protein expression on a large scale [24]. As such, it is highly likely that some of these low intensity peaks for masses in-between these main 5 glycoform are indeed these less common hybrid structures.

Alongside the expected masses, salt adducts of the **a** glycoform with sodium (Na, MW: 23) and ammonium acetate (CH_3COONH_4, MW: 77) are also observed. The formation of these adducts is not unexpected as sodium is a common adduct present in mass spectrometry analysis and likewise ammonium acetate was used as the buffering salt [25]. In summary, several glycoforms of RNase B from a commercial bovine pancreas sample are observed in the ESI-MS spectra which is in agreement with the glycoforms previously reported in the literature. The protein was therefore taken forward for the complexation studies with the boronic acid monomer.

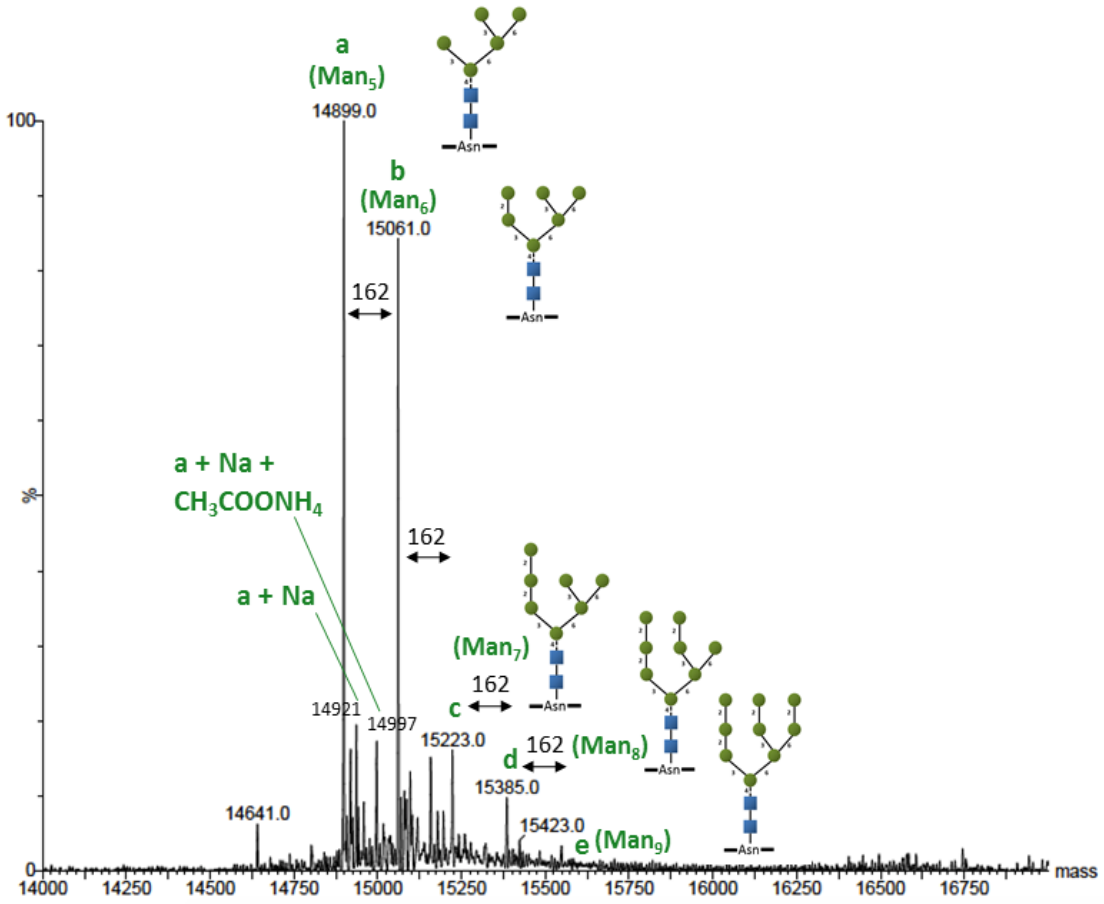

Figure 4.3: ESI-MS intensities of the RNase B protein sample in ammonium acetate buffer. Five glycoforms (**a, b, c, d** and **e**) of RNase B are present as expected, each sequentially separated by a mannose residue. Salt adducts of the **a** glycoform with sodium (Na) and ammonium acetate (CH_3COONH_4) were also observed.

3.1.3 ESI-MS of RNase B with x20 Boronic Acid Excess

The first conditions examined in the complexation study were with a x20 excess of the boronic acid monomer relative to the protein. The resultant spectra from solvating the two molecules in 0.1 % ammonium acetate buffer shows masses for four of the five glycoforms observed in the control spectra as expected, but with additional peaks at 15,071 Da and 15,232 Da corresponding to glycoforms **a** and **b,** each bound to one boronic acid monomer. For example, for glycoform **a**: 14,899 + 172 = 15,071 (figure 4.4). The presence of these higher masses for the complexed

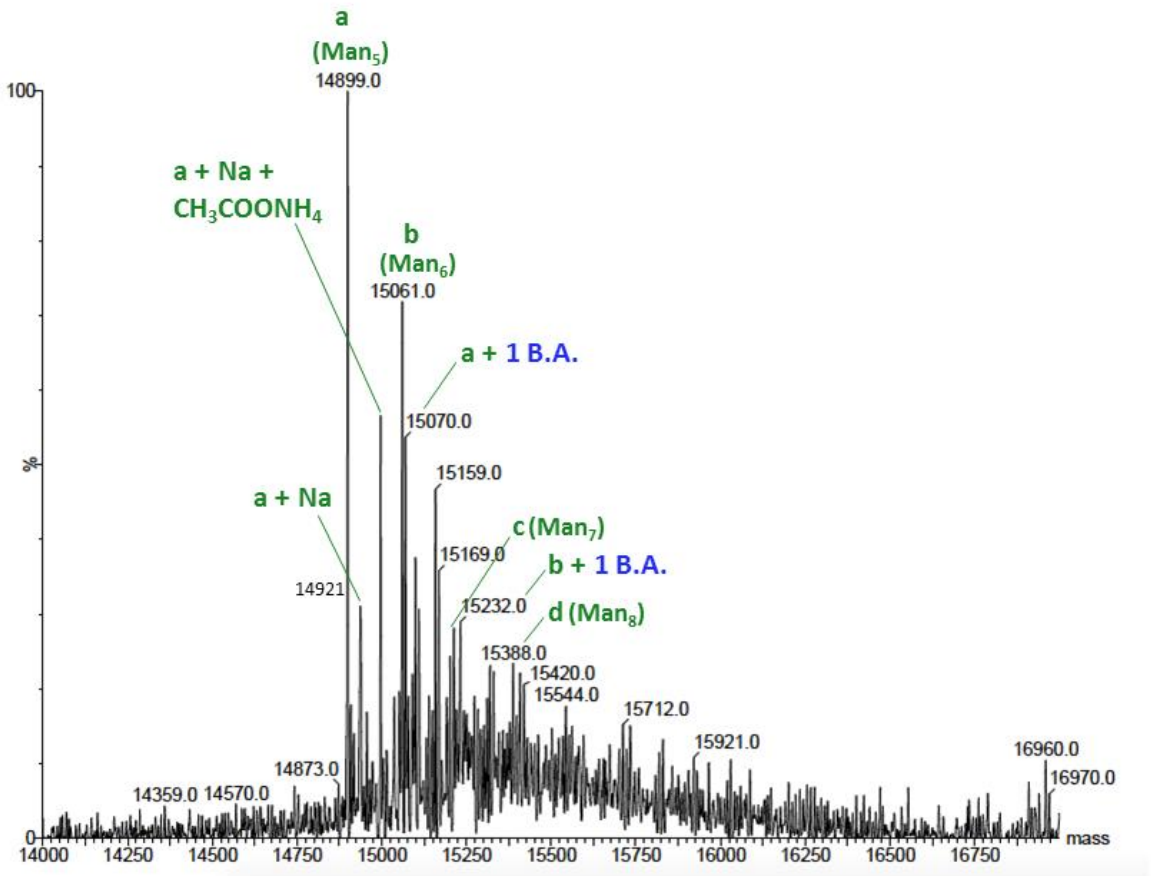

Figure 4.4: ESI-MS of the RNase B protein sample mixed with x20 excess of 3-acrylamidophenyl boronic acid in 0.1% ammonium acetate buffer. Of the five glycoforms **a** and **b** show complexation with one boronic acid monomer.

glycoforms were expected as it is known that the boronic acid can bind the *cis* diols in aqueous solution [5, 26]. However given the excess of monomer employed relative to the moles of protein this was much less binding than we anticipated.

To investigate the lack of binding, we examined whether this was possibly a solvation issue and that by incorporating a proportion of a polar, organic solvent to co-solvate the 3-acrylamidophenyl boronic acid the degree of complexation could be improved. However, as the RNase B molecule is a protein and therefore should reside in an aqueous, buffered environment to prevent its denaturation, the use of an organic solvent in principal should be limited to a small percentage [13, 27]. Furthermore, when selecting the appropriate organic solvent to act as co-solvent its polarity was carefully considered as it must be polar enough to still dissolve in the aqueous buffer and not phase separate. For this reason methanol (MeOH) was chosen as a suitable co-solvent as it has a polarity index of 0.76 (close to the polarity of water at 1.00) and has also been used in various percentages in other studies involving proteins [15-19]. Furthermore, the utilisation of MeOH as a co-solvent has also previously been shown to increase the association constant (K_a) of a benzoboroxole (a type of *o*-hydroxyalkyl arylboronic acid) with the fructose monosaccharide [28] as well as being used to co-solvate another type of benzoboroxole in a fructose molecular imprinting study [29]. MeOH was therefore an acceptable solvent for this purpose and so the experiment was repeated using the x20 excess of monomer, but with the monomer and RNase B incubated in a solution of 75 % (v/v) buffer and 25 % (v/v) MeOH.

3.1.4 ESI-MS of RNase B with x20 Boronic Acid Excess with 25 % (v/v) MeOH

As figure 4.5 shows, the consequent result of including 25 % (v/v) MeOH within the incubation solution is a significant improvement in the degree of binding observed between the boronic acid and the glycoforms of RNase B. Binding of up to 5 monomers to the Man_5 (**a**) glycoform produced ionised masses of 15,074, 15,241, 15,419, 15,592, and 15,763. Moreover, binding of up to 5 monomers was also observed for the Man_6 (**b**) glycoform to produce masses of 15,246, 15,407, 15,573, 15,752, and 15,923.

However, it is evident that as the degree of complexation of each glycoform increases, the relative intensities of the masses for the more highly bound glycoforms decreases. This is not entirely unexpected as the binding of the boronic acid monomer is in constant equilibrium with the diol (as previously shown in figure 4.2) and so not all diol binding sites may be filled upon ionisation of the molecule during the ESI process despite the excess. Moreover, the most intense ionised masses are still observed for the uncomplexed Man_5 (**a**) and Man_6 (**b**) glycoforms, which would indicate that not all the RNase B is binding the monomer. However, it is important to note that the intensities observed within all these ESI-MS studies are not directly quantifiable as the ionised species in solution may vaporise to a different degree and therefore may fail to reach the detector. As such this data should strictly be taken as a qualitative and not quantitative study of the complexes.

In summary, this result demonstrates the importance of solvating the boronic acid monomer to therefore enable it to covalently bind the mannose residues to form complexes with the RNase B glycoforms. Up to 5 monomers have shown to bind to

the main Man_5 and Man_6 glycoforms with this excess, as expected. Following this encouraging result, we then examined whether using an even higher excess of boronic acid, in this case x100 excess relative to each molecule of RNase B, would produce a higher degree of complexation particularly for the Man_7, Man_8 and Man_9 glycoforms than the x20 excess. The experiment was therefore repeated with the x100 excess and the spectra compared.

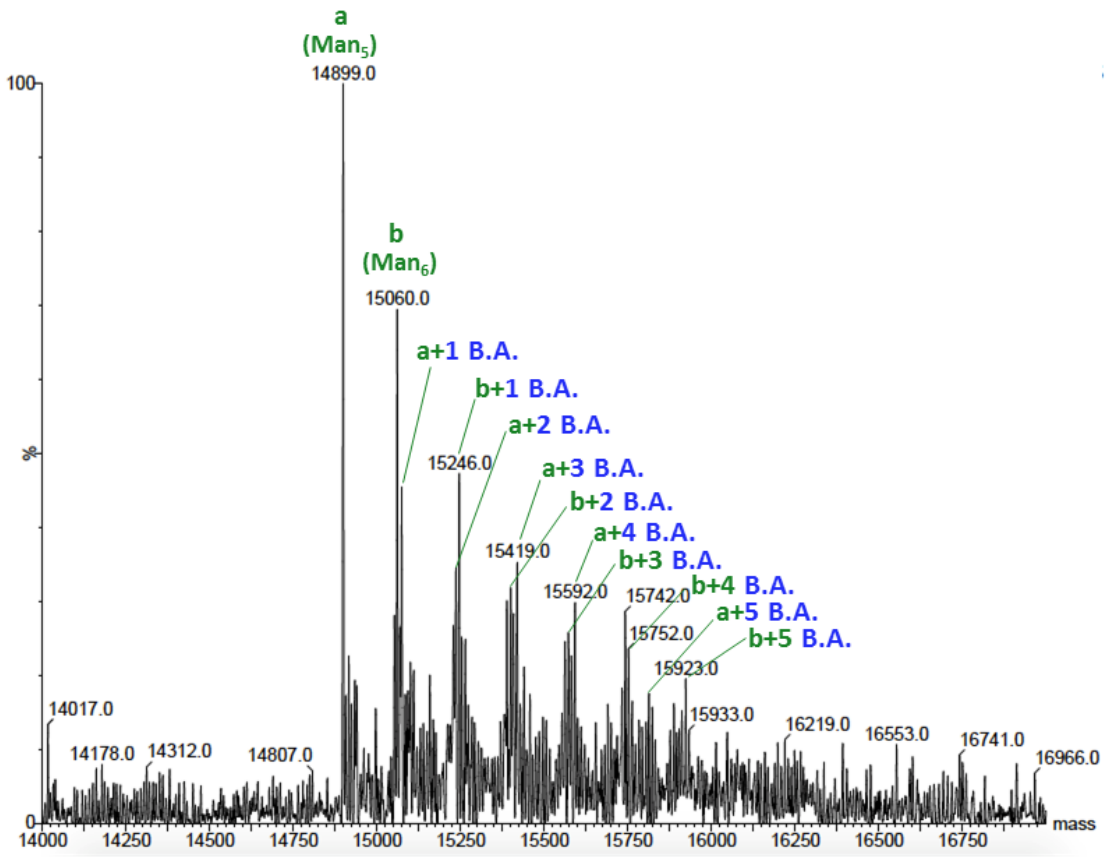

Figure 4.5: ESI-MS of the RNase B protein sample mixed with x20 excess of 3-acrylamidophenyl boronic acid in 75 % (v/v) ammonium acetate buffer and 25 % (v/v) MeOH. Of the five glycoforms, **a** and **b** show multiple complexation with the boronic acid monomer with up to 5 monomers bound to each.

3.1.5 ESI-MS of RNase B with X100 Boronic Acid Excess in 25 % (v/v) MeOH

The resultant ESI-MS spectra for the x100 complexation study is shown in figure 4.6. As aforementioned, the purpose of increasing the excess of the boronic acid monomer is to further push the equilibrium of the reaction shown in figure 4.2 to the right to form additional covalent bonds with the glycan chains of the RNase B. As figure 4.6 shows, the intensity of the signals for the RNase B glycoforms bound to between 1 to 5 monomers generally increases, however as aforementioned this data cannot be taken quantitatively. Furthermore, the spectra shows higher molecular weight ionised masses that were not present in the x20 excess conditions which could indicate that the higher molecular weight glycoforms (i.e. the Man_7 to Man_9 glycoforms) are binding to the monomer. However it should be noted that for these larger ionised masses the molecular weights peaks are harder to accurately assign due to the combined effects of the salt adducts, ranging ESI charges (i.e. from +1 to +3) and potential crossover between the molecular weights. Therefore pinpointing definitive masses in order to assign particular complexed structures is not possible. However, further analysis for example by separating the five glycoforms by HPLC analysis and then complexing them individually could enable these higher molecular weight masses to be accurately distinguished. Moreover, this would help to elucidate whether all the mannose diol groups are in the right spatial orientation to bind the boronic acid monomers without inhibition by steric hindrance.

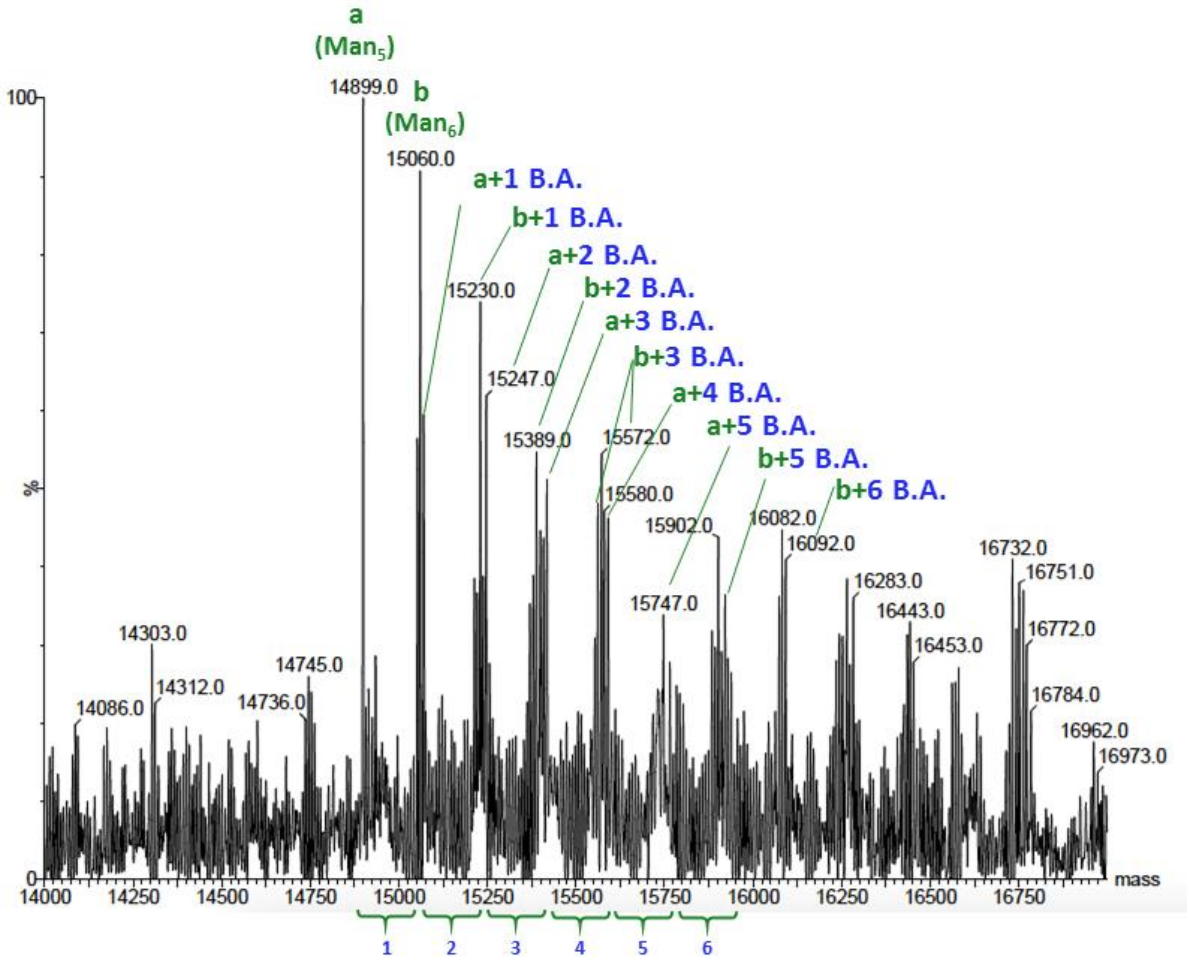

Figure 4.6: ESI-MS of the RNase B protein sample mixed with X100 excess of 3-acrylamidophenyl boronic acid in 75 % (v/v) ammonium acetate buffer and 25 % (v/v) MeOH. Of the five mannose glycoforms **a** and **b** show multiple complexation with the boronic acid monomer with up to 5 monomers bound to each.

In summary, these results show that the boronic acid monomer can bind as expected to the multiple mannose residues of the RNase B protein. However, in order to show that this is indeed *via* the mannose residues of the glycan and not the polypeptide backbone of the protein, further control studies using the non-glycosylated homologue of RNase B, RNase A, were undertaken. Under the same conditions as for RNase B, RNase A was complexed with the 3-acrylamidophenyl boronic acid monomer and the ESI-MS masses analysed to observe if covalent binding was observed. The following section reports the results of these control measures.

3.1.6 ESI-MS of the RNase A Control

As with the RNase B ESI-MS control study, the RNase A was first dissolved in a 0.1 % ammonium acetate buffered solution without 3-acrylamidophenyl boronic acid and then subjected to ESI-MS (in this case negative mode). The resultant spectral masses were then analysed as shown in figure 4.7. The spectra reports a mass at 13,680 Da (**a**) that corresponds to the molecular ion peak of the RNase A protein previously reported within the literature [30]. As the protein is not glycosylated the spectra does not exhibit multiple glycoforms and hence only one mass is observed. However, as was likewise observed for the RNase B, the protein is forming adducts with salts present in the solution to produce sequential shifts of 98 or 99 Da from the **a** peak. These correspond with adduct formation with both sodium (Na, MW:23) and ammonium acetate (CH_3COONH_4, MW:77). In summary, only one mass from a commercial sample of RNase A from bovine pancreas is observed in the ESI-MS spectra, alongside several protein-salt adducts at higher molecular weights, as expected. Following confirmation of the correct ionised mass peak, the RNase A was then taken forward for the complexation studies with the boronic acid monomer in the 25 % (v/v) MeOH solvent systems.

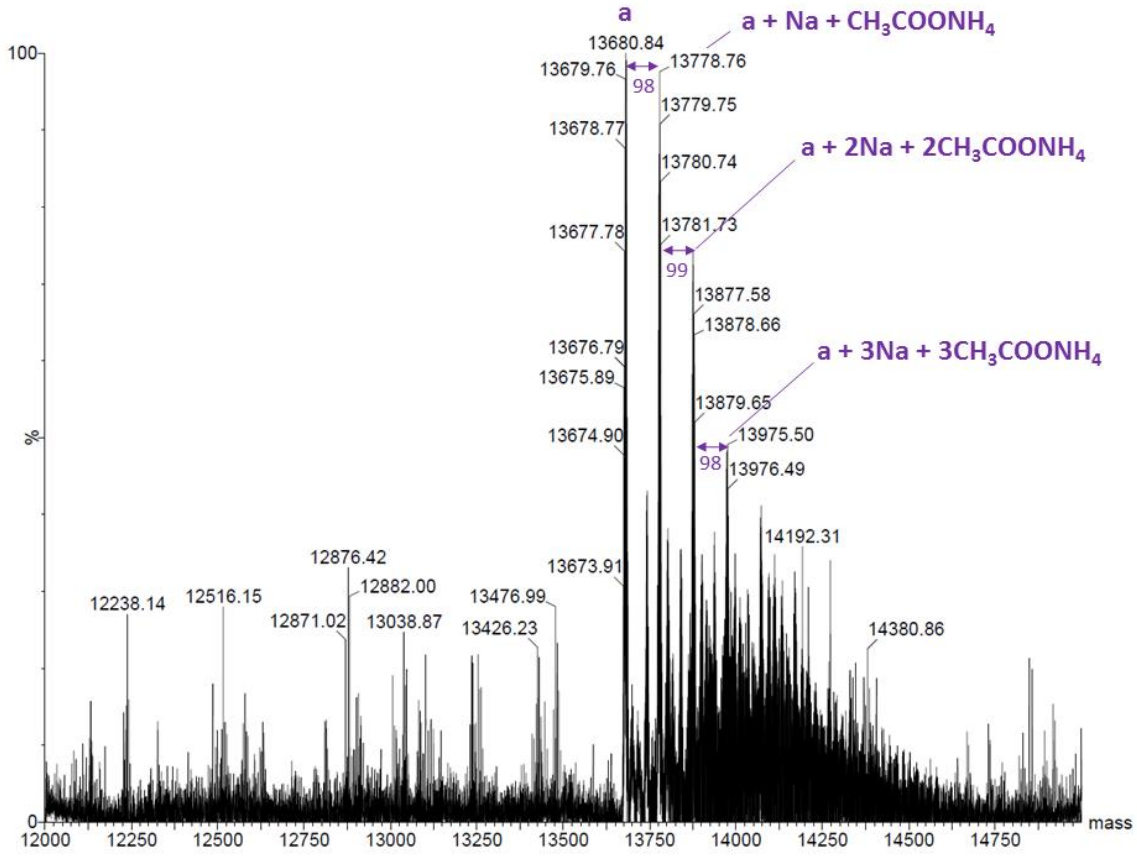

Figure 4.7: ESI-MS of the RNase A protein sample in buffer. Only one mass for the RNase A protein is observed as expected, however masses for several salt adducts of the protein with sodium and ammonium acetate are also present.

3.1.7 ESI-MS of RNase A with X20 Boronic Acid Excess with 25 % (v/v) MeOH

As figure 4.8 shows, upon mixing the RNase A with a x20 excess of the boronic acid monomer in 75 % (v/v) buffer with 25 % (v/v) MeOH we observe no appearance of higher molecular weight ionised masses to indicate that covalent complexation has occurred. This is as expected as the RNase A is non-glycosylated and thus there are no available mannose residues for the monomer to bind. This data also demonstrates that the boronic acid is not covalently binding to the amino acid residues of the protein backbone and therefore reinforces that the binding observed for RNase B must indeed occur through the mannose units of the glycan.

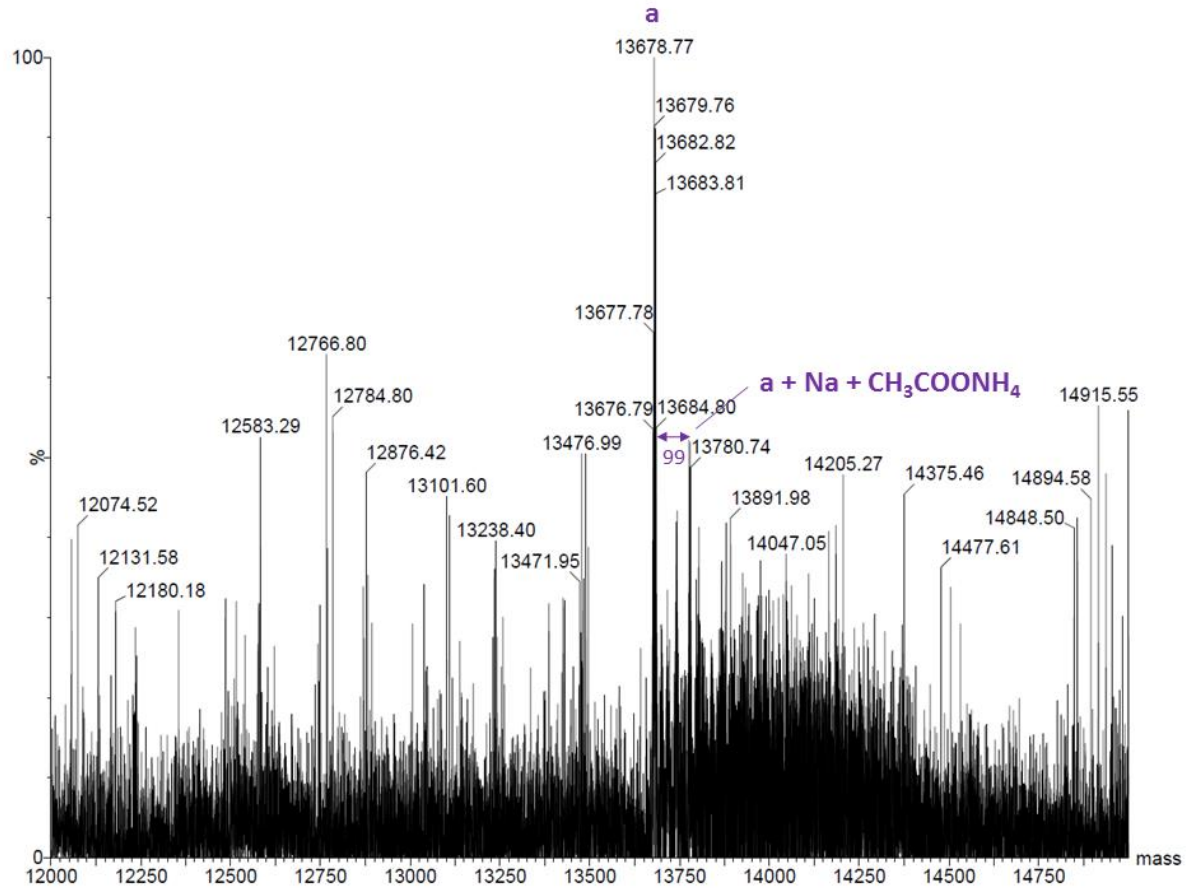

Figure 4.8: ESI-MS of the RNase A protein sample mixed with x20 excess of 3-acrylamidophenyl boronic acid in 75 % (v/v) ammonium acetate buffer and 25 % (v/v) MeOH. No complexation with the boronic acid monomer is observed as expected.

Interestingly, we observe a loss of intensity for several of the salt adducts of **a** that were observed in the control. This is likely due to the excess monomer competing with the salt ions in solution to prevent them from binding to the protein. It should also be noted that the signal to noise in this spectra is higher than previously witnessed for the RNase B spectra, which is due to a lower overall signal caused by less ionisation of the available masses. Finally, to complement this result we then examined if this lack of binding is retained with a x100 monomer complexation.

3.1.8 ESI-MS of RNase A with X100 Boronic Acid Excess with 25 % (v/v) MeOH

As figure 4.9 shows, further increasing the boronic acid ratio to a x100 excess likewise does not produce any ionised masses to indicate covalent complexation of the monomer with the protein. The only observable mass observed is from the molecular ion peak of the RNase A protein (**a**) and no higher masses related to complexation are observed. Similarly to figure 4.8, the addition of the monomer to the solution appears to have once more prevented salt adduct formation with the protein, again most likely to ionic competition in solution for the protein. In summary, we observe no ionised masses in either the x20 or x100 ESI-MS studies to indicate that covalent complexation of the monomer with the RNase A protein has occurred. This is as we hypothesised due to the lack of an available glycan. Furthermore, from these studies we also confirm that the site of monomer binding to RNase B must be occurring through the sugar residues of its glycan as expected, and not through the backbone moieties of the protein.

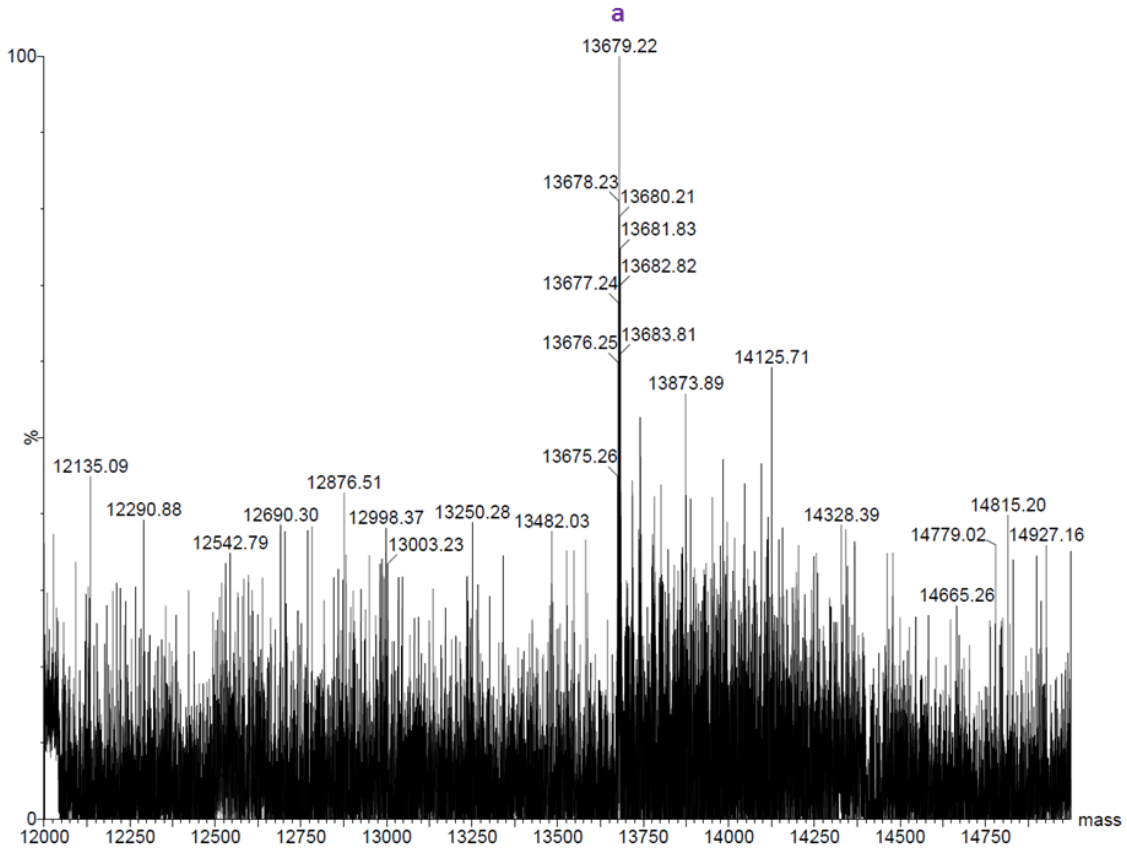

Figure 4.9: ESI-MS of the RNase A protein sample mixed with x100 excess of 3-acrylamidophenyl boronic acid in 75 % (v/v) ammonium acetate buffer with 25 % (v/v) MeOH. No complexation with the boronic acid monomer is observed despite this high monomer concentration.

3.2 Overall Conclusions from the ESI-MS of RNase B and RNase A with 3-Acrylamidophenyl Boronic Acid Complexations

In this study whereby either RNase B or RNase A from commercial samples of bovine pancreas were mixed in two different solvent conditions with varying excesses of a boronic acid monomer, we demonstrate that covalent binding of the monomer to RNase B occurs through the mannose residues of the proteins' N-glycan.

We first demonstrated that despite using an aqueous buffer with a x20 excess of boronic acid for the complexation study we observed the addition of only 1 monomer to the two most abundant RNase B glycoforms, Man_5 (**a**) and Man_6 (**b**). This was concerning as boronic acid- sugar binding has been reported in numerous studies within the literature [5, 31, 32]. Moreover, aqueous conditions have typically been employed in these studies with no obvious indication of issues regarding the lack of a boronic acid-sugar interaction. However, when 25 % (v/v) MeOH was included as a co-solvent within the aqueous complexation buffer the resultant ionised masses demonstrated the successful binding of up to 5 monomers with both the Man_5 (**a**) and Man_6 (**b**) RNase B glycoforms. This therefore clarified that a proportion of a polar, organic solvent is required to facilitate this interaction and this study is the first to demonstrate ESI-MS evidence for ionised masses that correspond with covalently bound complexes of these two species. As such it offers new insight into the interaction of this functional monomer with this post-translational feature.

However, the subsequent use of MeOH to achieve these RNase B-boronic acid complexes then posed the question of whether the inclusion of an organic solvent compromises the conformational structure of the protein. As aforementioned, proteins typically reside in buffered, aqueous environments with appropriate levels of salt to ensure their 3-dimensional (3D) structure is maintained. If the solvent conditions are not closely monitored and controlled this could lead to the denaturation of the protein. To examine if this occurs, CD can be employed to examine the proteins' tertiary structure, i.e. the folding of the proteins secondary structural elements such as α-helices and β-sheets.

As covered in detail in Chapter 2, CD is a measure of the difference in the adsorption, A, of left-handed (A_L) and right-handed (A_R) circularly polarised light

($\Delta A = A_L - A_R$) by a chiral chromophore [33]. A CD spectra is therefore the sum of these differences in absorption and for proteins distinct transitions within the ultraviolet (UV) region of the electromagnetic spectrum are expected from 180-220 nm [34-36]. These transitions arise due to regions of highly ordered arrays of chromophores existing within the polypeptide molecule such as α-helices and β-turns and β-sheets [37]. As shown in figure 4.10, α-helices produce three peaks in the CD spectra comprising an intense, positive peak at 190 nm alongside two broader, negative peaks at 208 and 222 nm [36]. Conversely, β-sheet containing proteins are more disordered and produce a negative peak at 180 nm and 215 nm alongside a positive peak at 195 nm [37].

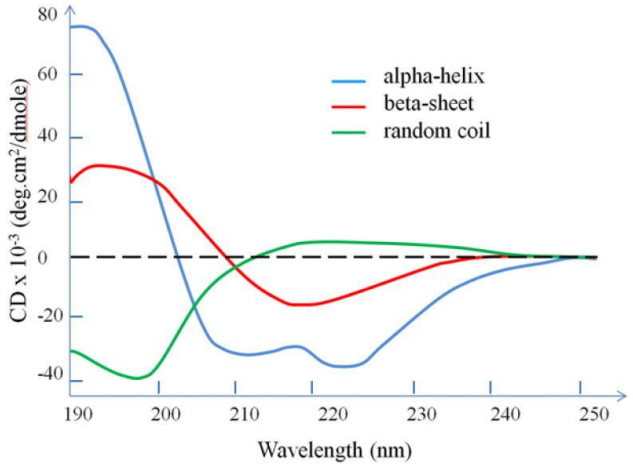

Figure 4.10: Depicts the CD absorbances for the three basic secondary structures (α- helix (blue), β-sheet (red) and random coil (green)) of polypeptides. Taken from [38].

The CD spectra of RNase A and RNase B have previously been reported within the literature, however no cases examining its CD spectra in co-solvent conditions to our knowledge have been reported [20, 21, 39]. Therefore the following section details CD studies of RNase B in various aqueous-organic solvation conditions alongside appropriate control studies.

3.3 Study of the Conformational Structure of RNase B by CD

3.3.1 Effect of MeOH on the Conformational Structure of RNase B by CD

In the first CD study of RNase B we examined the far-UV (190-260 nm) spectra of the protein at 25 °C in varying solvation conditions. In this case, the percentage of MeOH as the co-solvent was gradually increased at various increments from 1-50 % (v/v). Based on the outcome of this MeOH co-solvation data, we then report two further positive controls where a thermal heat ramp was employed to deliberately induce structural denaturation of RNase B. For all these studies RNase B was dissolved in either 0.1 M potassium phosphate buffer or alongside a stated proportion of MeOH (%, v/v) as required. The pH for all studies was adjusted to 8.6 to match the pH required by the 3-acrylamidophenyl boronic acid monomer from the ESI-MS studies.

3.3.2 Far-UV CD of RNase B in Increasing Percentages of MeOH

Figure 4.11 shows the far-UV CD spectra of the RNase B protein in a range of MeOH co-solvation conditions. Firstly, the spectral shape observed for RNase B in the 0 % MeOH buffer control is comparable with that previously observed within the literature for RNase A [21]. Despite the protein having slightly more β-sheets than α-helices, α-helical contributions to the spectra are much more intense and overlap spectrally with those of the β-sheet [20]. Consequently, the spectrum is predominantly α-helical in content and hence has similarity in its shape with a typical α-helix spectra [40]. Furthermore, previous studies of the far-UV CD of RNase A have shown that the CD spectral shape arises from the similar proportions of α-

helices, β-sheets and random coils present, which in concert produce the generally 'disordered' spectra observed here [41]. Overall, direct comparison of the spectra observed in figure 4.11 with those reported in the literature for RNase A show the two are comparable [41].

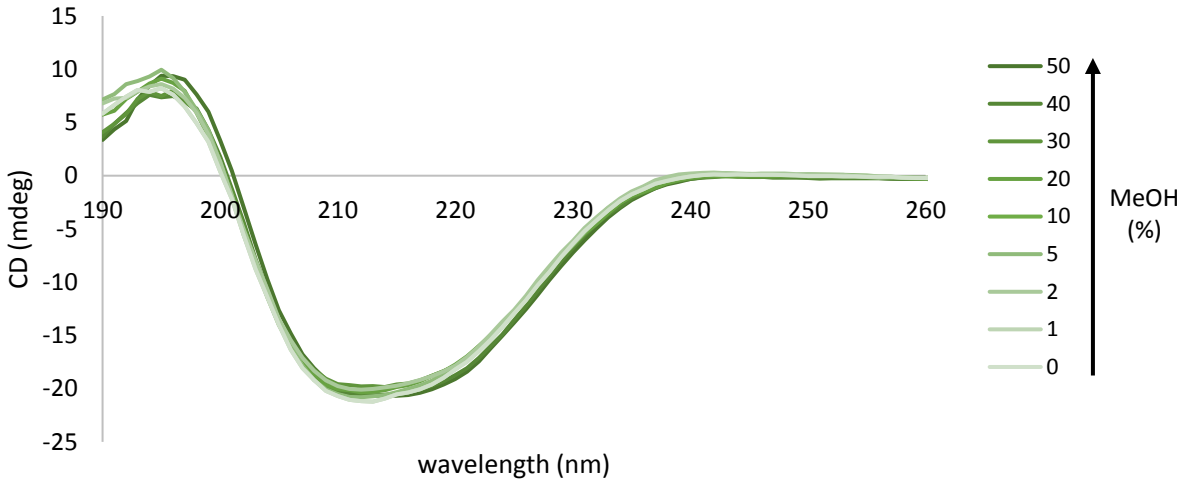

Figure 4.11: Far-UV CD spectra of 25 μM RNase B observed with increasing percentages (v/v) of MeOH.

If we then examine the spectra observed with 1 % MeOH (v/v) in contrast with the 0 % MeOH, there are no observable shifts at any wavelength to suggest changes have occurred in the conformational structure of RNase B upon MeOH inclusion. Likewise, the spectra continue to show no changes despite the further increases in the percentages of MeOH from 5 % to 50 % (v/v). This indicates that the proteins secondary structure elements are unaffected by these co-solvation conditions and are therefore stable. This was surprising as with higher percentages of MeOH it would not be unreasonable to hypothesise that folding changes may be observed, as proteins as a general class are known to be sensitive to environmental changes.

Therefore, as a positive control to further ensure that the spectra observed in figure 4.11 were indeed for RNase B in its native conformation, we proceeded to conduct a thermal melt of the protein to intentionally induce denaturation under two sets of conditions, the first being i) in solely buffer and ii) in buffer with 30 % (v/v) MeOH. The temperature for both studies was first set at 25 °C and then sequentially increased at intervals of 5 °C to finish at 90 °C. The resultant spectra are as shown in figures 4.12, a and b, respectively.

3.3.3 Thermal Melts of RNase B in Either 0 or 30 % (v/v) MeOH

Examination of the thermal melt of RNase B in the 0 % (v/v) MeOH conditions, as shown in figure 4.12, **a** firstly show that the spectra observed at 25 °C is as expected and in agreement with the previous spectra observed at 25°C in figure 4.11. Initially, during the course of the melt in figure 4.12, the spectrum remains constant at the lower temperature intervals from 30-45 °C; however at 50°C we observe a transition in the spectra to indicate the start of the denaturation. Over the course of this unfolding event, we observe an increase in the signal at 222 nm, from -18.5 mdeg at 25 °C to -10.3 mdeg at 90 °C. Likewise, we observe a shift in the spectra maxima at 210 nm that correspond to a loss of alpha helical structure that was likewise observed by Steela *et al* in their thermal melt study of RNase A [20]. However, if we then directly compare the spectra from figure 4.12, **a** against figure 4.12, **b** that reports the thermal melt of the protein in 30 % (v/v) MeOH, clear differences between the denaturation profiles in the two solvation conditions are apparent.

At 25 °C, the figure 4.12**, b** system shows an identical spectra to the respective spectra observed at 25 °C in both figure 4.12, **a** and figure 4.11. This again reiterates that the presence of MeOH has no effect on the proteins structure at room temperature. Likewise, as was observed with the 0 % (v/v) MeOH thermal melt, the spectral shape remains constant for the lower temperature intervals from 30-45 °C. However, as was also observed for figure 4.12, **a** denaturation is apparent at 50 °C which indicates the initial unfolding of the secondary structural elements. Similarly over the course of the thermal unfolding event, we observe an increase in the ellipticy at 222 nm, from -17.5 mdeg at 25 °C to -12.3 mdeg at 90 °C. Furthermore, we also observe a shift in the spectrum maxima at 210 nm that correspond with a loss of alpha helical structure of the RNase B. Overall, the spectral shape shows similar changes to the 0 % melt, however the two show differing final spectral profiles.

In order to further analyse the changes observed in the spectra from these two solvation conditions, using linear interpolation a plot of the proportion of protein in its folded state was calculated using the elliptical values from 222 nm. Calculation of these folded proportions can then be used to determine the thermal denaturation transition midpoint (T_m) for each of the solvation conditions, which provides insight into the stability of the protein under these solvation conditions.

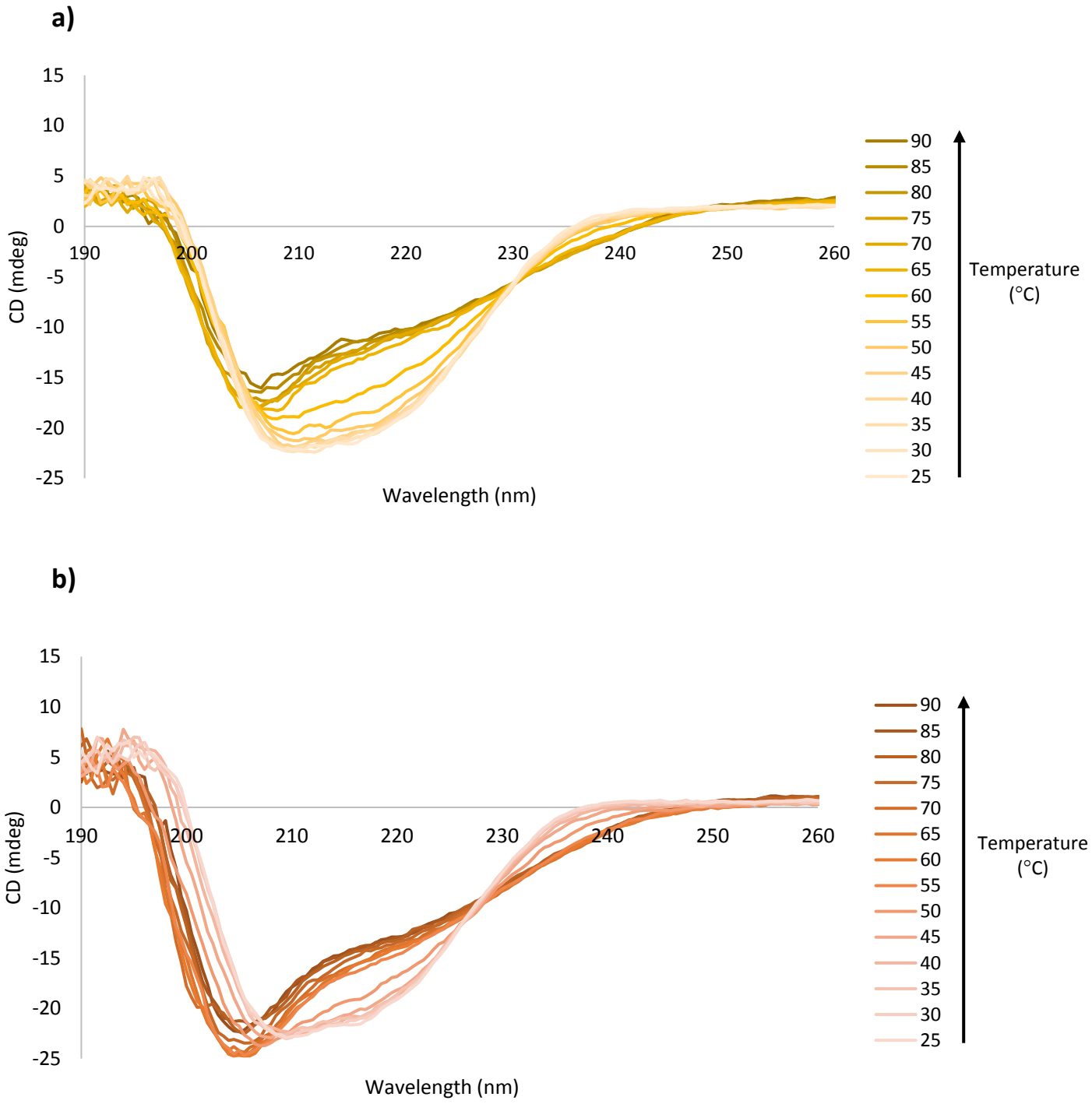

Figure 4.12: Change in the CD spectra of 25 μM RNase during a thermal melt in either **a)** buffer or **b)** buffer with 30 % MeOH.

3.3.4 Comparison of the Denaturation Profiles of RNase B in 0 or 30 % (v/v) MeOH.

The thermal denaturation profiles calculated from the elliptical changes at 222 nm for RNase B in the two solvent systems are shown in figure 4.13. The elliptical change at this wavelength corresponds to changes in the *n*-π* transition of the peptide-backbone and as such can be used to examine the unfolding of the secondary structure [42]. The thermal denaturation transition midpoint (T_m) is the temperature at which the molecule is 50 % unfolded. Firstly, we observe that both the 0 and 30 % MeOH thermal melts follow a single sigmoidal transition of the protein typical of most polypeptide structures [18].

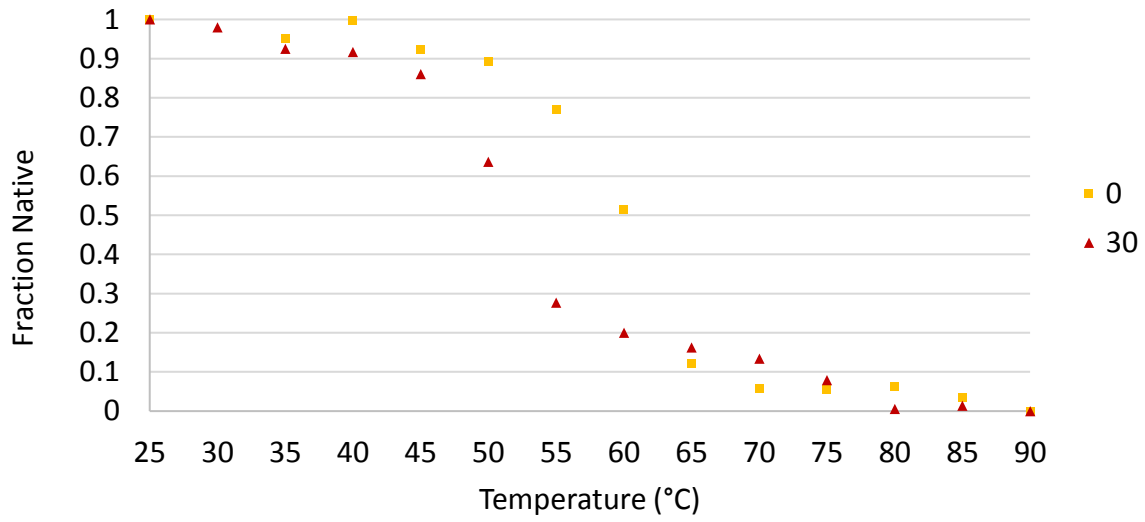

Figure 4.13: Thermal denaturation profiles of RNase B in the 0 % MeOH (squares) and 30 % MeOH (triangles) from the ellipticies at 222 nm.

The T_m for RNase B in the buffer conditions was 60 °C which is in agreement with values previously observed for RNase B and RNase A within the literature [41, 43]. However, the T_m for the RNase B in the 30 % MeOH system was 8 °C lower at 52 °C, which indicates that the MeOH acts to destabilise the RNase B protein to initiate

it to unfold at a lower temperature. This difference in the T_m for the two solvation systems could explain the distinctly different final denatured profile of RNase B at 90 °C. However, further investigation with for example catalytic assays, ^{1}H NMR and intrinsic tryptophan fluorescence intensity to provide insight into the kinetic and thermodynamic events of these events would be required to elucidate the precise conformational changes occurring at the relevant residues during this process.

In summary, using a 30 % (v/v) proportion of MeOH as a co-solvent appears to act as a destabiliser of the protein to leave half of the sample unfolded at a temperature that is 8 °C lower than with buffer alone. However, the inclusion of MeOH at temperatures below 50 °C does not affect its stability as no difference in the far-UV spectra is observed at these temperatures. In summary, we can conclude that using 30 % (v/v) MeOH with RNase B at room temperature will not adversely affect the native structure of the protein.

3.4 Overall Conclusions from the CD Study of RNase B in MeOH and their Relation to the ESI-MS Complexation Study

In this study, the conformational structure of RNase B from bovine pancreas was examined in various solvation conditions by far-UV CD. We hypothesised that the inclusion of the MeOH as a co-solvent could potentially cause unwarranted changes in the proteins secondary structure (α-helices or β-sheets), which could destabilize the protein and cause it to unfold. If so, changes in the far-UV CD spectra would be observed due to unfolding of these secondary structural elements.

In the first far-UV CD study at room temperature (25 °C), we showed the spectra for the natured conformation of RNase B in aqueous, buffered conditions. We then

reported that this spectral shape is maintained despite including increasing amounts of MeOH from 1 % up to 50 % (v/v). To our knowledge, this is the first study of RNase B that provides evidence that MeOH inclusion within the solution does not interfere with the proteins secondary structure elements.

We then reported from thermal melt studies of the protein in buffer (whereby denaturation was deliberately induced to determine the melting temperature of the molecule) that RNase B unfolds at a temperature of 60 °C. When compared against a parallel thermal melt which included 30 % (v/v) MeOH the two thermal profiles showed different melting temperatures alongside different final spectral configurations that directly relate to the proportion of secondary structures present. From the fraction native analysis derived from these far-UV melts, we show that the presence of the MeOH lowers the temperature at which RNase B starts to denature by 8 °C. As such, the MeOH is acting as a destabiliser to the structure at these higher temperatures and furthermore affects the overall unfolding of the protein to produce different spectral profiles at the final 90 °C temperature.

However, we also reported that at the lower temperatures of 25-45 °C the 30 % (v/v) proportion of methanol does not affect the protein structure as no spectral changes at these temperatures from the native spectra were observed. This therefore indicates that the secondary structural elements are unaffected despite MeOH exposure and therefore we can conclude that the protein is stable and resides in its natures, native conformation in 30 % (v/v) MeOH solvated conditions at room temperature.

If we relate the outcomes of these CD studies back to the earlier ESI-MS complexation studies of the protein with the boronic acid monomer, we can therefore

conclude that employing a 25 % (v/v) proportion of MeOH to facilitate complexation at room temperature will not adversely affect the conformation of RNase B. As such, the complexes of the 5 RNase glycoforms bound to the boronic acid monomer shown in the ESI-MS data can be taken forward to be imprinted with the knowledge that the protein will not denature in the required solvation conditions. The following chapter will therefore bring together the knowledge from these studies together with the polymer system developed in Chapter 3 to create imprints for the RNase B glycoprotein.

References

1. Fu, D., Chen, L., O'Neill, R.A., *A detailed structural characterization of ribonuclease B oligosaccahride by 1H NMR spectroscopy and mass spectrometry.* Carbohydr Res, 1994. **261**(2): p. 173-186.
2. Tarelli, E., Byers, H.L., Homer, K.A., Beighton, D., *Evidence for mannosidase activities in Streptococcus oralis when grown on glycoproteins as carbohydrate source.* Carbohydr Res, 1998. **312**(3): p. 159-164.
3. Inc, S.A. *RNase B Glycoprotein Standard from bovine pancreas*. 2018 NA [cited 2018 08.10.2018]; PDF Product Information Technical Bulletin]. Available from: https://www.sigmaaldrich.com/catalog/product/sigma/r1153?lang=en&region=GB.
4. G Robert, E.T., K A. Homer, *Production of an Endo-β-N-Acetylglucosaminidase Activity Mediates Growth of Enterococcus faecalis on a High-Mannoes-Type Glycoprotein.* Journal of Bacteriology, 2000. **184**(4): p. 882-890.
5. Nishiyabu, R., et al., *Boronic acid building blocks: tools for sensing and separation.* Chem Commun (Camb), 2011. **47**(4): p. 1106-23.
6. Lin, C.Y., et al., *A comparative study of glycoprotein concentration, glycoform profile and glycosylation site occupancy using isotope labeling and electrospray linear ion trap mass spectrometry.* Anal Chim Acta, 2012. **728**: p. 49-56.
7. Liu T1, L.J., Zeng R, Shao XX, Wang KY, Xia QC., *Capillary Electrophoresis - Electrospray Mass Spectrometry for the Characterization of High-Mannose-type N-Glycosylation and Differential Oxidation in Gycoproteins.* Anal Chem, 2001. **73**(24): p. 5875-5885.
8. Thaysen-Andersen, M., S. Mysling, and P. Hojrup, *Site-specific glycoprofiling of N-linked glycopeptides using MALDI-TOF MS: strong correlation between signal strength and glycoform quantities.* Anal Chem, 2009. **81**(10): p. 3933-43.
9. Zhang, L., et al., *Boronic acid functionalized core-satellite composite nanoparticles for advanced enrichment of glycopeptides and glycoproteins.* Chemistry, 2009. **15**(39): p. 10158-66.
10. *Springer Protocols - Mass Spectrometry of Glycoproteins*. Methods in Molecular Biology, ed. S.M.P. J J. Kohler. Humana Press.
11. Sparbier. K, K.S., Kessler. I, Wenzel. T, and Kostrzewa. M, *Selective isolation of glycoproteins and glycopeptides for MALDI-TOF MS Detection Supported by Magnetic Nanoparticles.* Journal of Biomolecular Techniqus 2005. **16**(4): p. 407-413.

12. Lee, J.H., et al., *Immobilization of aminophenylboronic acid on magnetic beads for the direct determination of glycoproteins by matrix assisted laser desorption ionization mass spectrometry.* J Am Soc Mass Spectrom, 2005. **16**(9): p. 1456-60.
13. Griebenow. K, a.K.A.M., *On protein Denaturation in Aqueous-Organic Mixtures but Not in Pure Organic Solvents.* J Am Chem Soc, 1996. **118**(47): p. 11695–11700.
14. Bhattacharjya. S, B.P., *Effects of organic solvents on protein structures observation of a structured helical core in hen egg white lysozyme in aqueous DMS.* PROTEINS: Structure, Funciton and Genetics, 1997. **29**: p. 492-507.
15. Pazhang, M., et al., *The combinatorial effects of osmolytes and alcohols on the stability of pyrazinamidase: Methanol affects the enzyme stability through hydrophobic interactions and hydrogen bonds.* Int J Biol Macromol, 2018. **108**: p. 1339-1347.
16. Zhang, N., et al., *Crystal Structure and Biochemical Characterization of an Aminopeptidase LapB from Legionella pneumophila.* J Agric Food Chem, 2017. **65**(34): p. 7569-7578.
17. Sinha, R. and S.K. Khare, *Effect of organic solvents on the structure and activity of moderately halophilic Bacillus sp. EMB9 protease.* Extremophiles, 2014. **18**(6): p. 1057-66.
18. Kamal, M.Z., et al., *Lipase in aqueous-polar organic solvents: activity, structure, and stability.* Protein Sci, 2013. **22**(7): p. 904-15.
19. Tokunaga, H., et al., *Reversible Activation of Halophilic beta-lactamase from Methanol-Induced Inactive Form: Contrast to Irreversible Inactivation of Non-Halophilic Counterpart.* Protein J, 2017. **36**(3): p. 228-237.
20. SIMONA D. STELEA, P.P., ALBERT S. BENIGHT, AND and T.A. KEIDERLING, *Thermal unfolding of ribonuclease A in phosphate at neutral pH: deviations form the two-state model.* Protein Science, 2001. **10**: p. 970-978.
21. Catanzano. F, G.G., Cafaro. V, *Circular dichroism study of ribonuclease A mutants containing the minimal structural requirements for dimerization and swapping.* 1998.
22. Joao, H.C.a.D., R .A, *Effect of glycosylation on protein structure and dynamics in ribonuclease B and some of its individual glycoforms.* Eur. J. Biochem, 1993. **218**: p. 239-244.
23. Kawasaki, N., Ohta, M., Hyunga, S., Hashimoto, O., Hayakawa, T., *Analysis of Carbohydrate Heterogeneity in a Glycoprotein Using Liquid Chromatography Mass Spectrometry and Liquid Chromatography with tandem mass spectrometry.* Anal Biochem, 1999. **269**(2): p. 297-303.
24. Aldrich, S. *Technical Bulletin: Ribonuclease B Glycoprotein Standard, Proteomics Grade*. [cited 2018 06/09/2018]; Product Information Sheet]. Available from: https://www.sigmaaldrich.com/content/dam/sigma-aldrich/docs/Sigma/Bulletin/r1153bul.pdf.

25. Cech, N.B. and C.G. Enke, *Practical implications of some recent studies in electrospray ionization fundamentals.* Mass Spectrom Rev, 2001. **20**(6): p. 362-87.
26. Brooks, W.L. and B.S. Sumerlin, *Synthesis and Applications of Boronic Acid-Containing Polymers: From Materials to Medicine.* Chem Rev, 2016. **116**(3): p. 1375-97.
27. Khabiri, M., et al., *Interaction of organic solvents with protein structures at protein-solvent interface.* J Mol Model, 2013. **19**(11): p. 4701-11.
28. Marie Berube, M.D., and Dennis G. Hall*, *Benzoboroxoles as Efficient Glycopyranoside-Binding Agents in Physiological Conditions: Structure and Selectivity of Complex Formation.* J. Org. Chem, 2008. **73**: p. 6471-6479.
29. Schumacher, S., et al., *Molecular imprinting of fructose using a polymerizable benzoboroxole: Effective complexation at pH 7.4.* Polymer, 2011. **52**(12): p. 2485-2491.
30. Pedrali, A., et al., *Characterization of intact neo-glycoproteins by hydrophilic interaction liquid chromatography.* Molecules, 2014. **19**(7): p. 9070-88.
31. Cheng, Y., et al., *A new class of fluorescent boronic acids that have extraordinarily high affinities for diols in aqueous solution at physiological pH.* Chemistry, 2010. **16**(45): p. 13528-38.
32. Wu, G., et al., *Template size matched film thickness for effectively in situ surface imprinting: A model study of glycoprotein imprints*. Vol. 5. 2015.
33. Martin S.R., B.P.M., *Absorption and Circular Dichroism Spectroscopy*. Calcium-Binding Protein Protocols: Volume 2: Methods and Techniques. Vol. 173. 2002: Springer, Totowa, NJ.
34. Rocchitta, G., et al., *Enzyme Biosensors for Biomedical Applications: Strategies for Safeguarding Analytical Performances in Biological Fluids.* Sensors (Basel), 2016. **16**(6).
35. Kelly, S.M., T.J. Jess, and N.C. Price, *How to study proteins by circular dichroism.* Biochim Biophys Acta, 2005. **1751**(2): p. 119-39.
36. Jiang, J., et al., *Ultraviolet spectroscopy of protein backbone transitions in aqueous solution: combined QM and MM simulations.* J Phys Chem B, 2010. **114**(24): p. 8270-7.
37. Greenfield, N.J., *Methods to estimate the conformation of proteins and polypeptides from CD data.* Anal Biochem, 1996. **235**(1): p. 1-10.
38. Wei, Y., A.A. Thyparambil, and R.A. Latour, *Protein helical structure determination using CD spectroscopy for solutions with strong background absorbance from 190 to 230nm.* Biochim Biophys Acta, 2014. **1844**(12): p. 2331-7.
39. Catanzano, F., et al., *Circular dichroism study of ribonuclease A mutants containing the minimal structural requirements for dimerization and swapping.* International Journal of Biological Macromolecules, 1998. **23**(4): p. 277-285.

40. Greenfield, N.J., *Using circular dichroism spectra to estimate protein secondary structure.* Nat Protoc, 2006. **1**(6): p. 2876-90.
41. Catanzano. F, G.G., Cafaro. V, <*Circular dichroism study of ribonuclease A mutants containing the minimal structural requirements for dimerization and swapping.pdf*>*.* 1998.
42. Joao, H.C.a.D., R .A, *Effects of glycosylation on protein structure and dynamics in ribonuclease B and some of its individual glycoforms.* European Journal of Biochemistry, 1993. **218**(1): p. 239-244.
43. Gotte, G., M. Libonati, and D.V. Laurents, *Glycosylation and specific deamidation of ribonuclease B affect the formation of three-dimensional domain-swapped oligomers.* J Biol Chem, 2003. **278**(47): p. 46241-51.

Chapter 5: Synthesis of Glycoprotein Molecular Imprints

Abstract: *This chapter details the synthesis and development of a molecular imprint that is specific and selective for the glycoprotein, RNase B. Herein, we explore the parameters that can affect the success of achieving an imprint using this system that includes examining the thickness and ratio of boronic acid used within the polymer with respect to RNase B.*

We first examine the effect of optimising the pH of the polymerisation solution developed in Chapter 3 on the poly(MEBA) thickness. We then explore imprinting the RNase B complex developed in Chapter 4 using this newly optimised system.

In the imprinting studies, we first examine the effect of the polymer thicknesses on the selectivity and specificity of three different MIP systems for the RNase B target using SPR. The response of these systems to RNase B alongside its non-glycosylated homologue and two other non-homologous control proteins is reported, as well as the binding responses of their respective NIP controls.

The MIP with the optimal thickness was then taken forward to examine the effect of varying the ratio of boronic acid monomer within the imprints on the imprinting response. To coincide with these SPR studies we also report the surface characterisation of these imprinted surfaces using contact angle, ellipsometry, AFM and XPS.

Finally, the chapter concludes with discussing the overall outcomes of the imprinting studies and the future work that could be undertaken to further develop this imprinting system in order to provide the ideal platform to imprint other proteins.

1.0 Development of the Polymerisation Protocol for Imprinting

The overall aim of this chapter is to synthesise a molecular imprint that is selective for RNase B. As outlined in the strategy presented at the end of in Chapter 1, we aim to achieve good specificity for this target glycoprotein by using a 3-dimensional display of boronic acids within the imprinted polymer's design. In Chapter 3, we first demonstrated the controlled growth of the poly(MEBA) surfaces from the 11-DMTBD SAMs to the desired thickness of 8.1 ± 0.8 nm. The next stage of the project's strategy is to therefore bring together this platform

alongside the learning outcomes from the ESI-MS RNase B-boronic acid complexation studies in Chapter 4 to create a glycoprotein imprinting platform with a 3-dimensional display. The ideal imprint will show a high affinity and selectivity for RNase B whilst demonstrating minimal binding to other control proteins, such as its non-glycosylated homologue RNase A, and other glycosylated proteins.

As discussed in Chapter 1, during the duration of this thesis a number of glycoprotein imprinting systems have been published. These systems have used boronic acid to target the glycans of glycoproteins to facilitate imprint formation. However, these protocols only use the glycan-boronate interactions to immobilise the glycoprotein or free glycan upon a 2-dimensional (2-D) surface which is then polymerised around to create the imprinting sites [1-5]. These methods show that glycoprotein selective imprints are possible. However, they only use the boronic acids in a 2-D, planar arrangement across the exposed face of the substrate surfaces and therefore limit the boronic acids to only interacting with the sugars of the glycan in one plane. The disadvantages of these methods is that only a small number of the *cis* diol binding sites of the glycan(s) can be bound and therefore a significant number of diol binding sites could still be targeted. Our method therefore aims to synthesise an imprint that enables multiple boronic acids to bind the sugars of the glycan so that when imprinted these functional monomers reside within a 3-dimensional display within the receptor site that is spatially and functionally compatible with the glycoprotein, as shown in figure 5.1.

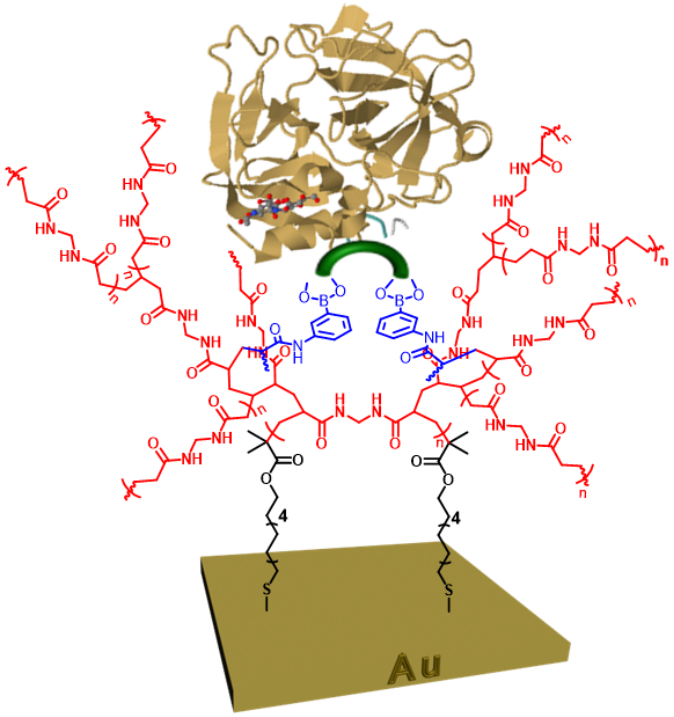

Figure 5.1: Schematic diagram of the proposed glycoprotein molecular imprints. The boronic acid monomers are arranged within a 3-dimensional display within the imprinting sites that enables the specificity and selectivity for the target to be achieved.

To our knowledge, there have been no reports of glycoprotein imprinting systems that are designed in this way. Furthermore, the majority of the aforementioned imprinting systems are reported for nanoparticles, whereas our system is developed to be used on an SPR chip. The protocol designed to synthesise the imprints is outlined in figure 5.2.

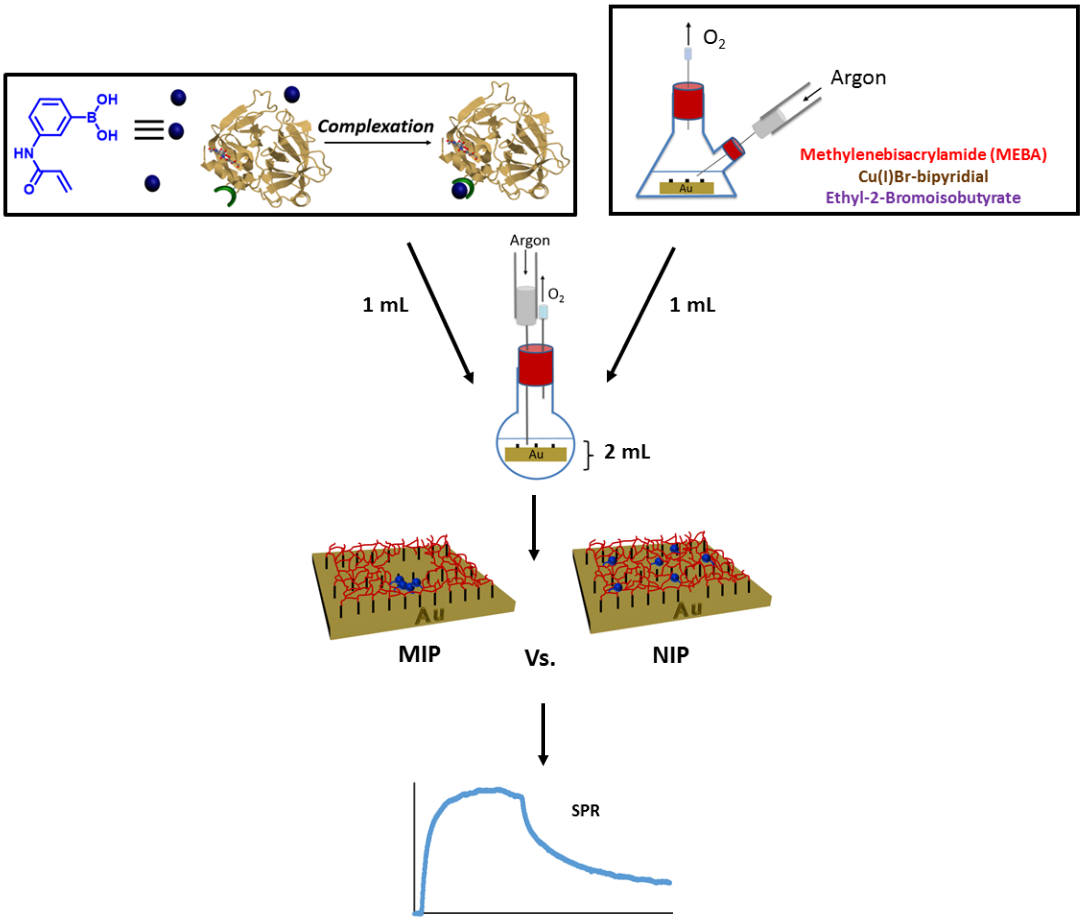

Figure 5.2: Schematic diagram of the imprinting protocol. For each imprint 1 mL of the complexation solution is mixed with 1 mL of the polymerisation solution and the polymerisation is then triggered by the addition of the sacrificial initiator, E-2-BB.

As the schematic shows, the protocol is a simple setup that brings together a) 1 mL of the glycoprotein complexation solution with b) 1 mL of the polymerisation solution (within which the 11-DTMBD SAM was already submerged) to form c) 2 mL of the imprinting solution. Following incubation, the polymerisation is then triggered using an injection of E-2-BB to produce the imprints of the RNase B protein within the polymer matrix. These imprints are then tested using SPR for their sensitivity and selectivity towards their RNase B target.

2.0 Objectives

1 Further optimise the polymerisation system developed in chapter 3 for imprinting by raising the pH to 8.6 using tertiary amines as a base.

2 Characterise the resultant pH optimised poly(MEBA) surfaces with contact angle, ellipsometry and XPS.

3 Take forward this polymerisation system and investigate its imprinting capabilities using RNase B by:

   a. First characterising each imprint with contact angle, ellipsometry, XPS and AFM

   b. Elucidate the RNase B rebinding capabilities for each imprint with SPR to ascertain the optimal imprinting thickness

4 Further optimise the most viable imprinting system by examining the ratio of boronic acid monomer within the imprints by SPR.

2.1 Optimisation of the poly(MEBA) Polymerisation Protocol pH

As aforementioned in Chapter 4, the pH of the complexation solution must reside above the boronic acid monomer's pKa of 8.2 in order to maintain its tetrahedral complexation with the RNase B protein. Furthermore, as evidenced from the mass spectrometry results the RNase B-boronic acid monomer complex also requires a 25 % (v/v) portion of MeOH to enable the monomer to bind the 1-2 or 1-3 *cis* diols of the proteins' glycan chain and the absence of MeOH results in a failure of the 2 species to covalently bind.

When adapting our polymerisation scheme to be compatible with these limitations it was therefore imperative to first ensure that the native pH of the polymerisation solution matched these requirements as well as confirm that the addition of the MeOH solvent does not alter the reaction to adversely change the thickness of the polymer layer. Upon examination the native pH of the polymerisation solution was measured as 6.9 and so a suitable base was therefore required to raise the pH to 8.6. However, the addition of large quantities of conventional bases such as potassium or sodium hydroxide to ATRP systems have been reported to have detrimental effects on reaction kinetics [6]. This is due to the excess OH^- ions generated from the bases causing disproportionation of the $[X\text{-}Cu^{II}L_m]$ deactivating species to generate a new complex $[Cu^{II}L_m(OH)]$ [6]. The OH^- ion in this new copper complex is a much stronger ligand than H_2O molecules of the solvent or dissociated halide ions (X^-) and the result is loss of control of the K_{act} and K_{deact}. To therefore prevent catalytic interference we chose to use tetraethyl ethylenediamine (TEEN) as the base with which to increase the polymerisation solution as this tertiary amine has been shown to not interfere with the coordination sphere of copper catalytic complexes [7]. To coincide with these conditions, the pH of the RNase B-boronic acid monomer complexation solution to be used in the imprinting was likewise adjusted to 8.6 using TEEN.

Following these pH adjustments polymerisations were then undertaken using the protocol shown in figure 5.3 and the resultant thicknesses and contact angles of the surfaces measured over time. As the purpose of these studies was to elucidate the poly(MEBA) thicknesses from these pH optimised conditions that can then be used as a reference for the thicknesses of the later imprinting

studies, neither the boronic acid monomer nor RNase B were included within the solutions.

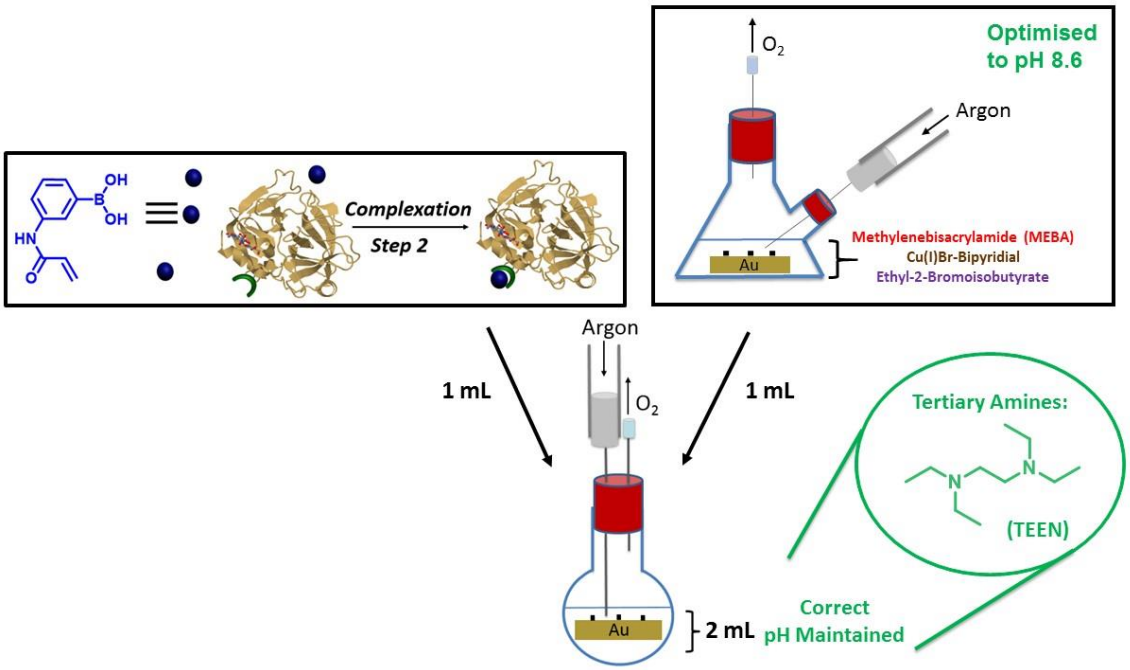

Figure 5.3: Schematic diagram of the imprinting protocol. For each imprint 1 mL of the complexation solution is mixed with 1 mL of the polymerisation solution and the polymerisation is then triggered by the addition of the sacrificial initiator, E-2-BB.

2.1.1 Contact Angle and Ellipsometry of the pH Optimised poly(MEBA) Surface

The contact angle and ellipsometry results of the pH optimised polymerisations are shown in figure 5.4. The poly(MEBA) surface thickness increases over time as expected before plateauing to show no further increase from 30 minutes incubation onwards. The 11-DTMBD initiator SAMs at T=0 report a thickness of 1.7 ± 0.1 nm which then increases to 2.6 ± 0.2 nm, 3.2 ± 0.4 nm, and 4.5 ± 0.4 nm with 5, 10 and 20 minutes polymerisation, respectively. This increase corresponds to the growth of the poly(MEBA) layer from the SAM surface and proves that the polymerisation under these new conditions is still viable.

Furthermore, the respective advancing and receding angles sequentially decrease over time with the continued formation of the poly(MEBA) layer. For example, the advancing contact angle decreases from 73.3 ± 0.6 ° from the initiator SAM at T=0, to 68.2 ± 3.1 °, 44.5 ° ± 5.7 ° and 34.0 ± 3.1 ° for the 5, 10 and 20 minute poly(MEBA) surfaces, respectively. These decreases are due to the highly hydrophilic poly(MEBA) layer hydrogen bonding with the water droplet through their N-H and C=O moieties. Overall, the sequential decreases observed in the contact angle values correlates with the increase in thickness over time due to the formation of the poly(MEBA) layer.

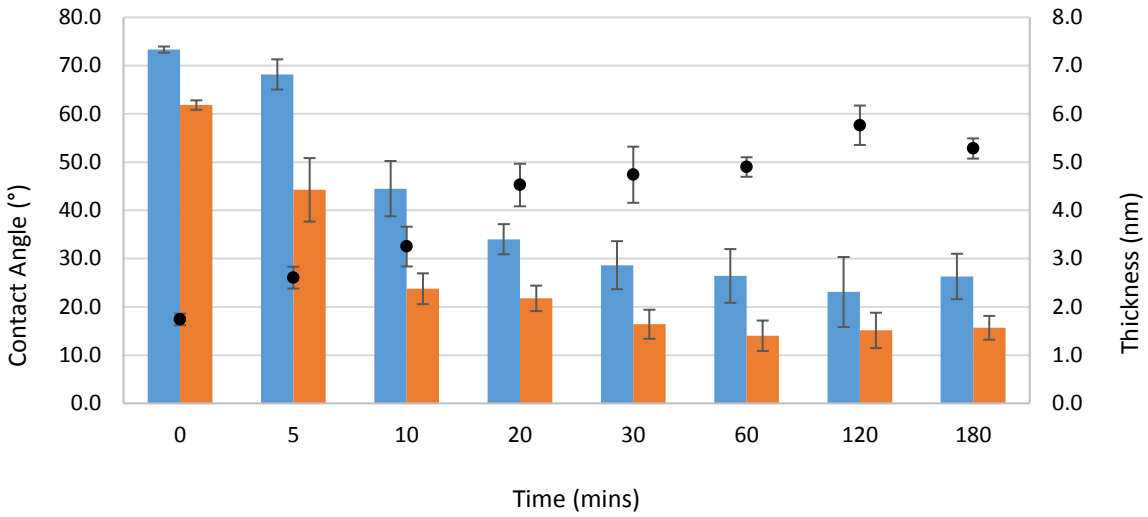

Figure 5.4: Reports the changes in thickness and advancing and receding contact angle values of the poly(MEBA) surface synthesised at pH 8.6 over time.

Following these initial increases observed in the polymer thickness in the first 20 minutes, the polymer growth then plateaus despite further incubation within the reaction solution. Moreover, the thicknesses for the 30, 60, 120 and 180 minute incubations were reported as 4.7 ± 0.6 nm, 4.9 ± 0.2 nm, 5.8 ± 0.4 nm and 5.3 ± 0.1 nm, respectively. Likewise, the advancing contact angles for the 30, 60, 120 and 180 minute incubations remains stable between 28.6 ± 5.0 ° and 23.1 ± 7.2 °

as the surface shows no further change. In summary, the polymer shows growth of a few nm within the first 30 minutes of incubation, following which no further growth is observed.

If we compare the resultant thickness of 4.7 ± 0.6 nm from 30 mins incubation from this pH 8.6 study to the previous thickness obtained at a pH of 6.9 of 8.1 ± 0.8 nm in Chapter 3, we observe that the new conditions produce a thinner poly(MEBA) layer. This difference is likely due to earlier termination of the polymer chains from radical combination of the polymer surface [8]. However, this effect cannot be solely attributed to the higher pH employed as both the solvation conditions (due to the addition of salts and MeOH) and the pH were adjusted.

Nevertheless, the thickness observed with these pH adjusted conditions is still within the appropriate range (between 5-10 nm) to attempt RNase B imprints as the protein's dimensions (3.8 x 2.8 x 2.2 nm) are still compatible with this thickness. This polymerisation protocol was therefore used as the foundation to synthesise both imprinted (MIP) and non-imprinted (NIP) surfaces, with the thicknesses observed in figure 5.4 acting as a guide for these studies. However, before proceeding with the imprinting the poly(MEBA) surface was also characterised using XPS to further confirm the formation of this non-imprinted (NIP) polymer layer by observing the resultant chemical environments.

2.1.2 XPS of the pH Optimised poly(MEBA) Surface

The XPS survey scan of the poly(MEBA) surface revealed the presence of Au, C, S, O, N and Br elemental species, as expected. The high resolution scans as

shown in figure 5.5 then further confirmed the synthesis of the polymer by the presence of the appropriate chemical environments for the C (1s), S (2p), O (1s), N (1s) and Br (3p) elements.

Firstly, the S (2p) spectra (figure 5.5, b) shows one chemical environment consisting of two doublets that corresponds to the bound and unbound S $2p_{3/2}$ and S $2p_{1/2}$ orbitals from the underlying thiols of the SAM at 161.8 eV, 162.9 eV, 163.6 eV and 164.8 eV, respectively. Deconvolution of the C (1s) spectra (figure 5.5, c) then shows four carbon environments for the polymer, as expected. The first is a sharp, singlet at 285.4 eV corresponding to the C-C of the alkanethiols of the SAM and the polymer layer. The second environment is found at a binding energy close to the C-C energy at 285.3 eV that corresponds with the C-Br environments of the terminal groups of the polymer chains and from the sacrificial initiator (S.I) species, ethyl-2-bromoisobutyrate (E-2-BB), used to trigger the polymerisation. The presence of Br is also confirmed in the Br (3d) (figure 5.5, f) scans that report peaks for the Br $3d_{5/2}$ and Br $3d_{3/2}$ binding energies, respectively. Furthermore, the B (1s) (figure 5.5, g) region overlaps with the Br (3p) region and hence shows peaks for the Br $3p_{3/2}$ and Br $3p_{1/2}$ energies, respectively. It should be reiterate that in this case no boron is present within the sample, however the purpose of including this scan is to later aid the reader in identifying boron within other samples. Overall, the presence of Br on the surface is collectively confirmed from the C (1s), Br (3d) and B (1s) high resolution spectra. However, as two bromide species (i.e. the initiator SAM and E-2-BB sacrificial initiator) were present in the polymerisation reaction we cannot accurately quantify the percentage of Br present.

The third C (1s) environment is found at a binding energy of 287.2 eV consistent with the C-O of the underlying initiator molecules. Finally, the fourth C (1s) environment found at the highest binding energy of 288.7 eV corresponds with the C=O moieties from both the ketone groups of both the ester bonds of the underlying initiators and the polymerised MEBA. Similar to the two environments observed in the C (1s) scans, the O (1s) spectra likewise reports two oxygen environments deconvoluted from a broad peak to show the C=O and C-O moieties at 532.0 eV and 532.6 eV, respectively. The C=O area is much larger than the C-O environment due to the large number of amide moieties from the MEBA polymers. As is typical for polymer structures, the C=O environment is found at a lower binding energy than the C-O unlike the arrangement observed for the 11-DTMBD SAMs. This phenomena is a common feature of pure polymers as observed in the database by Beamson and Briggs [9]. Finally, the N (1s) high resolution scan shows a sharp peak at 400.2 eV corresponding to the N-H moieties of the MEBA molecules. Quantification of the C=O to N-H moieties reported a 1.3:1 ratio which in in line with the expected ratio of 1:1.

In summary, the XPS spectra the poly(MEBA) surface from the pH optimised protocol shows the presence of all expected chemical environments to indicate successful polymerisation from the 11-DTMBD initiator SAM. Of note, the appearance of the N (1s) peak, alongside the increases observed for the C=O environment in both the C (1s) and O (1s) scans confirms the addition of the MEBA monomers to the surface.

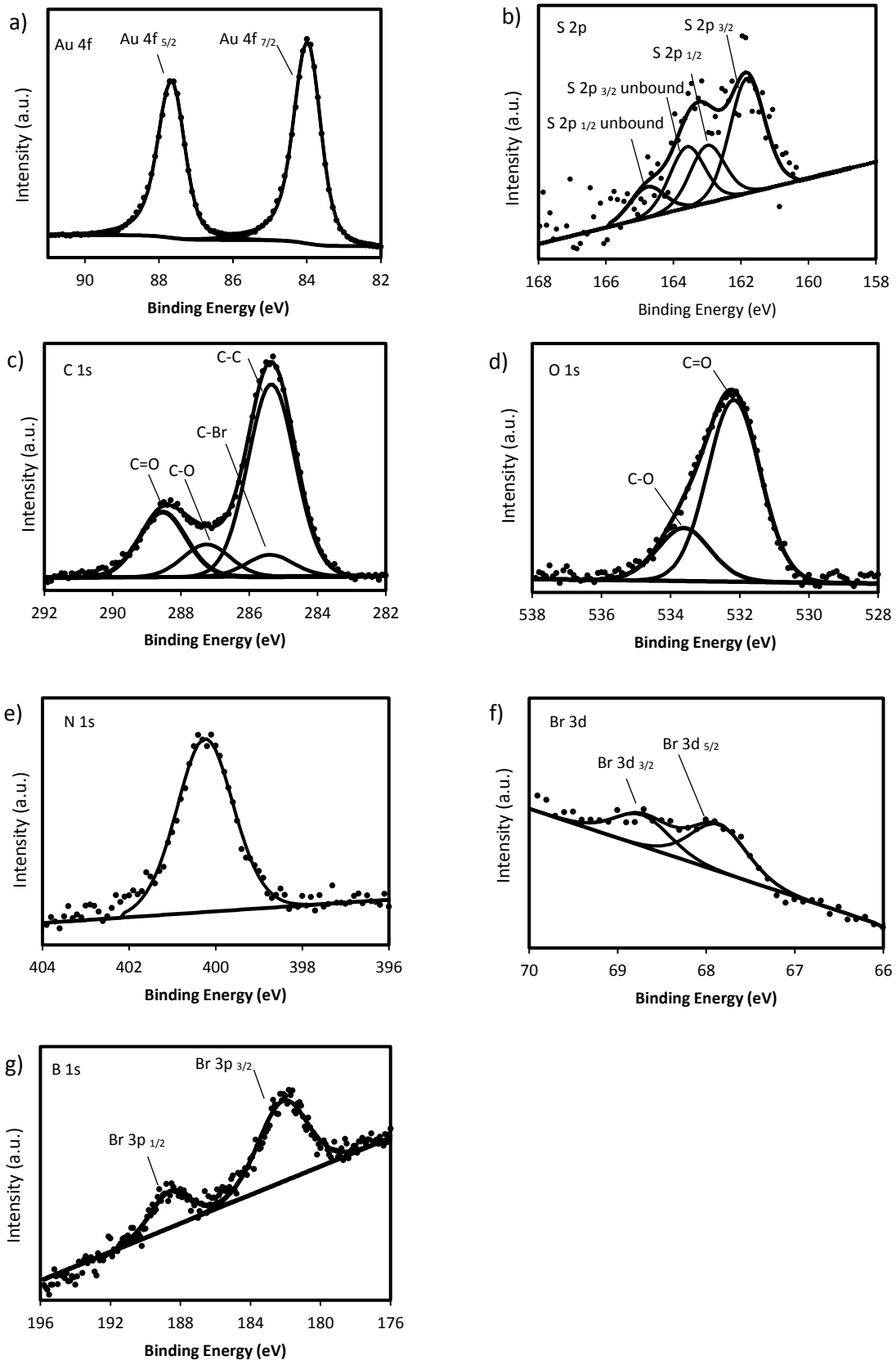

Figure 5.5. High resolution XPS spectra of a) Au 4f, b) S 2p, c) C 1s, d) O 1s, e) N 1s f) Br 3d and g) Br 3p peaks of the poly(MEBA) surface.

3.0 Imprinting of the RNase B Glycoprotein

Following the successful characterisation of the poly(MEBA) surface, imprints within this matrix for the RNase B glycoprotein were then undertaken. The imprints were formed using the aforementioned protocol in figure 5.6, however in all cases 3-acrylamidophenyl boronic acid monomer was included within the polymerisation system to form poly(MEBA-co-BA) surfaces. Surfaces where the RNase B glycoprotein was included within the system as the template molecule are referred to as MIPs (figure 5.6, a), whereas those without protein are non-imprinted as hence referred to as NIPs (figure 5.6, b).

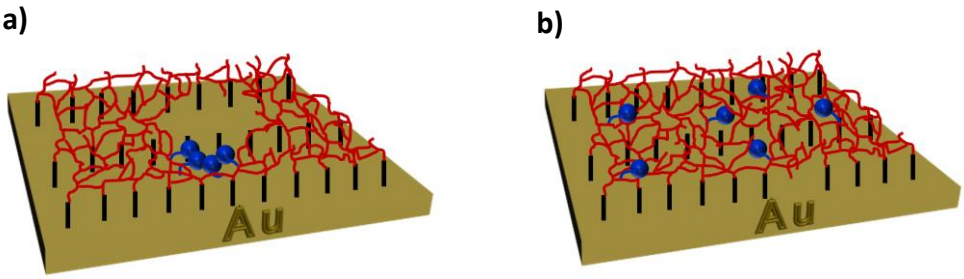

Figure 5.6: Basic schematic representation of a MIP (a) and NIP (b) poly(MEBA) surface.

Following earlier work undertaken by our group, a 10 % proportion of boronic acid monomer was selected (with respect to 90 % MEBA) for the first set of imprints, for which the proportion of RNase B was then calculated to give a ratio of 10:1 boronic acid monomer:RNase B [10]. Three imprinting polymerisation times of 10, 20 and 60 minutes were undertaken to examine whether the specificity and selectivity of the surfaces were affected by the surface thickness. Once synthesised each MIP (and NIP control) was extensively washed with an acidic solution and then water to remove any bound protein from the surface. The MIPs and NIPs were first characterised using ellipsometry, contact angle,

AFM and XPS, following which the SPR binding responses to a range of glycosylated and non-glycosylated proteins were then examined.

3.1 Ellipsometry and Contact Angle of the Poly(MEBA-co-BA) MIPs and NIPs

Figure 5.7 reports the contact angle and ellipsometry results for the three poly(MEBA-co-BA) MIP and NIP polymerisation times. The 10 minute MIPs and NIPs were selected for the first imprinting attempts as from the pH optimised study this polymerisation time resulted in a thin poly(MEBA) NIP of 3.2 ± 0.4 nm.

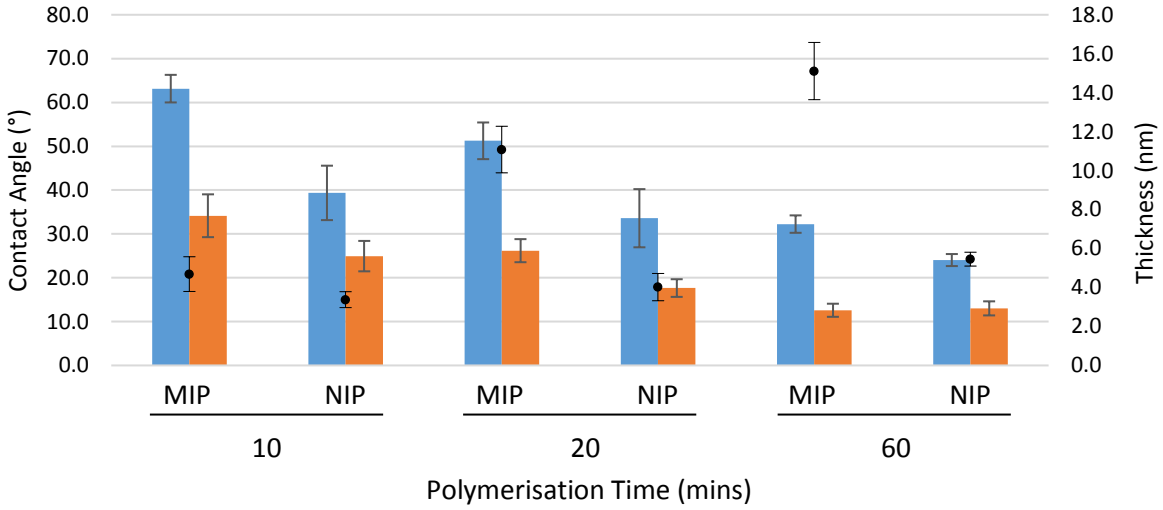

Figure 5.7: Shows the changes in thickness (black circles) as well as the advancing (blue) and receding (red) contact angles for the poly(MEBA-co-BA) MIPs and NIPs (n=3).

Firstly, the 10 minute poly(MEBA-co-BA) NIPs reported a thickness of 3.4 ± 0.4 nm which is in agreement with the 10 minute poly(MEBA) NIP thickness. Furthermore, the 10 minute NIPs also reported advancing and receding contact angles of 39.4 ± 6.2 °and 24.9 ± 3.5 °, respectively, which are likewise in agreement with the 44.5 ± 5.7 °and 23.9 ± 3.2 ° angles previously observed for

the 10 minute poly(MEBA) NIPs. However, when compared to the respective NIP controls, the 10 minute poly(MEBA-co-BA) MIPs showed a distinct difference in both their thickness and contact angle values.

Firstly, the MIPs advancing and receding angles were higher at 63.1 ± 3.1 ° and 34.2 ± 4.5 °, respectively. These values are closer to the values observed for the underlying initiator SAM of 73.3 ± 0.6 ° and 61.8 ± 1.0 °. One would first assume that this indicates that less polymerisation of the surface has occurred, as addition of the highly hydrophilic MEBA polymer to the NIP surfaces has previously shown to decrease both contact angles. However, the ellipsometry measurements reported an increase in the MIP thickness to 4.7 ± 0.9 nm to indicate that the surface has indeed polymerised. Moreover, the MIPs are 1.3 nm thicker than their NIP controls which was surprising considering the aforementioned contact angle values. These characteristic differences indicated that the addition of the protein is enabling the formation of two distinctly different surfaces.

If we then compare the 10 minute MIPs and NIPs to the 20 minute poly(MEBA-co-BA) MIPs and NIPs, both of these surfaces again polymerised as expected. The NIPs reported a thickness of 4.0 ± 0.7 nm that is in agreement with the value of 4.5 ± 0.4 nm of the previous 20 minute poly(MEBA) NIPs. However, the poly(MEBA-co-BA) MIPs once again reported a greater thickness of 11.1 ± 1.2 nm. Furthermore, the MIPs advancing and receding contact angles were 51.2 ± 4.2 ° and 26.2 ± 2.6 °, respectively, which are once again higher than the 33.6 ± 6.6 ° and 17.7 ± 2.0 ° of their NIP control. This again reiterates that the presence of the template protein is affecting the characteristics of the resultant polymer

layer by increasing the rate of the propagation of the polymer chains to produce thicker poly(MEBA-co-BA) layers.

Finally, examination of the 60 minute poly(MEBA-co-BA) MIPs and NIPs reported thicknesses of 15.1 ± 1.5 nm and 5.5 ± 0.4 nm, respectively, once again showing that the MIPs are thicker than their control. Similarly, the MIPs reported higher advancing and receding angles of 32.2 ± 2.0 ° and 12.6 ± 1.5 °, respectively, than the 24.0 ± 1.4 ° and 13.0 ± 1.6 ° of their NIP control.

Collectively, this data consistently shows that the MIPs show greater thicknesses with much higher deviation in the thickness than their respective NIPs. This effect is due to the protein template causing a decrease in the segmental mobility of the monomers (i.e. the monomers movement within solution is more inhibited than in the non-imprinted solution due to being associated with the protein), which subsequently acts to catalyse the reaction and has previously been observed in the literature [11, 12]. Moreover, all the MIPs reported higher advancing contact angles than those observed for their NIP controls despite their greater average thickness. This difference between the MIPs and NIPs advancing and receding contact angles highlights that there must be topographical differences between the two surfaces. These differences directly relate to the hysteresis value, which is simply the difference between the advancing and receding angles ($H = \theta_{adv} – \theta_{rec}$).

Smooth, homogenous surfaces will measure advancing and receding angles that are closer in value to one another to report smaller hysteresis values. However, heterogeneous surfaces can have large differences in their local roughness, as well as differences in their chemical and spatial heterogeneity. This consequently

produces large differences between their advancing and receding angles, which in turn produces higher hysteresis values.

In this case, large hysteresis values of 28.9 °, 25.0 ° and 19.6 ° are observed for the 10, 20 and 60 minute MIPs, respectively, which are greater than the 15.5 °, 15.9 ° and 11.0 ° values observed for the respective NIP controls. Furthermore, the higher advancing angles observed for the MIPs in comparison with their NIP controls indicates that due to this heterogeneity the wettability of the surfaces is hindered by trying to overcome local energy barriers of the imprinted surface.

These results collectively show that the presence of the template proteins during MIP synthesis produces less homogenous surfaces due to the impressions of the protein formed within the polymer matrices. Their varied nanotopography can therefore induce hydrophobicity within the surfaces to cause the increases observed in their contact angles [13].

In order to further understand these topographical differences between each poly(MEBA-co-BA) MIP and NIP surfaces AFM was employed to examine the surfaces topographies and roughness in detail.

3.2 Tapping Mode AFM of the Poly(MEBA-co-BA) MIPs and NIPs

The results of the tapping mode AFM studies are shown in figure 5.8, which depict examples of the 3D images for the 10 mins (a), 20 mins (b) and 60 mins (c) NIPs and MIPs, respectively. Firstly, examination of the 3D surface profiles reveals that all three NIPs are consistently smooth and show homogenous polymerisation from the initiator SAM surface. The polymers are uniform with no unexpected structures present within the matrices. In contrast, the

nanotopographies of the MIPs are significantly different in comparison with their respective NIPs. All MIPs have a complex and heterogeneous nanostructure, which is vastly different from the smooth and homogenously polymerised NIPs.

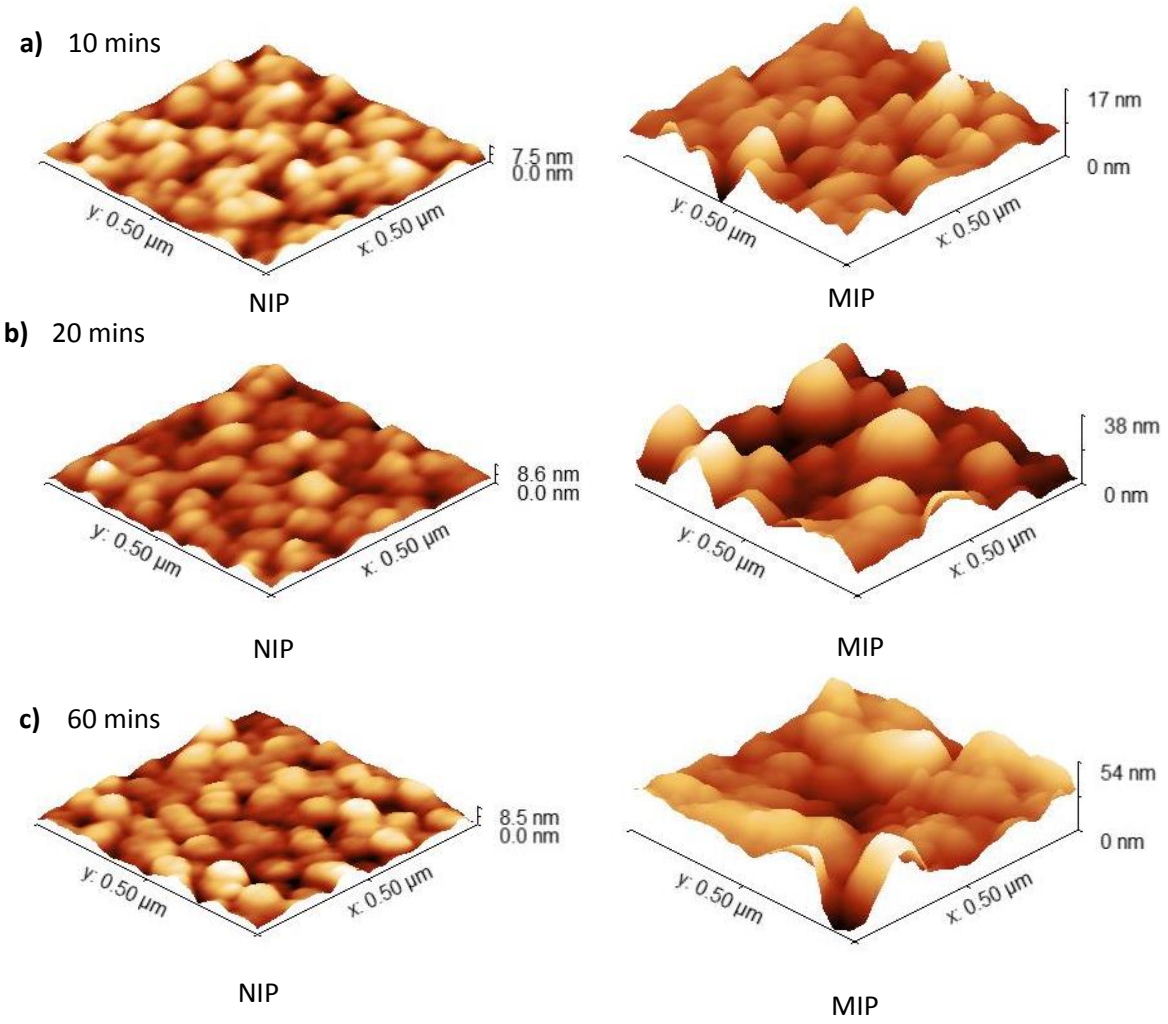

Figure 5.8: Examples of the 3D AFM images (0.5µm^2) that visualise the topography of the poly(MEBA-co-BA) NIPs (left) and MIPs (right) incubated in the polymerisation solutions for either 10 mins (a), 20 mins (b) or 60 mins (c). It should be noted that the *z* heights shown on the 3D projections are only representative of the maximum *z* height of a single pixel of the image and are not thickness values for the surfaces.

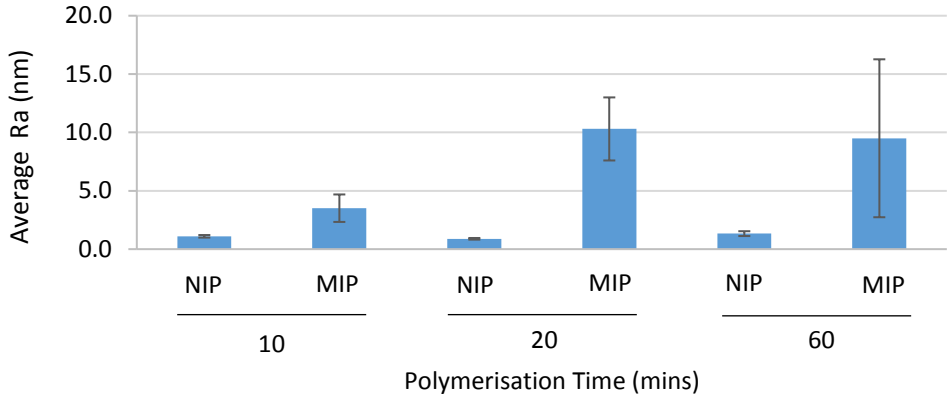

Figure 5.9: Reports the average Ra roughness of the 10, 20 and 60 minute polymerised NIPs and MIPs (n=9).

Furthermore, these nanotopographical differences in the MIP and NIP surfaces correspond with significant differences in the average Ra roughness of their surface profiles. As shown in figure 5.9, the 10 min, 20 min and 60 min NIPs are consistently smooth with only minor variation in their average roughness of 1.1 ± 0.1 nm, 0.9 ± 0.1 nm and 1.7 ± 0.2 nm, respectively. In contrast, the MIPs sequentially show large increases in their average roughness with increasingly large variation from 3.5 ± 1.2 nm, to 10.3 ± 2.7 nm and 9.5 ± 6.8 nm for the 10 mins, 20 mins and 60 mins incubations, respectively.

In summary, the AFM results reveal that the NIP and MIP surfaces show distinct differences in their nanotopographies and roughness. The NIPs are homogenous in their polymerisation which produces smooth and uniform polymer layers, whereas the presence of the protein in the MIP polymerisation solutions produces increasingly rough and heterogeneous surfaces. Collectively, these differences explain the increased hydrophobicity previously observed in the contact angle studies of the MIPs. It is well known that nanotopographical differences in materials can induce superhydrophobicity in surfaces and in this

case the heterogeneity of the MIPs is responsible for the increases in their contact angles [13, 14]. Moreover, the sequential increase in the Ra roughness's and the variation of these values for the MIPs explains the increases in the variation of the thickness values previously measured by ellipsometry. Following the AFM analysis, XPS of the MIP and NIP surfaces were also undertaken to examine if differences in the elemental composition of the two were evident.

4.0 XPS of the Poly(MEBA-co-BA) MIPs and NIPs

The XPS analysis of the poly(MEBA-co-BA) MIP and NIP surfaces likewise identified distinct differences between each of the surface types. To provide a succinct overview for the reader, the 60 minute surveys are shown in figure 5.10 whilst the 20 minute scans can be found in the appendix. Due to the poor SPR results obtained from the 10 minute polymerisations as discussed later, these surfaces were not analysed with XPS.

The wide scans firstly identified that the binding energies, notably of the Au peaks, from the MIPs are attenuated by the background due to the thickness of the polymer. XPS relies on the escape of electrons from the sample surface and in this case the 60 minutes MIPs are thicker than the 10 nm (3λ inelastic mean free path) ideal analysis depth. This results in the electrons buried deep within the polymer layer failing to escape to subsequently produce the curved shapes and steep rise in the wide scan backgrounds (figure 5.10, a). On the other hand, the NIPs (figure 5.10, b) show wide scans typical of surfaces with limited attenuation as their backgrounds are flatter and the Au peaks more apparent. This is because their thicknesses are lower than the 3λ inelastic mean free path

limit and so their electrons are not impeded from escaping from within the polymer.

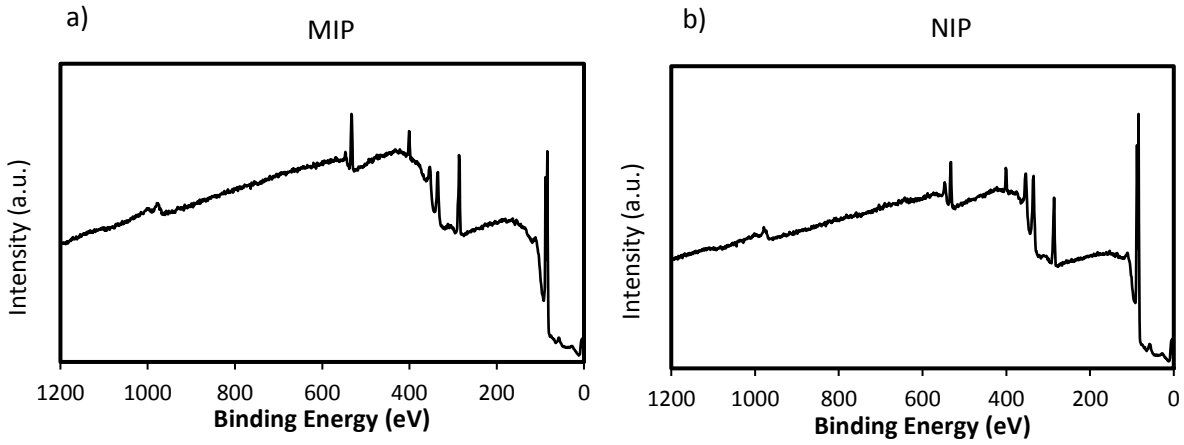

Figure 5.10: Wide scans of the XPS Binding energies of the 60 minute (a) MIP and NIP surfaces.

The high resolution scans for the MIPs and NIPs then further identified the presence of all the expected elements and their environments for both surfaces.

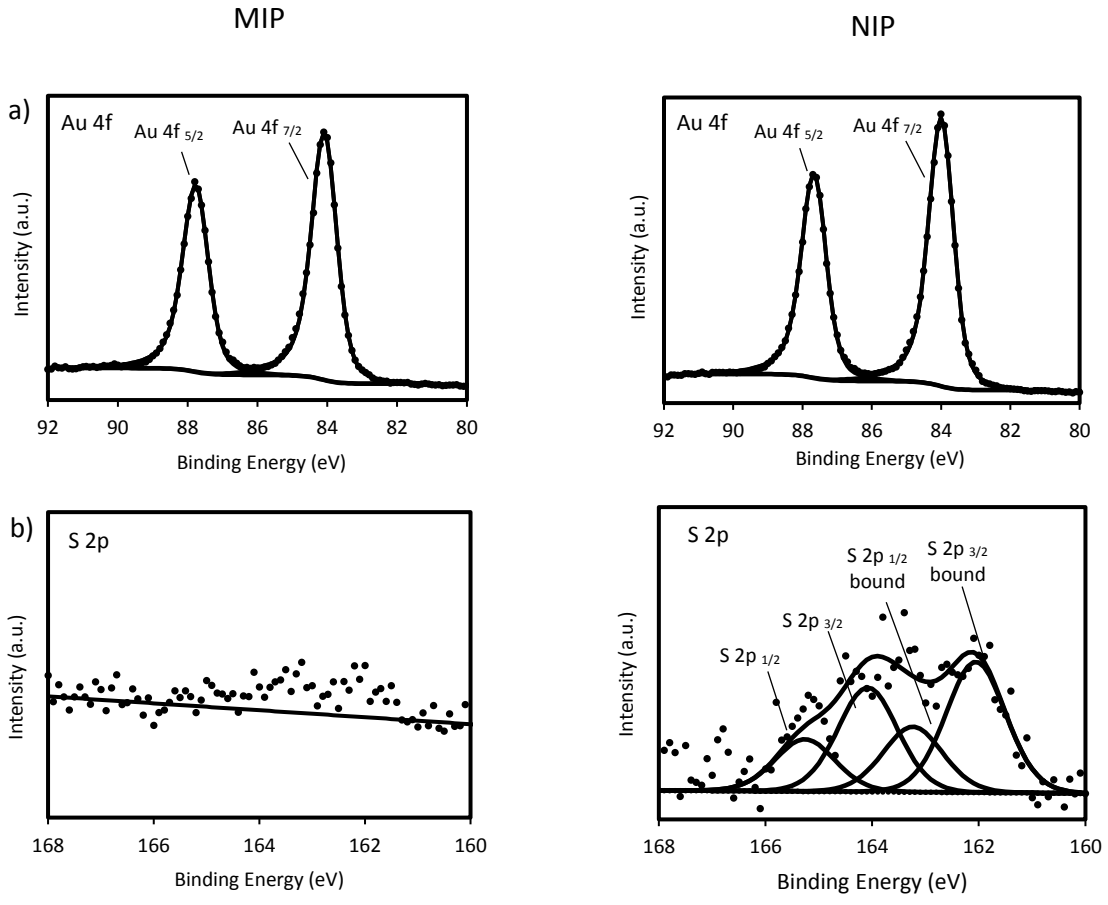

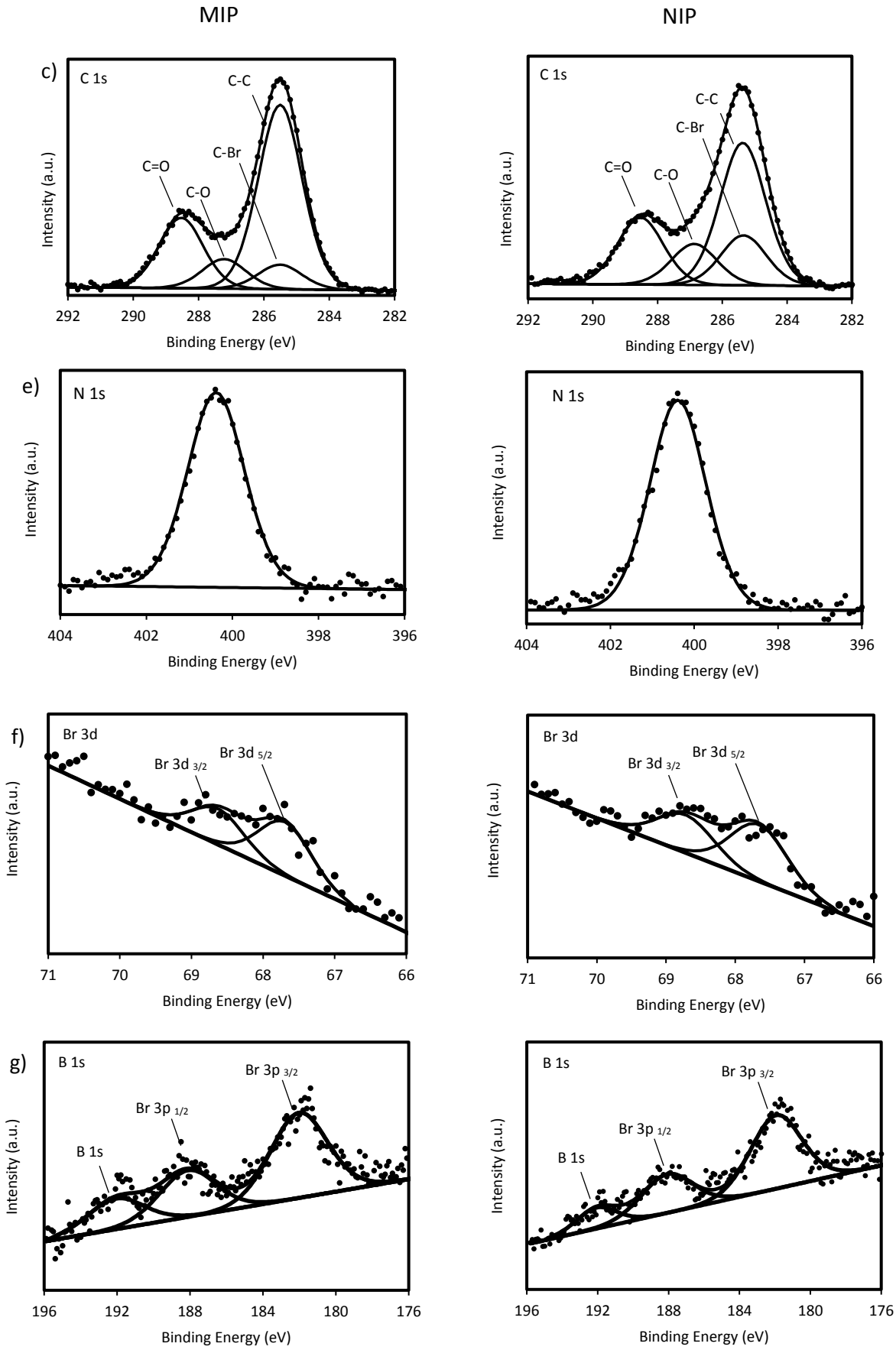

Figure 5.11. High resolution scans of the 60 minute MIP (left) and NIP (right) of a) Au 4f, b) S 2p, c) C 1s, d) O 1s, e) N 1s, f) Br 3d and g) B 1s and Br 3p.

Comparison of the high resolution scans firstly show the attenuation of the S (2p) signal from the MIP surface (figure 5.11, b), whereas the thiol peaks from the underlying SAM are clearly visible from the thinner, NIP surface. This is in agreement with the wide scans that likewise reported the attenuation of the binging energies from the thicker MIP surface. Comparison of the two C (1s) spectra (figure 5.11, c) then show that both surfaces report all four C-C, C-Br, C-O and C=O environments in line with the poly(MEBA) NIPs previously shown.

Both surfaces also show the appropriate signals for their O (1s) scans. Deconvolution of the O (1s) scans reveal the presence of both the C=O and C-O environments. As was observed with the aforementioned poly(MEBA) O (1s) scans, the C=O peaks are both found at a lower energy as they arise from the amide groups of the ester of the underlying initiator as well as from MEBA and 3-acrylamidophenyl boronic acid monomers. Next, both N (1s) scans report a singlet from the collective N-H of the MEBA and 3-acrylamidoboronic acid monomer residues. The contributions to the N-H environments from the amide bonds of the 3-acrylamidophenyl boronic acid monomers reside at the same binding energy as the N-H of the MEBA monomers. Therefore their contributions to this area cannot be distinguished from one another and so cannot be quantified. Similarly the amount of Br cannot also not be quantified as it arises from the two initiator SAM and E-2-BB sources, however as was previously observed in the poly(MEBA) polymers, both the MIP and NIP Br (3d) scans (figure 5.11, f) show a doublet for the Br $3d_{5/2}$ and Br $3d_{3/2}$ binding energies.

Finally, before discussing the B (1s) scans it is important to first note that boron is well known for being a difficult element to detect by XPS analysis as it requires a very low pass energy and several hundred repeat scans to visualise. In this

case, the inclusion of 10 % boronic acid monomer within the polymerisation solution may not directly translate to the same percentage within the total amount of the polymer found on the surfaces. Here, both the MIP and NIP B (1s) scans report peaks at ~192.2 eV to indicate the presence of boron within the polymers arising from the 3-acrylamidophenyl boronic acid monomer. However, the amount of boron present cannot be quantified as the B (1s) peaks are found next to the peaks for the Br ($3p_{3/2}$) and Br ($3p_{1/2}$) binding energies. As the Br ($3p_{1/2}$) peaks overlap with the B (1s) peaks this does not allow for accurate quantification of the boron areas. For this reason the boron peaks can only be taken qualitatively, but nonetheless the absence of a boron peak in the aforementioned poly(MEBA) scans at 192.2 eV provides evidence of the presence of boron within these samples. In summary, both the MIP and NIP surfaces show the expected XPS high resolution spectra to indicate that both surfaces polymerised as expected.

5.0 Conclusions from the MIP and NIP Surface Characterisations

In conclusion, we have shown from the thorough characterisation of each polymerised surface with a number of techniques that there are distinct differences in the thickness and structural topographies of the MIP surfaces in comparison with their respective NIPs. As evidenced by the ellipsometry and AFM studies, the presence of the protein template during polymerisation causes the MIP surfaces to be thicker and rougher than their NIP controls. Previous studies have shown that the presence of proteins within imprinting studies can cause an increase the reaction kinetics resulting in larger polymer thicknesses

therefore this phenomenon is not novel [11, 12]. The increased MIP thicknesses also resulted in the attenuation of their XPS signals due to the inhibition of electron escape from the surfaces. The NIPs in comparison are thinner and smoother and show limited attenuation of their XPS signals.

These differences arise from the inclusion of the RNase B protein within the MIP polymerisation inducing heterogeneity of the surface structure which provides evidence for the formation of the imprinting sites within the matrix. The following section will therefore examine the binding of a range of proteins to these surfaces to determine if imprints within the MIPs that show selectivity for RNase B have indeed been formed.

6.0 SPR Results of the MIPs and NIPs

Each poly(MEBA-co-BA) MIP and NIP was tested for its selectivity in binding the RNase B target as well as a range of protein controls using SPR. Briefly, each protein was injected across the surfaces at a range of concentrations and the responses at $R_{equilibrium}$ measured. Following each injection the surface was regenerated by an acidic wash to remove the protein. The range of protein controls included the non-glycosylated homologue of RNase B, RNase A, as well as two other glycosylated proteins - α1-acid glycoprotein and horse-radish peroxidase (HRP). The characteristics of each of these proteins are shown in table 5.2. The table illustrates that these proteins show a range of sizes, charges and percentage glycosylation to give a representative selection of different qualities that can contribute to the binding response.

Table 5.1: Characteristics of each of the proteins tested with SPR

Protein	RNase B	RNase A	α1-acid glycoprotein	HRP
Molecular Weight (g/mol)	14,700	13,700	44,000	44,000
Glycosylation (%)	9	0	45	21
Dimensions	3.8 x 2.8 x 2.2	3.8 x 2.8 x 2.2	5.9 x 4.2 x 3.9	4 x 6.7 x 11.7
pI	9.2-9.6	9.2-9.6	2.8- 3.8	9

Of the three polymerised surfaces, the first tested with SPR were the 10 minute MIPs and NIPs. Both surfaces binding responses to the proteins at $R_{equilibrium}$ are reported in figure 5.12. Firstly, the responses of both surfaces to any of the proteins tested was relatively low and neither the MIPs nor NIPs showed any discernible selectivity for any one protein over another. RNase B produced the highest binding response observed from the MIPs, however the response is indistinguishable from the responses from RNase A, α1-acid glycoprotein or HRP. Furthermore, as shown in table 5.1 the surface shows a low affinity towards RNase B of 85.5 ± 31.9 μM as well as showing a low selectivity of 1.7 fold for RNase B when compared with RNase A. In comparison, the non-imprinted NIPs show a similar scale of binding responses to each of the proteins to the MIPs.

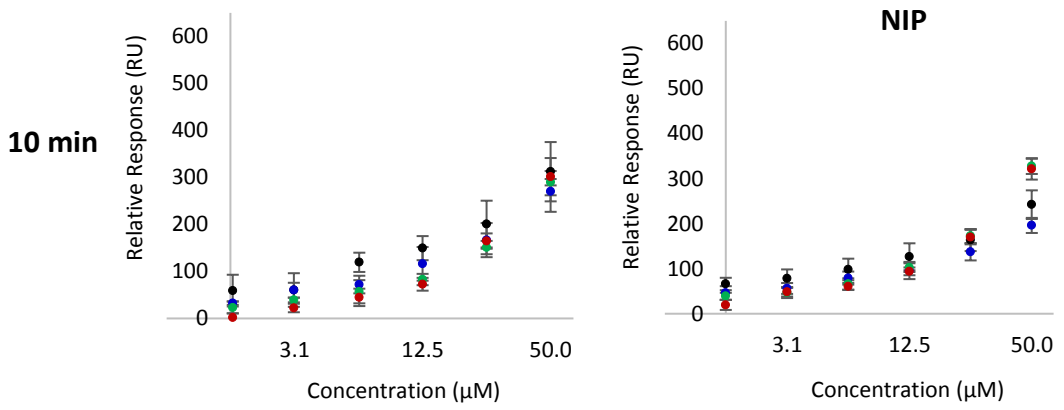

Figure 5.12: SPR responses of the 10 minute MIP (left) and NIP (right) at $R_{equilibrium}$ to RNase B (black), RNase A (blue), α1-acid glycoprotein (green) and HRP (red).

Collectively, the lack of any selectivity towards RNase B from the MIP surfaces indicates that in this case 10 minutes polymerisation with this system is not sufficient in providing the desired imprinting efficacy. As the surfaces thickness was previously determined as 4.7 ± 0.9 nm with ellipsometry we hypothesise that this lack of selectivity for its target arises due to the polymer layer being too thin which subsequently impairs the formation of the imprinting sites with either enough functionality (i.e. a lack of boronic acid incorporated within the surface in complementary spatial arrangement for RNase B) or perhaps depth to produce a desirably selective response. Following this initial disappointing result, we then decided to test the 20 and 60 minute MIPs for their imprinting capabilities in order to establish whether imprinting for a longer polymerisation time could yield the desired imprinting effect.

6.1 SPR Results of the 20 and 60 minute MIP and NIP Surfaces

The SPR $R_{equilibrium}$ responses for the 20 and 60 minute MIP and NIP surfaces are reported in figure 5.13 alongside the calculated affinities for each protein in table 5.2.

If we first examine the response of the 20 minute MIPs, the surfaces show significantly higher binding to all concentrations of RNase B in comparison with the three protein controls. Furthermore, from the values shown in table 5.2, the 20 minute MIPs exhibit a good affinity of 14.2 ± 2.1 μM for RNase B in comparison with the affinities of 63.3 ± 7.2 μM, 105.4 ± 11.6 μM and 75.3 ± 8.5 μM, for the RNase A, α1-acid glycoprotein and HRP controls, respectively. Moreover, the 20 minute MIPs show a 4.5 fold selectivity to RNase B than its

non-glycosylated homologue, RNase A. In contrast, the 20 minute NIPs show a similar response to that observed by the 10 minute NIPs, whereby no particular protein binds the surface with any selectivity due to the lack of imprinted sites.

Overall, the binding response shown to RNase B from the 20 minute MIP surfaces demonstrates that the imprinted cavities specific for this protein have been formed within the polymer matrix as hypothesised. Moreover, the 4.5 fold selectivity of the surface for RNase B over RNase A shows that the inclusion of the functional boronic acid monomer within the imprinting sites enhances the binding of RNase B as hypothesised by the diols binding the sugars of the protein's glycan chain. The MIP's weak affinity for the two other glycosylated proteins (α1-acid glycoprotein and HRP) further illustrates that despite their high percentage of glycosylation that could enable their glycans to interact with the boronic acid moieties, the spatial arrangement of the boron monomers is not complementary to facilitate these interactions. Moreover, the larger dimensions of these two proteins also prevents them from fitting into the binding sites of the MIP surfaces.

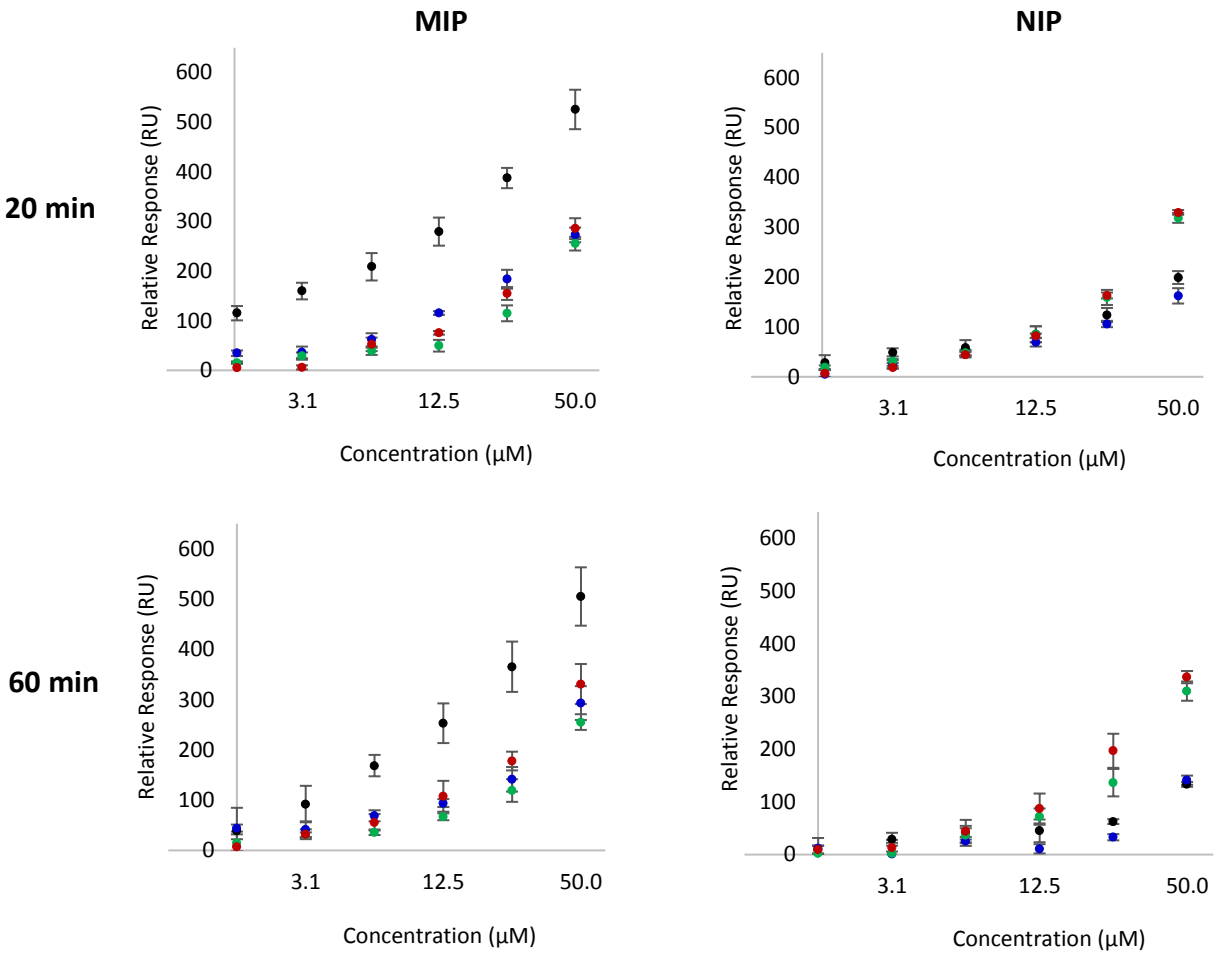

Figure 5.13: SPR responses of the 20 minute (left) and 60 minute (right) MIPs and NIPs at $R_{equilibrium}$ to RNase B (black), RNase A (blue), α1-acid glycoprotein (green) and HRP (red).

Table 5.2: Reports the K_D and selectivity values for each of the proteins affinities for the MIPs polymerised for 10, 20 or 60 minutes.

	Polymerisation Time (mins)	10	**20**	60
K_D MIPs (µM)	RNase B	85.3 ± 31.9	14.2 ± 2.1	21.5 ± 4.6
	RNase A	145.5 ± 52.9	63.3 ± 7.2	61.6 ± 11.3
	α1-acid glycoprotein	186.3 ± 67.1	105.4 ± 11.6	123.3 ± 21.6
	HRP	237.7 ± 85.0	75.3 ± 8.5	77.4 ± 14.0
	Selectivity (K_{DA}/K_{DB})	1.7	**4.5**	2.9

In comparison with the 20 minute surfaces, the 60 minute surfaces likewise demonstrated that imprinting within this polymer matrix is possible. As was observed for the 20 minute NIPS, no selectivity for any particular protein including RNase B is apparent from the 60 minute NIPs however the MIPs exhibited selectivity for RNase B over all the control proteins. As with the 20 minute MIPs, the sequential increase in the response of the 60 minute MIPs to increasing concentrations of RNase B is observed which indicates that cavities well-matched to the structure and functionality of RNase B have been formed within the polymer. The MIPs exhibit a slightly lower affinity for RNase B of 21.5 ± 4.6 μM in comparison with 14.2 ± 2.1 μM reported for the 20 minute MIPs, and furthermore the selectivity of the imprint for RNase B over RNase A was also lower at 2.9 fold. Moreover, in this case the 60 minute MIPs only begin to show selectivity for RNase B from 6.3 μM.

This loss of selectivity at the lower protein concentrations could be attributed to the thicker polymer layer of the 60 minute MIPs as observed in the aforementioned ellipsometry studies resulting in poor mass transport issues at lower protein concentrations, where the protein's diffusion from solution is slower than its rate of association into the imprinting sites [15]. In this instance, the surface is therefore limited by the rate of the protein's diffusion from solution. This can in some cases be overcome, for example, by increasing the flow rate of the injected analyte or altering the protocol to decrease the number of imprinting sites [16]. Furthermore, an explanation for the slightly lower affinity observed for the 60 minute MIPs for RNase B could be attributed to the increased heterogeneity in the imprinted polymer structure as shown by the larger variation in the Ra roughness and thicknesses from the previous AFM and ellipsometry

studies. This may have resulted in a slightly less optimal arrangement of the boronic acids within the sites in comparison with the 20 minute MIPs and as the affinity of the 60 minute MIPs for RNase A is unaffected this is not unreasonable to hypothesise.

Nonetheless, as the 20 minute MIPs offered good sensitivity and selectivity for RNase B at all concentrations tested it was the optimal imprinted surface to then take forward for further study of the interaction of the surfaces with their target.

6.2 Conclusions from the SPR Studies of the 10, 20 and 60 minute MIPs and NIPs

From the above results where the binding affinities of 10, 20 and 60 minute MIPs and NIPs towards a range of proteins were examined using SPR, it is apparent that at least 20 minutes polymerisation is necessary in order to create an imprinted surface with sites that shows selectivity for RNase B. The 10 minute MIPs showed a low response to the RNase B glycoprotein and were not able to be distinguish RNase B over the three other protein controls, RNase A, α1-acid glycoprotein and HRP. This lack of target selectivity indicated that the surfaces did not have sufficient imprinting capabilities to bind RNase B. From the 3D AFM images of the MIPs and their low Ra roughness this could be attributed to a lack of imprinted pockets formed within the surface polymer to bind RNase B. Moreover, another possibility is that any pockets that are formed within the surface do not contain a suitable arrangement of the boronic acid moieties within them for RNase B due to thinness of the polymer to therefore selectively bind this target.

However, in comparison the 20 and 60 minute MIPs both showed a distinction for binding RNase B with a higher affinity than the control proteins which can be attributed to the longer polymerisation time enabling the formation of compatible sites for this glycoprotein to be formed within their polymer matrices. Out of the two systems, the 20 minute MIPs showed a greater sensitivity for the RNase B target than the 60 minute MIPs. This enhanced selectivity appears to arise from the more optimal thickness and boronic acid arrangement within these MIPs for binding the target [16].

In summary, 20 minutes polymerisation is the optimal imprinting system out of the three incubation times examined and so this platform was taken forward for further development. Having established that this imprinting procedure is viable we wished to ascertain whether the affinity for RNase B could be further enhanced by changing the ratio of boronic acid monomer within the imprints relative to RNase B. As shown in Chapter 4 from the mass spectrometry data, the binding of the boronic acid monomer to the glycan chain of RNase B can be influenced by its solvation with an organic solvent, as well as the ratio at which the two are incubated. Having previously resolved the solvation issue using 25 % (v/v) MeOH which was then integrated into the imprinting procedure, we chose to employ a 10:1 ratio of the boronic acid monomer to RNase B as an initial complexation ratio based on previous work by our group [10]. However, we then wished to elucidate whether increasing the ratio of this functional monomer could further improve the selectivity and sensitivity of the 10:1 imprints as increasing the ratio of boronic acid produced more complexation in the mass spectrometry studies. We therefore undertook the same 20 minute polymerisation procedure

but used a 15:1 or 20:1 ratio of boronic acid relative to RNase B to synthesise the MIPs.

6.3 Optimisation of the Boronic Acid Ratio within the MIPs and NIPs

As before the binding affinities for RNase B and the three protein controls were tested with SPR. The results of these boronic acid imprints are shown in figure 5.14 alongside the 10:1 MIPs previously reported. Firstly, both the 15:1 and 20:1 MIPs demonstrate selectivity for RNase B over the control proteins at all the concentrations tested, with similar binding responses to those observed for the 10:1 MIPs. This therefore shows as was observed with the 10:1 MIPs that imprinting sites complementary to RNase B are being formed within the polymer matrices to achieve this selectivity. However, as shown in table 5.3 both the 15:1 and 20:1 MIPs exhibited increasingly lower affinities for RNase B of 19.7 ± 2.1 μM and 23.0 ± 2.6 μM, respectively, in comparison with the affinity of 14.2 ± 2.1 μM observed for 10:1 MIPs. Furthermore, both MIPs also showed lower selectivities for RNase B over RNase A of 2.1 and 2.6, respectively, than the 4.5 fold previously observed with the 10:1 MIPs.

These decreases in affinity for RNase B with increasing ratios of the boronic acid monomer could be attributed to the decrease in the respective proportion of MEBA cross linker employed within each system. As the proportion of the MEBA used within the polymerisations of each of these imprints was adjusted (i.e. lowered) to account for the respective increases in the proportion of boronic acid monomer, contributions from the weaker electrostatic interactions (such as Van der Waals forces and hydrogen bonding) of MEBA within the imprinting sites may

be reduced. It is known that whilst such non-covalent interactions are individually weak, synergistically their net effects can be strong and essential to achieving high binding selectivity and sensitivity. If the proportion of MEBA therefore incorporated within the imprinted cavities is reduced whilst the proportion of the boronic acid is increased, this could negatively impact upon the net affinity of the MIPs for RNase B. Another factor that could also be influencing the affinities of the 15:1 and 20:1 MIPs for RNase B is a change in the porosity of the polymer as a result of the decreased proportions of MEBA. A looser overall polymer network will produce an increase in the MIP porosity which could result in lower affinities of the imprinting sites for RNase B as the spatial arrangement (i.e. the density) of the moieties within the pocket can decrease.

In summary, these results suggest that using a 10:1 ratio of BA:RNase B when synthesising the MIPs provides the best binding affinity and selectivity towards RNase B. However, we should also consider the response of each of the NIP surfaces when clarifying which MIP is the optimal platform. When we compare the binding results of each of the MIPs to their respective NIPs, we observe that as the proportion of the boronic acid monomer increases within the polymerisations so too does the non-selective binding response of the NIP surfaces to the control proteins. As was observed for the 10:1 NIPs, the 15:1 NIPs show no selectivity in their binding to any particular protein, however the overall binding responses to all the proteins increases. This can be attributed to a higher proportion of negative boronic acids randomly arranged within the polymer of the NIPs encouraging more non-specific binding interactions with the external charged regions of the proteins alongside the changes in the polymer porosity.

Interestingly, the 20:1 NIPs then begin to show a low level of selectivity for RNase B despite the random arrangement of the boronic acids within the surface, which could be due to the change in porosity of the surface enabling the polymer to easily bind the RNase B glycan. However, this is not ideal when considering the optimal systems as if we then compare these responses to the respective 20:1 MIP the difference between the MIP and NIP systems has consequently decreased with this increase in boronic acid.

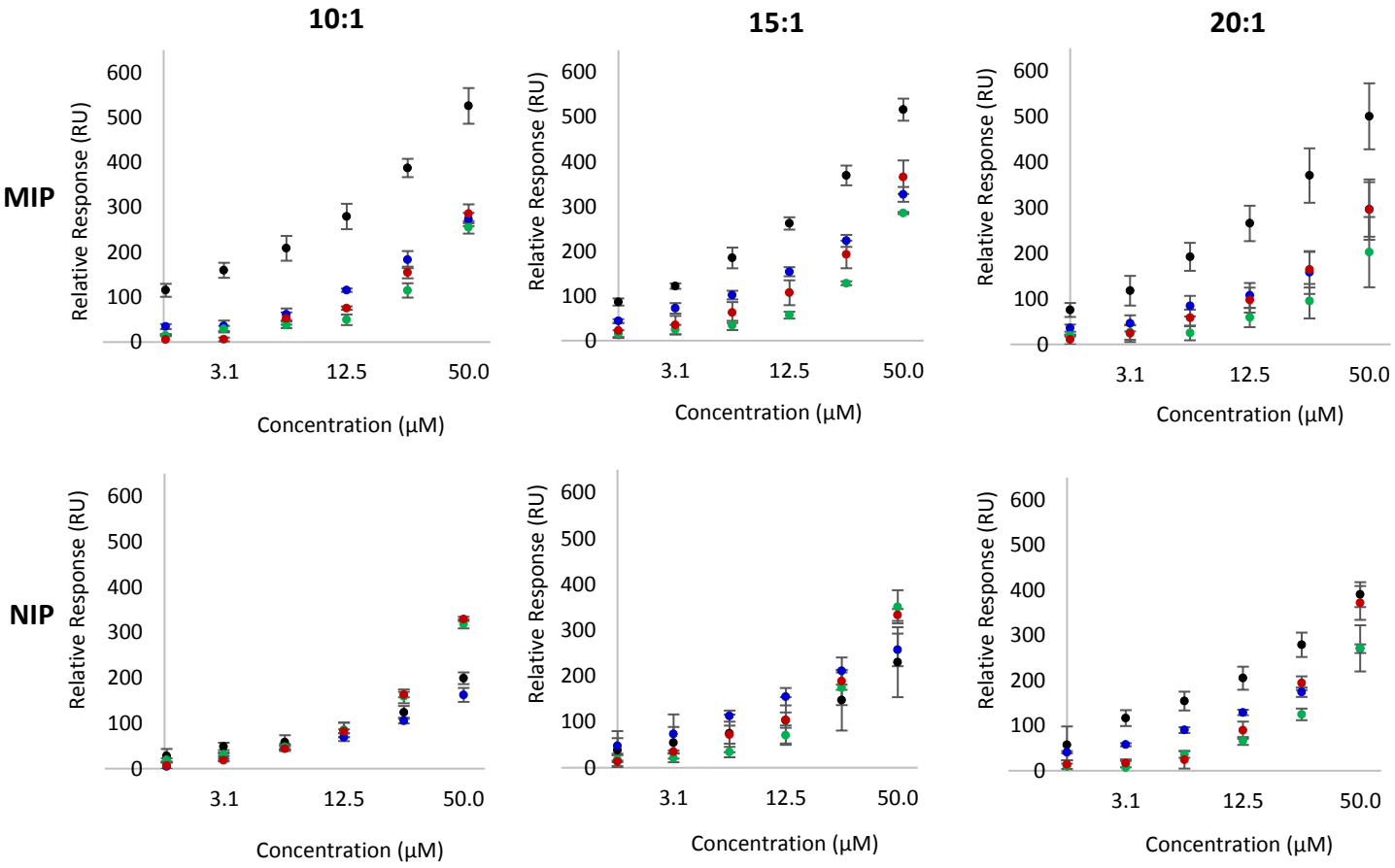

Figure 5.14: Comparison of the SPR responses of the 10:1, 15:1 and 20:1 Boronic Acid:RNase B MIPs (top) and NIPs (bottom) at $R_{equilibrium}$ to RNase B, RNase A (blue), α1-acid glycoprotein (green) and HRP (red).

Table 5.3: Reports the K_D and selectivity values for each of the proteins affinities for the MIPs formed using incubations ratios of either 10:1, 15:1 or 20:1 of the boronic acid monomer:RNase B.

	Ratio of BA:RNase B	**10:1**	15:1	20:1
K_D MIPs (μM)	RNase B	14.2 ± 2.1	19.7 ± 2.1	23.0 ± 2.6
	RNase A	63.3 ± 7.2	40.8 ± 3.7	60.6 ± 6.0
	α1-acid glycoprotein	105.4 ± 11.6	135 ± 11.2	217.3 ± 20.0
	HRP	75.3 ± 8.5	69.9 ± 6.1	90.5 ± 8.6
	Selectivity (K_{DA}/K_{DB})	**4.5**	2.1	2.6

Collectively, this data indicates that increasing the molar equivalents of boronic acid past 10:1 is detrimental to achieving the ideal molecular imprint for RNase B using this system. As the molar equivalents of boronic acid are increased within the MIPs the sensitivity and selectivity towards RNase B consequently decreases due to the decrease in the non-covalent binding contributions from the MEBA molecules within the imprint cavities, alongside the increase in the porosity of the polymer network impacting the binding efficacy of the MIP [17]. This is supported by the increased non-specific binding responses with increased molar equivalents of boronic acid observed in the NIPs. Taken collectively, these results indicate that the 10:1 system remains the superior surface as it shows the best affinity and selectivity for RNase B, alongside exhibiting the greatest difference in the binding responses when compared with its respective NIP control.

6.4 Overall Conclusions of the Fabricated RNase B MIP Sensor

In summary, we have shown the fabrication and optimisation of a novel imprinted sensor for the glycoprotein, RNase B. We first show that the selectivity of the imprinting system to the RNase B target relies upon the polymerisation time of the imprint synthesis. A longer polymerisation time produced a surface with sufficient polymer to create imprints for its target. This system is able to preferentially identify the target glycoprotein over its non-glycosylated homologue, as well as over other glycosylated proteins, by incorporating a functional boronic acid monomer that targets the sugars of the RNase B glycan. Unlike other glycoprotein imprinting platforms, these functional monomers are arranged within a 3D display within the polymer which creates pockets that exhibit the ideal spatial size and functional arrangement to bind RNase B.

We then further optimised the most suitable imprinting system by examining the effect of increasing the proportion of the boronic acid monomer that is incorporated within the imprint. Overall, the imprints synthesised with either 15:1 or 20:1 ratios of boronic acid monomer:RNase B both produced selective responses for the target protein, however their affinities and selectivity's were not superior to the original 10:1 imprint. We hypothesise that this can be attributed to the decrease in the proportion of the MEBA incorporated within the imprinting pockets, as well as an increase in the porosity of the imprinted polymer.

In summary, we conclude from these studies that 20 minutes imprinting with a 10:1 boroncic acid to RNase B ratio is the most suitable for synthesising molecular imprints for RNase B using this novel system. The system shows a good affinity for RNase B comparable to the affinities of some weaker (K_D = >10

μM) antibodies and with further development to improve the affinity of the pockets and decrease non-specific interactions this system could offer potential to replace the use of antibodies in sensing applications.

References

1. Liu, Z., et al., *Boronate-Affinity Glycan-Oriented Surface Imprinting: A New Strategy to Mimic Lectins for the Recognition of an Intact Glycoprotein and Its Characteristic Fragments.* Angew Chem Int Ed Engl, 2015. **54**(35): p. 10211-5.
2. Wang, H., et al., *Magnetic nanoparticles with dendrimer-assisted boronate avidity for the selective enrichment of trace glycoproteins.* Chemical Science, 2013. **4**(11): p. 4298.
3. Saeki, T., et al., *Orientationally Fabricated Zwitterionic Molecularly Imprinted Nanocavities for Highly Sensitive Glycoprotein Recognition.* Langmuir, 2018. **35**(5): p. 1320-1326.
4. Wang, S., et al., *Affinity-tunable specific recognition of glycoproteins via boronate affinity-based controllable oriented surface imprinting.* Chemical Science, 2014. **5**(3): p. 1135.
5. Bie, Z., et al., *Precision Imprinting of Glycopeptides for Facile Preparation of Glycan-Specific Artificial Antibodies.* Anal Chem, 2018. **90**(16): p. 9845-9852.
6. Fantin, M., et al., *Understanding the Fundamentals of Aqueous ATRP and Defining Conditions for Better Control.* Macromolecules, 2015. **48**(19): p. 6862-6875.
7. Yu, Q., Kandegedara, A., Xu, Y., and Rorabacher, D.B., *Avoiding Interferences from Goods Buffers - a contiguous series of noncomplexing tertiary amine buffers covering the entire range of pH 3-11.* Anal Biochem, 1997. **253**(1): p. 50-6.
8. Xiao, D. and M.J. Wirth, *Kinetics of Surface-Initiated Atom Transfer Radical Polymerization of Acrylamide on Silica.* Macromolecules, 2002. **35**(8): p. 2919-2925.
9. Beamson, G.B., D., *High Resolution XPS of Organic Polymers: The Scienta ESCA300 Database* ed. N.Y. Wiley Interscience 1992.
10. Stephenson-Brown, A., Acton, A., Preece, J.A., Fossey, J., Mendes, P.M., *Selective glycoprotein detection through covalent templating and allosteric click-imprinting.* Chem Sci, 2015. **6**(9): p. 5114-5119.
11. Oral, E. and N.A. Peppas, *Dynamic studies of molecular imprinting polymerizations.* Polymer, 2004. **45**(18): p. 6163-6173.
12. Culver, H.R. and N.A. Peppas, *Protein-Imprinted Polymers: The Shape of Things to Come?* Chemistry of Materials, 2017. **29**(14): p. 5753-5761.
13. Shirtcliffe, N.J., et al., *An introduction to superhydrophobicity.* Advances in Colloid and Interface Science, 2010. **161**(1): p. 124-138.

14. Fan, J. and Y. Zhao, *Nanocarpet effect induced superhydrophobicity.* Langmuir, 2010. **26**(11): p. 8245-50.
15. Zhang, Z., et al., *Uniform core–shell molecularly imprinted polymers: a correlation study between shell thickness and binding capacity.* RSC Adv., 2014. **4**(60): p. 31507-31514.
16. Schuck, P. and H. Zhao, *The role of mass transport limitation and surface heterogeneity in the biophysical characterization of macromolecular binding processes by SPR biosensing.* Methods Mol Biol, 2010. **627**: p. 15-54.
17. Golker, K. and I.A. Nicholls, *The effect of crosslinking density on molecularly imprinted polymer morphology and recognition.* European Polymer Journal, 2016. **75**: p. 423-430.

Chapter 6: Conclusions and Future Work

1.0 Conclusions

The work within this thesis has described the fabrication of a molecularly imprinted sensing platform that is specific and selective for the model glycoprotein, RNase B. Within this study, we have examined the parameters that affect the binding affinity of these imprints for RNase B alongside their affinities for several control proteins. The platform was synthesised using ATRP to create polymer layers within which impressions of the RNase B protein were moulded that were then tested for their binding capabilities using SPR.

Firstly, the self-assembly of two different initiator monolayers (MUBP or 11-DTMBD) were examined for their suitability as the foundation to which the polymer layers were then grown. Once the most suitable and reliable SAM was identified the poly(MEBA) layers were then grown from these surfaces and the polymerisation conditions optimised for their concentration, volume and pH. The poly(MEBA) layers were finally characterised with several surface techniques.

In parallel with these polymerisations, we also undertook mass spectrometry studies to examine the complexation of the RNase B glycoprotein with a functional boronic acid monomer. The complexation conditions were optimised by addressing solvation issues and finally the conformational stability of the protein was shown to be viable in the required solvation conditions with CD.

Once the complexation and polymerisation conditions were finalised, the polymer surfaces were then imprinted using the RNase B-boronic acid monomer complexes and the binding responses of these synthetic receptors evaluated by SPR. The

binding responses were shown to be influenced by both the polymer thickness and the ratio of the boronic acid monomer:RNase B template. The optimal system used a 10:1 ratio of the complex with 20 minutes polymerisation to produce a selective and sensitive RNase B imprinting platform. With further development and optimisation this novel imprinted platform could be applied to specific glycoproteins of clinical interest.

Briefly:

Chapter 3

Described the study of several self-assembled monolayers, crucially MUBP and 11-DTMBD, in order to elucidate the most suitable and reliable monolayer from which to polymerise using ATRP. Firstly, MUD and UDT SAMs were extensively characterised, following which the MUD SAMs were functionalised to form MUBP initiator SAMs. However, when characterised the extent of MUBP functionalisation was shown to vary between samples which consequently produced significant variation in the polymer layer thicknesses. This issue therefore required a new SAM to be explored in order to reliably produce polymers with limited variation in their thickness. This was overcome by synthesising 11-DTMBD SAMs that enabled uniform poly(MEBA) surfaces to be reliably formed using ATRP. Elucidation of the optimal ATRP polymerisation conditions were shown to be influenced by the concentration of the MEBA monomer, as well as the ratios of the copper catalyst. The scaling down of the system then further showed that the ATRP reaction remains viable when undertaken at a smaller volume. In this way we were able to control the poly(MEBA) thickness to within the desired 5-10 nm range suitable for imprinting glycoproteins whilst using the minimal volume of reactant solution.

Chapter 4

Described the study of the complexation between the five glycoforms of the RNase B glycoprotein and the 3-acrylamidophenyl boronic acid monomer to provide insight into this binding relationship that was later exploited in the imprinting studies. ESI-MS showed that when mixed the two species form a complex as expected, however this is dependent upon the appropriate solvation of the monomer with a proportion of organic solvent (MeOH). Initial studies showed limited complexation in solely buffered solution, whereas addition of the MeOH enabled the degree of complexation to be substantially increased. CD studies finally confirmed that exposure of the RNase B to the MeOH solvent does not cause abhorrent conformational changes to the tertiary structure of the glycoprotein to therefore denature the protein.

Chapter 5

Illustrated the development of a novel imprinting platform for RNase B by combining the systems developed in Chapters 3 and 4. Several MIP surfaces differing in their polymerisation time and boronic acid ratio were extensively characterised and their binding affinities analysed using SPR. The results showed that the optimal imprinting system required at least 20 minutes polymerisation, as well as selecting a 10:1 ratio of boronic acid with respect to the template protein. The latter produces a MIP with a selectivity akin to weaker (>10 μM) antibodies and so further development of this system could offer a platform that could replace such receptors.

2.0 Future Work:

The work presented in this thesis is the first to create a glycoprotein imprint that uses a combination of a glycoprotein template pre-complexed with a functional boronic acid monomer that is then polymerised within an ATRP system to produce imprinted sites that show selectivity for RNase B over its non-glycosylated homologue. This is the first work to demonstrate the fabrication of an RNase B imprint where the boronic acids are arranged within a 3-D display within a poly(MEBA) matrix to promote selectivity for the glycosylated target.

The next stage of this project would be to develop the polymerisation system in order to imprint different glycoforms of the same protein. It would be interesting in this case to isolate an RNase B glycoform, for example Man_5 or Man_6, from the other glycoforms found in commercial samples to then use as the template protein for imprinting. Following the synthesis of an individual glycoform imprint the next stage would be to test whether the imprint shows specificity and selectivity for that one glycoform whilst ideally showing no response to the other four remaining glycoforms. If we could demonstrate specificity and selectivity for one particular glycoform over another through the elegant arrangement of the boronic acid moieties within the MIP cavities we could then use this system to imprint clinically relevant glycoproteins such as PSA.

The first step towards achieving this goal would be the requirement to scale down the imprinting procedure so that a lower and more biologically relevant concentration of the template RNase B glycoprotein could be used, as shown in figure 7.1. At present, the system presented in this thesis requires a high concentration (0.23 mM) of RNase B per imprint, however µM or nM template concentrations are required as clinically relevant glycoproteins are expensive and require laborious purification procedures to obtain. The next step should therefore confirm that the SPR response obtained using this 'scaled-down' system still shows the appropriate selective response to RNase B but also that the scale of response to RNase B is still

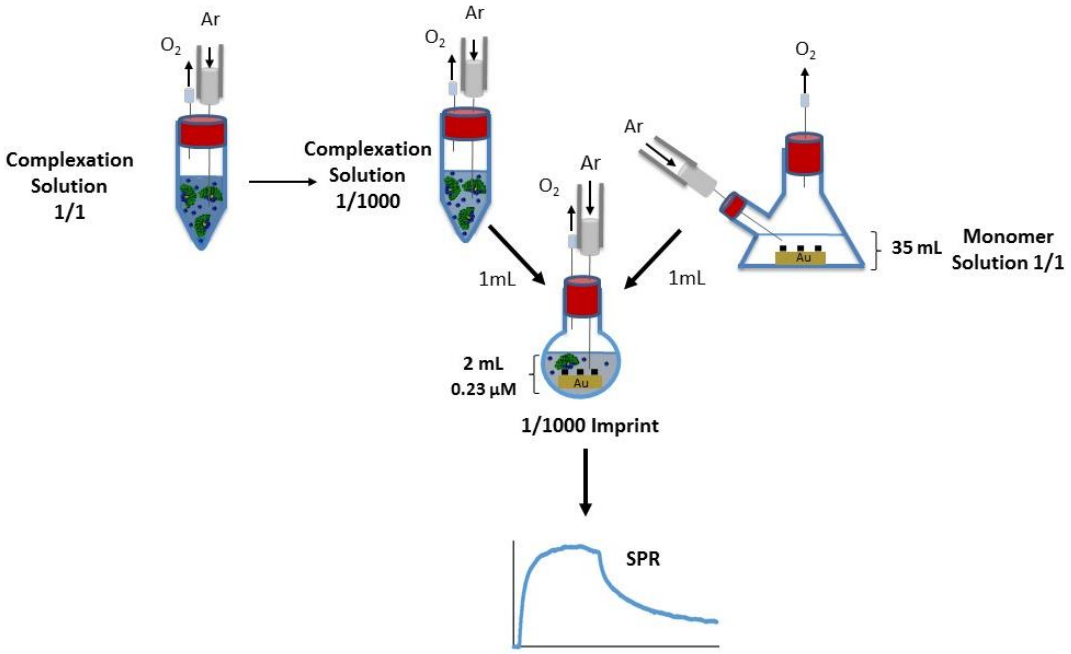

Figure 6.1: Schematic of the proposed scaled-down imprinting strategy, in this case using an imprinting solution with a final concentration within the µM range. First, the original complexation solution (with a protein concentration in the mM range i.e. the 1/1 solution) is diluted a thousand fold to the µM range. Following dilution, 1 mL of this solution is then combined with 1mL of the monomer solution to form 2 mL of the imprinting solution with a protein concentration that is also within the µM range. This solution is then used to form the imprinted surfaces. SPR is then used to evaluate the binding affinity of the imprints to their target protein.

significant. This is crucial as the number of imprinting sites could be significantly lower due to the concentration of the template protein being lowered.

Following the confirmation that the scaled down procedure is successful, the protocol could then be used to explore imprinting of the individual RNase B glycoforms. The idea of this strategy is to synthesise an imprint using only one of the Man_5-Man_9 RNase B glycoforms. This could be undertaken by first separating each of the glycoforms using HPLC analysis. A HILIC column could be used to separate the most abundant Man_5 glycoform from the remaining glycoforms, which could then be complexed with boronic acid and used as the template for the glycoform specific imprint as per the optimised HPLC separation protocol developed by Pedrali *et al. [1]*. The remaining mannose glycoforms – Man_6, Man_7, Man_8 or Man_9 - could then be used to test the specificity and selectivity of the Man_5 imprint. The ideal system would show only binding towards the Man_5 glycoform to create a glycoform specific imprint.

If this system failed another approach that integrates the system recently used by Takeuchi *et al.* with our approach could be explored [2]. As before the first step would be HPLC separation of the RNase B glycoforms. The second step would be the complexation of for example Man_5 with the boronic acid monomer. We would then immobilize this complexed glycoform onto a mixed SAM made of the 11-DTMBD initiator alongside an alkanethiol that can be covalently bound to an amino acid residue of the glycoforms' polypeptide backbone. With this method only nM-pM concentrations of the glycoform complex are required with the added advantage that the glycan remains bound to multiple boronic acids. The platform can then be polymerised using our optimised approach with ATRP, following which the complex

is then uncoupled from the surface and the imprint tested as before with the other four Mannose glycoforms.

Within both these proposed systems, the polymers porosity could be further examined to explore whether altering the rigidity of the polymer network can improve the selectivity and sensitivity of these systems for the imprinted RNase B glycoform. As previously shown from the study optimising the ratio of boronic acid within the imprints, the proportion of cross linker employed within the imprint synthesis affects the rigidity and porosity of the polymer that can then affect the affinity of the imprinted sites for their target. Furthermore, in this instance 3-acrylamidophenyl boronic acid was the only mono-functional monomer employed, however the incorporation of a further mono-functional monomer such as N-isopropylacrylamide (NIPAAm) or acrylic acid (AA) could also be explored as these molecules could promote weaker interactions (such as hydrogen bonds or Van der Waals forces) to counteract the effects of decreasing the proportion of cross linker.

Finally, an avenue for further development for all these proposed systems is to investigate not only 3-acrylamidophenyl boronic acid but also other vinyl boronic acids with different pKas as the functional monomer within the imprint design. As explained in Chapter 1, the pKa of a boronic acid can be varied by controlling the electron withdrawing groups or intramolecular bonds within the molecule. This therefore enables the boronic acid to be tuned to any specific conditions required by the target glycoprotein. By incorporating different boronic acids or benzoboroxole moieties within the imprint design glycoproteins that are susceptible to denaturation at more alkaline pHs (such as with pH 8.6 used within this system with the 3-acrylamidophenyl boronic acid) can still be imprinted. If these avenues are explored

and developed it is possible that different imprinting protocols suited to various glycoproteins of clinical importance could be viable.

References

1. Pedrali, A., et al., *Characterization of intact neo-glycoproteins by hydrophilic interaction liquid chromatography.* Molecules, 2014. **19**(7): p. 9070-88.
2. Saeki, T., et al., *Orientationally Fabricated Zwitterionic Molecularly Imprinted Nanocavities for Highly Sensitive Glycoprotein Recognition.* Langmuir, 2018. **35**(5): p. 1320-1326.

Chapter 7: Methods and Materials

1.0 Chemicals and Materials

All chemicals and solvents were purchased from Merck Companies (Aldrich Chemicals, Sigma Aldrich and Fischer Chemical) with all used as received. x10 Phosphate buffered saline (PBS) solutions were purchased (Fisher Bio-Reagents). RNase B from bovine pancreas, RNase A from bovine pancreas, α_1-acid glycoprotein from bovine plasma and HRP from horse radish root were all purchased from Sigma Aldrich. Polycrystalline gold substrates for the contact angle, ellipsometry, AFM and XPS studies consisting of 100 nm Au layer on silicon wafer were purchased from George Albert PVD (Germany). For SPR studies, polycrystalline gold substrates of 49 nm Au layer on glass were purchased from Reichert.

2.0 NMR Spectroscopy

All ^{1}H NMR spectra were undertaken on a Bruker AV300 FT/NMR Spectrometer (300 MHz) at room temperature, with shifts measured in ppm. All spectra were measured relative to $CDCl_3$ and data processed using MestReNova Version 6.1 (Mestrelab Research). J coupling constants are reported in Hz, and the multiplicity of the signals is expressed as: s= singlet, d=doublet, t=triplet q=quartet, m=multiplet.

3.0 Ellipsometry Measurements

The thickness of the SAM and polymer surfaces were measured with spectroscopic ellipsometry using a Jobin-Yvon UVISEL ellipsometer with a xenon light source. The incident angle of the light was fixed at 70 ° for all measurements and the wavelength range was 220-800 nm. The calculation of the film thicknesses were based on a three-phase ambient atmosphere/SAM/Au model. The SAM was assigned a refractive index of 1.49 and assumed to be isotropic. The thicknesses were reported using averages of at least 3 independent surfaces with 3 measurements obtained from each surface (n=9) and the standard deviation was calculated from these values.

4.0 Dynamic Contact Angle Measurements

All contact angle measurements were taken using an Attension Theta Contact Angle Meter (Biolin Scientific). An automated microsyringe was used to inject and retract the water droplet onto and from the surfaces from which the advancing and receding angles were then measured by recording the change in the pinning angle by video (acquisition rate 35 frames per second). OneAttension software was then used to analyse the advancing and receding angles. For each surface type (i.e. SAM or polymer) a least 3 measurements each from 3 individual chips were taken (n=9) from which the average and standard deviation values were then calculated.

5.0 XPS Measurements

XPS spectra were acquired using either i) an Escalab 250: Thermo Scientific K-Alpha or ii) a Kratos Axis Supra system. Both systems used a monochromatic Al kα source with a photon energy of 1486.68 eV and for each measurement a spot size of 0.2 mm^2 was used with a take-off angle of 90 ° to the surface of the plane. All measurements were undertaken at a pressure of ~7.5 x 10^{-9} Torr. The SAM samples were taped onto a stainless steel plate using Shintron tape and clipped with stainless steel clips. Each SAM measurement was undertaken with the charge neutraliser on to prevent charging issues. However, for any polymer samples (poly(MEBA) or poly(MEBA)BA)) the charge neutraliser was turned off as this prevented charging of the surfaces. The high resolution spectra were obtained using a pass energy of 40 eV and 0.1 increments. Survey scans were obtained using a pass energy of 200 eV and 0.4 increments. Sensitivity factors for all samples were: S (2p), 1.67; Au (4f 7/2), 9.58; Au (4f 5/2), 7.54. N (1s), 1.8; B (1s), 0.486; C (1s), 1.0; Br (3d 5/2), 1.68; Br (3d 3/2), 1.16; O (1s), 2.93.

6.0 SPR Measurements

All protein SPR experiments were run on a Reichert SR7000DC Dual Channel Spectrometer (NY, USA). All SPR chips were purchased from Reichert (Depew, NY, USA). Each chip was placed on top of 1 µL Index matching oil already deposited onto the base of the SPR prism, following which the channel was attached and a baseline established using the running buffer at 40 µL/min. The running buffer used for all experiments was degassed 1 x PBS containing 96 mM glycine, 10 mM HEPES, and 0.01 % sodium dodecyl sulfate adjusted to pH 8.6 using potassium

hydroxide. Before each measurement the acidic regeneration buffer (consisting of equal parts of 75 mM malonic, phosphoric, oxalic and formic acid) was run across the surface to remove any contaminates during set up. The protein solutions were injected across the polymer surfaces at 40 µL/min for 10 mins, following which the running buffer was used for the 15 minute dissociation phase. The surfaces were then regenerated using the acidic regeneration buffer for 10 minutes. Data sets were analysed using Scrubber 2 (BioLogic Software, Campbell, Australia). All SPR responses at R_{equilm} were plotted against the concentration of the injected proteins (*Cp*) and fitted to a 1:1 steady-state model using Scrubber 2. The model uses a non-linear, least-squared regression to fit data to a Langmuir Isotherm as shown in equation 7.1. *KD* is the dissociation constant for the binding of the proteins to the MIPs and R_{max} is the maximum response when all available MIP sites are occupied.

$$Requilm = (\frac{Cp}{Cp + KD})Rmax \qquad \text{Equation 7.1}$$

7.0 Mass Spectrometry Measurements

The RNase B mass spectrometry experiments were performed on a Synapt-G2-Si High Definition Mass Spectrometer with a Quantof mass analyser (Waters Corporation, 34 Maple Street Milford, MA 01757 USA) in positive mode. Samples were infused by direct injection using a Waters Alliance e2695 Module. The mobile phase was 50 % water, 50 % acetonitrile and 0.05 % Formic Acid. The heated capillary was maintained at 100 °C for all experiments. Electrospray ionisation was performed with a capillary voltage of 2.5 kV and the sample cone set at 40 V.

The RNase A mass spectrometry experiments were performed on a Xevo-G2-XS-ToF Time of Flight Mass Spectrometer (Waters Corporation, 34 Maple Street Milford,

MA 01757 USA) in negative mode. Samples were infused by direct injection using a Waters Alliance e2695 Module. The mobile phase was 50 % water, 50 % acetonitrile and 0.05 % Formic Acid. The heated capillary was maintained at 100 °C for all experiments, with a source offset of 80-100 V. Electrospray ionisation was performed with a capillary voltage of 2.5 kV and the sample cone set at 40 V.

8.0 AFM Imaging

All AFM images were acquired using an Asylum Research MFP-3D AFM (Oxford Instruments, UK) operating in Intermittent Contact Mode at a temperature of 18 ^{o}C and a relative humidity of <40 %. Images were composed of 512 x 512 pixels and the scanning velocity was 10 μm/s. Rectangular pyramidal-tipped Si cantilevers (PPP-NCL, Windsor Scientific, UK) were employed; their nominal length, width, and tip diameter were 225 μm, 38 μm and <10 nm respectively. Images were analysed using Scanning Probe Image Processor software (Image Metrology, Denmark). Images were then presented using Gwyddion software (Version 2.51)

9.0 CD Measurements

CD spectra were measured using a Jasco J1500 CD Spectrometer (ASCO UK Ltd., Great Dunmow, Essex). All experiments were undertaken using a 400 μL quartz crystal cuvette with a 1 mm path-length. For the non-heat ramp RNase B experiments the temperature was kept constant at 25 °C. The measured wavelength range was between 270-190 nm, with a data pitch of 0.1 nm and scanning speed of 100 nm/min. 5 repeat accumulations were used to generate each measurement.

Each final spectra was subtracted from the equivalent buffer blank. For the heat ramp experiments, the temperature was increased using a Peltier Accessory from 25 °C to 90 °C, over 5 °C increments. The temperature of the solution was likewise monitored to compare against the ambient temperature using a probe within the cuvette.

10.0 SAM Preparation

10.1 Formation of the Pure UDT and MUD SAMs

All SAMs were prepared upon polycrystalline Au substrates (George Albert PVD, Beschichtungen, Germany) with a 100 nm Au layer deposited silicon wafer with a roughness of <2.5 nm. The Au substrate was cut using a diamond tipped pen into ~1 cm^2 chips following which each chip was cleaned using Piranha Solution (70 % (v/v) H_2SO_4 with 30 % (v/v) H_2O_2) for 10 minutes. The chips were washed with Ultra High Pure (UHP) water for 1 minute, rinsed with HPLC grade EtOH (Fischer Scientific) and then incubated in 3 mL of 1mM solutions of UDT or MUD. The SAMs were left to incubate for 24 hours to enable self-assembly, then were removed from the incubation solutions, rinsed with HPLC grade EtOH and dried using a stream of Argon.

10.2 Formation of the Mixed UDT and MUD SAMs

The mixed UDT:MUD SAMs were prepared ~1 cm^2 chips cleaned with piranha solution for 10 minutes, following which they were incubated in the mixed UDT:MUD solutions to a final concentration of 1 mM. The 1 mM solutions of set ratios of UDT:MUD were made from 5 mM stock solutions of UDT (22.4 µL UDT (0.841 g/cm^3) in 19,977.6 µL EtOH) and MUD (20.5 mg in 20 mL EtOH) For example, for a 3:1 ratio of UDT:MUD, 1.5 mL of 5 mM UDT was added to 0.5 mL of 5 mM MUD together with 8 mL EtOH to give 10 mL of these mixed thiols. Each cleaned Au chip was then incubated in 3 mL of the 1 mM solution for 24 hours to form the SAMs. The chips were removed from the incubation solutions, rinsed with HPLC grade EtOH and dried using a stream of Argon.

11.0 Synthesis of 11-DTMBD

11.1 Synthesis of 11-DTBD from MUD.

Following Shah *et al.* (2000), MUD (1.97 mmol, 0.4044 g) was dissolved in 15 mL dichloromethane (DCM) in a round bottomed flask, to which was added 10 % sodium hydrogen carbonate (2 mL) [1]. Bromine (1 mmol, 160 mg, density: 159.9 g/mol) was added dropwise to the well stirred mixture (figure 7.1, **a**). The colour of the bromine quickly disappeared upon addition to the flask. The solution was then left to react overnight for 14 hours.

20 mL DCM was then added to the mixture, the organic phase separated and the remaining 2 mL aqueous phase extracted with DCM (40 mL). The organic phases

were combined and dried with magnesium sulfate (~10 g). The solution was vacuum filtered to remove the magnesium sulfate and the solution transferred to a round bottomed flask. The solvent was then evaporated off to give nearly pure disulfide (0.4 g, 99%). The ^{1}H NMR spectra for MUD and 11-DTBD are shown in figure 7.2, **a** and **b**, respectively. The resonance shifts of the 11-DTBD in $CDCl_3$ are as follows: (300 MHz) δ = 1.304 (36 H, CH_2), 1.579 (4 H, CH_2), 2.703 (t, *J* = 7.3, 4H, SCH_2), 3.657 (dd, *J* = 11.9, 4H, OCH_2). As shown in figure 7.2, the integrals and resonance shifts for both molecules are as expected, with the SC**H**$_2$ quartet of MUD (orange) becoming a triplet and shifting downfield upon formation of the disulfide, whilst the OC**H**$_2$ quartet (blue) remains constant.

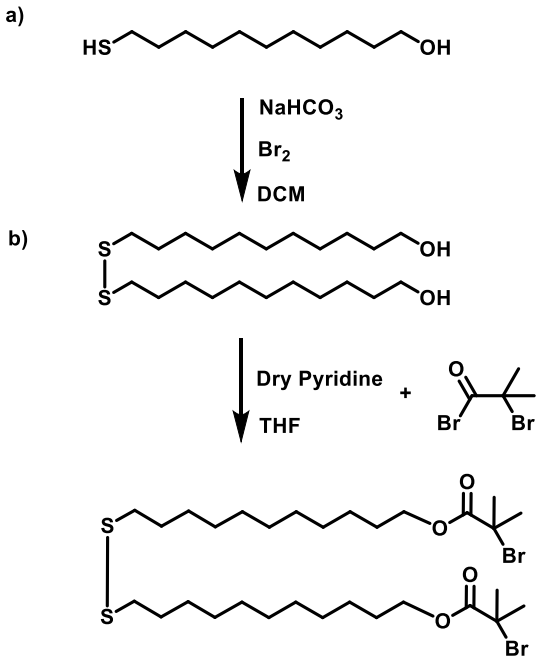

Figure 7.1: Synthesis of 11-DTBD from MUD (**a**) and 11-DTMBD from 11-DTBD (**b**).

11.2 Reaction of the Di-thiol with Acid Bromide

Following Belegrinou *et al.* (2010), 2-bromo-2-methylpropionyl bromide (267.42 µL, 2.164 mmol) was added to 10 mL anhydrous tetrahydrofuran (THF) in a pressure

equalised funnel under an argon atmosphere (figure 7.1, **b**) [2]. The 11-DTBD was added to a separate, stirred solution of 30 mL THF and dry pyridine (175.03 µL, 2.16 mmol) and kept at 0-5 °C also under an argon atmosphere. The 10 mL solution containing the acid bromide was then slowly added dropwise to the 30 mL disulfide solution. The reaction was stirred for 2 hrs at 0-5 °C and then for a further 16 hrs at room temperature (RT). Afterwards the reaction was diluted with DCM (60 mL) and extracted with cold 1 N HCl (2 × 100 mL), saturated $NaHCO_3$ (1 × 100 mL) and saturated NaCl (1 × 100 mL). The organic phase was retained and all aqueous phases were back extracted with DCM (1 × 100 mL). The solvent was removed using a rota-vac and the crude product (0.4 g) was purified by chromatography on silica gel in hexane/DCM 1:1. The purified product (0.2 g, 28.9 %) was a clear, colourless oil as previously reported by Belegrinou *et al.* [1, 2].

The ^{1}H NMR spectra for 11-DTBD and 11-DTMBD are shown in figure 7.3, **a** and **b**, respectively. The resonance shifts of the 11-DTMBD in $CDCl_3$ are as follows: (300 MHz)*:* δ = 1.30 (s, 20 H, CH_2), 1.39 (m, 8 H, C**H$_2$**CH_2CH_2O/S), 1.39 (m, 8 H, C**H$_2$**CH_2CH_2O/S), 1.69 (m, 8 H, C**H$_2$**CH_2O/S), 1.96 (s, 12 H, CH_3), 2.70 (t, *J* = 7.5 , 4 H, CH_3), 4.19 (t, *J* = 6.6, 4 H, OCH_2). Due to the formation of the ester bond the OC**H**$_2$ resonance (blue) shifts downfield due to the increase in polarity and becomes a triplet due to the loss of the terminal hydroxyl proton. Furthermore, the appearance of the C**H**$_3$ peak [3] also demonstrates that the addition of the bromoisobutyrate to the end of the dithiol was successful. Finally, the 11-DTMBD initiator was characterised with electrospray ionisation mass spectrometry (positive mode) as shown in figure 7.4 to further confirm the correct synthesis of the molecule (calculated $[M+H]^+$ = 727.2, observed $[M+H]^+$ = 727.2).

12.0 Formation of the 11-DTMBD SAMs

A 20 mM stock solution of the 11-DTMBD was made using 28.38 mL of HPLC grade EtOH added to the 0.2 g of purified 11-DTMBD. 1 mM solutions of 11-DTMBD were then serial diluted from this stock (for example, 1 mL of the 20 mM stock was added to 19 mL EtOH) and 3 mL of the solution incubated with each cleaned Au substrate to form the 11-DTMBD SAMs. The chips were removed from the incubation solutions, rinsed with HPLC grade EtOH and dried using a stream of Argon.

13.0 Polymerisations from the MUBP and 11-DTMBD SAMs

Polymerisations from both the MUBP and 11-DTMBD were initiated using ethyl-2-bromoisobutyrate (E-2-BB, 0.14 g). The SAMs were added to individual polymerisation solutions containing *N,N'*-Methylenebisacrylamide (MEBA, 0.5 g), 2,2'-bipyridyl (2-bpb, 2.2 mg) and Cu(I)Br (1.0 mg) dissolved in 35 mL of degassed (using argon) ultra-high pure H_2O. The MEBA was dissolved first, the solution was degassed to remove oxygen for 1 hr, following which the 2-bpb was added and finally the Cu(I)Br. The SAM chips were then added to this 35 mL solution and then the E-2-BB was injected. The chips were polymerised for 30 minutes, during which the solution was continually degassed using a slow stream of argon, after which they were then were removed from the polymerisation solution, rinsed extensively for 3 minute with ultra-high pure H_2O, then with HPLC grade EtOH and finally dried under a stream of argon. They were then characterised with ellipsometry.

14.0 Optimisation of the Polymerisation Condition from the 11-DTMBD SAMs

Polymerisations from the 11-DTMBD SAMs were initiated by injecting 1.02 µL of E-2-BB as a sacrificial initiator. From the following initial amounts of each components of the polymerisation system for system **a** (i.e. 35 mL ultra-high pure H_2O, 0.5 mg MEBA, 2.2 mg 2,2'-bipyridial and 1.0 mg Cu(I)Br) the stoichiometry of the individual components were then sequentially adjusted as shown in table 7.1. As before, the MEBA was dissolved first in the ultra-high pure H_2O, the solution was degassed to remove oxygen for 1 hr, following which the 2-bpb was then added and finally the Cu(I)Br and Cu(II)Br if required.

Table 7.1:

	a	**b**	**c**	**d**	**e**	**f**
H_2O (mL)	35	70	70	70	70	70
MEBA (mg)	0.5	0.5	0.25	0.25	0.25	0.25
2,2,-bipyridine (mg)	2.2	2.2	2.2	2.2	2.2	2.2
Ethyl-2-Bromoisobutyrate (µL)	1.02	1.02	1.02	1.02	1.02	1.02
Cu(I)Br (mg)	1.0	1.0	1.0	1.0	1.0	1.0
Cu(II)Br (mg)	/	/	/	1.6	2.3	3.1

The SAM chips were then added to each system and then E-2-BB injected to initiate the reaction. The chips were likewise polymerised for 30 minutes, during which the solution was continually degassed using a slow stream of argon. They were then were removed from the polymerisation solution, rinsed extensively for 3 minute with ultra-high pure H_2O, then with HPLC grade EtOH and finally dried under a stream of argon. They were then characterised with ellipsometry. For the 'scaled- down' polymerisations, an argon purged syringe was used to take 2 mL from the 70 mL of

the system **e** polymerisation solution, which was then deposited under argon within a 10mL round-bottomed flask sealed with a rubber septum already containing the SAM chip. The E-2-BB was then injected and the chips polymerised for 30 minutes and rinsed and dried following the above procedure.

15.0 Optimisation of the pH of the Polymerisation Condition of System e

To adjust the pH of the system **e** polymerisation conditions, the polymerisation solution was first set up with all components (MEBA, 2,2'-bipyridial, Cu(I)Br and Cu(II)Br) added as previously stated, however the concentration of all these components were doubled by using 35 mL of ultra-high pure H_2O. This was to account for the later dilution of 1 mL of this stock with the 1mL of 'complexation' solution per polymer surface. To monitor the native pH of the 35 mL solution, a portable meter was inserted into a gap in the septum. To increase the pH to 8.6 the tertiary amine tetraethyl ethylenediamine (TEEN) from a pre-prepared degassed stock solution (i.e. 200 µL TEEN in 19.8 mL of ultra-high pure H_2O) was then injected dropwise into the vessel.

To coincide with this, 7.5 mL of 10x phosphate buffered saline (PBS) adjusted to pH 8.6 with TEEN was added to 2.5 mL HPLC grade MeOH to give 10 mL of 'complexation solution' and left for 2 hours. Following degassing for 1 hr, using an argon purged syringe 1 mL of the 'complexation solution' was then added to 1 mL of the system **e** polymerisation solution within a 10mL round-bottomed flask sealed with a rubber septum already containing the 11-DTMBD SAM chip. The E-2-BB was then injected and the chips polymerised for set times, following which they were immediately removed from the solution, rinsed extensively for 3 minute with ultra-

high pure H_2O, then with HPLC grade EtOH and finally dried under a stream of argon. They were then characterised with ellipsometry and contact angle.

16.0 Polymerising the 10:1 MIPs and NIPs using the pH Optimised Polymerisation Protocol

For the MIP and NIP polymerisations, the complexation solution was likewise prepared using 75 % (v/v) 10x PBS and 25 % (v/v) MeOH at pH 8.6 as above, however 3-acrylamidophenyl boronic acid (BA) was added to this solution in the NIP polymerisations, and both BA and RNase B were added in the MIP polymerisations.

For the 10:1 BA:RNase B MIP studies, 0.88 mg BA with 6.8 mg of RNase B was to 0.75 mL 10x PBS with 0.25 mL HPLC MeOH pre-adjusted with TEEN to pH 8.6 to form 1 mL of the complexation solution. The complexation solution was left for 2 hours to allow the RNase B and BA of the MIP solutions to complex at this 10:1 incubation ratio. The complexation solutions for the NIP surfaces were prepared in the same way but without RNase B.

During this time, the 35 mL stock of the pH optimised polymerisation solution system **e** was prepared as per section 15.0 however due to the addition of the BA monomer, the amount of MEBA was adjusted to 0.225 g to account for the change in monomer stoichiometry. Following degassing of the ‘complexation solution’ for 1 hr with argon, 1 mL of the ‘complexation solution’ was then added to 1 mL of the system **e** polymerisation solution within a 10mL round-bottomed flask sealed already containing the SAM chip using an argon purged syringe. For the MIPs, the final concentration of RNase B within each 2 mL of this solution was 0.23 mM.

The chips were then left to equilibrate within these 2 mL MIP or NIP polymerisation solutions for 5 minutes before the E-2-BB was then injected and left to polymerise for either 10, 20 or 60 minutes. Following the polymerisations, each chip was immediately removed from the solution, and then rinsed extensively with ultra-high pure H_2O, then the SPR acidic regeneration solution (to remove any RNase B bound to the surfaces), then again with ultra-high pure H_2O, for 3 minutes respectively. Each chip was then rinsed with HPLC grade EtOH and finally dried under a stream of argon.

17.0 Polymerising the 15:1 and 10:1 MIPs and NIPs using the pH Optimised Polymerisation Protocol

For the 15:1 and 20:1 MIP and NIP polymerisations, the same procedure as reported in section 16.0 was employed, however the amounts of BA per 1mL of complexation solution increased to 1.32 mg and 1.76 mg, respectively. For the MIPs, the amount of RNase B per 1 mL of complexation solution was kept constant at 6.8 mg. To account for the addition of the BA within the final 2 mL MIP or NIP polymerisations, the amount of MEBA within the 35 mL stock solution of the pH optimised polymerisation solution system **e** was adjusted to 0.213 g and 0.200 g, respectively.

As before following degassing of the 'complexation solution' for 1 hr with argon, 1 mL of the 'complexation solution' was then added to 1 mL of the system **e** polymerisation solution within a 10mL round-bottomed flask sealed already containing the SAM chip using an argon purged syringe. The chips were then left to equilibrate within these 2 mL 15:1 or 20:1 MIP or NIP polymerisation solutions for 5 minutes before the E-2-BB was then injected and left to polymerise for 20 minutes. Following the

polymerisations, each chip was immediately removed from the solution, and then rinsed extensively with ultra-high pure H_2O, then the SPR acidic regeneration solution (to remove any RNase B bound to the surfaces), then again with ultra-high pure H_2O, for 3 minutes respectively. Each chip was then rinsed with HPLC grade EtOH and finally dried under a stream of argon.

18.0 Calculation of the Ra Roughness from AFM of the MIP and NIP Surfaces

The Ra roughness of the NIP and MIP surfaces were calculated using the 'Statistical Quantities' tool of Gwyddion software (Version 2.51). Here, random points across the chip surfaces were selected and the Ra values recorded. The average Ra roughness was calculated from 3 points each from 3 individual chips (n=9).

19.0 CD of RNase B with Increasing Percentages (v/v) of MeOH

For both the increasing MeOH and thermal melt RNase B CD experiments, each sample was prepared using 0.1 M Potassium Phosphate Buffer pre-adjusted to pH 8.6. A stock of 1mM stock of RNase B was prepared using this buffer which was left for 20 mins to equilibrate, before being diluted with fresh buffer to 50 μM. For each variation in the % of MeOH (v/v), 1 mL of the 50 μM RNase B solution was mixed with 1 mL of buffer containing the proportion of MeOH at twice the required final MeOH % (v/v) to give 2 mL of 25 μM RNase B in the buffer/MeOH mixed solution. (For example: 1 mL 50 μM RNase B was mixed with 1 mL 100 % (v/v) MeOH to produce 25 μM RNase B in 50 % (v/v) MeOH). Once made each sample was wrapped in parafilm to prevent MeOH evaporation, incubated for 12 hours to

equilibrate and then measured with CD. For all experiments the cuvette was sealed with parafilm to prevent evaporation of the MeOH.

20.0 Complexations of RNase B with 3-Acrylamidophenyl Boronic Acid for ESI-MS

The buffer used in all ESI-MS studies was 0.1 % (w/w) ammonium acetate adjusted to pH 8.6 using KOH. The RNase B control was made by dissolving RNase B in buffer to a final concentration of 0.1 mM. For the RNase B x20 3-acrylamidophenyl boronic acid (BA) complexation study in buffer, 0.55 mg BA was added to 2.2 mg RNase B in 1.445 mL buffer to a final concentration of 0.1 mM. For the RNase B x20 BA complexation study in 75 % (v/v) buffer and 25 % (v/v) MeOH, 0.62 mg BA was added to 2.4 mg RNase B in 1.645 mL (of 1.234 mL buffer + 0.411 mL HPLC MeOH) to a final concentration of 0.1 mM. For the RNase B x100 BA complexation study in 75 % (v/v) buffer and 25 % (v/v) MeOH, 3.62 mg BA was added to 2.78 mg RNase B in 1.893 mL (of 1.419 mL buffer + 0.473 mL HPLC MeOH) to a final concentration of 0.1 mM.

The RNase A control was made by dissolving RNase A in buffer to a final concentration 0.1 mM. For the RNase A x20 BA complexation study in 75 % (v/v) buffer and 25 % (v/v) MeOH, 0.72 mg BA was added to 2.6 mg RNase A in 1.898 mL (of 1.423 mL buffer + 0.475 mL HPLC MeOH) to a final concentration of 0.1 mM. For the RNase A x100 BA complexation study in 75 % (v/v) buffer and 25 % (v/v) MeOH, 3.625 mg BA was added to 2.6 mg RNase A in 1.898 mL (of 1.423 mL buffer + 0.475

mL HPLC MeOH) to a final concentration of 0.1 mM. All complexations were left for 12 hours before then being submitted for ESI-MS.

21.0 Appendix

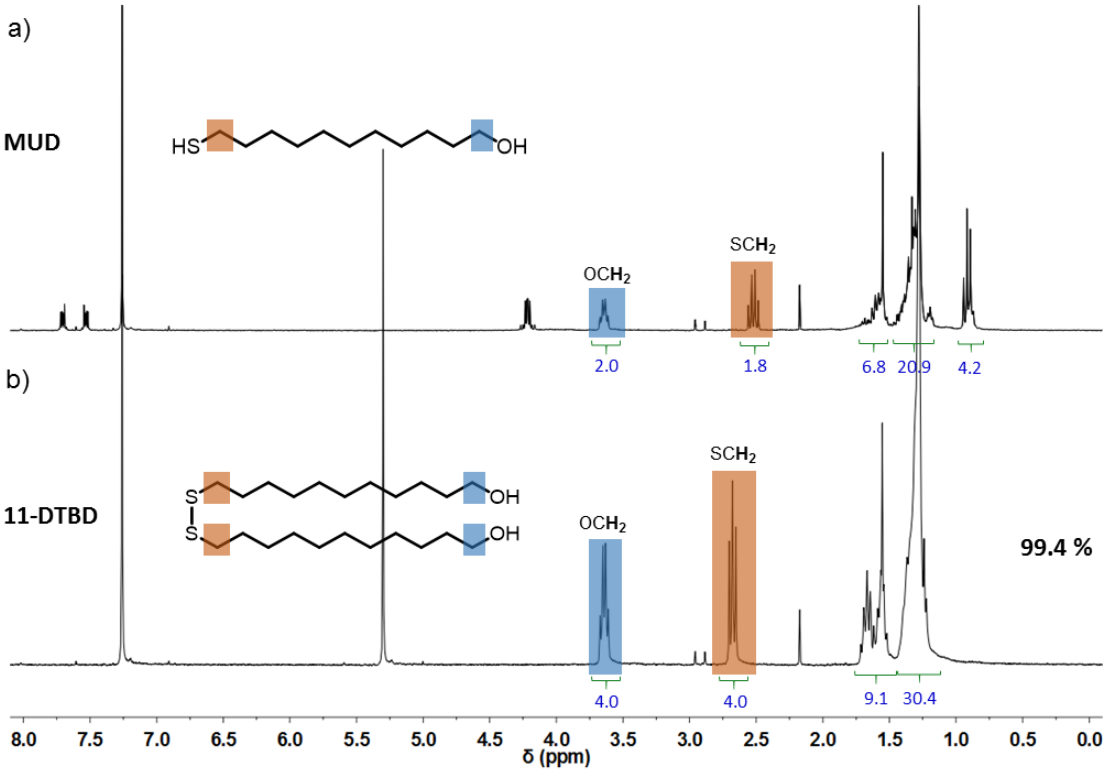

Figure 7.2: ^{1}H NMR spectra of MUD (**a**) and 11-DTBD (**b**). The integrals and resonance shifts for both molecules are as expected.

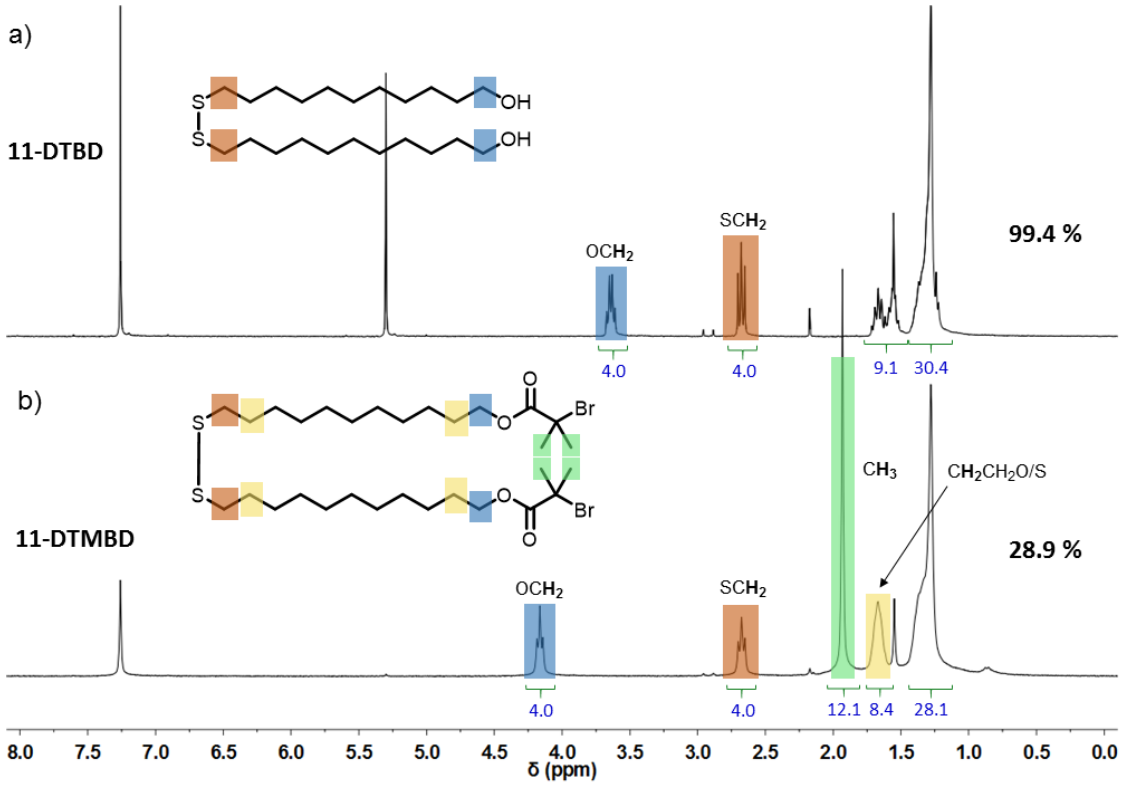

Figure 7.3: ^{1}H NMR spectra of 11-DTBD (**a**) and 11-DTMBD (**b**). The integrals and resonance shifts for both molecules are as expected.

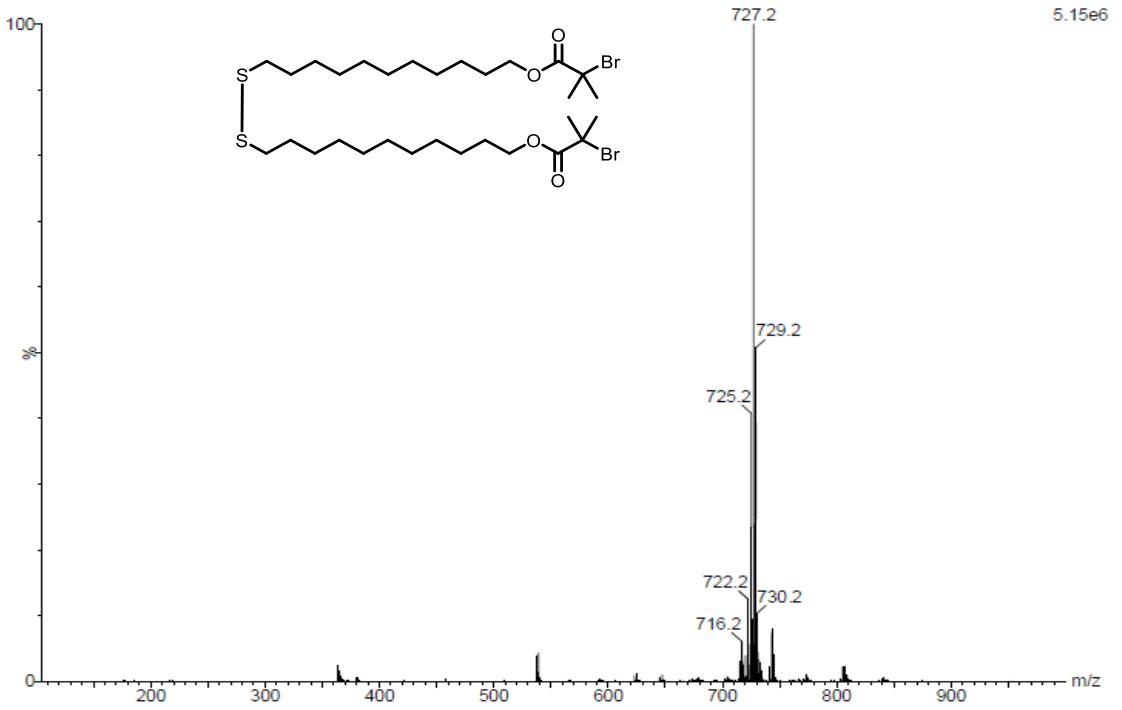

Figure 7.4: Mass Spectrometry Spectra of 11-DTMBD. The ionised mass peak at 727.2 corresponds with the correct mass of the molecule that has formed a salt adduct with sodium.

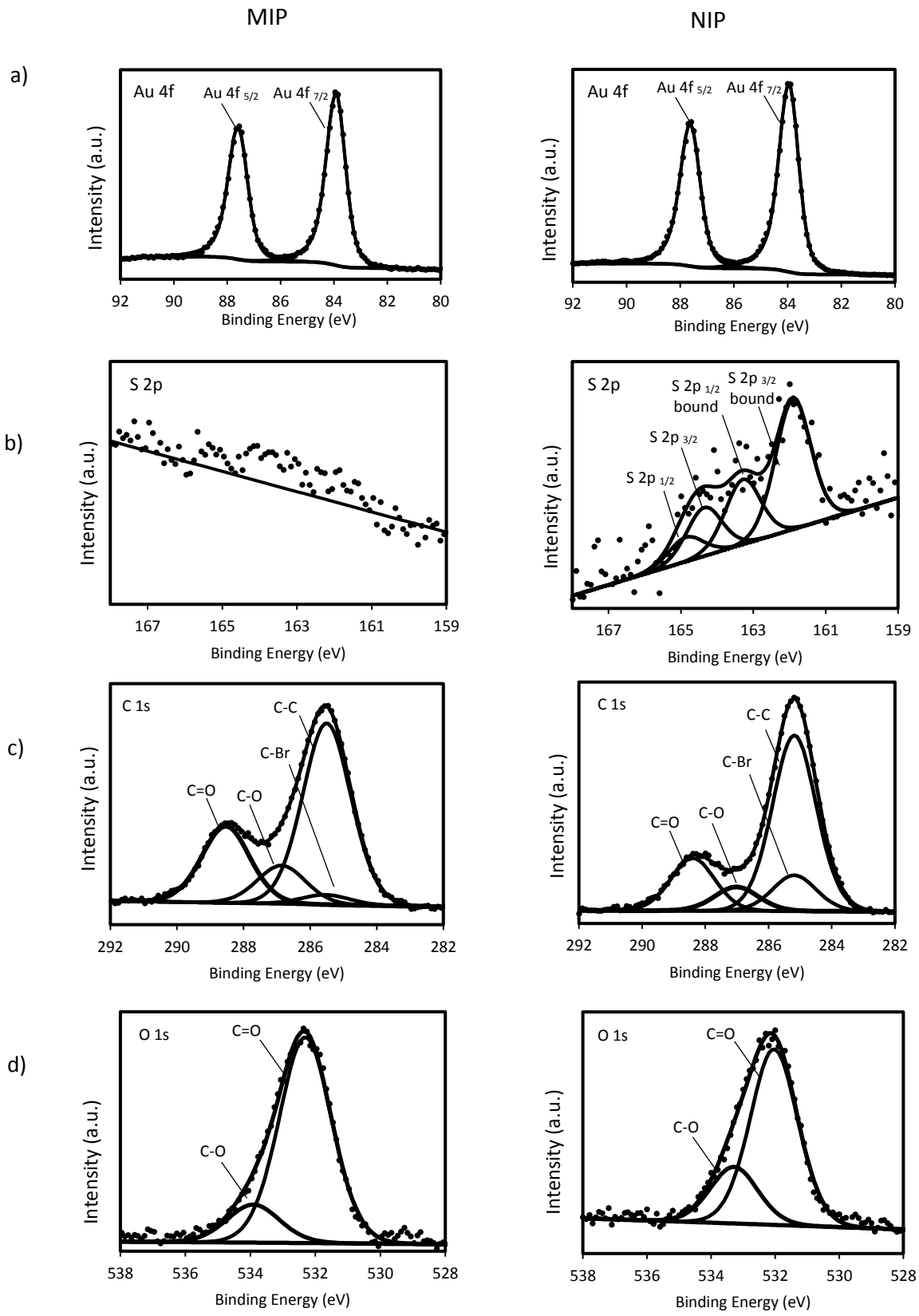
MIP
NIP
a)
Au 4f
Au 4f 5/2
Au 4f 7/2
Intensity (a.u.)
92 90 88 86 84 82 80
Binding Energy (eV)
b)
S 2p
S 2p 1/2 bound
S 2p 3/2 bound
S 2p 3/2
S 2p 1/2
167 165 163 161 159
c)
C 1s
C-C
C-Br
C=O
C-O
292 290 288 286 284 282
d)
O 1s
538 536 534 532 530 528

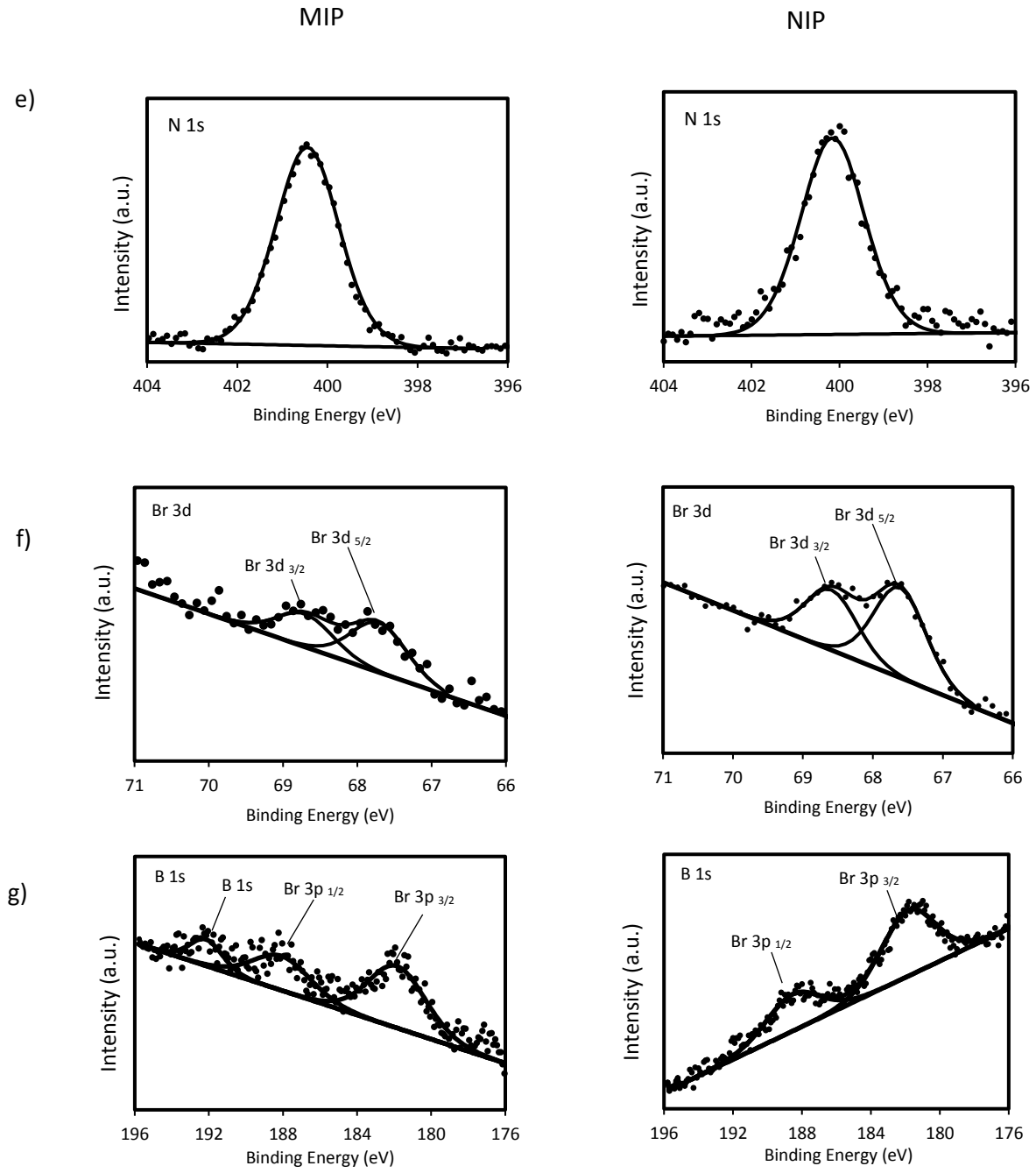

Figure 7.5: High resolution XPS scans of the 20 minute MIP (left) and NIP (right) of a) Au 4f, b) S 2p, c) C 1s, d) O 1s, e) N 1s, f) Br 3d and g) B 1s and Br 3p (Relevant to Chapter 5.0).

References

1. Shah, R.R., Merreceyes, D., Hendrick, J.L., *Using Atom Transfer Radical Polymerisation To Amplify Monolayers of Initiators Patterned by Microcontact Printing into Polymer Brushes for Pattern Transfer.* Macromolecules, 2000. **33**: p. 597-605.
2. Belegrinou, S., et al., *Efficient Two-Step Synthesis of 11,11'-Dithiobis[1-(2-bromo-2-methylpropionyloxy)undecane], a Conventional Initiator for Grafting Polymer Brushes from Gold Surfaces via ATRP.* Synthetic Communications, 2010. **40**(20): p. 3000-3007.
3. Greenfield, N.J., *Using circular dichroism spectra to estimate protein secondary structure.* Nat Protoc, 2006. **1**(6): p. 2876-90.